ISSN en trámite

Geofísica Internacional

Revista Trimestral Publicada por el Instituto de Geofísica de la Universidad Nacional Autónoma de México

México
Volume 52 Number 2
April- June
2013

— Geofísica Internacional —

GEOFÍSICA INTERNACIONAL, Año 52, Vol. 52, Núm. 2, abril - junio de 2013 es una publicación trimestral, editada por la Universidad Nacional Autónoma de México, Ciudad Universitaria, Alcaldía Coyoacán, C.P. 04150, Ciudad de México, a través del Instituto de Geofísica, Circuito de la Investigación Científica s/n, Ciudad Universitaria, Alcaldía Coyoacán, C.P. 04150, Ciudad de México, Tel. (55)56 22 41 15. URL: http://revistagi.geofisica.unam.mx, correo electrónico: revistagi@igeofisica.unam.mx. Editora responsable: Andrea Rostan Robledo. Certificado de Reserva de Derechos al uso Exclusivo del Título: 04-2022-081610251200-102, ISSN: en trámite, otorgados por el Instituto Nacional del Derecho de Autor (INDAUTOR). Responsable de la última actualización Saúl Armendáriz Sánchez, Editor Técnico. Fecha de la última modificación: 31 de marzo 2013, Circuito de la Investigación Científica s/n, Ciudad Universitaria, Alcaldía Coyoacán, C.P. 04150, Ciudad de México.

Geofísica Internacional

Vol. 52, Núm. 2, abril-junio de 2013

Contents

Geofísica
Internacional

Ometepec-Pinotepa Nacional, Mexico Earthquake of 20 March 2012 (Mw7.5): A preliminary report.

Universidad Nacional Autónoma de Méxic Seismology Group

Geofísica Internacional (2013) 52-2: 93-110

Original paper

Microscopy and rock magnetism of fine grain-size titanomagnetite from the Jacupiranga Alkaline Complex, Brazil: unearthing Ti-magnesioferrite nanoparticles

Luis M. Alva-Valdivia*, María de la Luz Rivas-Sánchez, Jesús Arenas-Alatorre, Avto Goguitchaishvili and Omar Ferreira Lopes

Received: November 07, 2011 ; accepted: November 15, 2012 ; published on line: March 22, 2013

Resumen

Se seleccionaron muestras muy finas de zonas mineralizadas del complejo Jacupiranga de la mina Cajatí para efectuar la identificación cristalográfica de nanoestructuras de titano-magnesioferrita (TMf) embebidas en titanomagnetita (TM) usando microscopía de transmisión de alta resolución (TEM). Se redujo un concentrado magnético a partir de muestras de piroxenita (sitios 4 a 7), después se dividió en fracciones de rangos de tamaño distintos: 26±2 μm, 19±1 μm, 13±1 μm, 9±1 μm, 6±1 μm and 6–0.1 μm. Las muestras mineralizadas de piroxenita y carbonatita se caracterizaron por: difracción de rayos-X, microscopía de luz transmitida y reflejada, y microscopía electrónica de barrido con análisis multielemental. La muestra de concentrado más fino (MC_6) se analizó por microscopía TEM y campo anular obscuro de ángulo alto y espectroscopía Ramán.

Se midieron las propiedades magnéticas de las distintas fracciones granulométricas, mostrando cambios drásticos cuando los tamaños de grano pasan de tamaños micro a nanométricos. El porcentaje de susceptibilidad magnética dependiente de la frecuencia ($\chi_{fd\%}$) arrojó valores altos (10.2%) para las fracciones más finas (6±1 μm y 6–0.1 μm), lo que se atribuyó a las fracciones dominantes de partículas superparamagnéticas. Los tamaños de grano nanométrico y < 6 μm de TMf en partículas de TM requirió de un campo magnético de hasta 249 mT para alcanzar la saturación durante los experimentos de magnetización remanente isotermal. La coercitividad y la magnetización remanente de esas muestras aumentaron cuando los tamaños de las partículas disminuían, probablemente debido a efectos de acoplamiento paralelo. Los experimentos de susceptibilidad magnética versus calentamientos se efectuaron dos veces en la misma muestra (<35 nm), mostrando que la repetibilidad durante el segundo calentamiento se debe probablemente a la formación de nuevas nanopartículas de TMf, y al crecimiento de las ya existentes durante el proceso del primer calentamiento.

Palabras clave: nanopartículas de titanomagnesioferrita, propiedades magnéticas, mineralogía, efecto del tamaño de grano, complejo alcalino Jacupiranga, Brasil.

L.M. Alva-Valdivia*
M.L. Rivas-Sánchez
Laboratorio de Paleomagnetismo
Instituto de Geofísica
Universidad Nacional Autónoma de México
Ciudad Universitaria, 04510
México DF, México
*Corresponding author: lalva@geofisica.unam.mx

J. Arenas-Alatorre
Departamento de Materia Condensada
Instituto de Física
Universidad Nacional Autónoma de México
Ciudad Universitaria, 04510
México DF, México

A. Goguitchaishvili
Laboratorio Interinstitucional de Magnetismo Natural
Instituto de Geofísica
Universidad Nacional Autónoma de México
Campus Morelia, Michoacán, México

O. Ferreira Lopes
Universidade Federal do Paraná
Departamento de Geologia
Jardim das Américas
Curitiba, Paraná, Brazil

Abstract

Very fine samples from the mineralized zones of the Jacupiranga complex at the Cajatí mine were selected for crystallographic identification of Ti-magnesioferrite (TMf) nanostructures embedded in titanomagnetite (TM) using high-resolution transmission electron microscopy (TEM). A magnetic concentrate obtained of pyroxenite samples (sites 4 to 7) was reduced and divided into fractions of distinct range sizes: 26±2 μm, 19±1 μm, 13±1 μm, 9±1 μm, 6±1 μm and 6–0.1 μm. The mineralized samples of carbonatite and pyroxenite were characterized by X-ray diffraction, transmitted and reflected light microscope, and scanning electron microscope with multielemental analysis. The finest magnetic concentrate sample (MC_6) was analyzed under high-resolution transmitted electron microscopy (TEM) and high angle annular dark field and Raman spectroscopy. Magnetic properties were measured for the distinct granulometric fractions, showing drastic changes when grain sizes go beyond the frontier from micro to nanometer sizes. Frequency-dependent magnetic susceptibility percentage ($\chi_{fd\%}$) report higher values (10.2%) for the finer fractions (6±1 μm and 6–0.1 μm) attributed to dominant fractions of superparamagnetic particles. Nanometer and < 6 μm grain size TMf in TM particles require a magnetic field up to 249 mT to reach saturation during the isothermal remanent magnetization experiment. Coercivity and remanent magnetization of these samples increase when the particle size decreases, probably due to parallel coupling effects. Magnetic susceptibility versus temperature experiments were conducted two times on the same (< 35 nm) sample, showing that the repetition during the second heating is probably due to the formation of new TMf nanoparticles and growth of those already present during the first heating process.

Key words: TMf nanoparticles, magnetic properties, mineralogy, grain size effect, Jacupiranga Alkaline Complex, Brazil.

Introduction

The ubiquity of tiny particles of minerals -mineral nanoparticles- in mineral deposits, oceans and rivers, atmosphere and soils are providing scientists with new ways of understanding Earth's processes. Our planet's physical, chemical, and biological processes are influenced or driven by the properties of these minerals. The way in which these infinitesimally small minerals influence Earth's systems is more complex than previously thought (Hochella *et al*., 2008).

Minerals have an enormous range of physical and chemical properties due to a wide range of composition and structure, including particle size. Nanominerals, however, have one critical difference: a range of physical and chemical properties, depending on their size and shape. This difference changes our view of the diversity and complexity of minerals, and how they influence Earth systems (Hochella, 2008).

Nanoscale structures are critical in determining the magnetic properties of minerals. Harrison (2007) describes that the fundamental importance of magnetism at this length scale has been overlooked in the past, leaving a number of long-standing paleomagnetic and rock-magnetic observations that could not be explained (Feinberg *et al*., 2007). Examples include the origin of strong and stable magnetic anomalies on Mars and the phenomenon of self-reversed thermoremanent magnetization (McEnroe *et al*., 2004). This gap in understanding arose because the technology required to study mineral magnetism with nanometer resolution had not been developed. We have now begun to establish quantitative links between the nanoscale structure of natural magnetic minerals and their macroscopic magnetic properties (Harrison, 2007).

For this study, we used the paleomagnetic samples from eight sites of the Jacupiranga alkaline-carbonatitic complex, Cajati mine, located at the southeastern region of Brazil (48°09'W, 24°41'S). The carbonatite belongs to the Jacupiranga Ultramafic Alkaline Complex of Early Cretaceous age (131 Ma, Ruberti *et al*., 2000). This Complex has an oval shape in a regional map showing Brazil and the study area (Figure 1).

One of its silicate rocks is widely known as "jacupirangite". Among carbonatitic phases, there are different compositions (calciocarbonatites to magnesiumcarbonatites) forming independent plugs, dykes and dyke swarms. The main mineralized geological setting can be recognized as formed by carbonatitic portions (both of calcic and dolomitic composition) separated by specific features as well as other lithological ore types, like minor portions of phoscoritic composition.

The aim of this study is to report the unearthing of TMf nanoparticles embedded in TM (finest magnetic concentrate) by crystallographic analysis of nanostructures using high-resolution TEM, and to determine the effect on the rock magnetic properties of its grain-size, and its influence on the origin and deposition environment.

Experimental methods and sample description

The eight paleomagnetic rock sampled sites (described in detail by Alva-Valdivia *et al*., 2009) are as follows: Site 1, coarse grain carbonatite;

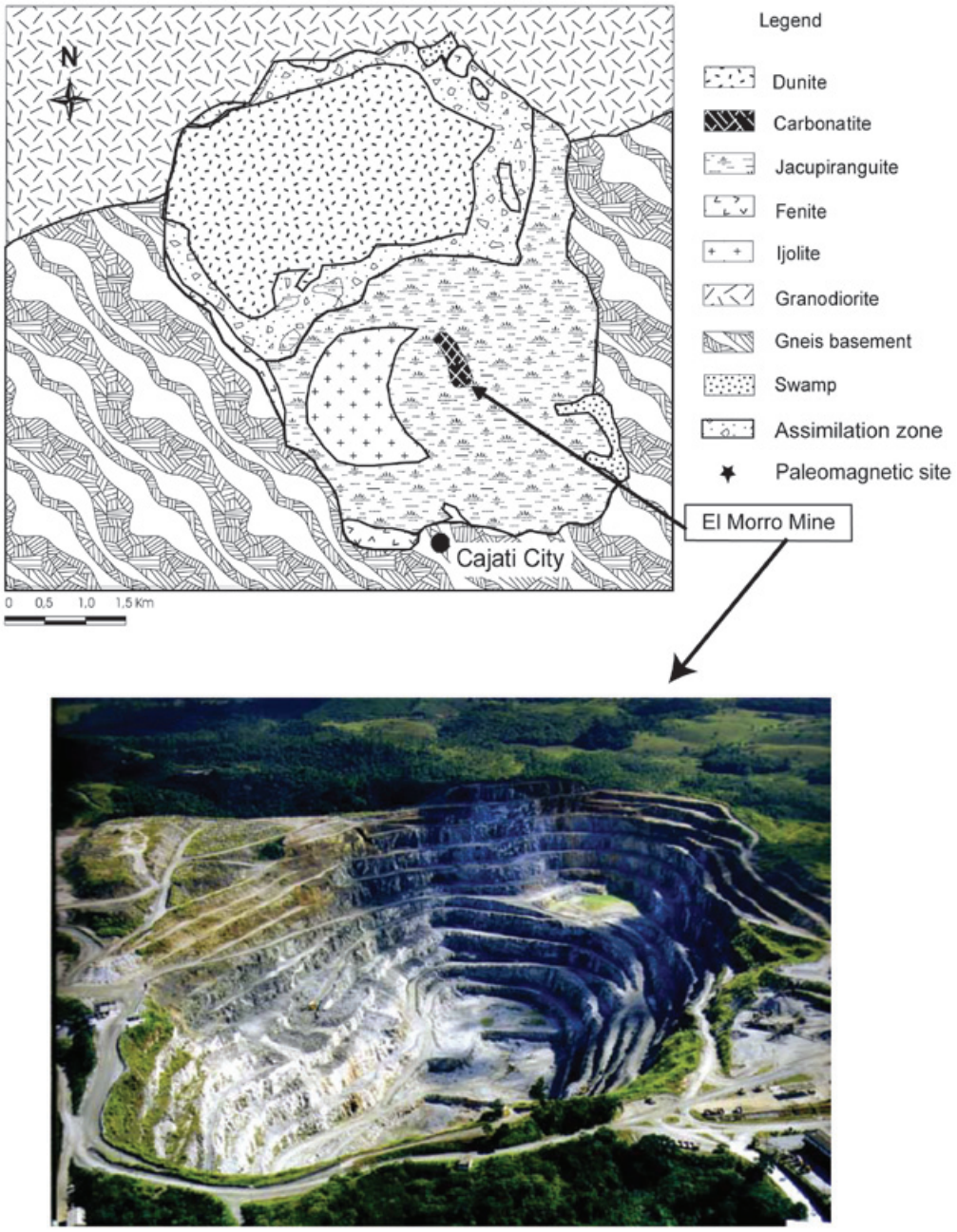

Figure 1. Location of the study area: precise location of sampled sites is in figure 1 of Alva-Valdivia *et al*. (2009).

Site 2, medium grain carbonatite; Site 3, fine grain carbonatite; Site 4, 5 and 6, pyroxenite Jacupiranga; Site 7, carbonatite- pyroxenite contact; and Site 8, granodiorite intrusive.

We select one paleomagnetic standard rock specimen (1" diameter and 2.2 cm long) from each pyroxenite site (4 to 7). Then all of the four samples were crushed together and put in a magnetic separator to get a magnetic concentrate of different grain-size fractions using the "hydrocycle method" (Rivas-Sánchez *et al*., 2009 describe in detail the equipment and crushing processes). Each specific size fraction was prepared with an average variation around one micron. Granulometric fractions are: MC_1 (26 ± 2 μm); MC_2 (19 ± 1 μm); MC_3 (13 ± 1 μm); MC_4 (9 ± 1 μm); MC_5 (6 ± 1 μm); and MC_6 (6 ~ 0.1 μm). These size fractions and the sample containing TMf nanoparticles (MC_6) were characterized according to their crystalline, physicochemical and magnetic properties.

Transmitted and reflected light microscopy study was done with a Leica DM-LP model; for X-ray diffraction (XRD) we used a Geiger-Flex model Rigaku difractometer, setting in an aluminum sample-holder of a non-oriented fraction, in the angular interval 2θ of 4° to 80° at two distinct velocities (1/2° by minute and 1° by minute); electron probe X-ray micro-analyzer (EPMA) JEOL, JXA 8900-R for multi-elemental analyses via WDS; Raman spectrometry was achieved by using a source of monochromatic infrared laser irradiation (dispersed radiation by molecules at a fixed angle was registered); and high-resolution TEM with a JEOL 2010 FEG FASTEM.

Magnetic susceptibility at varying frequencies was measured by using a Bartington Instruments MS2 linked to a MS2B dual frequency sensor. We used low frequency (χ_{lf} = 470 Hz) and high frequency (χ_{hf} = 4700 Hz) to detect qualitatively the presence of ultrafine grain size carriers of superparamagnetic (SP) behavior. The magnetic susceptibility as a function of temperature was determined by means of a Bartington MS2 susceptibilimeter, with a MS2W sensor coupled to a MS2WFP furnace. To measure the hysteresis parameters and isothermal remanent magnetization (IRM) acquisition and backfield demagnetization curves, we used an alternating field-force gradient magnetometer, Micromag 2900.

Results

Mineralogy and microscope analyses

Optical Microscopy

Alva-Valdivia *et al*. (2009) report petrography of the rock units, which have been studied again in order to look for details in the oxide minerals (Fe and Fe-Ti) and choose micro-areas with high probability of nanoparticle mineral occurrence.

At least one polished section from each site was studied by optical microscopy and EPMA in order to determine the composition and mineral textural relationships, which was later verified by XRD and Raman spectroscopy, as follows:

1) Carbonatites show an alotriomorphic granular mosaic of grain size ranging from 300 to 7,000 µm, formed mainly by non-metallic minerals of the carbonate group, as: calcite, dolomite and aragonite, all associated to apatite with minor amount of olivine (forsterite), phlogopite, pectolite, zircon and zirkelite. The metallic minerals are present in minor proportion and correspond to: magnetite, titanomagnesioferrite, scarce geikielite and sulfides (pyrite, pyrrothite and marcasite), filling open spaces between the primary minerals.

2) The pyroxenites have coarse-granular grain texture (220 to 1000 µm), composed mainly by non-metallic minerals: hedenbergite, diopside, and less apatite, Fe-Mg spinel and scarce quartz. The metallic minerals are: titanomagnetite, ilmenite, magnesioferrite, titanomaghemite (TMg) and titanohematite (TH), in minor proportion. These metallic minerals are filling open spaces in the host rock. Massive TM range in grain size from 380 µm to 6000 µm, with approximately 12% of Ti content slightly altered to TH, observed with graphic and lamellar intergrowths of ilmenite and ferrian spinel in a trellis type texture (Figure 2).

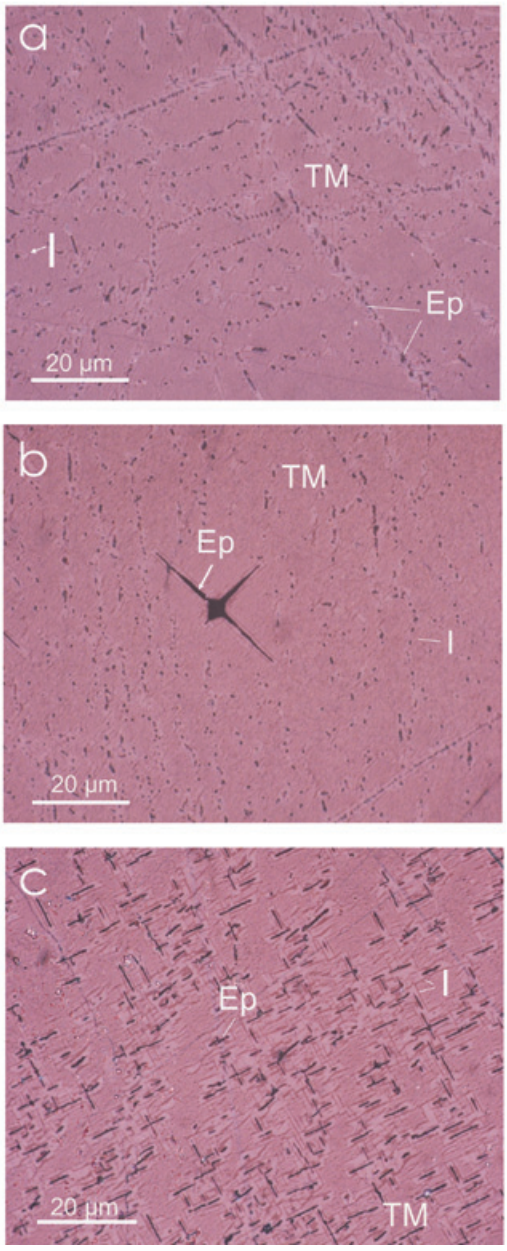

Figure 2. Representative photomicrographs of TM in pyroxenites using parallel nichols and reflected light. (a) ilmenite exsolutions (I) and Fe spinel (Ep); (b) ilmenite exsolutions and acicular shape of Fe spinel; and (c) exsolved ilmenite lamellas and Fe spinel.

3) Alva-Valdivia *et al*. (2009) confirmed the effect of hydrothermal processes in both rock types, as indicated by the next factors: a) In the carbonatite, the magnetite is massive and because of their relationship with rock forming mineral, suggests post-crystallization in relation to these minerals maybe during the latest phase of magmatic differentiation (possibly a high-temperature hydrothermal phase); b) In the pyroxenite, the TM form an altered metasomatic texture with pyroxene grains, suggesting the effect of hydrothermal processes of primary mineralization produced by the intrusive rock. They also report the presence of ionic exchange, Fe^{2+} by Mg in the mineralization of both rock types. In the carbonatite, they did not distinguish Ti in the selected micro-zones of magnetite and magnesioferrite, contrasting with the pyroxenite samples that show up to 10% of Ti in both titanomagnetite and magnesioferrite.

Summarizing, the petrographic characterization of the Jacupiranga complex, define two rock hosts type: carbonatite and pyroxenite. In these both rock types, Fe oxide minerals (magnetite and TM, respectively) are affected in its crystalline structure by partial substitution of Fe^{+2} by Mg, with formation to magnesioferrite. Being conspicuous the Ti enrichment of oxide mineral (Fe and Fe-Mg) of the pyroxenite. Optical microscopy shows a non-usual roughly texture of the TM with abundant ilmenite emulsion-type exsolution, magnesioferrite and Fe-spinel slightly detected at high amplification. Most of the exsolution measured are below 0.1 μm.

Mineral chemistry

Table 1 show results of mineral chemistry and structural formula of oxide minerals (Fe and Fe-Ti) identified in the carbonatite and pyroxenite. The quantitative chemical analyses were done by EPMA. In the carbonatite, the oxide minerals correspond to magnetite and magnesioferrite. In the pyroxenite, oxides show particular chemical characteristics in its structural formula, being conspicuous the TiO_2 presence. We named TM and TMf, with a structural formula of Ti content up to 12 and 14%, respectively. The Fe-Ti oxide corresponds to ilmenite.

In both rock types (carbonatite and pyroxenite), the oxide minerals are replaced by geikielite, and partial ion substitution of Fe^{+2} by Mg was observed, while geikielite is enriched in Fe.

X-ray diffraction (XRD)

To verify the occurrence of magnesioferrite, maghemite and hematite in the pyroxenite and ultramafic rocks, we used XRD, these minerals have an important amount of Ti, which was confirmed by the multielemental analyses of EPMA results via WDS. Because of the Ti presence, we add the prefix 'titano' to the minerals, changing to TMf, TMg and TH.

A mineralogical characterization by XRD analyses was done in an original natural sample (Table 2) that confirmed the magnesioferrite, maghemite and hematite presence. Figure 3a, and 3b shows well-defined peaks in the XRD spectra.

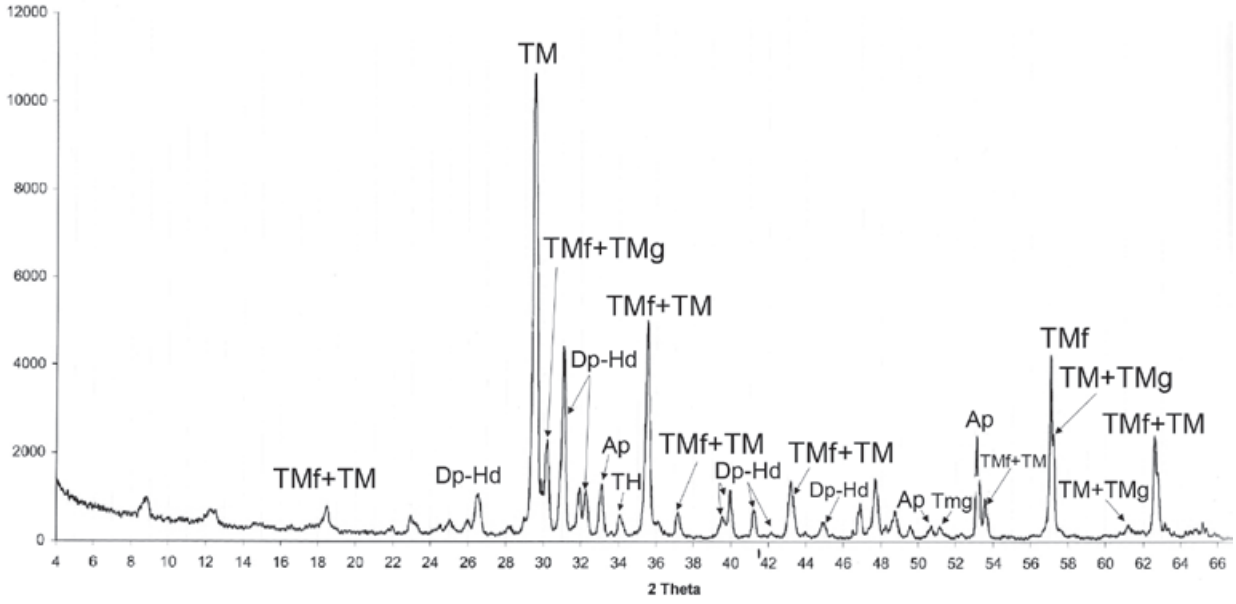

Figure 3a. XRD spectrum of the pyroxenite (Jacupiranga). TM, Ti-magnetite; TMf, Ti-magnesioferrite; TMg, Ti-maghemite; TH, titanohematite; Dp, diopside-hedenbergite; Ap, apatite.

Table 1. Mineral chemistry and structural formula of Fe oxides in pyroxenite.

Oxides and ions	1 Magnetite	2 Magnetite	3 Magnetite	4 Magnesio-ferrite	5 Magnesio-ferrite	6 Geikielite	7 Geikielite	8 Geikielite
Fe_2O_3	61.403	65.402	65.827	87.252	77.266	---	---	---
FeO	27.696	29.499	29.691	---	---	27.404	27.893	23.773
TiO_2	2.881	2.934	---	1.163	1.656	54.997	55.373	58.228
MnO	0.612	---	0.012	---	1.061	2.592	4.764	5.173
MgO	3.829	1.731	1.452	8.367	9.926	9.039	7.349	8.043
CaO	---	0.024	----	0.779	0.329	0.352	0.074	0.310
Cr_2O_3	---	0.349	0.332	---	---	---	1.417	---
NiO	0.636	---	0.936	0.738	0.986	2.129	---	1.451
SiO_2	0.459	---	0.209	0.819	0.626	0.885	---	0.379
Al_2O_3	---	---	0.186	0.734	1.933	---	---	---
Na_2O	2.044	---	0.073	0.327	3.897	---	---	0.705
K_2O	---	---	---	---	---	---	---	---
Σ	99.56	99.939	98.718	100.179	97.680	97.398	96.870	98.062
Fe^{+3}	13.891	14.868	15.349	17.899	16.180	---	---	---
Fe^{+2}	6.963	7.453	7.694	---	---	1.106	1.133	0.941
Ti	0.651	0.667	---	0.238	0.347	1.997	2.023	2.073
Mn	0.156	---	0.003	---	0.250	0.106	0.196	0.207
Mg	1.716	0.779	0.671	3.399	4.116	0.653	0.532	0.567
Ca	---	0.008	---	0.227	0.098	0.018	0.004	0.016
Cr	---	0.083	0.081	---	---	---	0.054	---
Ni	0.154	---	0.233	0.162	0.221	0.083	---	0.055
Si	0.138	---	0.065	0.223	0.174	0.226	---	0.096
Al	---	---	0.068	0.236	0.634	---	---	---
Na	1.191	---	0.044	0.173	2.103	---	---	0.065
K	---	---	---	---	---	---	---	---
Σ	24.861	23.858	24.208	25.557	24.123	4.189	3.942	4.020

Oxides and ions	9 Titano-magnetite	10 Titano-magnetite	11 Titano-magnetite	12 Titano-magnetite	13 Titano-mag-nesioferrite	14 Ilmenite	15 Geikielite	16 Geikielite
Fe_2O_3	52.018	54.403	53.229	54.797	72.253	---	---	---
FeO	23.462	24.583	24.009	23.916	---	42.439	25.812	24.468
TiO_2	12.182	12.917	13.007	12.920	14.839	42.424	60.620	60.905
MnO	1.626	1.127	0.486	0.885	0.695	0.252	0.366	1.288
MgO	3.554	3.352	3.589	3.174	5.086	9.638	11.542	10.357
CaO	---	0.401	0.190	---	0.426	0.374	0.034	0.618
Cr_2O_3	0.489	0.447	0.491	0.241	---	1.707	0.496	0.468
NiO	0.680	---	0.749	0.576	0.400	---	---	---
CoO	2.485	0.086	1.716	0.299	1.076	1.432	0.095	---
V_2O_3	---	---	0.425	0.023	---	0.253	---	0.576
SiO_2	0.395	---	0.125	0.450	0.215	---	---	---
Al_2O_3	2.428	2.453	2.188	2.450	4.925	1.203	0.207	0.232
Na_2O	0.483	0.395	0.212	0.073	---	0.280	0.714	0.184
K_2O	---	---	---	---	---	---	---	---
Σ	99.802	100.164	100.416	99.804	99.915	100.002	99.886	99.096
Fe^{+3}	11.184	11.584	11.315	11.667	14.166	---	---	---
Fe^{+2}	5.606	5.817	5.672	5.659	---	1.770	0.981	0.935
Ti	2.617	2.748	2.763	2.749	2.908	1.592	2.072	2.092
Mn	0.393	0.270	0.116	0.212	0.153	0.010	0.014	0.049
Mg	1.513	1.413	1.511	1.338	1.975	0.717	0.782	0.705
Ca	---	0.121	0.058	---	0.118	0.020	0.002	0.030
Cr	0.110	0.099	0.109	0.054	---	0.067	0.018	0.017
Ni	0.156	---	0.170	0.131	0.084	---	---	---
Co	0.569	0.019	0.388	0.067	0.225	0.057	0.004	---
V	---	---	0.079	0.004	---	0.008	---	0´017
Si	0.113	---	0.035	0.127	0.056	---	---	---
Al	0.818	0.818	0.729	0.817	1.513	0.071	0.011	0.013
Na	0.268	0.217	0.116	0.040	---	0.070	0.063	0.016
K	---	---	---	---	---	---	---	---
Σ	23.347	23.106	23.061	22.865	21.198	4.382	3.947	3.857

CARBONATITE:

1, 2, 3 Euhedral magnetite. Site 1

4, 5 Massive magnesioferrite. Site 1

6, 7, 8 Magnetite and magnesioferrite surrounded by geikielite, also filling open spaces between these minerals.

PIROXENITE JACUPIRANGA:

9, 10, 11, 12 Massive titanomagnetite

13 Titanomagnesioferrite exsolution in titanomagnetite

14 Ilmenite emulsion type exsolutions in the titanomagnetite

15, 16, 17 Geiquielite surrounding titanomagnetite and filling open spaces in this.

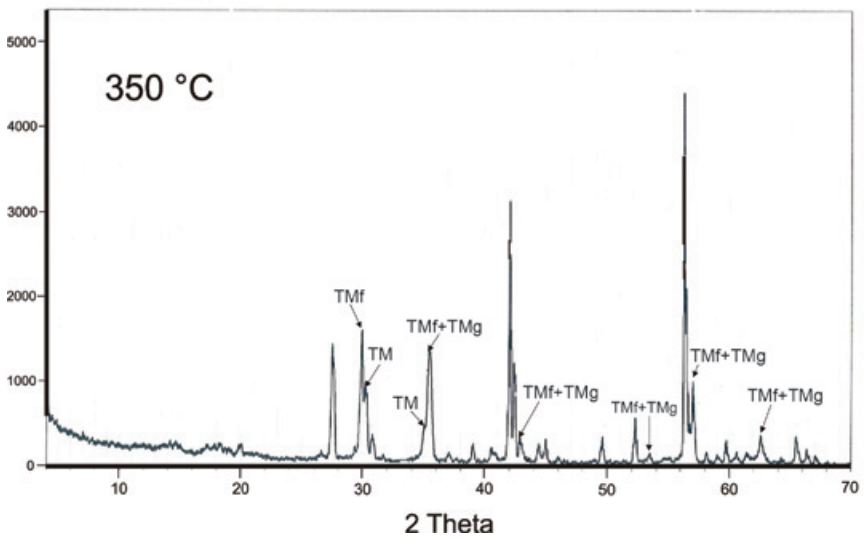

Figure 3b. The sample was annealed at 350ºC, and the residual material was analyzed by XRD. The diffraction spectra pattern (and structure) of Ti-maghemite increase with temperature.

Table 2. XRD results.

Sample	Mineral phase
Pyroxenite Jacupiranga	Magnetite: Fe_3O_4 [19-629] Magnesioferrite: $MgFe_2O_4$ [36-0396] Pyroxene group: diopside-hedenbergite: Ca(Mg, Fe) $[Si_2O_6]$[11-654, 25-160] Apatite: $CaF(Po_4)3$ [15-876] Maghemite: γ-Fe_2O_3 [4-0755] Hematite: α-Fe_2O_3 [89-0599]

Also, we got the mineral chemistry composition of the iron oxides identified in the carbonatite and pyroxenite host rocks, respectively, Table 1 (1 - 5 and 9 - 13).

Raman spectroscopy

We studied six samples of sites MC_4 and MC_5 corresponding to the ultramafic rocks (pyroxenite). Fine to ultrafine size of ilmenite disseminated in TM was identified by optical microscopy, showing exsolution emulsion-type shape. Figure 4 shows some Raman spectra examples of ilmenite from the Jacupiranga pyroxenite. These spectra show three distinctive peaks (ilmenite Raman), which appear at 220, 398 and 680 cm^{-1}, confirming that ilmenite is certainly present in this rock.

Raman spectra of selected regions of TM are shown in Figure 5. Magnetite is clearly identified by three peaks slightly moved regarding their wavenumber (cm^{-1}) due to the Ti presence. This spectra support the presence of TM with a content of TiO_2 up to 12%. We show the first TM Raman analysis, which allowed to establish their structural characteristics and assert their classification (chemical composition was determined by WDS).

High resolution TEM

TMf nanoparticles and likely ilmenite nanoparticles were identified in samples corresponding to the ultrabasic (pyroxenite) rocks. Nanoparticles are 5 to 10 nm size.

The crystallographic analysis of TMf structures was made with the purpose to determine the structural characteristics and assert its classification. We obtained (Figure 6) dark and clear (bottom) field high resolution and Fast Fourier Transform (FFT) (upper right) images by using the high resolution TEM. Each mineral nanostructure was crystallographically studied, measuring interplanar distances and getting their diffraction patterns.

TMf of nanometer scale was identified oriented along the edge [1 1 2] with interplanar distances d_1 = 2.98 Å, d_2 = 1.48 Å that correspond to the planes (220) and (311), respectively (Figure 6).

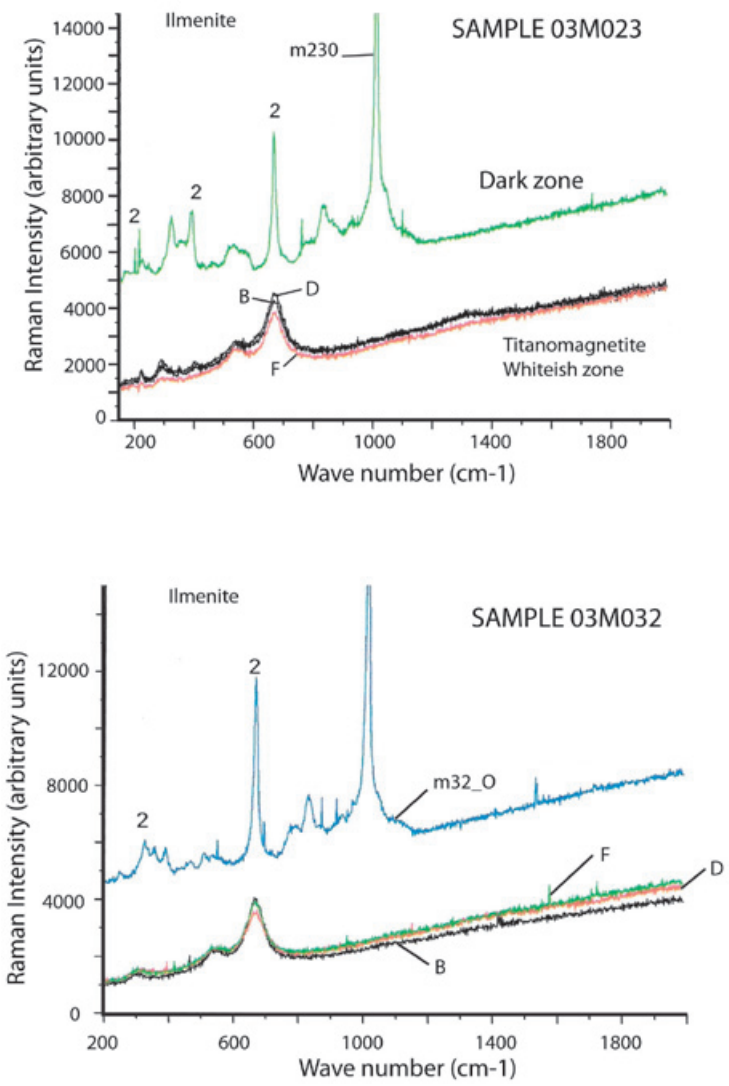

Figure 4. Raman spectra of selected regions indicating ilmenite from samples 03M023 and 03M032.

The possible ilmenite is oriented along the edge [1 0 4] with interplanar distances d_1 = 2.72 Å, d_2 = 2.52 Å that correspond to the planes (104) and (110), respectively, unfortunately was not possible to get a clear image of this mineral.

Rock and mineral magnetic properties of the pyroxenite

Frequency-dependent magnetic susceptibility percentage ($\chi_{fd\%}$).

We used a very small amount of natural material (magnetic concentrate) in order to avoid saturation of equipment and to reach better uniformity of the sample during the measurement. Carbonatites were not used for this experiment because they did not show any evidence (optical microscopy) of nanoparticles presence. The selected-analyzed samples by this technique correspond to TM and TMf with size range from 26 μm up to 0.1 μm (MC_1, MC_2, MC_3, MC_4, MC_5 and MC_6) (Table 3). We used the model proposed by Dearing *et al*. (1996) using theoretical predictions and data from synthetic grains and environmental samples, to suggest an interpretation of our results of frequency-dependent magnetic susceptibility: $\chi_{fd\%}$ < 5 in TM samples of 0.2 to 7 μm grain size are attributed to grains formed by the union of (assemblages) extremely fine particles (< 5 nm), together with the mineral concentration and grain size distribution; TM grain size of 0.1 μm to 26 μm range were identified with abundant inclusions of TMf nanoparticles; the fraction between 9 and 26 μm report low values of $\chi_{fd\%}$ < 5 attributed to the micro-nanometer textural association that mask the SP signal; finally, we obtained high values of $\chi_{fd\%}$ (9.6 and 10.2) for the fractions ranging from 0.1 to 6 μm, respectively (samples MC5 and MC6, Table 3), which suggests an important proportion of extremely fine particles (< 5 nm) of SP behavior.

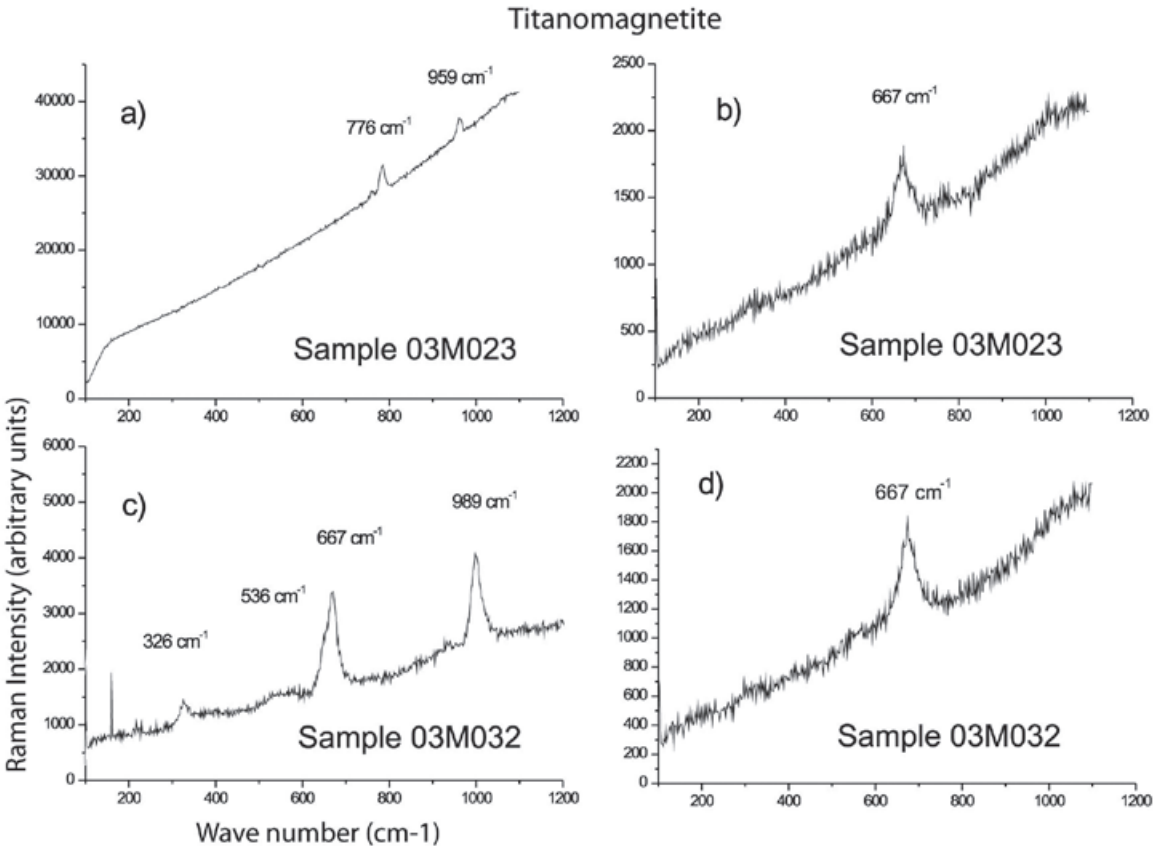

Figure 5. Raman spectra of selected regions pointing out to TM from pyroxenite Jacupiranga.

Rivas-Sánchez *et al*. (2009) reported similar values for samples with abundant magnetite nanoparticles included in berthierine: $\chi_{fd\%}$ = 3.4% in a magnetite sample constituted by 0.2 to 7 μm sizes, which are magnetite nanoparticles aggregates in a berthierine matrix. Corresponding Mössbauer spectroscopy for these samples indicate a 45.2% of SP particles, 44.8% for the ferromagnetic fraction, and a 10% of a paramagnetic fraction, of the total grain content. By association, these results support our conclusion about the SP dominant proportion grains in the sample of this study.

Magnetic susceptibility versus high temperature

Susceptibility vs. high temperature (*k*-*T*) experiments were carried out on the same samples described in Table 3. These magnetic concentrates (corresponding to TM with abundant ilmenite and TMf emulsion-type exsolutions) included samples

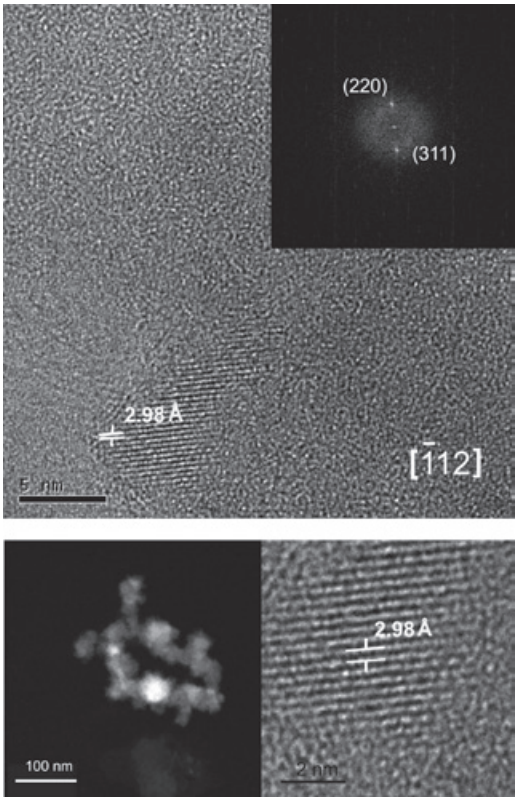

Figure 6. TMf nanostructure image obtained by high-resolution TEM (inset box shows the fast Fourier transform (FFT) analysis.

Table 3. Frequency dependent parameters and $\chi_{fd\%}$ of distinct magnetite grain size.

Sample	Size (μm)	Weight (g)	χ_{lf}	χ_{hf}	χ_{fd}	$\chi_{fd\%}$
MC_1	26 ± 2	1.1090	1018.03	991.88	0.025	2.57
MC_2	19 ± 1	0.7464	1158.89	1134.78	0.020	2.08
MC_3	13 ± 1	0.5068	1213.49	1156.27	0.047	4.71
MC_4	9 ± 1	0.5397	1013.53	972.76	0.040	4.02
MC_5	6 ± 1	0.6125	1182.04	1067.76	0.096	9.66
MC_6	6 ~ 0.1	0.6169	650.52	584.05	0.102	10.22

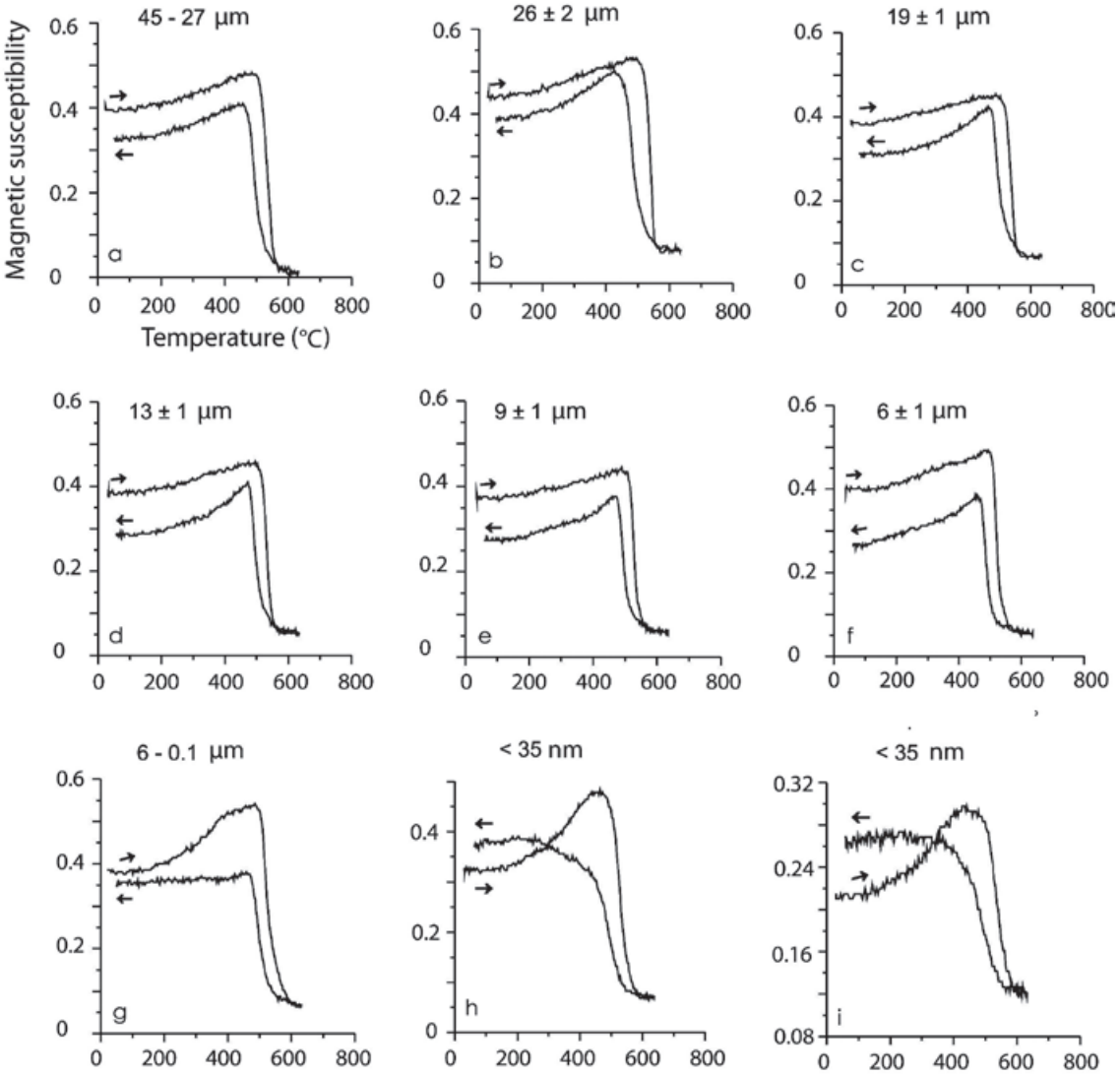

Figure 7. High-temperature *k-T* curves. Arrows indicate the heating/cooling curve. Experiments were done using magnetic concentrates of TM and TMf associated to ilmenite in agglomerated fractions of micrometric scale (a-g) and nanometric (h, i). The spectrum of (i) is the second run of the same heating as (h) in order to see the repeatability of this process during cooling phase.

in a size spectra from 45 to 9 μm show typical TM heating curves (soft Hopkinson peak and Curie temperature >550 °C) with slightly lower values on the cooling curves, effect of oxidation or partial transformation of TM to TMg (due to large amount of ilmenite and TMf exsolutions less than 1 μm size and inclusive at nanometer level). Dunlop and Özdemir (1997) describe that the multi-domain (MD) grains have a very soft Hopkinson peak, in comparison with those of single-domain (SD) grains. Accordingly, these curve types are typical for MD and SD grain sizes, considering that MD are > 2.0 μm and SD between 0.03 to 0.1 μm (Figure 7). Typical curves for minor grain size less than 6 μm (sample MC_6) shows a Hopkinson peak more conspicuous, related to a major content of < 1 μm particle size. In general, all curves show a delay during the oxidation from TM and TMf by temperature effect, with Curie temperatures higher that expected, 550 °C, the cooling curves are always lower than heating ones but the last two experiments, < 35 nm.

According to data presented in Table 2, magnesioferrite should be detectable in the *k-T* curves, which is not supported by the magnetic data because of the simple reason that our samples are magnetic TM concentrates. So, the least amount of magnetic minerals in these experiments obscures (mask) the possible response of the magnesioferrite.

Finally, two magnetic susceptibility versus temperature experiments of the same (< 35 nm) sample show that the repeatability during the second heating is probably due to the formation of new TMf nanoparticles and growth of those already present during the first heating process. Comparable results were reported by Rivas-Sánchez *et al*. (2009): 1) magnetite nanoparticles showed major resistance to heating; 2) formation of new magnetite nanoparticles; and 3) growing of those nanoparticles already present.

Hysteresis properties and isothermal remanent magnetization (IRM)

Hysteresis loop experiments obtained at room temperature at magnetic field strengths up to 1.5 T for the samples containing TM and magnesioferrite microparticles and range sizes described in Table 3 are shown in Figure 8. Table 4 shows a summary of the hysteresis parameters. The saturation remanent magnetization (Mrs), the saturation magnetization (Ms), and coercive force (Bc) were calculated after correction for the paramagnetic contribution. The coercivity of remanence (Bcr) was determined by applying progressively increasing backfield after saturation.

The general behavior of the hysteresis shaped loops like a ramp very close to the origin suggest TM, which is supported by the microscopic observations already described. These interpretations confirm the information coming from magnetic susceptibility experiments acquired with distinct frequencies that report high values of $\chi_{fd\%}$ for samples of particle size between 6 μm to 6-0.1 μm attributed to a dominant proportion of SP particles. It is remarkable that coercivity (Bc), in general, increase as the grain size decrease: from 26 μm, Bc= 14.6 mT up to Bc= 32.2 mT for sample size ranging from 6 to 0.1 μm. The Bcr/Bc ratio ranges from 1.784 to 1.590 and Mrs/Ms varies between 0.1491 and 0.2943 (Table 4). Rivas-Sánchez *et al*. (2009) obtained similar results by using agglomerates of magnetite nanostructures classified in micrometer sizes.

The hysteresis parameter plot indicates that all values fall in the PSD region (Figure 9). Day diagram (Day *et al*., 1977) shows a clear migration of the magnetization and coercivity ratios from PSD to SD, as grain size decreases.

Typical IRM acquisition curves for the TM – TMf of the same samples are shown in Figure 8 (inset).

Table 4. Hysteresis parameters.

Sample	Mr (μAm^2)	Ms (μAm^2)	Mr/Ms	Hc (mT)	Hcr (mT)	Hcr/Hc	W (mg)	Ms/W (Am^2/Kg)
26± 2 μm	15.60	104.6	0.1491	14.66	26.16	1.784	6.8	15.382
19± 1 μm	19.37	120.5	0.1607	15.42	25.54	1.656	12.0	10.041
13± 1 μm	19.16	107.7	0.1780	16.82	27.36	1.626	7.9	13.632
9± 1 μm	18.32	94.36	0.1941	18.39	29.94	1.628	6.4	14.743
6± 1 μm	25.87	118.6	0.2181	21.02	33.99	1.617	6.3	18.825
6~0.1μm	21.43	72.80	0.2943	32.20	51.22	1.590	12.6	5.777

W = weight

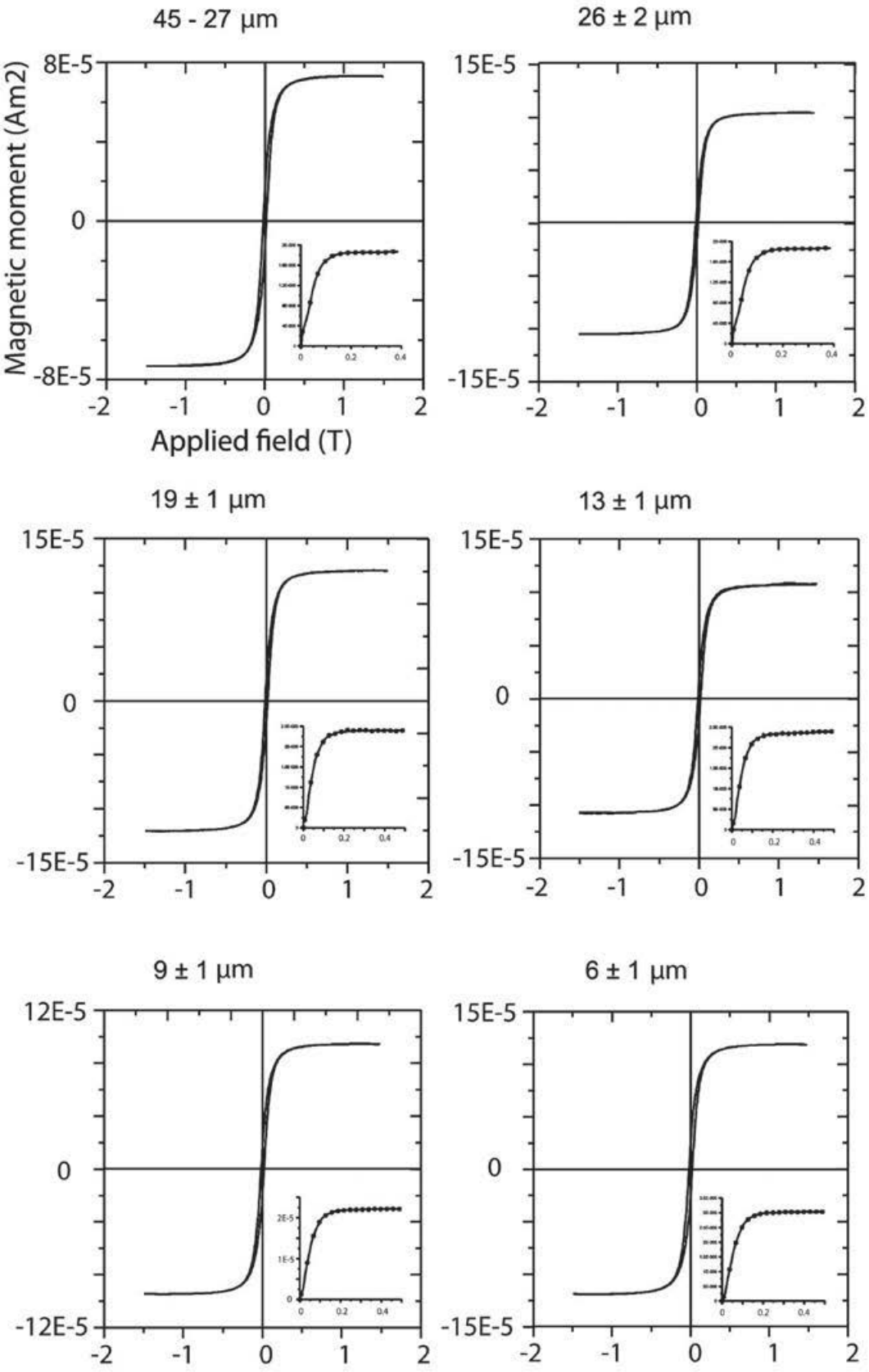

Figure 8. Hysteresis loops with paramagnetic correction for typical samples. Samples correspond to TM and TMf particles of distinct size ranges. Inset show isothermal remanent magnetization curves.

Figure 8. (Cont.)

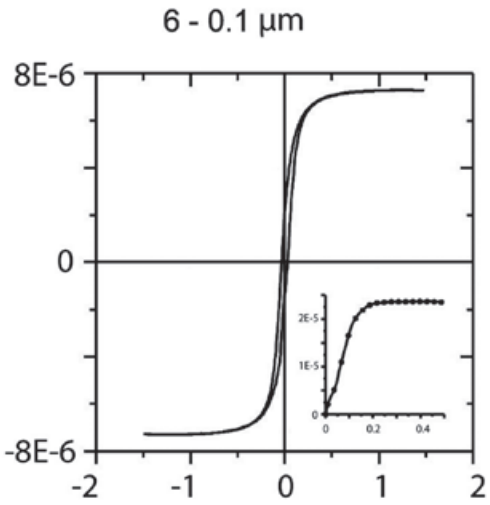

Major size samples show a rapid increase of the magnetization at low magnetic field and as the grain size decreases, a slightly larger magnetic field is required to get the saturation. The values to get this saturation are as follows: samples with sizes from 26 to 19 µm need 188 mT; samples ranging in size from 13 to 9 µm need 221 mT; and finally, samples with sizes lower than 6 µm require a magnetic field of 249 mT. All samples hold an important amount of SP particles. Rivas-Sánchez *et al*. (2009), conclude that the behaviour of magnetic properties is attributed to their atomic packing, textural arrangement, grains size, and that magnetite nanoparticle agglomeration requires that its magnetic domains display a distinctive behaviour in which SP properties and a major coercitive force require a major magnetic field intensity to reach saturation field.

Petrogenesis and metallogenesis

Alva-Valdivia *et al*. (2009) and Alva-Valdivia and López-Loera (2011) reported mineralogical and physical-chemical properties (host rocks and magnetic minerals). In this work, we did detailed observations of oxide minerals, their alteration minerals, mineralogical associations and textural relationships, which allow us to establish the paragenetic sequence of ultramafic rocks: a) In the carbonatite this is magnetite – magnesioferrite - geikielite; and b) In the pyroxenite this is TM – ilmenite – TMf – TMg – geikielite - TH. It is significant in this last sequence the roughly felted texture of the TM and its relation with micro- and nanometric scale TMf and ilmenite, which later were confirmed by high-resolution TEM observations.

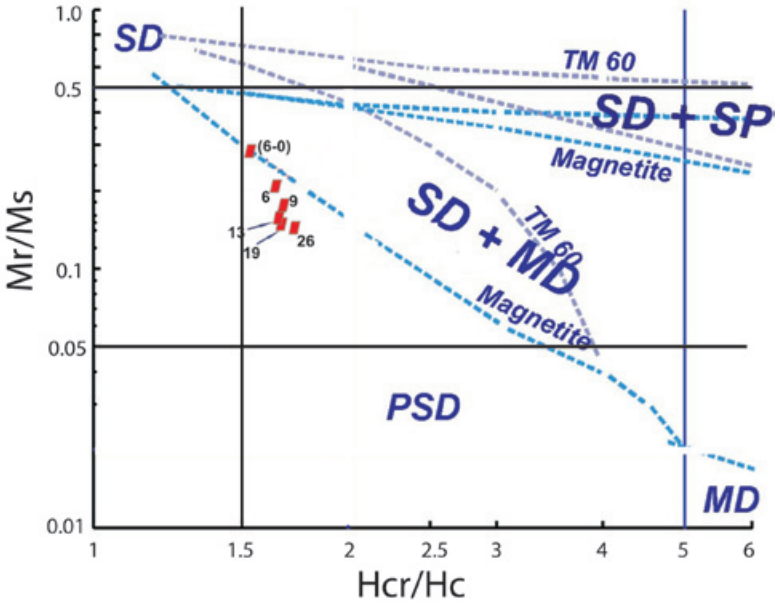

Figure 9. Day plot data for each fraction grain size (see numbers in microns).

The paragenetic sequence of the magnetic minerals in carbonatite and pyroxenite are distinctive of the magmatic and hydrothermal conditions during their formation, which is controlled by its crystallization-differentiation order, where the hydrothermal phase is the last one.

The chemical nature and structural formula of the magnetic mineralogy in carbonatite, shows 0 to < 2% TiO_2 content in the magnetite-magnesioferrite sequence, which is contrary to the magnetic mineralogy of the pyroxenite with TiO_2 >10% content suggesting the use of "titano" prefixe to the magnetic mineral name of the pyroxenite.

The magnetic mineralization of carbonatite and pyroxenite are analogous mineralizations affected by partial substitution of Fe-ferrous by Mg. This type of ionic exchange was produced by circulation Mg-rich hydrothermal solution through porous and open spaces that substitute the Fe^{+2} of the magnetic mineralogy, making it Mg-rich. This process allowed that mineralization changed gradually from a magmatic body to high temperature hydrothermal, where Mg-rich magnetite and TM produced magnesioferrite and TMf in the carbonatite and pyroxenite, respectively.

The progressive change of primary mineralization is produced by a complex system of hydratation reactions and ionic exchange between the primary mineralization of the intrusive body and solutions, changing the composition of the hydrothermal fluid, its pH and the redox state (Tornos, 1997). The mineralization change gradually and its mineral chemistry and textural relations (size-shape) are affected drastically up to reach equilibrium. This progressive equilibrium process can explain the TMf, and possibly Fe-spinel and ilmenite nanoparticles formation. Ilmenite and Fe-spinel nanoparticles, in the pyroxenite, probably were formed during the last magmatic differentiation process.

We show quantitative results in terms of well-identified grain-size distribution that support the general theoretical basis of frequency-dependent magnetic susceptibility (Table 3) (Dearing *et al*., 1996). We observed the effect in natural TM comprising TMf particles with micro- to nanometer grain size.

Ti-magnetite and TMf particles ranging from 9 to 26 μm, provided low values for $\chi_{fd\%}$ < 5, probably due to the close association (amalgamation) of magnetic domains at micro-nanometer scale, where TM mask the SP signal of the TMf nanoparticles.

The results of a magnetic susceptibility vs. high temperature experiment of the < 35 nm of TM containing TMf nanoparticles sample produces a repetible curve (Figure 7 bottom right), which repeated in rapid succession suggest the probable formation of new TMf nanoparticles, which is similar to the results obtained by Rivas-Sánchez *et al*. (2009) and Hirt and Gehring (1991).

The first evidences of a hydrothermal process in carbonatite and pyroxenite are indicated by the next factors:

1. Texture (size-shape). In the carbonatite, magnetite is massive and surrounds the minerals forming the rock as apatite, forsterite, carbonates and phlogopite (Figure 10b, d, e, f), demonstrating its later crystallization to these forming minerals during the last magmatic differentiation phase that could be high-temperature hydrothermal. In the pyroxenite, TM formed afterwards showing a metasomatic texture with pyroxene grains (hedenbergite), evidencing the hydrothermal fluid reaction with the primary mineralization (TM with ilmenite exsolutions) of the intrusive rock previously consolidated. This event favored the TMf nanoparticle formation with Ti.

2. Fe^{+2} by Mg ionic exchange occurs in the metallic mineralization of carbonatite and pyroxenite. In the carbonatites, magnetite contains up to 4% of MgO and when this increase magnetite is transformed into magnesioferrite. In general, magnetite shows reaction borders when is in contact with dolomite (Figure 10e, f). The pyroxenite, TM and ilmenite exsolutions contain MgO, which remains constant from 3.5% and 9.5%, respectively, and TiO_2 is up to 10%. It is important to observe that in the carbonatite samples there are magnetite and magnesioferrite contained in some microareas with almost nothing Ti, contrary to the pyroxenite Jacupiranga samples.

3. Mineral chemistry. The TiO_2 content in the magnetite and magnesioferrite of the carbonatite is almost zero, in contrast with the TiO_2 of the TM and TMf of the pyroxenite that remains constant from 12% to 13%, as well as MgO in minor amounts to 3.5% and less that 1.7% of MnO (Table 1). The magnesioferrite contains more than 5% of MgO and few amounts of TiO_2 and MnO close to that of magnetite (Figure 11). Fe-mineralization of both rock types is replaced by geikielite along its borders and cross lines forming well developed parallel lamellas.

4. The paragenetic sequence of metallic mineralization of carbonatites and pyroxenites was inferred since the evidences showed above, which are closely related to their texture and mineral chemistry. So, we propose a hydrothermal effect in

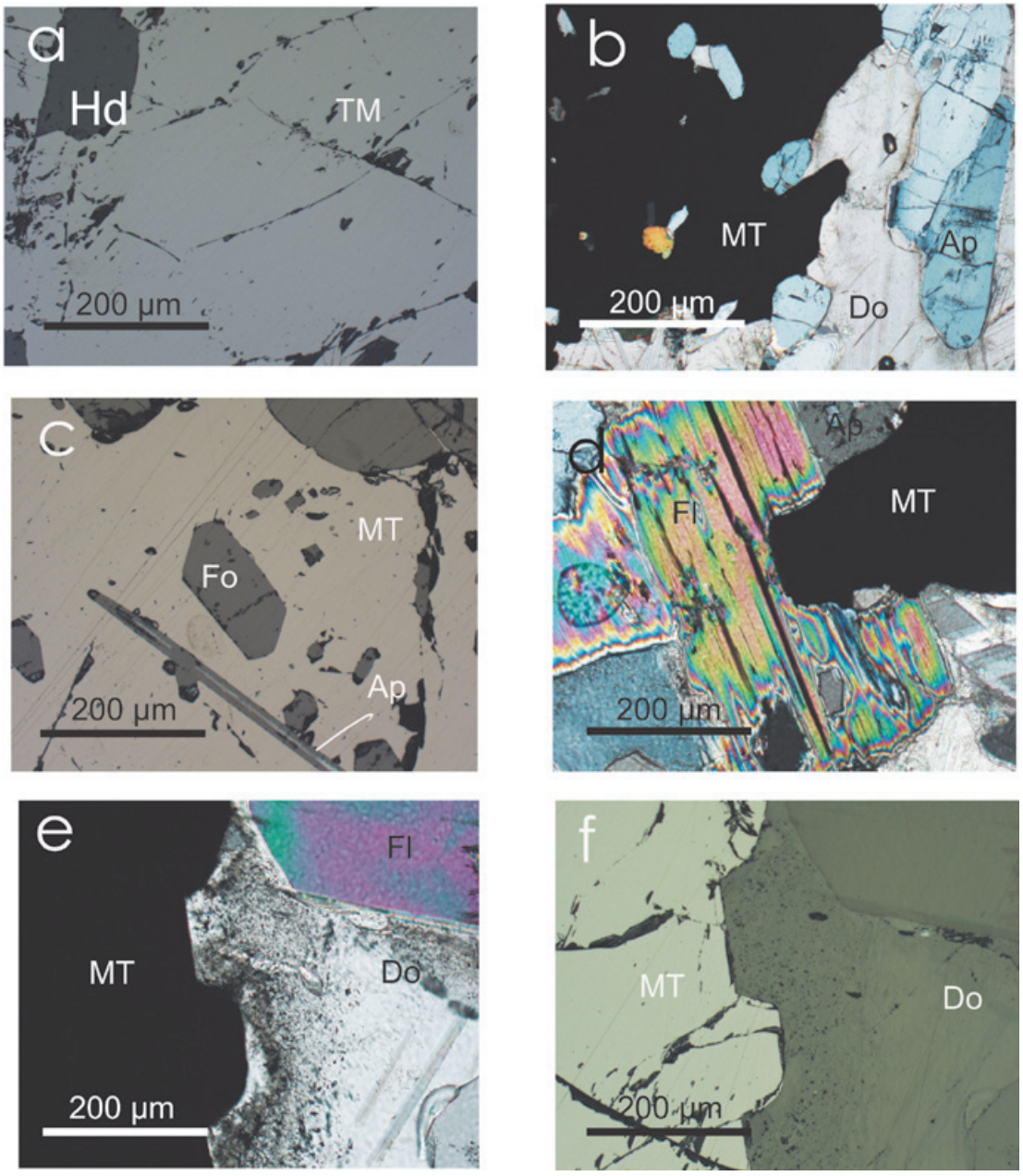

Figure 10. Optical microscope microphotographs of distinct textural aspects of massive Ti-magnetite (TM) in piroxenite and magnetite (M) in carbonatite with associated minerals: a) Massive Ti-magnetite with hedenbergite (Hd); b) Magnetite surrounding euhedral and subhedral crystal of apatite (Ap) and dolomite (Do); c) Forsterite (Fo) and apatite in the massive magnetite; d) Phlogopite sheet (Fl) cut by massive magnetite; and f) Massive magnetite in contact with dolomite, showing reaction borders and possible ionic exchange.

both rock types that occurred at the last magmatic differentiation phase. This process provoked metasomatism in the pyroxenite by reaction of the hydrothermal fluid with pyroxene intrusive massif that favored a chemical-mineralogical and textural change of the primary TM and ilmenite. All of this has an effect on its chemical composition that was enriched with Mg and its later partial transformation of the TM to TMf. It took also place a drastic change of its texture, forming TMf nanoparticles, and possibly spinel and ilmenite at nanometer scale. In the carbonatite, the hydrothermal process happened possibly at the same time that the formation of magnetite, enriched in Mg, forming the magnesioferrite. The geikielite was deposited later and replaced to the magnetite-magnesioferrite.

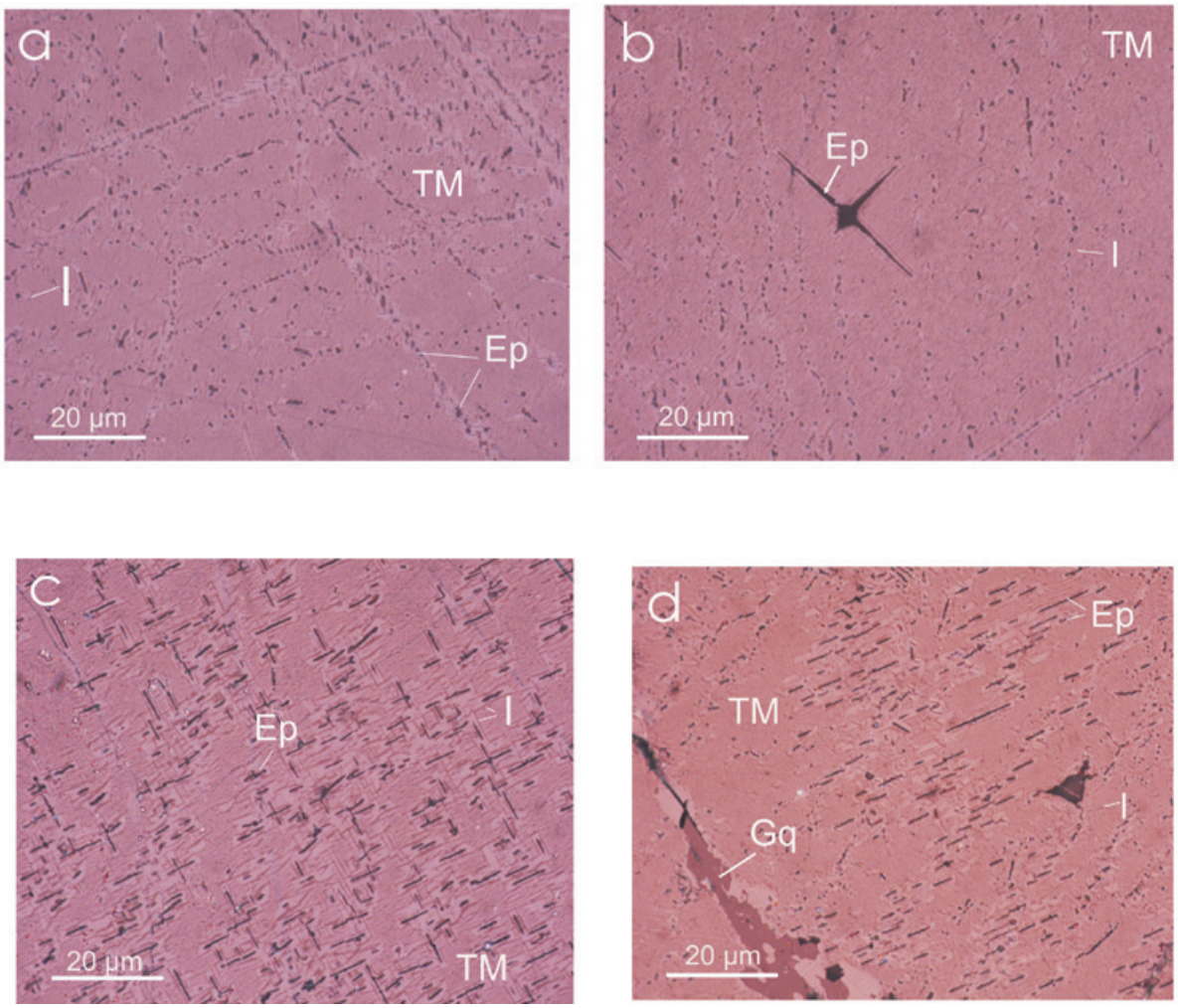

Figure 11. Optical microphotographs of metallic minerals in the pyroxenite: a-d) TM with abundant ilmenite (I) exsolutions and Fe spinel (Ep) homogeneously distributed.

Discussion

Our first results (Alva-Valdivia *et al*., 2009) show a complex mineralogy of the pyroxenite respect to the carbonatite that led to a detailed mineralogical study using magnetic concentrates of distinct grain sizes ranges. The magnetic concentrate is characterized by TM particles with TMf inclusions of nanometer and micrometer scale, ilmenite emulsion-type and Fe-spinel acicular exsolution. The ilmenite textural characteristics suggest that it is very probable to find it at nanometer scale. A minor proportion of TM particles are partly altered to TMg through the concave fractures and TH replacing TM along their cross lines forming trellis type texture associated to geikielite, pyroxene (hedenbergite-diopside) and apatite. An estimated proportion of metallic minerals of this sample is: TM, 51%; TMf, 22%; ilmenite, 6%; Fe spinel, 5%; Ti-magemite, 4% and Ti-hematite, 3%.

XRD analyses confirmed the existence of magnesioferrite and maghemite, their chemical composition and the structure formula: finding the TMf in our pyroxenite samples. Raman spectroscopy verified the ilmenite.

EPMA (using WDS) defined the chemical formula and structure of the complex Fe-Ti oxide minerals, being relevant for the Ti detection. We use the name of TM and TMf, for a structural formula of TiO_2 content up to 12% and 14%. The mentioned studies guide the selection of samples to perform the high-resolution TEM that identified the TMf nanoparticles of 5 to 10 nm size.

The magnetic concentrate is characterized by TM particles of less than 26 µm grain size, with TMf inclusions of nanometer and micrometer scale. The TM particles also have ilmenite emulsion-type and Fe spinel acicular exsolutions,

Mg (Al, Fe)$_2$ O$_4$, both homogeneously distributed. Ilmenite textural characteristics suggest that it is very probable to find it at nanometer scale. An estimated proportion of metallic minerals of this sample is: TM, 51%; TMf, 32%; ilmenite, 10%; and Fe spinel 7%. Because of its chemical characteristics, we use the name of TMf, with a structural formula of Ti content up to 8%. The HRTEM study was performed using the magnetic concentrate of MC6 sample.

The rock magnetic properties of the Fe-Ti oxides ($\chi_{fd\%}$, *k-T* curves, hysteresis properties and IRM acquisition curves) support the finding of extremely fine particles (nanometer size) forming bigger (micrometer size) amalgamated particles. Sometimes, the rock magnetic signal are masked by stronger magnetic minerals (TM), making very difficult the definition of weaker magnetic TMf minerals.

We found by high resolution TEM that the TM and TMf form micrometer and nanometer crystalline structures, with specific and distinctive interplanar distances: for 3.00 Å and 2.56 Å TM, and 2.98 Å for TMf. The differences in grain size, represented by TM microparticles interacting with TMf nanostructures give rise to an interference in the ferromagnetic and SP signal, with the increase of the hysteresis parameters and important changes in the magnetization with decreasing of micrometer particle size.

Typical curve for *k-T* experiments of minor grain size less than 6 μm (sample MC$_6$) shows a Hopkinson peak more conspicuous, related to a major content of particles < 1 μm. In general, all curves show a delay during the oxidation from TM and magnesioferrite by temperature effect, with Curie temperatures higher that expected, 550 °C, the cooling curves are always lower than the heating ones excepting the last two experiments, < 35 μm.

These two magnetic susceptibility versus temperature experiments of the same (< 35 nm) sample show that the repeatability during the second heating is probably due to the formation of new TMf nanoparticles and growth of those already present during the first heating process. Similar results were reported by Rivas-Sánchez *et al*. (2009): magnetite nanoparticles showed major resistance to heating; and therefore to the new nanoparticle formation; and growing of those already existing during the *k-T* experiments.

The general behavior of the hysteresis curves is, like a ramp, very close to the origin.

The TM and TMf form micrometer and nanometer crystalline structures, with specific and distinctive interplanar distances: 3.00 Å and 2.56 Å for TM, and 2.98 Å for TMf, obtained by high resolution TEM. The differences in grain size, represented by TM microparticles interacting with TMf nanostructures provoke an interference in the ferromagnetic and SP signal, with the increase of the hysteresis parameters and important changes in the magnetization with decreasing of micrometer particle size.

Conclusions

This TMf particle study enabled to establish a better knowledge of their magnetic properties, mineralogical association and textural relationship (size-shape) with the TM. All of these information help to establish the paragenetic sequence and consequently the source of mineralization and deposition conditions.

The experience acquired during the progress of this work, demonstrate that TMf nanoparticles act like genetic guide regarding the environment conditions during their formation.

We identified TMf, and possibly spinel and ilmenite nanoparticles using the high-resolution TEM, which was supported by magnetic studies (magnetic susceptibility measured with distinct frequencies, magnetic susceptibility vs. high temperature curves, hysteresis analysis and IRM acquisition curves), and of course the mineralogical, chemical, mineral and textural relations of Fe-mineralization within carbonatite and pyroxenite. All of this supports the hypothesis of a high-temperature hydrothermal event during the final magmatic crystallization-differentiation process. This event affected the primary Fe-mineralization of the pyroxenite and at the same time of the carbonatite, producing the TMf in the pyroxenite by substitution of Fe^{+2} by Mg, as well as later deposition of geikielite and pyrite, pyrrhotite and marcasite.

Based on the mentioned magnetic properties, it was possible to choose sampling suggesting the presence of magnetic oxide nanoparticles, doing easier to look for the pursued nanoparticles by crystallographic and high-resolution TEM studies.

Acknowledgments

We are grateful for the kind cooperation of the engineering staff of Planejamento de Lavra/ Geologia, BUNGE Fertilizantes S/A Unidade Cajati. This research was funded by the CONACyT project No. 105194 and PAPIIT-UNAM project IN108711. We acknowledge to Dr. J. M. Yañez Limón and Dr. J. Trapaga from CINVESTAV for performance of Raman spectroscopy analyses, and C. Linares and M. Reyes for his great help in the EPMA study.

Bibliography

Alva-Valdivia L.M., Perrin M., Rivas-Sánchez M.L., Goguitchaichvili A., Lopez-Loera H., Ferreira Lopes O., Bastos Bonás T., 2009, Rock magnetism and microscopy of the Jacupiranga alkaline-carbonatitic complex, southern Brazil. *Earth Planets Space*, 61, 161–171.

Alva-Valdivia L.M., López-Loera H., 2011, A review of iron oxide transformations, rock magnetism and interpretation of magnetic anomalies: El Morro Mine (Brazil) a case study. *Geofísica Internacional,* 50, 341-362.

Day R., Fuller M., Schmidt V.A., 1977, Hysteresis properties of TMs: grain size and compositional dependence, Phys. *Earth Planet. Inter*., 13, 260–267.

Dearing J.A., Dann R.J.L., Hay K., Lees J.A., Loveland P.J., Maher B.A., O'Grady, 1996, Frequency-dependent susceptibility measurements of environmental materials, *Geophys. J. Int.*, 124, 228–240.

Dunlop D., Özdemir O., 1997, Rock-Magnetism, fundamentals and frontiers, Cambrige University Press, 573 pp.

Feinberg J.M., Harrison R.J., Kasama T., Simpson E.T., Dunin-Borkowski R.E., 2007, Electron Holography and Rock Magnetism: IRM Quarterly, 16, 4, p. 5.

Harrison R.J., 2007, The magnetic personality of minerals: from nano-scale microstructures to planetary-scale anomalies. Geol. Soc. Am. Denver Annual Meeting. Abstracts with Programs, 39, 6, p. 416.

Hirt A.M., Gehring A.U., 1991, Thermal Alteration of the Magnetic Mineralogy in Ferruginous Rocks. *J. Geophys. Res*., 96, B6, 9947–9953.

Hochella M.F., Jr., 2008, Nanogeoscience: From origins to cutting edge applications. *Elements,* 4, 373-378.

Hochella M.F. Jr., Lower S.K., Maurice P.A., Penn R.L., Sahai N., Sparks D.L., Twining B.S., 2008, Nanominerals, mineral nanoparticles, and Earth systems. *Science,* 319, 5870, 1631-1635, DOI: 10.1126/science.1141134.

McEnroe S.A., Skilbrei J.R., Robinson P., Heidelbach F., Lagenhorst F., Brown L.L., 2004, Magnetic anomalies, layered intrusions and Mars. *Geophys. Res. Let.,* 31, L19601, doi:10.1029/2004GL020640.

Rivas-Sánchez M.L., Alva-Valdivia L.M., Arenas-Alatorre J., Urrutia-Fucugauchi J., Perrin M., Goguitchaichvili A., Ruiz-Sandoval M., Ramos-Molina M.A., 2009, Natural magnetite nanoparticles from an iron-ore deposit: size dependence on magnetic properties, *Earth Planets Space,* 61**,** 151-160.

Ruberti E., Gomes C.B., Melchor G.C., 2000, The Jacupiranga Carbonatite Complex: geological and petrological aspects of the Jacupiranga alkaline-carbonatite association, southern Brazil, Post-Congress Field Trip Aft 08 Guidebook, International Geological Congress, Part I: 1–21, Rio de Janeiro, Brazil.

Tornos F., 1997, Procesos de alteracion y relleno hidrotermal sobre rocas silicoaluminınıcas, Atlas de asociaciones minerales en lamina delgada, Universidad de Barcelona, 249–271.

Geofísica Internacional (2013) 52-2: 111-120

Original paper

Geostatistical simulation of spatial variability of convective storms in Mexico City Valley

Javier Méndez-Venegas*, Martín A. Díaz-Viera, Graciela S. Herrera and Arturo Valdés-Manzanilla

Received: November 11, 2011; accepted: January 15, 2013; published on line: March 22, 2013

Resumen

La precipitación es uno de los factores principales del ciclo hidrológico y el conocimiento de su distribución espacial es fundamental para la predicción de otras variables ambientales íntimamente relacionadas como son: el escurrimiento, las inundaciones, la recarga de los acuíferos. La mayor parte de la precipitación en la Ciudad de México es producida por tormentas convectivas, caracterizadas por una alta variabilidad espacial, lo cual implica que la modelación de su comportamiento sea muy compleja. En el presente estudio se aplicaron técnicas de simulación estocástica con enfoque geoestadístico para modelar la variabilidad espacial de la precipitación de tres tormentas convectivas. El análisis de los resultados muestra que usando la metodología propuesta se obtienen distribuciones espaciales de lluvia que reproducen las características estadísticas presentadas en la información disponible.

Palabras clave: geoestadística, variabilidad espacial de la precipitación, simulación secuencial Gaussiana, cosimulación, tormentas convectivas, radar meteorológico.

Abstract

Precipitation is one of the main components of the hydrological cycle and knowledge of its spatial distribution is fundamental for the prediction of other closely related environmental variables, for example, runoff, flooding and aquifer recharge. Most of the precipitation in Mexico City is due to convective storms characterized by a high spatial variability, implying that modeling its behavior is very complex. In this work stochastic simulation techniques with a geostatistical approach were applied to model the spatial variability of the rainfall of three convective storms. The analysis of the results shows that using the proposed methodology spatial distributions of rain are obtained that reproduce the statistical characteristics present in the available information.

Key words: geostatistics, rainfall spatial variability, sequential Gaussian simulation, cosimulation, convective storms, meteorological radar.

J. Méndez-Venegas
G. S. Herrera
Instituto de Geofísica
Universidad Nacional Autónoma de México
Ciudad Universitaria
Delegación Coyoacán, 04510
México D.F., México
**Corresponding author: lemendez84@yahoo.com.mx*

M. A. Díaz-Viera
Programa de Recuperación de Yacimientos
Instituto Mexicano del Petróleo
Del. Gustavo A. Madero

A. Valdés-Manzanilla
División Académica de Ciencias Biológicas
Universidad Juárez Autónoma de Tabasco
Villahermosa, Tabasco

Introduction

One of the most modern instruments to estimate rainfall is meteorological radar. It cover a large area (about 200 km in radius); although the estimates are not precise, due to inherent errors of the instrument itself: anomalous propagation, attenuation, etc.; to its surroundings: beam blocking due to mountains, false echoes, evaporation, etc. (Zawadzki, 1984); and to the estimation algorithms (Seo and Krajewski, 2011). The rain gauge has been the traditional instrument for rainfall estimation due to its good precision, though representativeness of its measurements is of a few meters around the instrument. Many countries of the world, to take advantage of both instruments, have systems that estimate rainfall based on a combination of meteorological radar and rain gauge estimates. However, rainfall estimation becomes very complicated when the spatial distribution is very variable, which is the case of convective or electrical storms. Various geostatistical techniques to estimate rainfall using Kalman filters (Anhert *et al*., 1986) or geostatistical estimation methods such as kriging (Krajewski, 1987) have been developed.

Since 1995 a network of 13 C-band Doppler meteorological radar equipment exists in Mexico (Valdés-Manzanilla and Aparicio, 1997). Their main objectives are to monitor the tropical cyclones in or near the Mexican national territory and to estimate rainfall with hydrological purposes. One of these radar stations is near the metropolitan area of Mexico City, at the top of Cerro de la Catedral. Also, a network of digital rain gauges with telemetry, owned by the government of Mexico City, covers much of the city area.

Because of that, Valdés-Manzanilla and Herrera (2002) designed a rainfall estimation method using both sources of meteorological information. A Kalman filter was used to calculate optimally, in real time, the mean error between rainfall estimated by radar and the one estimated by rain gauges. After applying this technique to two convective storms, the root mean square error was reduced by 1.3 and 1.9 mm during the entire storm.

Díaz-Viera, *et al*. (2009) explored different variants of kriging to estimate rainfall in the Mexico City metropolitan area using radar and rain gauge data. Their estimates obtained by cokriging with a model of linear corregionalization and collocated cokriging generated better estimates of the rainfall than obtained by ordinary kriging.

Becerra-Soriano (2009), in her master's thesis, continued these two investigations. Her objective was to evaluate the cokriging method for estimating rainfall combining radar and rain gauges measurements and using all radar images from two storms in the Mexico City area. As part of the assessment, a calculation of runoff volume was included, in order to estimate the water volume that would go into the Mexico City drainage system.

Geostatistical estimation techniques like kriging-the best unbiased linear estimators (Chilès and Delfiner, 1999)-may be optimal in the sense of minimizing the estimation error variance, but are strongly dependent on data quantity, spatial position and, the worst, they do not reproduce the spatial correlation. These techniques can generate unrealistic rainfall spatial distributions (Young, 2008; and Curtis and Clyde, 1999).

An alternative method for spatial estimation is a simulation approach, which, by definition, reproduces the statistical behavior of the phenomenon. Specifically, geostatistical simulation methods can generate multiple realizations that are statistically equivalent in terms of the first and second-order moments (Chilès and Delfiner, 1999). Here, the application of geostatistical simulation methods to model rainfall spatial variability is considered.

An antecedent to the present work is the master's thesis of Méndez-Venegas (2008), where he performed a simulation using only rain gauge data and a cosimulation using both rain gauge data and radar images for a single storm. The applied simulation method was sequential Gaussian (Alabert and Massonat, 1990). This paper is an extension of his work to a set of three convective storms in Mexico City.

Here, two simulations for each storm: a univariate simulation (Z^S) using only rain gauge data and a cosimulation (Z^{CS}) using rain gauge data and radar images are performed. To evaluate the results, their statistics were satisfactorily compared with those of the data.

Rain gage and radar image data

The radar data was obtained at the C-band Doppler meteorological radar station of the National Meteorological Service on Cerro de la Catedral, overlooking the metropolitan area of Mexico City (Figure 1). The radar images used are 8 bits images of 240 x 240 km with a resolution of 1 km^2. A pixel covers an area of 1 km x 1 km in a pseudo-CAPPI presentation at 4 km above sea level every fifteen minutes (Valdés-Manzanilla and Aparicio, 1997). The precipitation data is from 61 rain gauges of the Water System of Mexico City and radio reporting, every minute, of the accumulated rainfall during the storm. These rain gauges are of tipping-bucket kind with telemetry and a density of one rain gauge for every 30 km^2 (Díaz-Viera, *et al*., 2009).

The accumulated rainfall per hour for each type of measurement is calculated. The radar records an image with values of reflectivity (Z) every 15 minutes, these images to values of rain intensity (R) using a Z-R relationship are converted, subsequently four consecutive radar images are averaged for rainfall intensity to obtain effective cumulative rainfall in one hour. The relation $Z = 300R^{1.4}$ recommended by the manufacturer is used (Valdés-Manzanilla and Herrera- Zamarrón, 2000).

For rain gauge data digital files for the date and time of the storm are used. Each rain gauge has a counter that is incremented by one each time it registers a shower of 1/4 mm (Rosengaus, 2000). The cumulative rainfall per hour is calculated.

Rain gauges Z_g (Table 1) and radar images Z_r (Figures 2, 3, 4) were recorded in Mexico City during 13, 15 and 16 July 1997 (referred thereafter as storm 1, 2 and 3). Storm 2 has the largest number of gauge data (50), while storm 1 has only 23 gauge measurements. On Figures 2, 3 and 4 the gray scale images correspond to one hour accumulated precipitation given in millimeters (mm), while the cross symbols represent the locations of gauge data for this storm.

Table 1. Rain gauge and radar data basic statistics for each storm.

Statistics	Storm 1		Storm 2		Storm 3	
	Rain Gauge (Z_g) (mm)	Radar (Z_r) (mm)	Rain Gauge (Z_g) (mm)	Radar (Z_r) (mm)	Rain Gauge (Z_g) (mm)	Radar (Z_r) (mm)
Number of observations	23	2106	50	2025	40	1404
Minimum	0.25	0.00	0.25	0.00	0.25	0.00
Mean	5.10	1.95	1.47	1.81	5.77	3.39
Maximum	30.50	55.60	7.75	15.50	27.50	74.00
Standard deviation	8.38	4.67	1.60	1.95	6.55	6.43
1st Quartil	0.25	0.00	0.31	0.30	0.75	0.20
Median	2.25	0.20	1.00	1.30	4.00	1.20
3rd Quartil	4.37	1.40	1.93	2.60	7.18	3.80

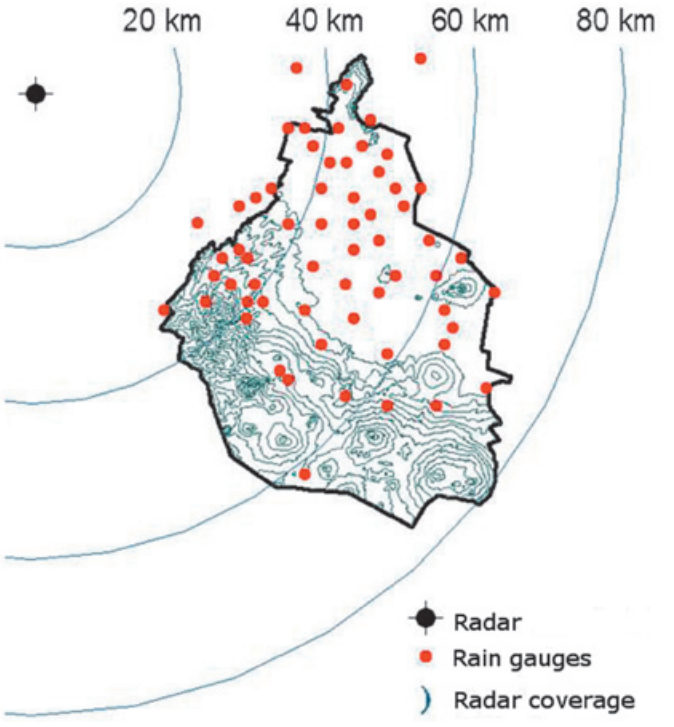

Figure 1. Location of meteorological radar on Cerro de la Catedral and the rain gauge network (red dots) of the Mexico City Water System (Rosengaus, 2000).

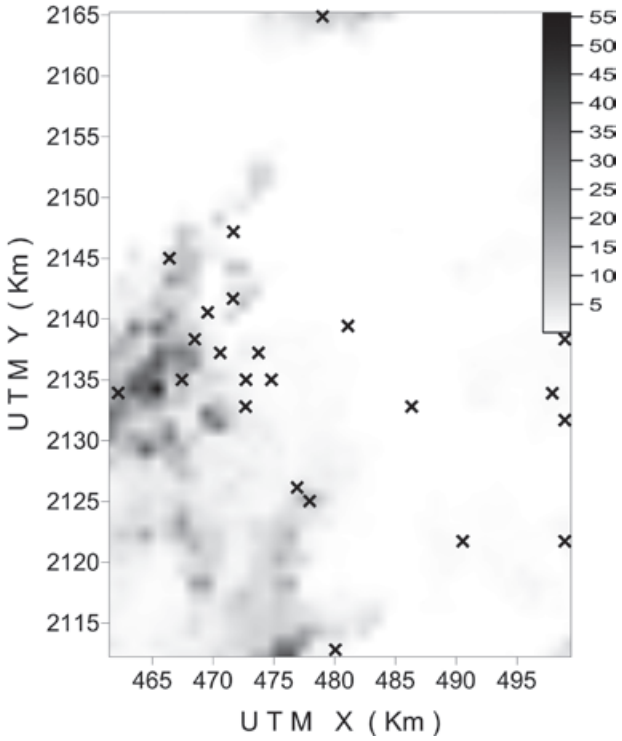

Figure 2. The gray scale image is one hour accumulated rainfall in millimeters (mm) calculated from radar images corresponding to storm 1. The cross symbols represent the locations where gauge data are available for this storm.

Geostatistical simulation methodology

Geostatistical methodology basically consists of three phases: exploratory data analysis, variographic analysis and estimation and/or simulation. The geostatistical simulation is applied in this work. Standard procedures are followed (Díaz-Viera, *et al*., 2009; and Méndez-Venegas, 2008).

Sequential Gaussian Simulation

Since the early 1990's, sequential Gaussian simulation has gained in popularity (Deutsch, 2002). A new simulated value is obtained from the estimated conditional probability distribution function using observational and previously simulated values in a neighborhood of a given location applying a kriging method (Chilès and Delfiner, 1999).

The theory behind sequential Gaussian simulation is based on using previously simulated value and input data throughout the simulation process. In practice, only the closest conditioning data are used.

Geostatical simulation of three storms

The sequential Gaussian method was applied using the rain gauge data and radar data. During the exploratory data analysis, several statistical parameters were computed (Table 1) and histogram graphics were generated. It was found that the data do not have normality; consequently, an anamorphosis transformation was applied to them, which ensured normality in the transformed data (Chilès and Delfiner, 1999).

Variograms were calculated and a model was adjusted to each using weighted least squares. The model with the lowest sum of squares errors was chosen and validated using cross validation. The

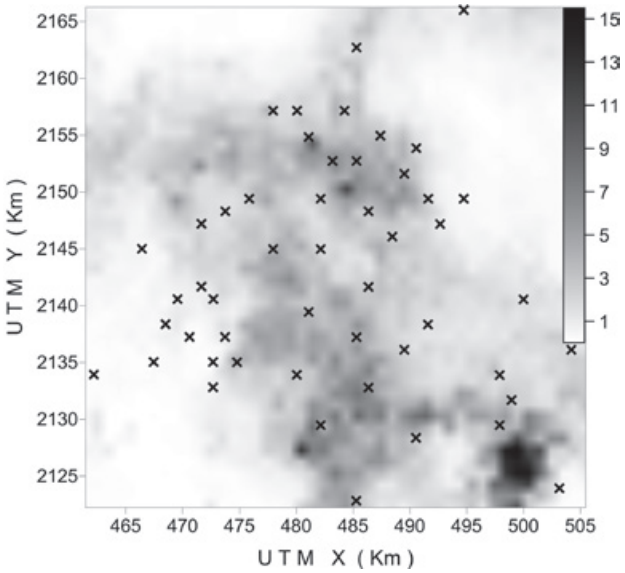

Figure 3. As in Figure 2, for storm 2.

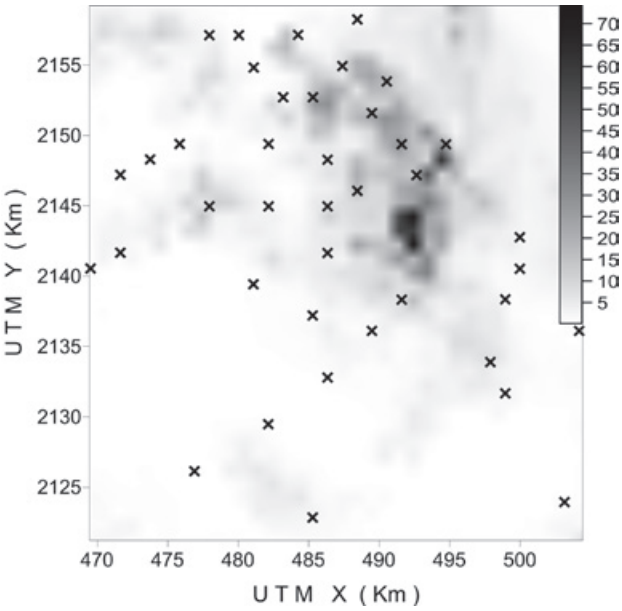

Figure 4. As in Figure 2, for storm 3.

leave-one-out method (Journel and Huijbregts, 1978) was used for cross-validation which involves removing each sample and estimating the value at that point using the kriging equations and the variogram model obtained. As a result, a map of the differences between actual and estimated values is obtained. The adjusted models were spherical.

Results and discussion

For the simulation of storm 1 (Figure 5) rain gauge data and the model shown in the first line of Table 4 were used. For the cosimulation of this storm (Figure 6) rain gauge and radar data of the corresponding storm and the model showed in Table 2 were used. The simulation of storm 2 (Figure 8) was done using rain gauge data and the model in the third line of Table 4; for the cosimulation (Figure 9) the rain gauges and radar data of storm 2 and the model shown in Table 7 were used. For storm 3, as in the previous two cases, the univariate simulation (Figure 11) only uses rain gauge data and a model (fifth line, Table 4) and the cosimulation (Figure 12) was done with all the information available and a model (Table 8).

Table 2. Variogram models in the linear corregionalization model for storm 1.

Variable	*Model*	*Nugget*	*Sill*	*Range (km)*
Rain gauge (Z_g^A)	*Spherical*	*0.3*	*1.05*	*20*
Radar (Z_r^A)	*Spherical*	*0.2*	*1.05*	*20*
Radar (Z_g^A) – Rain gauge (Z_r^A)	*Spherical*	*0.15*	*0.95*	*20*

Table 3. Rain gauge data, simulation and cosimulation basic statistics for storm 1.

Statistics	Rain gauge (Z_g)(mm)	Simulation (Z_g^s)(mm)	Cosimulation (Z_g^{cs})(mm)
Number of observations	23	2106	2106
Minimum	0.25	0.25	0.25
Mean	5.10	4.87	4.71
Maximum	30.50	30.50	30.50
Standard deviation	8.38	8.13	9.00
1st Quartil	0.25	0.25	0.25
Median	2.25	0.50	0.25
3rd Quartil	4.37	4.32	2.88

Table 4. Comparison the fitted variograms models for the rain gauge data versus the outcomes of the simulation.

Variable	Model	Nugget	Sill	Range (km)
Rain gauge data (storm 1)	Spherical	0.15	1.05	16
Simulation (storm 1)	Spherical	0.15	0.95	17
Rain gauge data (storm 2)	Spherical	0	1.11	13.81
Simulation (storm 2)	Spherical	0.05	1.2	14
Rain gauge data (storm 3)	Spherical	0.1	1.3	20
Simulation (storm 3)	Spherical	0.15	0.85	19

Table 5: Comparison the fitted variograms models for the rain gauge data with the linear corregionalization model versus the outcomes of the cosimulation.

Variable	Model	Nugget	Sill	Range (km)
Rain gauges data (storm 1)	Spherical	0.3	1.05	20
Cosimulation (storm 1)	Spherical	0.17	0.8	20
Rain gauges data (storm 2)	Spherical	0.22	1.06	21
Cosimulation (storm 2)	Spherical	0.17	0.95	21
Rain gauge data (storm 3)	Spherical	0.25	1.3	25
Cosimulation (storm 3)	Spherical	0.2	0.9	25

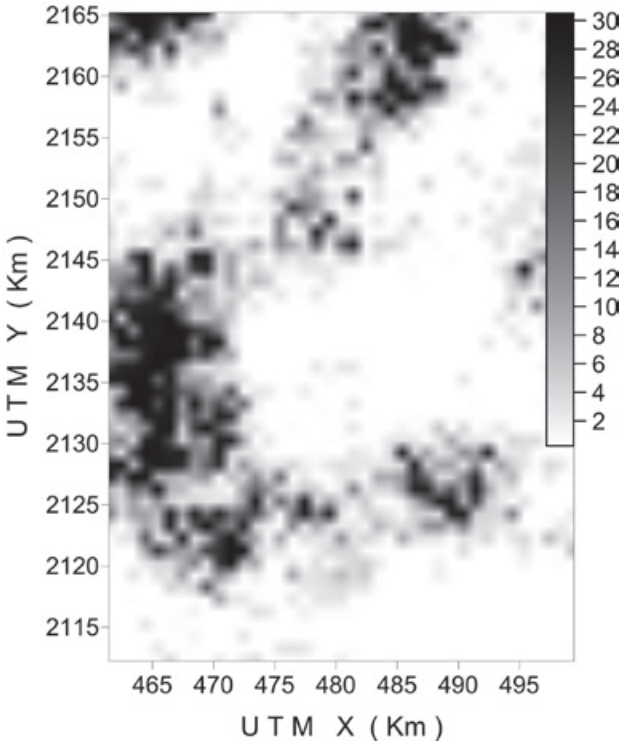

Figure 5. Simulation of one hour accumulated rainfall in millimeters for storm 1.

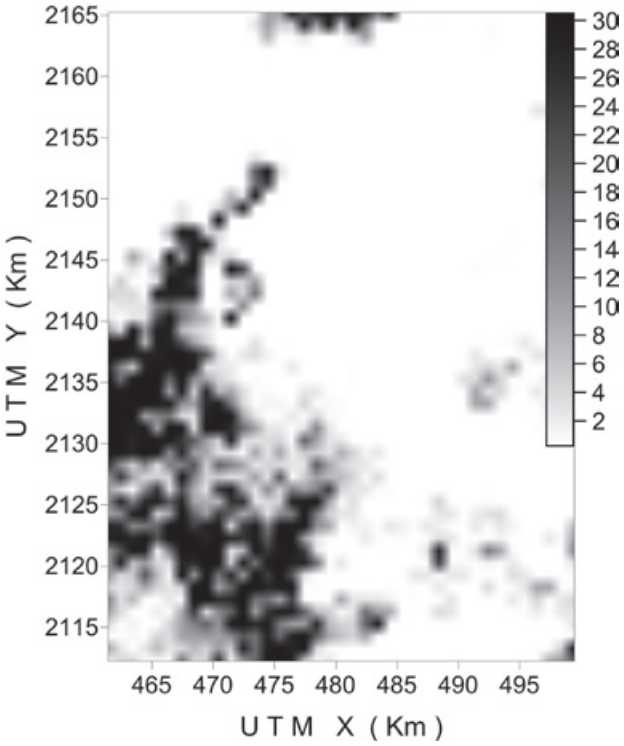

Figure 6. Cosimulation of one hour accumulated rainfall in millimeters for storm 1.

The superscript *A* indicates that the variable was applied the anamorphosis transformation.

Results for each storm were compared with the corresponding sample information. The simulations reproduce adequately the statistical values (Tables 3, 6 and 9), the histograms and box plots (Figures 7, 10 and 13), as the variogram model of the data (Tables 4 and 5).

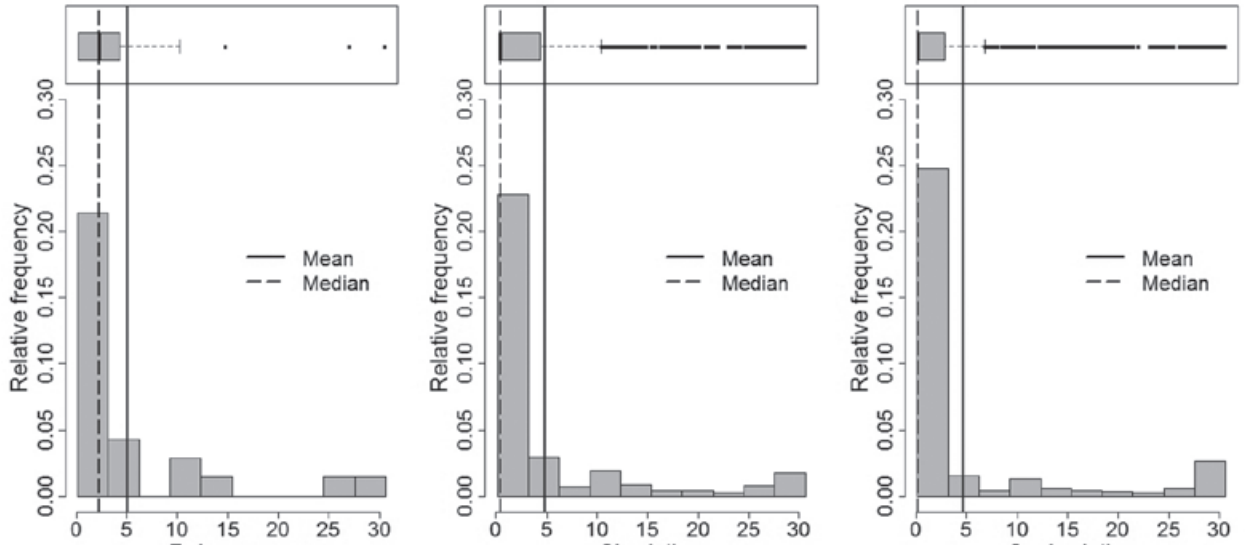

Figure 7. Histograms and box plots of rain gauge data Z_g, univariate Z_g^S and cosimulation Z_g^{CS} for storm 1 (mean value, solid line and median, dashed line).

Table 6. Rain gauge data, simulation and cosimulation basic statistics for storm 2.

Statistics	Rain gauge (Z_g)(mm)	Simulation (Z_g^s)(mm)	Cosimulation (Z_g^{cs})(mm)
Number of observations	50	2025	2025
Minimum	0.25	0.25	0.25
Mean	1.47	1.39	1.38
Maximum	7.75	7.75	7.75
Standard deviation	1.60	1.54	1.53
1st Quartil	0.31	0.25	0.25
Median	1.00	0.99	1.00
3rd Quartil	1.93	1.95	1.82

Table 7. Variogram models in the linear corregionalization model for storm 2.

Variable	Model	Nugget	Sill	Range (km)
Rain gauge (z_g^A)	Spherical	0.22	1.06	21
Radar (z_r^A)	Spherical	0.22	1.08	21
Radar (z_g^A) – Rain gauge (z_r^A)	Spherical	0.16	0.97	21

Table 8. Variogram models in the linear corregionalization model for storm 3.

Variable	Model	Nugget	Sill	Range (km)
Rain gauge (z_g^A)	Spherical	0.25	1.3	25
Radar (z_r^A)	Spherical	0.25	1.4	25
Radar (z_r^A) – Rain gauge (z_g^A)	Spherical	0.17	1.25	25

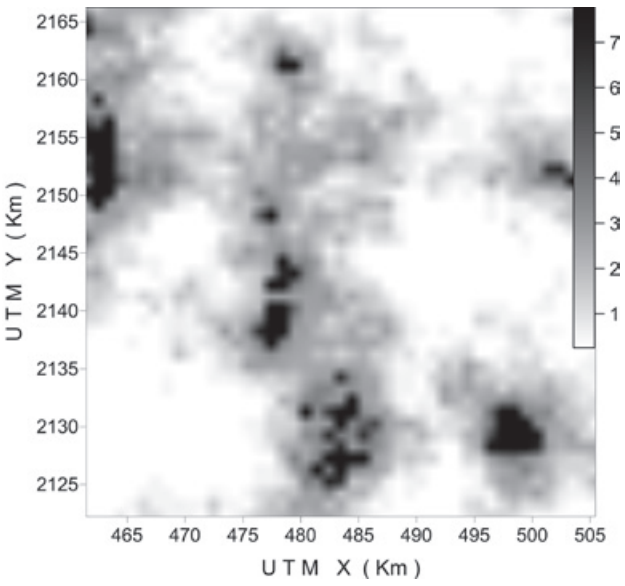

Figure 8. As in Figure 5, for storm 2.

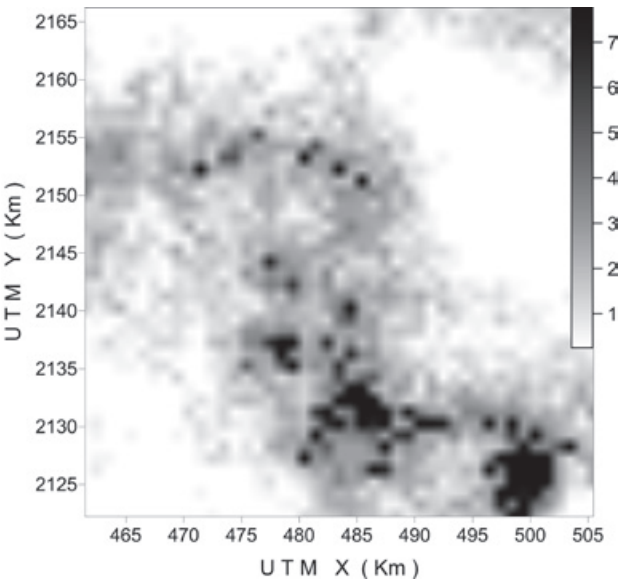

Figure 9. As in Figure 6, for storm 2.

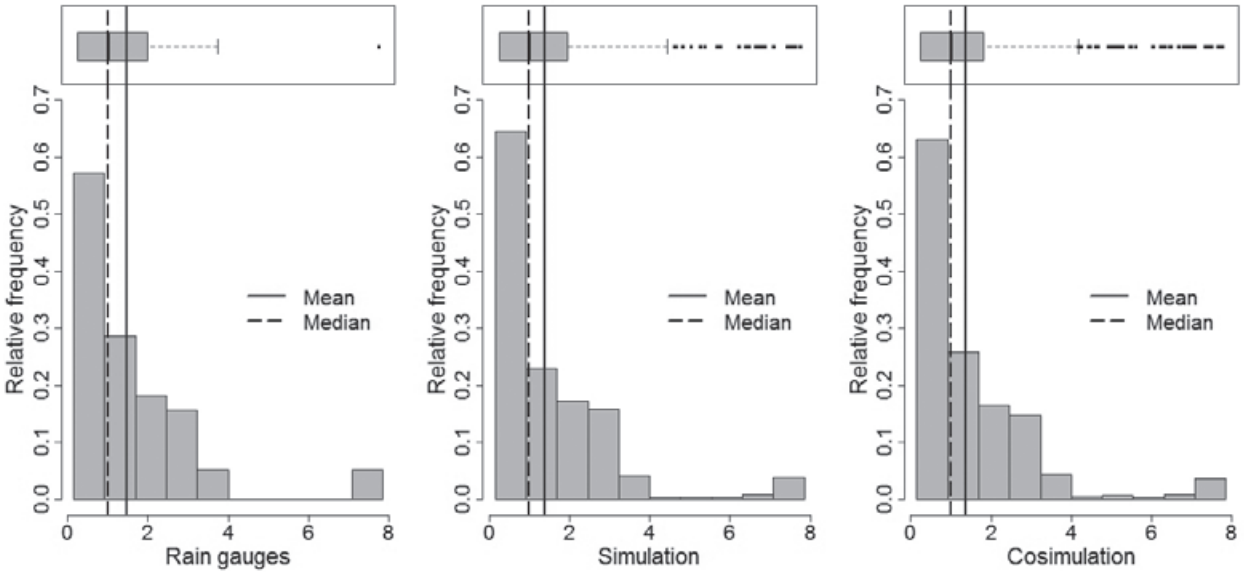

Figure 10. As in Figure 7, for storm 2.

Table 9. Rain gauge data, simulation and cosimulation basic statistics for storm 3.

Statistics	Rain gauge (Z_g)(mm)	Simulation (Z_g^s)(mm)	Cosimulation (Z_g^{cs})(mm)
Number of observations	40	1404	1404
Minimum	0.25	0.25	0.25
Mean	5.77	5.45	5.62
Maximum	27.50	27.50	27.50
Standard deviation	6.55	6.58	6.53
1st Quartil	0.75	0.55	0.25
Median	4.00	3.31	3.85
3rd Quartil	7.18	6.47	8.12

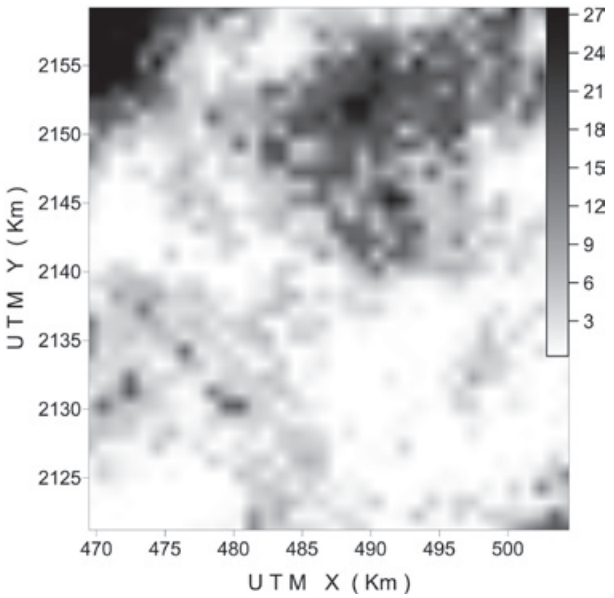

Figure 11. As in Figure 5, for storm 3.

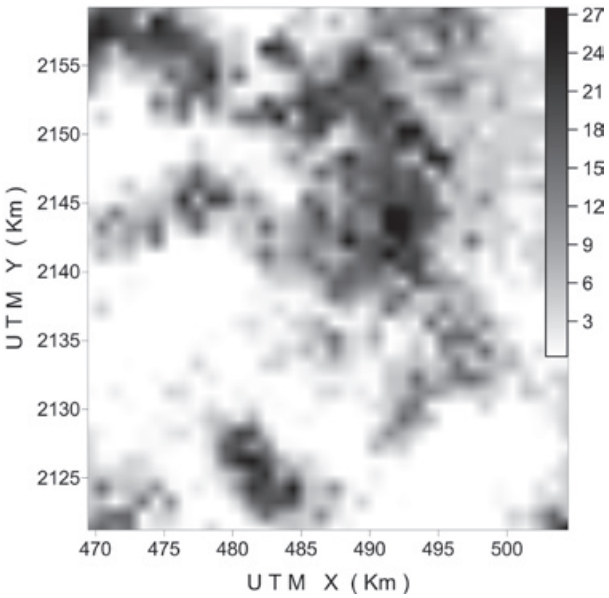

Figure 12. As in Figure 6, for storm 3.

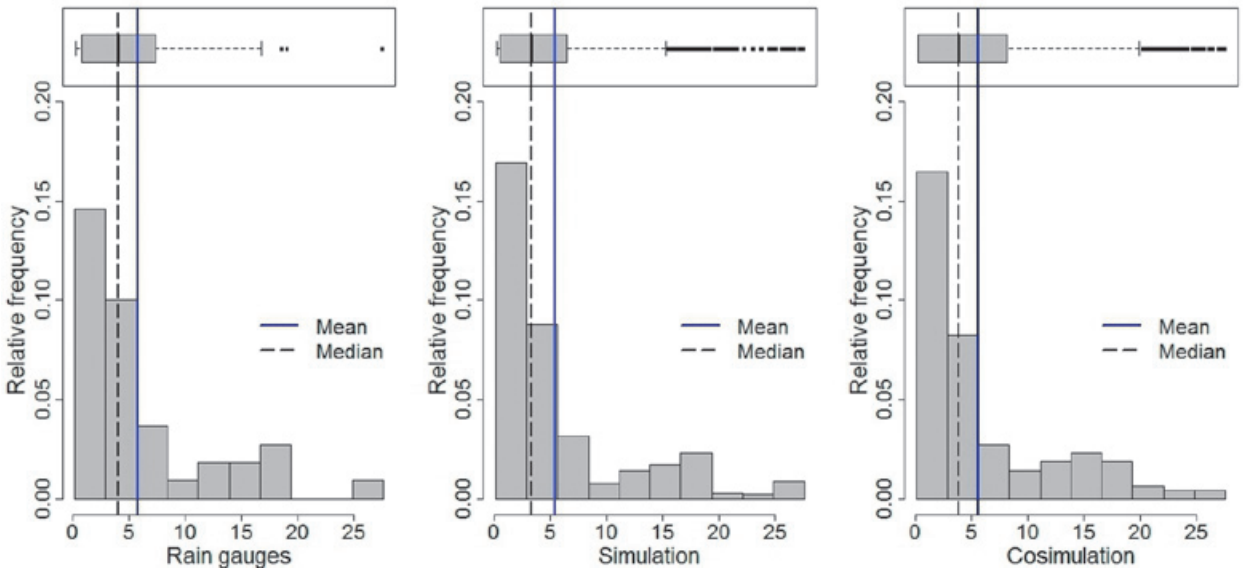

Figure 13. As in Figure 7, for storm 3.

For all storms, simulations estimate adequately precipitation. Comparison of radar images with simulations is complex because radar images are not taken at ground level. In radar images the precipitation falls in a small region and is greater than those recorded by rain gauges and from simulations, this may be due to evaporation of rainfall before it reaches the ground, because of high elevation of the radar beam over the valley of Mexico (Zawadzki,1984).

Conclusions

Spatial stochastic simulations using the sequential Gaussian method reproduce adequately data statistics (minimum, maximum, mean value, median, variance, histogram, variogram model, etc.) in both univariate and bivariate cases. Simulation can be an ideal tool to model the spatial distribution of rainfall.

When there is enough information to accurately estimate the variogram (Storm 2), simulations using only rain gauge data generated consistent estimations with the variability and the spatial distribution of the rainfall, but cosimulations with rain gauge data and radar images generated more precise and detailed estimations of the spatial distribution.

Using the simulation approach, rainfall distributions in storms could be generated from their statistical properties. Simulation is a powerful tool for studying the phenomena involved in precipitation.

For optimal performance of the simulation procedures, it is necessary to follow a methodology consistent with hypothesis, as those described here.

Bibliography

Anhert P., Krajewski W., Johnson E., 1986, Kalman Filter estimation of radar-rainfall fild bias. XXIII Conferencia en meteorología de radar. *Americ. Meteor. Soc., Snowmass*, 33-37.

Becerra-Soriano L., 2009, Estimación de lluvia en el Distrito Federal utilizando datos de pluviógrafos y de radar meteorológico, tesis de Maestría, UNAM.

Chilès P.J., Delfiner P., 1999, Geoestatistics: Modeling Spatial Uncertainty. Wiley. New Cork. 695 pp.

Collier C.G., 1983, A weather radar procedure for real-time procedure estimation of surface rainfall. *Q.J.R.M.S*., 109, 589-608.

Curtis D.C., Clyde B.S., 1999, Comparing Spatial Distributions of Rainfall Derived from Rain Gages and Radar. NEXRAIN Corporation Folsom.

Deutsch C., 2002, Geostatistical Reservoir Modeling. Oxford University Press, New York.

Díaz-Viera M., Herrera-Zamarrón G.S., Valdés-Manzanilla A., 2009, A linear coregionalization model for spatial rainfall estimation in the

Mexico City valley combining rain gages data and meteorological radar images. Revista Ingeniería Hidráulica en México, vol. XXIV, No. 3. pp. 63-90. Julio-septiembre 2009.

Fitzwilliams P., Rios T., Curtis D., Thornhill R., 2006, Use of Radar-Rainfall in GIS-Based Sewer Modeling. Government Engineering.

Journel A.G., Huijbregts Ch.J., 1978, Mining Geostatistics. Academic Press. New York, 590 pp.

Krajewski W.F., 1987, Cokriging radar-rainfall and rain gage data, *J. Geophys,*, 92. 9571-9580.

Matheron G. 1963. Principles of Geostatistics. *Economic Geology*, 58, 1246-1266.

Méndez-Venegas J., 2008, Modelación de la Distribución Espacial de la Precipitación en el Valle de la Ciudad de México Usando Técnicas Geoestadísticas, tesis de Maestría en Estadística, Colegio de Postgraduados, Campus Montecillo, Chapingo.

Rosengaus M., 2000, Manejo de Emergencias Hidrometeorológicas en la Ciudad de México. Primer Simposio Internacional Sobre Riesgos Geológicos y Ambientales de la Ciudad de México. México D.F.

Seo B.C., Krajewski W.F., Investigation of the scale-dependent variability of radar-rainfall and rain gauge error covariance. *Advances in Water Resources*, 34, 1, January 2011, 152-163.

Seo D.J., Krajewski W.F., Bowles D.S., 1990a, Stochastic interpolation of rainfall data from rain gages and radar using Cokriging. 1. Design of experiments. *Water Resources Research*, 26, 3, 469-477.

Seo D.J., Krajewski W.F., Bowles D.S., 1990b, Stochastic interpolation of rainfall data from rain gages and radar using Cokriging. 2. Results. *Water Resources Research*, 26, 5, 915-924.

Valdés-Manzanilla A., Aparicio F.J., 1997, The Mexican Doppler radar network. XVIII Conference of radar meteorology, Austin Tx, *Amer. Meteor. Soc*. 35-36.

Valdés-Manzanilla A., Herrera-Zamarrón G., 2000, Informe final del proyecto: diseño de un sistema de estimación de lluvia usando radar meteorológico. Jiutepec, México: Coordinación de Tecnología Hidrológica, Subordinación de Hidrometeorología, IMTA.

Valdés-Manzanilla A., Herrera G.S., 2002, Design of a rain estimation system using a meteorological radar. Developments in water science. *Computational methods in water resources*, 47, 2, 1765-1772.

Young H.B., Byung K.S., 2008, Radar Rainfall Adjustment by Kalman-Filter Method and Flood Simulation using Two Distributed Models. The fifth European conference on radar in meteorology and hydrology.

Zawadzki I., 1984, Factors affecting the precision of radar measurements of rain. Preprints of the 22nd. Conference on radar meteorology. AMS, Boston, Mass. 251-256.

Zhanga Z., Switzerb P., 2007, Stochastic space-time regional rainfall modeling adapted to historical rain gauge data. American Geophysical Union.

Geofísica Internacional (2013) 52-2: 121-133

Original paper

Rock-magnetic properties of topsoils and urban dust from Morelia (>800,000 inhabitants), Mexico: Implications for anthropogenic pollution monitoring in Mexico's medium size cities

Bertha Aguilar Reyes*, Francisco Bautista, Avto Goguitchaichvili, Juan Julio Morales Contreras, Patricia Quintana Owen, Claire Carvallo and Julie Battu

Received: January 10, 2012; accepted: January 15, 2013; published on line: March 22, 2013

Resumen

En el presente trabajo, investigamos la correlación entre algunos parámetros magnéticos y el nivel de contaminación por metales pesados en suelos urbanos de la ciudad de Morelia, en el occidente de México. El estudio magnético fue llevado a cabo en 98 muestras urbanas provenientes de diferentes tipos de uso de suelo. La mayoría de las muestras contienen minerales ferrimagnéticos como responsables de la magnetización, pertenecientes probablemente a las soluciones sólidas de las titanomagnetitas/titanomaghemitas. Esto es inferido a partir de las mediciones de susceptibilidad en función de la temperatura y de los experimentos de magnetización remanente isotérmica (MRI). Estas mediciones indican además, que la mayoría de las muestras se saturan casi completamente antes de los 300 mT. Adicionalmente, los valores S_{-200} (S_{-200} = IRM_{-200}/SIRM, donde IRM_{-200}= magnetización a campo inverso de 200 mT después de la saturación magnética) se encuentran entre 0.7 y 1.0, característicos de minerales de baja coercitividad magnética. Las curvas promedio de magnetización remanente isotérmica de saturación (SIRM) pueden ser usadas como un indicador del nivel de contaminación, ya que estas curvas muestran diferentes valores de saturación de acuerdo al nivel de contaminación por metales pesados: Cu, Ni, Cr y Sr. Estas asociaciones de (titano)magnetitas con metales pesados fueron observadas bajo el Microscopio Electrónico de Barrido, revelando algunos agregados complejos en lugar de las esférulas detectadas comúnmente.

Palabras clave: ambientemetría, magnetismo de rocas, metales pesados, contaminación urbana, agregados magnéticos.

Abstract

In this work, we investigate the correlation between some magnetic parameters and the level of contamination by heavy metals in urban soils from Morelia city, western Mexico. The magnetic study was carried out on 98 urban soils samples belonging to distinct land uses. Most of analyzed samples contain ferrimagnetic minerals as the responsible for magnetization, most probably corresponding to the titanomagnetites/titanomaghemites solid solutions. This is inferred from the susceptibility *vs.* temperature measurements and the isothermal remanent magnetization (IRM) experiments. These measurements also indicate that most of samples are almost completely saturated before 300 mT. Additionally, the S_{-200} values (S_{-200} = IRM_{-200}/SIRM, where IRM_{-200}= Back-field of 200 mT after magnetic saturation) are between 0.7 and 1.0, characteristic of low coercivity magnetic minerals. The averaged saturation isothermal remanent magnetization (SIRM) curves can be used as an indicator of pollution level, as these curves show different saturation values according to the level of contamination by heavy metals: Cu, Ni, Cr and Sr. These associations of (titano)magnetite with heavy metals were observed by Scanning Electron Microscope revealing some complex aggregates rather than commonly detected spherules.

Key words: environmetrics, rock-magnetism, heavy metals, urban pollution, magnetite aggregate.

B. Aguilar Reyes[1,2*]
F. Bautista[2],
A. Goguitchaichvili[1,2,3]
J. Morales[1,2]
J. Battu[1]
[1]Laboratorio Interinstitucional de Magnetismo Natural
Instituto de Geofísica – Sede Michoacán
Universidad Nacional Autónoma de México
Campus Morelia, 58089 Morelia, Mexico
[2]Laboratorio Universitario de Geofísica Ambiental
Centro de Investigaciones en Geografía Ambiental
Universidad Nacional Autónoma de México
Campus Morelia, 58089 Morelia, Mexico
[3]Physics Dept Paleomanetism Laboratory
University of Burgos, Spain
Laboratorio Paleomagnetico
Depto. de Física, Escuela Politecnica Nacional
Av. Cantabria s/n, Universidad de Burgos, 009006
Burgos, España

P. Quintana
Cinvestav-Mérida
Departamento de Física Aplicada
A.P. 73, Cordemex, 14 97310
Mérida, Yucatán, México

C. Carvallo
Institut de Minéralogie et de Physique des Milieux Condensés
Université Pierre et Marie Curie
Paris, France

*Corresponding author: baguilar@geofisica.unam.mx
Antigua Carretera a Pátzcuaro Núm. 8701
Col. Ex-Hacienda de San José de La Huerta, 58190
Morelia, México
tel: +52 443 3222777 ext. 42644, 42563

Introduction

Urban areas represent potential sources of magnetic pollution due to human activities: vehicle usage, industrial activity, and emissions from burning of fossil fuel, domestic and industrial. Other source includes power stations and metallurgic works (Chaparro *et al*., 2002; Goluchowska, 2001; Hullet *et al*., 1980; Hunt, 1986; Kapička *et al*., 1999; Kim *et al*., 2007; Kukier *et al*., 2003; Petrovský and Elwood, 1999; Strzyszcz *et al*., 1996; Sutherland, 2003; Thompson and Oldfield, 1986; Vassilev, 1992). Among these activities, the vehicles are used throughout the entire city, representing a source of widespread and growing pollution.

The magnetic particles derived by vehicular combustion are due to Fe impurities in fuel (Abdul-Razzaq and Gautam, 2001) as well as wear and friction of engine components. The fine magnetic particles (< 10 mm: PM10) represent a great danger when they are inhaled because they are easily absorbed into the human body, causing serious health problems such as cardiovascular diseases and respiratory illnesses (Becher *et al*., 2001; Donaldson *et al*., 1998; Gómez *et al*., 2002; Kim *et al*., 2003; Muxworthy *et al*., 2001). Additionally, the ultrafine particles (<0.1 mm, PM0.1) are proven to have worse health effects than fine particles (<2.5 mm, PM2.5) (Harrison and Yin, 2000; Lu *et al*., 2008; Wichmann and Peters, 2000). Furthermore, these particles can lodge in their structure other toxic metals like Pb, Zn, Ba, Cd and Cr (Harrison and Jones, 1995; Maher *et al*., 2008; Muxworthy *et al*., 2003) probably due to the affinity of Fe oxides with trace metals (Gautam *et al*., 2005; Hunt *et al*., 1984; Lu *et al*., 2007; Ma and Rao, 1997; Meena *et al*., 2011). In particular, Pb, Cu and Zn and ferromagnetic minerals are commonly associated with industrial activity and traffic pollution (Beckwith *et al*., 1986; Hanesch and Scholger, 2002; Li *et al*., 2001; Lu *et al*., 2005).

Therefore, the concentration of magnetic minerals may reflect not only magnetogenic pollutants but the content of toxic metals in urban soils and other environmental samples (Bityukova *et al*., 1999; Magiera *et al*., 2006, Maher *et al*., 2008). The magnetic method has been developed to provide a fast and inexpensive alternative for monitoring anthropogenic pollution.

Several studies have reported a good correlation between magnetic susceptibility and the heavy metal content (Bityukova *et al*., 1999; Desenfant *et al*., 2004; Ďurža, 1999; Fialova *et al*., 2006; Hanesch and Scholger, 2002; Hoffmann *et al*., 1999; Lecoanet *et al*., 2003; Muxworthy *et al*., 2003; Petrovský *et al*., 2000). These studies are generally site specific and correlations are linked to evidence of fly ash, pollution products from traffic and metallurgic plants.

In most of cases, it is very difficult to interpret the result because of soil composition and other factors which can have an influence on this magnetic property (Ruiping and Cioppa, 2006) such as biological activity in soils and the diamagnetic mineral content. A good correlation has been reported between the saturation isothermal remanent magnetization (SIRM) and heavy metals content in urban dust (Maher *et al*. 2008; Mitchell and Maher, 2009).

This study reports the results of magnetic measurements obtained for 98 samples of soils and urban dusts from Morelia, Mexico. The objective is to correlate the magnetic properties with heavy metal content, and to establish a relative level of pollution in each point referred to a natural background. In our case, this reference is a natural reserve located in the southeast of the city. We show that SIRM has a strong correlation with the metal content, for soil samples as well as urban dust, showing the different degrees of pollution according to the IRM acquisition curves. The magnetic particles have been identified trough SEM observations under spherical shapes and irregular aggregates of < 2 mm.

Methods

Description of the city

Morelia is situated on a valley in northeast of the state of Michoacan in central part of Mexico, at an altitude of 1900 m.

Morelia is the most populated city on the state of Michoacan and the twentieth of the whole country. The metropolitan area has 806822 inhabitants (INEGI, 2010). 597511 of them are concentrated in Morelia. The main economic activity includes services, among them financial, real estate and tourism, followed by the construction industry, manufacturing industry and ultimately the primary sector activities.

Morelia city has an average temperature of 17.5 ° C, and annual precipitation of 773.5 mm, with a subhumid climate. The prevailing winds come from southwest and northwest; the intensity varies 2.0 to 14.5 km / h in July and August.

The rock basement of the city is composed of rhyolite (commonly known as "cantera"), as well as unconsolidated volcanic materials, which is called "tepetate". The principal soils groups, in agreement with World Reference Base for Soil Resources are Luvisols, Andosols, Vertisols, Acrisols and Leptosols. The municipality has 69,750 ha of land, of which 20,082 are cultivated

(rainfed and irrigated), 36,964 ha are used for grassland, and 12,234 ha of forests. The rest is unproductive land (Oyama *et al*., 2011).

The industrial zone of Morelia covers 354 ha, and houses 180 enterprises. However, only 30% of them are manufacturing companies. The rest of them are warehouses and distribution centers. The industry is focused in production of: comestible oil, meal, plastic, resins, paper and other cellulose products; there is also the foundry and manufacture of electrical and hydraulic turbine generators. This city is then characterized by vehicular fuel combustion as the principal source of pollution, additionally to few local pollution sources.

Sampling

We collected a total of 98 topsoil samples (Figure 1) within the urban area based on use of land, according to Bautista *et al*. (2011): Housing (24), Equipment (16), Industrial (8), Mixed (28), Green areas (6), Ecological Reserves (5), Urban dusts (11). Equipment refers to areas occupied by institutions providing public services. Mixed refers to areas intended to commercial activities as well as housing and equipment. All samples were georeferenced using a GPS. Samples were taken in triplicate in each point, then the three samples were mixed to obtain only one homogeneous sample. We collected the first five centimeters of superficial soil by using PVC (polyvinyl-chloride) cores and then kept in PVC packages. The urban dust samples were collected by brushing 1 m^2 of previously delimited surface of asphalt.

The samples were air-dried and sieved through a 2-mm sieve. In order to proceed with magnetic measurements, soil material was placed into standard plastic cubes (11 cm^3).

Magnetic measurements

All magnetic measurements were carried out in the LIMNA facilities, National University of Mexico Campus Morelia. We used the Bartington MS2B susceptibilitymeter to measure the susceptibility (k) at high and low frequency (k_{hf} at 4700 Hz, k_{lf} at 470 Hz). From these k values, mass specific susceptibility χ was calculated. The thermomagnetic curves (k-T curves) were obtained by heating under air one sample from each site, from room temperature up to about 700°C, followed by cooling at the rate of 20°C/min. The T_C was calculated by differentiation on the heating curve.

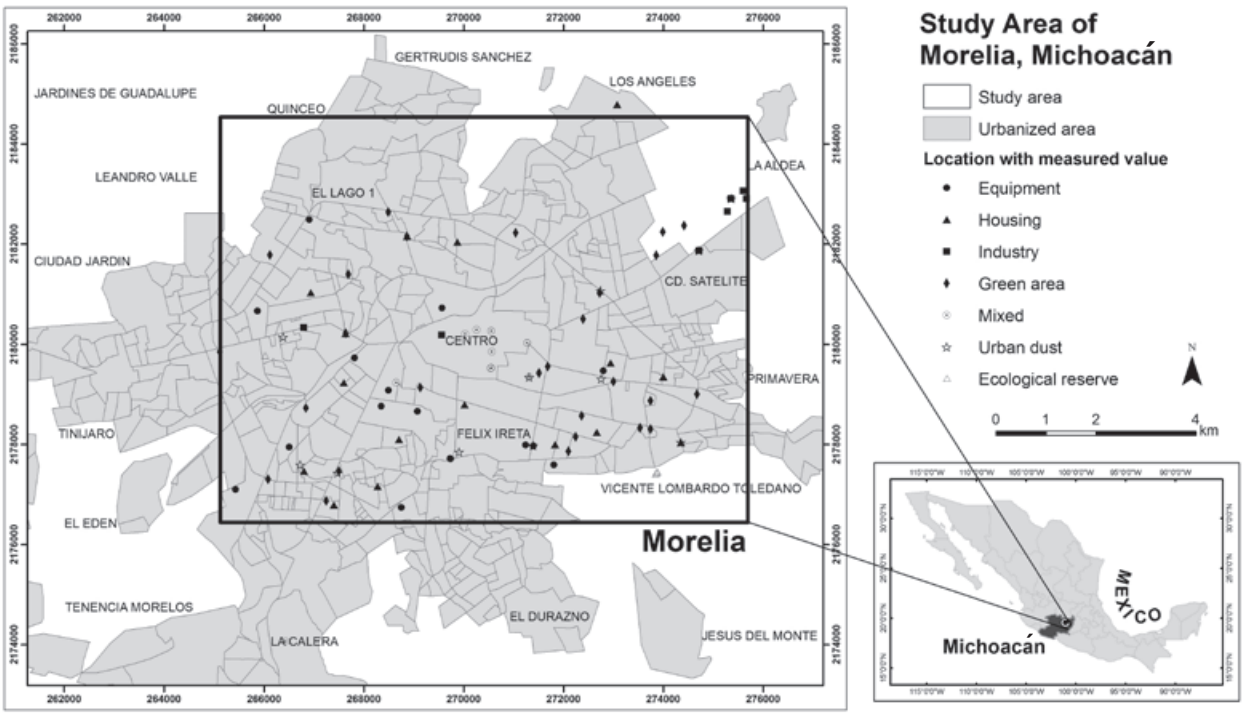

Figure 1. Map of Morelia, showing the localization of sampling sites.

Frequency-dependent susceptibility χ_{fd} [%] = $100(\chi_{lf} - \chi_{hf})/\chi_{lf}$ is used to determine the possible presence of superparamagnetic (SP) grains in the magnetic fraction (Dearing *et al*., 1996; Evans and Heller, 2003). At higher frequencies of applied magnetic field, a portion of the small SP grains is unable to follow the field changes and will no longer contribute to the susceptibility. Isothermal remanent magnetization (IRM) was acquired by placing samples in increasing magnetic fields at room temperature using a pulse magnetizer ASC IM-10. The IRM acquired at 700 mT is referred to as the saturation isothermal remanent magnetization (SIRM). Following the acquisition of SIRM, the back-field magnetization at 200 mT after magnetic saturation was obtained (IRM_{-200}). Then, we calculated the S_{-200} ratio ($S_{-200} = IRM_{-200}/SIRM$) to determine the proportion of low coercivity magnetic minerals. All remanent magnetizations were measured using an AGICO JR6 spinner magnetometer.

The observations under the Scanning Electron Microscope (SEM) were made on selected samples using a SEM/FRG ZEISS Ultra 55 scanning electron microscope, and the concentration of heavy metals was determined with the help of Noran System 7 EDS detector at SEM laboratory in the Institut de Minéralogie et de Physique des Milieux Condensés, Université Pierre et Marie Curie, Paris, France.

Chemical analyses

The powdered soils were pressed into pellets 1 cm wide, without any chemical treatment or binders; and put in a plastic sample holder covered with a mylar film. ED-XRF analyses were performed with a Jordan Valley EX-6600 spectrometer, equipped with a Si(Li) detector with a 20 mm^2 active area and 140 eV resolution at 5.9 keV and operated at a maximum of 54 kV and 4800 mA. Trace elements were acquired in air atmosphere using a changeable secondary target. Typical measurement time was 300 s. Each measurement was repeated five times in order to obtain the average concentration. Quantitative calculation was made through a fundamental parameter method. The experimental parameters were obtained by calibration of the whole system by means of geological standard reference materials (Lozano and Bernal, 2005).

Geostatistical analysis

We constructed a georeferenced data matrix based on SIRM values, and subsequently performed a geostatistical analysis by kriging interpolation (Isaaks and Srivastava, 1989; Webster and Oliver, 1990) using the Gamma Design Software (GS+, 2006). The maps were edited with ArcGIS 9 software (ESRI, 2004). The extreme data were put as points. We used the UTM projection, zone 14, horizontal datum ellipsoid and the World Geodetic System 84 (WGS84).

Main results and discussion

The thermomagnetic curves corresponding to each group of use of soil are plotted on Figure 2.

The samples from the ecological reserve (Figure 2e) show a reversible behavior. We see a first decay at about 350°C and the second one at 500°C, indicating the probable presence of two magnetic phases, maghemite and Ti-poor Ti-magnetite. No magnetic enhancement was noticed in this group of samples. For the rest of the samples, we observe a non reversible behavior and we notice a transformation during heating: the sample from equipment areas (Figure 2a) shows a continuous decay, starting at 300°C to 500°C, due to a variable composition within the series of Ti-magnetite; the calculated T_C is 507 °C. In contrast, samples from housing areas and "mixed sites" (Figure 2b and 2c), show a T_C of 578°C indicating the presence of an almost pure magnetite. Samples of these three types of land use show different degrees of magnetic enhancement; this may be explained by the conversion of ferric oxides (such as ferrhydrite) to maghemite or magnetite in the presence of soil organic matter (Hanesch *et al*., 2006).

The heating curve of the sample coming from industrial area (Figure 2d) shows two weak inflection points at ~330°C and 570 °C. The first one indicates the probable presence of maghemite (or pyrrhotite) while the second one indicates the presence of magnetite (Jordanova *et al*., 2004; Kapicˇka *et al*., 2001; Petrovsky and Kapicˇka, 2006). The magnetic phase is probably an impure magnetite because the T_C is slightly lower than 580°C (Dunlop and Özdemir, 1997).

The heating curve of urban dust (Figure 2f) shows a Hopkinson peak, judging by the gradual increase of susceptibility up to 460 °C and subsequent decrease down to 560 °C. This peak has been previously observed in k-T curves from polluted samples (Aguilar *et al*., 2011; Jelenska *et al*., 2004; Ruiping and Cioppa, 2006).

Figure 3 shows the average IRM acquisition curves by type of land use. These curves were obtained bay using the OriginPro Software. There is a clear difference between the un-polluted areas and the rest of samples: the SIRM value for urban dust is much higher than for the other samples. This parameter has been used as an indicator of the degree of pollution for urban dust (Mitchel and Maher, 2009, Yang *et al*. 2010), and river sediments (Chaparro *et al*., 2011). Some studies have found that remanence parameters are more robust tracers of magnetic particles derived from

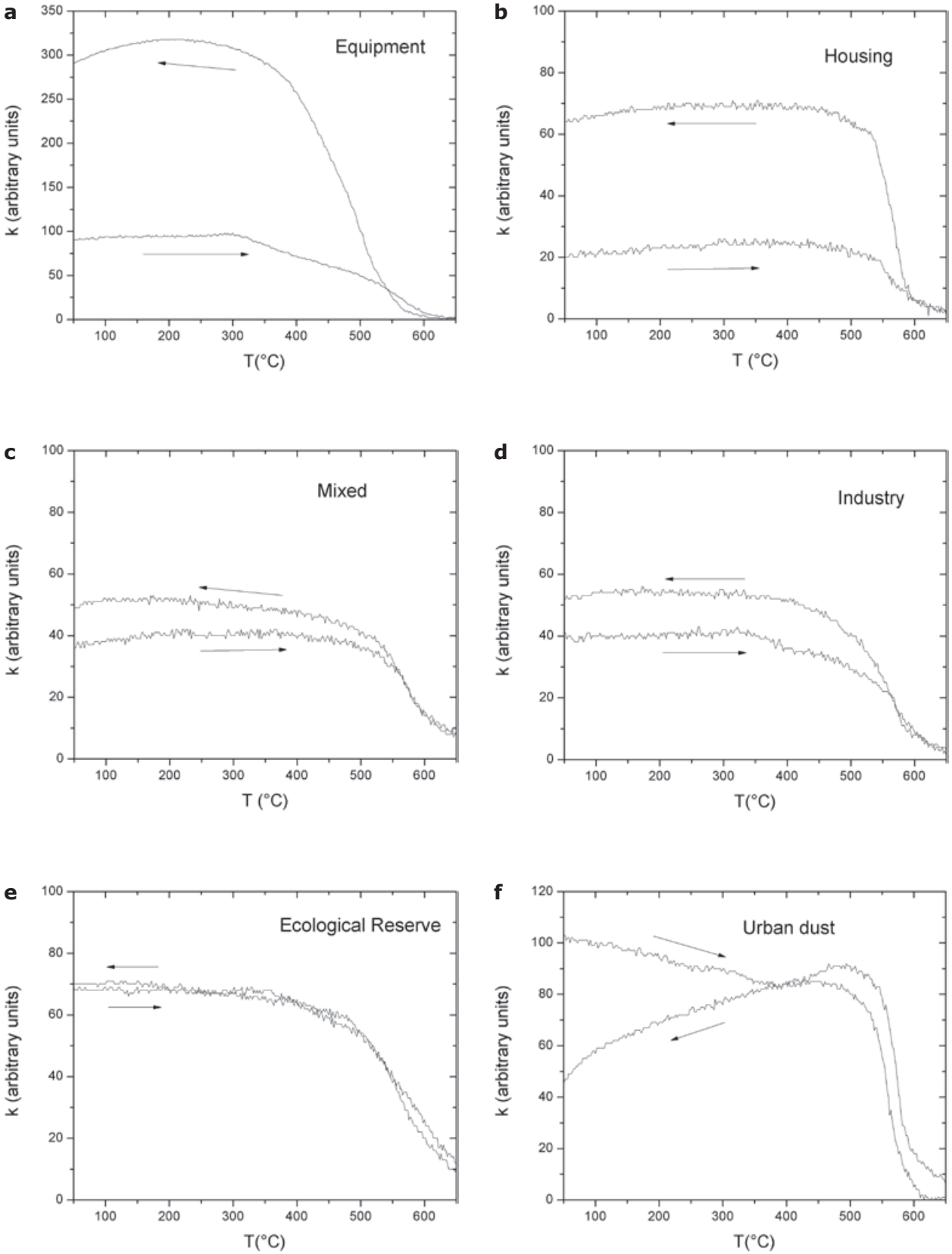

Figure 2. Thermomagnetic curves of samples from: a) Equipment, b) Housing, c) Mixed areas, d) Industrial area, e) Ecological reserve and f) Urban dust.

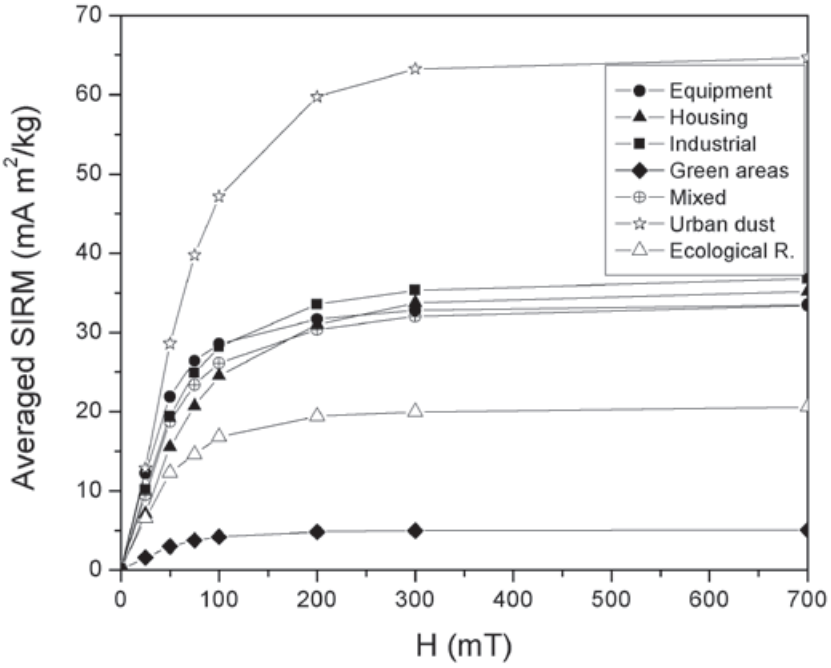

Figure 3. Averaged IRM acquisition curves for each group of samples according to use of land.

anthropogenic sources than susceptibility alone (Chaparro *et al*., 2003; Georgeaud *et al*., 1997; Yang *et al*., 2007). The IRM acquisition curves show a rapid saturation below 300 mT indicating that the magnetic minerals are dominated by low coercivity ferrimagnetic minerals.

Additionally, the S_{-200} values range between 0.7 and 1.0 for the majority of samples confirming the presence of low coercivity magnetic minerals -a ferrimagnetic phase- (Figure 4). In most of environmental studies, authors evaluate S_{ratio} by choosing an opposing DC field of 300 mT. In present work, we evaluate S_{-200} to detect small differences in coercivity; the S_{-300} is too close to 1.0 for the majority of samples of our case. Values of S_{-200} lower than 0.7 mean that magnetic carriers are Ti rich Ti-magnetite.

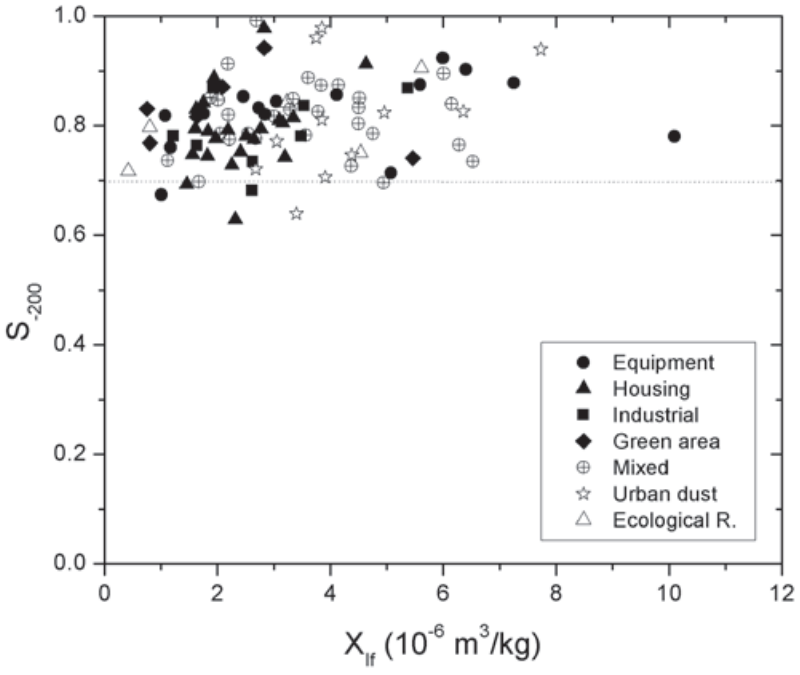

Figure 4. S_{-200} parameter as a function of low-frequency susceptibility.

The χ_{fd}% parameter (Figure 5) places the majority of samples between 2 and 10%, while some abnormal values (above 10%) are observed for some samples. The abnormal values (one sample from industry and one from green areas) are probably due to fertilizers or pesticides (Ruiping and Cioppa, 2006) because the majority of samples from ecological reserves, show values less than 5% hich points to low biological activity. Values above 8% are due to high levels of SP grains (Dearing *et al*., 1996) in soils magnetically enhanced by secondary magnetite/maghemite due to pedogenic processes. The values of urban dusts from Morelia are placed in a range from 0 to 7%, which indicates that the magnetic fraction is not dominated by SP grains (Maher 1988). For urban dust an average of 2% has been reported for several cities (Aguilar *et al*., 2011; Blundell *et al*., 2009; Kapicka *et al*. 2000; Lu & Bai, 2006; Shan and Lu 2005; Xie *et al*., 2001; Yang *et al*., 2007;). We assume that urban dust has a contribution from soils due to wind, which explains the values which are up to 7%.

We plot the relationship between SIRM and content of heavy metals (HM) (Figure 6). We observed a good correlation (R^2=0.62) between SIRM and the sum of contents of Sr, Cu, Ni and Cu. Lower values correspond to samples from ecological reserves and parks while the higher ones corresponds to samples from urban dust and industrial area. In contrast, we observed a very weak correlation between Pb and Zn levels with both χ_{lf} and IRM parameters (R^2 < 0.1). Yang *et al*. (2010) have reported an association of Cu and Ni with Fe, coming from vehicles emissions (PSD/MD grains) in road dusts. The linear correlation between trace metal and magnetic remanence in polluted areas is probably due to bounding tendency of Fe–Mn oxides with trace metals (Ma and Rao, 1997).

An important number of studies have indicated that soil type should be taken into account to discriminate the pollution signals using magnetic methods (Fialova *et al*., 2006; Hanesch and Scholger, 2005; Jordanova *et al*., 2008; Magiera *et al*., 2006; Ruipig and Cioppa, 2006). However, in our particular case, it is possible to obtain a very strong correlation between SIRM values and the pollution level, with no influence from the soil type. In the study area, the good correlation observed between Cu, Ni, Cr and Sr and magnetite, not only in urban dust but also in soils makes it possible to use SIRM measurements as a tool for mapping soils and urban dusts pollutions. According to Figure 7, the areas with the highest values of SIRM are in the west and southeast of the city. Ranges of SIRM values were defined in this study, as high (> 56), medium (28-56) and low (0.1-28). The degree of pollution detected does not appear to be conditioned by the prevailing winds, since they should affect more the east and the center of the city.

The urban dust and soil samples have been observed under the scanning electronic microscope (SEM). In all cases, we identified an association between magnetite and heavy metals. In figure 8a we showed a soil sample from a

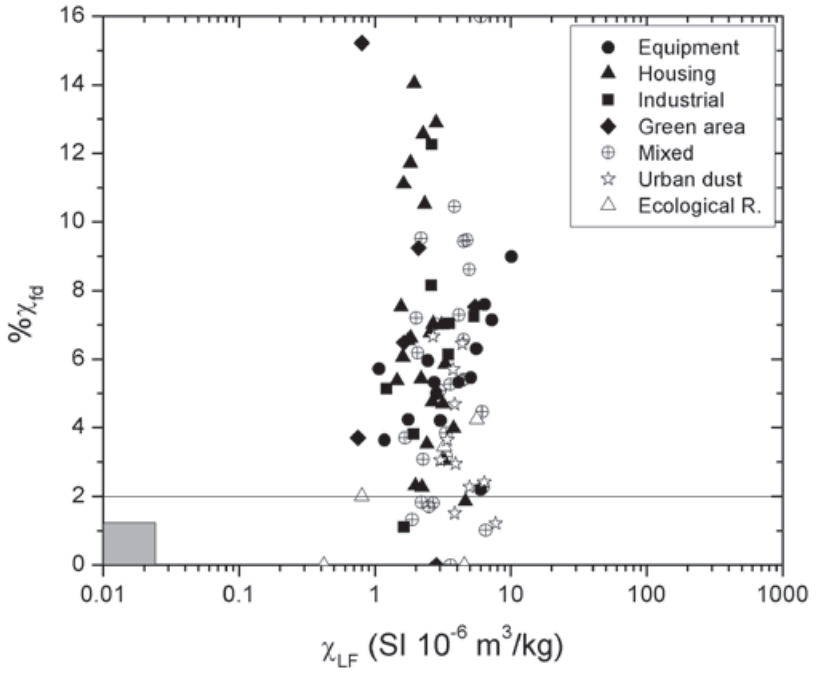

Figure 5. $\%\chi_{FD}$ as a function of susceptibility.

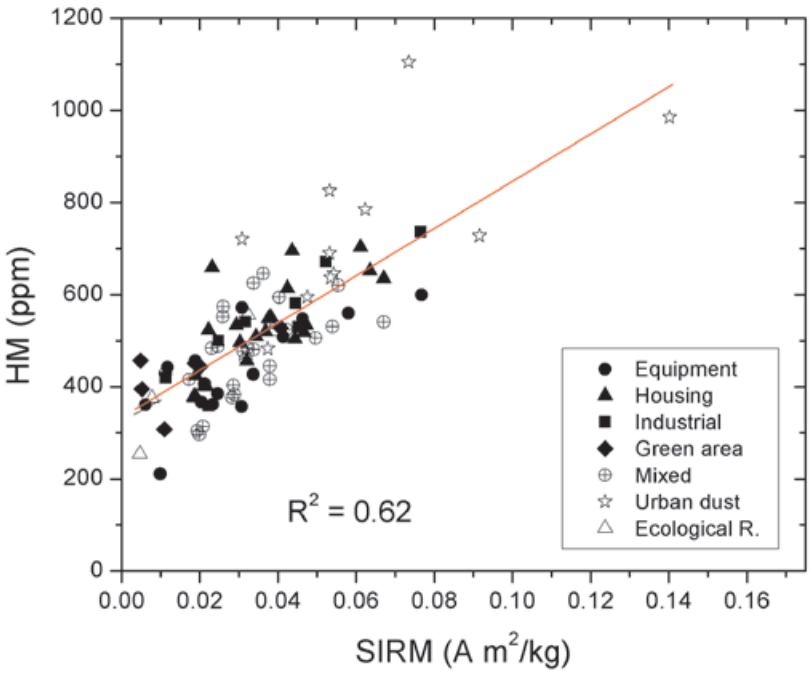

Figure 6. Correlation between SIRM values and the content of HM (HM = Ni+Cu+Cr+Sr).

"mixed area" in which we can observe particles of magnetite with a spherical shape (center) and as irregular shaped-aggregates (<1 mm). The punctual analysis (arrow) indicates mostly Fe associated with S and heavy metals as Cr, Ni and Cu. This association is probably produced from the abrasion or corrosion of the vehicle engine since these metals are used in making parts of automotive pieces (Kim *et al*., 2007; Maher *et al*., 2008). In figure 8b we show the results for an urban dust sample. We identified the irregular magnetic aggregates, composed mostly of pure

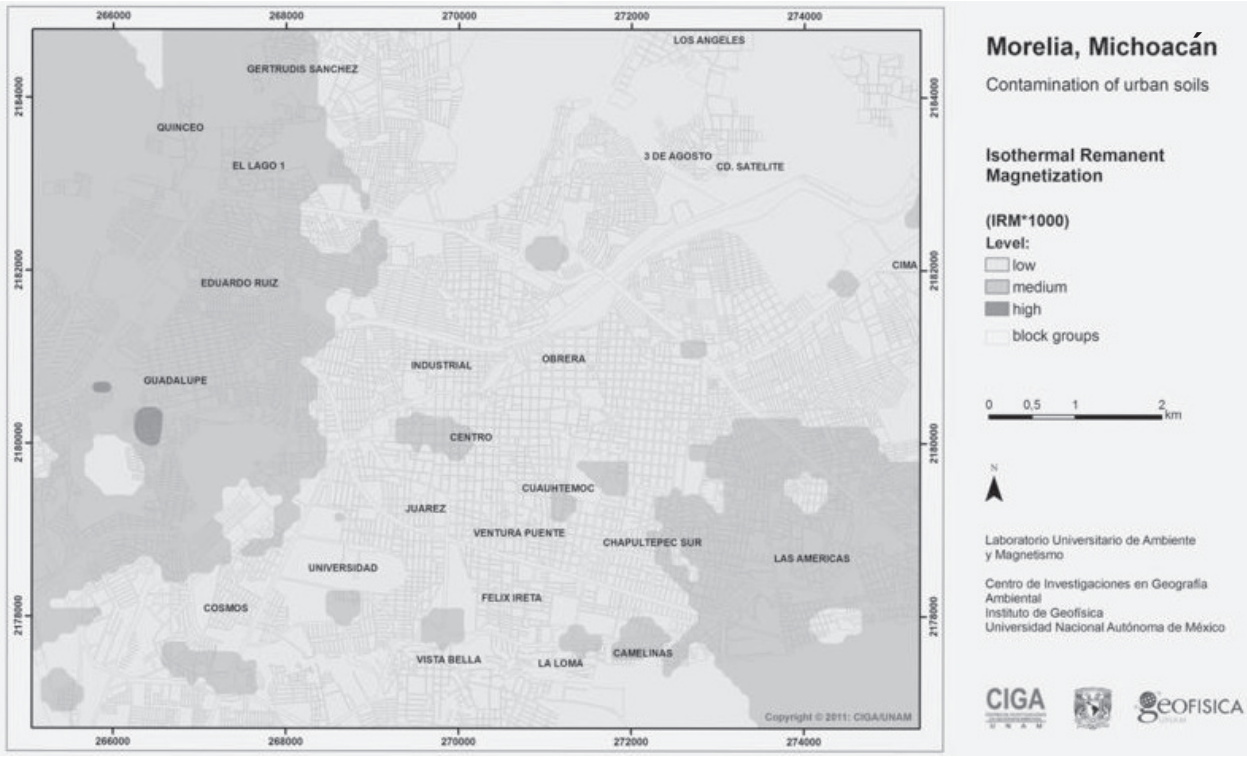

Figure 7. Geostatistical map of SIRM, according to ranges of values: high (> 56), medium (28-56) and low (0.1-28).

magnetite associated with S, Zn, Cr, Cu and Pb. The anthropogenic magnetic particles are usually dominated by magnetite (Kapička *et al*., 2001; Muxworthy *et al*., 2001) and this magnetic mineral has been identified as a combustion-derived component of vehicle exhaust materials (Abdul-Razzaq and Gautam, 2001) with spherical shapes and as aggregates (Maher *et al*., 2008; Moreno *et al*., 2003; Shilton *et al*., 2005). In fact, vehicle fuel combustion is the major source for Fe and Pb pollutants, rather than resuspension of roadside dust or from tyre, brake or other vehicle wear (Maher *et al*., 2008).

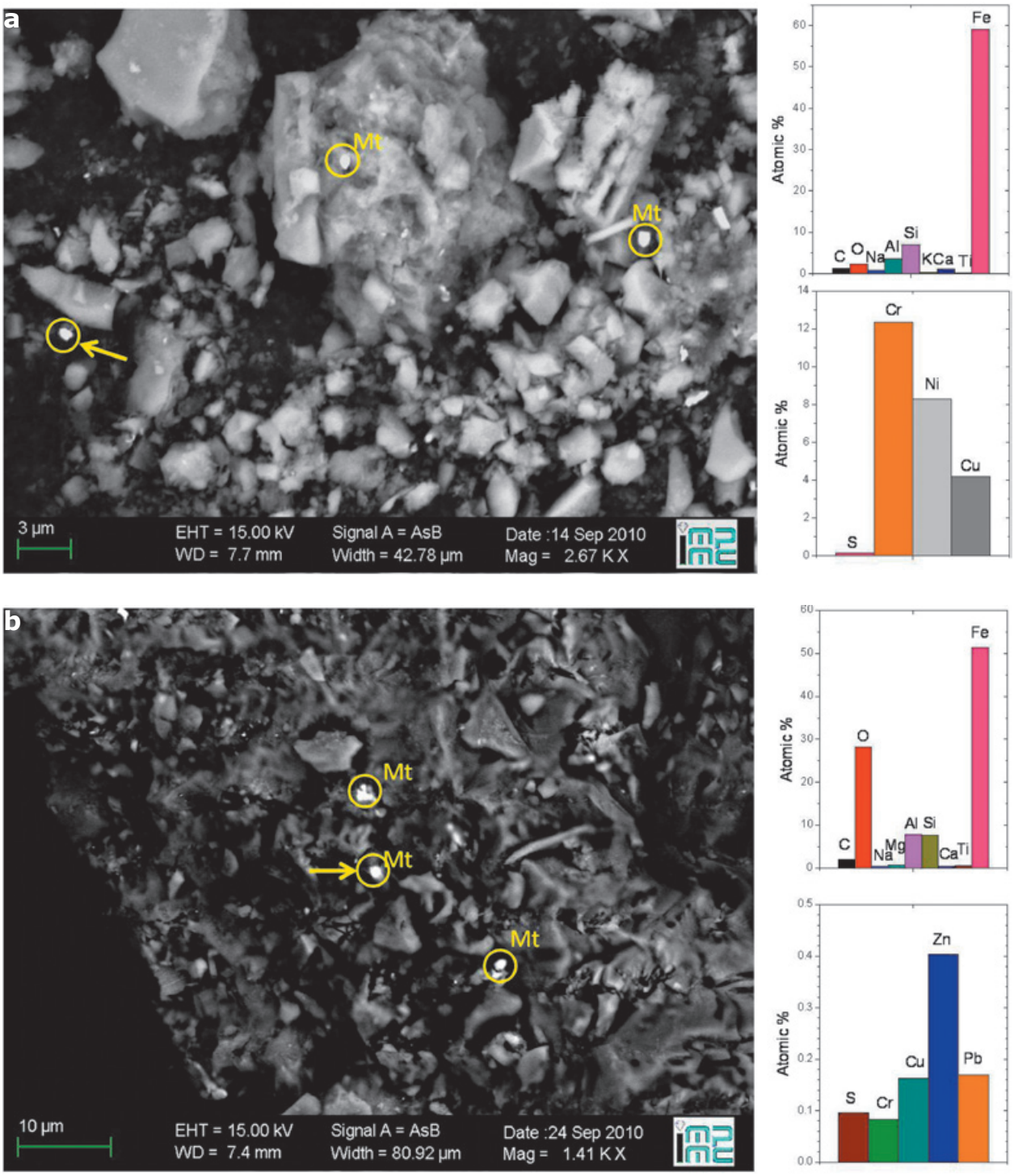

Figure 8. SEM observations and EDS analyses, showing the pure Fe associated to Ni, Cr and Cu (a) and magnetite, Mt, associated with heavy metals (b).

Conclusions

The urban, presumably unpolluted soils from Morelia (ecological reserves) contain maghemite and Ti-poor titanomagnetite as magnetic carriers. An impure magnetite was identified in the polluted samples, which almost exclusively comes from the vehicle combustion according to SEM observations performed on samples of soil and urban dust. These observations allowed us to identify spherical and irregular aggregates of ~1 mm, containing magnetite associated with S and heavy metals like Zn, Cr, Cu and Pb. We also identified irregular aggregates in which almost pure Fe is associated with Cr, Ni and Cu; this kind of particles probably comes from abrasion or corrosion of the vehicle engine and it is less common than previously described cases. A strong correlation between SIRM and the sum of the contents of Ni, Cr, Cu and Sr, was found. This correlation can be used as a proxy to determine different degrees of pollution by heavy metals in urban dust as well in urban soils.

Acknowledgements

This work was supported by the Universidad Nacional Autónoma de México through the projects CONACYT 118971 and PAPIIT IN 223110. The authors would like to thank Thomas Ihl for the map design and Ma. Carmen Delgado for the geostatistic analysis. We also thank Hector Franco and Francisco Bautista Delgado for sampling and to MSc D. Aguilar for the ED-XRF technical assistance. Dr. Avto Goguitchaichvili acknowledges the Conacyt and UNAM-PASPA sabattical program fellowships.

Bibliography

Abdul-Razzaq W., Gautamm M., 2001, Discovery of magnetite in the exhausted material from a diesel engine. *Appl. Phys. Lett.*, 78, 2018-2019.

Aguilar Reyes B., Bautista F., Goguitchaichvili A., Morton O., 2011, Magnetic monitoring of top soils of merida (southern mexico). *Stud. Geophys. Geod*., 55, 377−388.

Bautista F., Cram S., Sommer I., 2011, Suelos. In: Bautista F., Palacio J. L. & Delfín H. (Eds): Técnicas de muestreo para manejadores de recursos naturales. Centro de Investigaciones en Geografía Ambiental. Universidad Nacional Autónoma de México. Morelia, Michoacán, México.

Becher R., Hetland R.B., Refsnes M., Dahl J.E., Dahlman H.J., Schwarze P.E., 2001, Rat lung inflammatory responses after in vivo and in vitro exposure to various stone particles. *Inhal. Toxicol.,* 13, 789–805.

Beckwith P.R., Ellis J.B., Revitt D.M., 1986, Heavy metal and magnetic relationships for urban source sediments. *Phy. Earth Planet. Inter.,* 42, 67–75.

Bityukova L., Scholger R., Birke M., 1999, Magnetic susceptibility as indicator of environmental pollution of soils in Tallinn. *Phys. Chem. Earth* (A), 24, 829-835.

Blundell A., Hannam J.A., Dearing J.A., Boyle J.F., 2009, Detecting atmospheric pollution in surface soils using magnetic measurements: A reappraisal using an England and Wales database. *Environ. Pollut*., 157, 2878–2890.

Chaparro M.A.E., Bidegain J.C., Sinito A.M., Gogorza C.S.G., Jurado S., 2003, Preliminary results of magnetic measurements on stream-sediments from Buenos Aires Province, Argentina. *Stud. Geophys. Geod.,* 47, 121–145.

Chaparro Marcos A.E., Chaparro Mauro A.E., Rajkumar P., Ramasamy V., Sinito Ana M., 2011, Magnetic parameters, trace elements and multivariate statistical studies of river sediments from the south eastern India: a case study from Vellar River. *Environ. Earth Scie.*, 63, 2, 297-310.

Chaparro M.A.E., Gogorza C.S., Lavat A., Pazos S., Sinito A.M., 2002, Preliminary results of magnetic characterisation of different Soils in Tandil Region (Argentina) affected by the pollution of metallurgical factory. *Eur. J. Environ. Eng. Geophys*., 7, 35-58.

Dearing J.A., Dann R.J.L., Hay K., Lees J.A., Loveland P.J., Maher B.A., O'Grady K., 1996, Frequency dependent susceptibility measurements of environmental materials. *Geophys. J. Int.*, 124, 228-240.

Desenfant F., Petrovský E., Rochette P., 2004, Magnetic signature of industrial pollution of stream sediments and correlation with heavy metals: case study from South France. *Water Air Soil Pollut*., 152, 297-312.

Donaldson K., Li X.Y., MacNee W., 1998, Ultrafine (nanometre) particle mediated lung injury. *J. Aerosol Sci.*, 29, 553–560.

Dunlop D.J., Özdemir Ö., 1997, Rock Magnetism - Fundamentals and Frontiers. Cambridge University Press, Cambridge, 573 pp.

Ďurža O., 1999, Heavy metals contamination and magnetic susceptibility in soils around metallurgical plant. *Phys. Chem. Earth*, (A), 24, 541-543.

ESRI, 2004, Arc GIS 9, Getting Started with ArcGIS. Environmental Systems Research Institute, Inc., Redlands, USA.

Evans M.E., Heller F., 2003, Environmental Magnetism - Principles and Applications of Enviromagnetics. *Int. Geophysics Ser.*, 86, Academic press, Amsterdam, 293 p.

Fialova H., Maier G., Petrovský E., Kapi_cka A., Boyko T., Scholger R., MAGPROX Team, 2006, Magnetic properties of soils from sites with different geological and environmental settings. *J. Appl. Geophys.,* 59, 273-283.

Gautam P., Blaha U., Appel E., 2005, Magnetic susceptibility of dust-loaded leaves as a proxy for traffic-related heavy metal pollution in Kathmandu city, Nepal. *Atmos. Environ.,* 39, 2201–2211.

Georgeaud V.M., Rochette P., Ambrosi J.P., Vandamme D., Williamson D., 1997, Relationship between heavy metals and magnetic properties in a large polluted catchment: the Etang de Berre (south of France). *Phys. Chem. Earth*, 22, 211-214.

Goluchowska B.J., 2001, Some factors affecting an increase in magnetic susceptibility of cement dusts. *J. Appl. Geophys*., 48, 103-112.

Gómez B., Palacios M.A., Gómez M., Sanchez J.L., Morrison G., Rauch S., 2002, Levels and risk assessment for humans and ecosystems of platinum-group elements in the airborne particles and road dust of some European cities. *Sci. Total Environ.,* 299, 1–16.

GS+, 2006, Geostatistics for the Environmental Sciences, GS+ Users Guide, V.7. Gamma Design Software, Plainwell, Michigan, USA, 160 pp.

Hanesch M., Scholger R., 2002, Mapping of heavy metal loadings in soils by means of magnetic susceptibility measurements. *Environ. Geol.*, 42, 857-870, DOI: 10.1007/s00254-002-0604-1.

Hanesch M., Stanjek H., Petersen N., 2006, Thermomagnetic measurements of soil iron minerals: the role of organic carbon. *Geophys. J. Int*., 165, 53-61.

Harrison R.M., Jones M., 1995, The chemical composition of airborne particles in the UK atmosphere. *Sci. Tot. Environ*., 168, 195-214.

Harrison R.M., Yin J., 2000, Particle matter in the atmosphere: which particle properties are important for its effects on health?. *Sci. Total Environ*., 249, 85-101.

Hoffmann V., Knab M., Appel E., 1999, Magnetic susceptibility mapping of roadside pollution. *J. Geochem. Explor*., 66, 313-326.

Hullet L.D. Jr., Weinberger A.J., Nothcutt K.J., Ferguson M., 1980, Chemical species in fly ash from coal-burning power plants. *Science*, 210, 1356-1358.

Hunt A., Jones J., Oldfield F., 1984, Magnetic measurement and heavy metals in atmospheric particulates of anthropogenic origin. *Sci. Tot. Environ*., 33, 129-139.

Hunt A., 1986, The application of mineral magnetic methods to atmospheric aerosol discrimination. *Physics of the Earth and Planetary Interiors,* 42, 10–21.

INEGI - Instituto Nacional de Estadística y Geografía (2010). «Principales resultados por localidad 2010 (ITER)». http://www.inegi.org.mx/sistemas/ResultadosR/CPV/Default.aspx?texto=Morelia

Isaaks E., Srivastava R., 1989, Applied Geostatistics. Oxford University Press, Oxforf, U.K.

Jeleñska M., Hasso-Agopsowicz A., Kopcewicz B., Sukhorada A., Tyamina K., Kadzialko-Hofmokl M., Matviishina Z., 2004, Magnetic properties of the profiles of polluted and non-polluted soils. A case study from Ukraine. *Geophys. J. Int*., 159, 104-116.

Jordanova D., Hoffmann V., Fehr Th., 2004, Mineral magnetic characterization of anthropogenic magnetic phases in the Danube river sediments (Bulgarian part). *Earth Planet. Sci. Lett*., 221, 71-89.

Jordanova N., Jordanova D., Tsacheva T., 2008, Application of magnetometry for delineation of anthropogenic pollution in areas covered by various soil types. *Geoderma*, 144, 557-571.

Kapička A., Petrovský E., Ustjak S., Macháčková K., 1999, Proxy mapping of fly-ash pollution of soils around a coalburning power plant: a case study in the Czech Republic. *J. Geochem. Explor.*, 66, 291-297.

Kapička A., Jordanova N., Petrovský E., Ustjak S., 2000, Magnetic stability of power-plant fly ash in different soil solutions. *Phys. Chem. Earth,* 25, 431–436.

Kapička A., Jordanova N., Petrovský E., Ustjak S., 2001, Effect of different soil conditions on magnetic parameters of power-plant fly ashes. *J. Appl. Geophys.,* 48, 93–102.

Kim W., Doh S.J., Park Y.H., Yun S.T., 2007, Two-year magnetic monitoring in conjunction with geochemical and electron microscopic data of roadside dust in Seoul, Korea. *Atmos. Environ.,* 41, 7627e7641.

Kim Y.H., Kim K.S., Kwak N.J., Lee K.H., Kweon S.A., Lim Y., 2003, Cytotoxicity of yellow sand in lung epithelial cells. *J. Bioscience,* 28, 77–81.

Kukier U., Fauziah Ishak C., Summer M.E., Miller W.P., 2003, Composition and element solubility of magnetic and non-magnetic fly ash fractions. *Environ. Pollut*., 123, 255-266.

Lecoanet H., Léveque F., Ambrosi J.P., 2003, Combination of magnetic parameters: an efficient way to discriminate soil-contamination sources (south France). *Environ. Pollut*., 122, 229-234.

Li X.D., Poon C.S., Liu P.S., 2001, Heavy metal contamination of urban soils and street dusts in Hong Kong. *Appl. Geochem.,* 16, 1361–1368.

Lozano R., Bernal J.P., 2005, "Characterization of a new set of eight geochemical reference materials for XRF major and trace elements analysis". *Rev. Mex. C. Geol.*, 22, 329-344.

Lu S.G., Bai S.Q., Cai J.B., Xu C., 2005, Magnetic properties and heavy metal contents of automobile emission particles. *J. Zhejiang Univ. Sci.,* 6 (B), 731–735.

Lu S.G., Zheng Y.W., Bai S.Q., 2008, A HRTEM/EDX approach to identification of the source of dust particles on urban tree leaves. *Atmos. Environ.,* 42, 6431-6441.

Lu S.G., Bai S.Q., 2006, Study on the correlation of magnetic properties and heavy metals content in urban soils of Hangzhou City, China. *J. Appl. Geophys.,* 60, 1–12.

Lu S.G., Bai S.Q., Xue Q.F., 2007, Magnetic properties as indicators of heavy metals pollution in urban topsoils: a case study from the city of Luoyang, China. *Geophys. J. Int.,* 171, 568-580.

Ma L.Q., Rao G.N., 1997, Chemical fractionation of cadmium, copper, nickel and zinc in contaminated soils. *J. Environ. Qual.,* 26, 259–264.

Maher B.A., 1988, Magnetic properties of some synthetic submicron magnetites. *Geophys. J.,* 94, 83–96.

Maher B.A., Moore C., Matzka J., 2008, Spatial variation in vehicle-derived metal pollution identified by magnetic and elemental analysis of roadside tree leaves. *Atmos. Environ*., 42, 364-373.

Magiera T., Strzyszcz Z., Kapička A., Petrovský E., MAGPROX Team, 2006, Discrimination of lithogenic and anthropogenic influences on topsoil magnetic susceptibility in Central Europe. *Geoderma,* 130, 299-311.

Meena N.K., Maiti S., Shrivastava A., 2011, Discrimination between anthropogenic (pollution) and lithogenic magnetic fraction in urban soils (Delhi, India) using environmental magnetism, *J. Appl. Geophys*., 73, 121-129.

Mitchell R., Maher B.A., 2009, Evaluation and application of biomagnetic monitoring of traffic-derived particulate pollution. *Atmos. Environ.*, 43, 2095–2103.

Moreno E., Sagnotti L., Dinare's-Turrell J., Winkler A., Cascella A., 2003, Biomonitoring of traffic air pollution in Rome using magnetic properties of tree leaves. *Atmos. Environ.,* 37, 2967–2977.

Muxworthy A.R., Matzka J., Fernandez Davila A., Petersen N., 2003, Magnetic signature of daily sampled urban atmospheric particles. *Atmos. Environ*., 37, 4163-4169.

Muxworthy A.R., Matzka J., Petersen N., 2001, Comparison of magnetic parameters of urban atmospheric particulate matter with pollution and meteorological data. *Atmos. Environ.,* 35, 4379–4386.

Oyama A.K., López E., Fuentes J., 2011, Ordenamiento Ecológico Teritorial del Municipio de Morelia, Fase de Caracterización. CIEco-UNAM y H. Ayuntamiento de Morelia. Michoacán, México.

Petrovský E., Ellwood B.B., 1999, Magnetic monitoring of air-, land- and water-pollution. In: Maher B.A. and Thompson R. (Eds.), Quaternary Climates, Environments and Magnetism. Cambridge University Press, Cambridge, UK.

Petrovský E., Kapička A., Jordanova N., Knab M. and Hoffmann V., 2000. Low-field magnetic susceptibility: a proxy method of estimating increased pollution of different environmental systems. *Environ. Geol*., 39, 312-318.

Petrovský E., Kapička A., 2006, On determination of the Curie point from thermomagnetic curves. Journal of Geophysical Research 111, B12S27. doi:10.1029/2006JB004507.

Ruiping S., Cioppa M.T., 2006, Magnetic survey of topsoils in Windsor - Essex County, Canada. *J. Appl. Geophys*., 60, 201-212.

Shan H.D., Lu S.G., 2005, Mineral magnetism of power-plant fly ash and its environmental implication. Acta Miner. Sinica, 25, 141–146.

Shilton V.F., Booth C.A., Smith J.P., Giess P., Mitchell D.J., Williams C.D., 2005, Magnetic properties of urban street dust and their relationship with organic matter content in the West Midlands, *UK Atmos. Environ*., 39, 3651–3659.

Strzyszcz Z., Magiera T., Heller F., 1996, The influence of industrial emissions on the magnetic susceptibility of soils in Upper Silesia. *Stud. Geophys. Geod*., 40, 276-286.

Sutherland R.A., 2003, Lead in grain size fractions of road-deposited sediment. *Environ. Pollut*., 121, 229-237.

Thompson R., Oldfield F., 1986, Environmental Magnetism. Allen and Unwin, London, p. 227.

Vassilev S.V., 1992, Phase mineralogy studies of solid waste products from coal burning at some Bulgarian thermoelectric power plants. *Fuel*, 71, 625-633.

Webster R., Oliver M.A., 1990, Statistical methods in soil and land resource Surrey. Oxford University Press, New York, U.S.A.

Wichmann H.E., Peters A., 2000, Epidemiological evidence of the effects of ultrafine particle exposure. Philosophical Transactions of the Royal Society of London A 358, 2751–2769.

Xie S., Dearing J.A., Boyle J.F., Bloemendal J., Morse A.P., 2001, Association between magnetic properties and element concentrations of Liverpool street dust and its implications. *J. Appl. Geophys.,* 48, 83–92.

Yang T., Liu Q., Chan L., Cao G., 2007, Magnetic investigation of heavy metals contamination in urban topsoils around the East Lake, Wuhan, China. *Geophys. J. Int.,* 171, 603–612.

Yang T., Liu Q., Li H., Zeng Q., Chan L., 2010, Anthropogenic magnetic particles and heavy metals in the road dust: Magnetic identification and its implications. *Atmos. Environ,* 44, 1175-1185.

Geofísica Internacional (2013) 52-2: 135-152

Original paper

Effect of galvanic distortions on the series and parallel magnetotelluric impedances and comparison with other responses

Enrique Gómez-Treviño, Francisco Javier Esparza Hernández* and José Manuel Romo Jones

Received: February 09, 2012; accepted: January 17, 2013; published on line: March 22, 2013

Resumen

Las impedancias serie y paralelo del tensor magnetotelúrico se evalúan en relación con su relativa inmunidad a las distorsiones galvano-eléctricas. Las respuestas distorsionadas se modelan utilizando la descomposición del tensor en términos de giro, cizalla estática y rumbo de Groom y Bailey. Estos cuatro parámetros, junto con las impedancias sin distorsión, normalmente se consideran incógnitas y se obtienen de los datos mediante la solución de un problema inverso. En el presente trabajo utilizamos la descomposición como un modelo directo para simular sondeos distorsionados. Partiendo de respuestas 2-D sin distorsiones, el tensor se distorsiona suponiendo valores arbitrarios de giro, cizalla, estática y rumbo. Por definición las impedancias serie y paralelo son inmunes al rumbo porque son invariantes ante rotación. Adicionalmente, la impedancia serie es inmune a giros y a cizalla, y la impedancia paralelo sólo a giros. La impedancia paralelo depende de cizalla en la forma de un factor que desplaza hacia abajo las curvas de amplitud. Por otro lado, el efecto de la estática en ambas impedancias es más complicado que en el tensor mismo porque no se puede corregir con un simple desplazamiento de las curvas. En términos generales, hay un balance positivo por parte de las impedancias serie y paralelo sobre las respuestas TE y TM porque los invariantes filtran varias distorsiones. Se muestra que la condición de invariante no es suficiente para tener inmunidad a cualquiera de las distorsiones. Se utiliza para esto los valores característicos de Eggers, los cuales son inmunes sólo al rumbo, como todos los invariantes. Se muestra además que la invariancia tampoco es una condición necesaria para ser inmune a las distorsiones, según lo atestigua el tensor de impedancia, el cual depende del rumbo pero está libre de las demás distorsiones. Los desarrollos se ilustran utilizando sondeos de los conjuntos de datos COPROD2S1, COPROD2 y BC87.

Palabras clave: magnetotelurico, distorsiones galvanicas, invariantes.

Abstract

The series and parallel impedances of the magnetotelluric tensor are appraised in relation to their relative immunity to galvanic electric distortions. The distorted responses are modeled using the Groom-Bailey decomposition of the tensor in terms of twist, shear, statics and strike direction. These four parameters and the undistorted responses are normally considered as unknowns, and are obtained from field data through the solution of an inverse problem. In the present work we use the decomposition as a forward model to simulate distorted sounding curves. Starting with undistorted 2-D TE and TM responses, the tensor is distorted by assuming arbitrary values of twist, shear, static and strike direction. By default, both series and parallel responses are immune to the strike direction because they are invariants under rotation. In addition, series responses are immune to twist and shear and parallel responses only to twist. The dependence of the latter on shear is in the form of a real factor that shifts downwards the amplitude curves. On the other hand, the effect of statics on both series and parallel responses is more complicated than that on the impedance tensor because it cannot be accounted for by a simple shift of the curves. On the whole, there is a positive balance on the part of the series and parallel impedances over the TE and TM responses because some of the distortions are filtered out by the invariants. It is shown that invariance is not sufficient to be immune to any of the distortions. The example chosen is Eggers' eigenvalues, which are immune only to the by-the-fault strike direction. Invariance is not necessary either, as evidenced by the phase tensor, whose elements depend on strike but are immune to all distortions. The derivations are illustrated using soundings from the synthetic COPROD2S1 and field-recorded COPROD2 and BC87 data sets.

Key words: Magnetotelluric, galvanic distortions, invariants.

E. Gómez-Treviño
F.J. Esparza Hernández
J.M. Romo Jones
División de Ciencia de la Tierra
CICESE
Km 107 carretera Tijuana-Ensenada, 22860
Ensenada, Baja California, México.
*Corresponding author: fesparz@cicese.mx

Introduction

The series impedance is defined in terms of the sum of squares of the elements of the impedance tensor, and the parallel impedance in terms of the sum of squares of the elements of the admittance tensor, the inverse of impedance. Both quantities, series and parallel, are scalar measures of impedance and unlike the individual elements of the tensor, are invariant under rotation of the system of coordinates. Other properties include that series is particularly sensitive to underground resistors and that parallel is particularly sensitive to underground conductors (Romo *et al*, 2005). Beside these properties very little is known about these invariants. Two-dimensional (2-D) inversions of synthetic and field data throw very similar models to those obtained using the traditional TE and TM sounding curves. In particular, we have noticed that using TE and TM data that are corrected for galvanic effects produces results suspiciously similar to those obtained using uncorrected series and parallel responses (Antonio-Carpio *et al*., 2011). This could be due to a mere accident or it could be an indication of unknown properties of the two invariants. To clarify this issue it is necessary to make a rigorous appraisal of the effect of galvanic distortions on the series and parallel invariants.

The impedance tensor of a regional 2-D conductivity structure can be severely distorted by local 3-D structures that are inductively small, where inductively small means that their size is smaller than the skin depth. The distortions are due to perturbations of the regional electric field by local 3-D charge distributions, and to perturbations of the regional magnetic field by also local current distributions. In principle, the local 3-D structures can be included in the interpretation process as part of the sought model of the Earth. However, this is seldom done. Rather, the process is divided into two steps: the distortion issue is first settled in some way and then the undistorted data is properly interpreted. It is possible to deal with distortions separately because they are not completely arbitrary but follow some rules. The most important fact is that the impedance tensor distorted by electric effects can be simulated by a real tensor multiplied by the undistorted impedance (Berdichevsky and Dmitriev, 1976a; Bahr, 1988). This means that the basic physics and its mathematical representation are well understood. However, what matters in practice is to recover the undistorted impedances. To this end, Groom and Bailey (1989) proposed a factorization of the real distorting tensor that they call a physical decomposition. They introduced two concepts called twist and shear, which together with strike direction and static factors completely simulate distorted experimental impedances. Twist and shear are physically meaningful effects on electric fields that distort the impedance in distinctly mathematical terms. In fact, they can be distinctly identified in the numerical solution of the nonlinear inverse problem proposed by Groom and Bailey (1989). While it is true that the factorization is not unique, as noted by Caldwell *et al*. (2004), many practical applications attest for the validity of the model to simulate distorted impedances (*e.g.* Ledo and Jones, 2001).

When computing series and parallel impedances we do not know how the distortions propagate from the elements of the tensor to the invariants. Using Groom-Bailey's factorization the procedure to find out is straightforward but the result is far from trivial. The paper is written in a tutorial-review manner including results for the determinant, the classical invariant, and for Egger's (1983) invariant eigenvalues. This last application illustrates that the result for series and parallel modes is not due solely to their invariant character. A final discussion about the phase tensor of Caldwell *et al*. (2004) gives perspective to the other results, illustrating that invariance is not a necessary condition to avoid distortions.

Methodology

The algebra of distortions

Assume a two-dimensional (2-D) electrical resistivity distribution subject to plane electromagnetic waves from above. Placing the *x*-axis of a Cartesian coordinate system along strike, the components of the electric and magnetic fields are related as

$$\begin{pmatrix} Ex \\ Ey \end{pmatrix} = \begin{pmatrix} 0 & A \\ -B & 0 \end{pmatrix} \begin{pmatrix} Hx \\ Hy \end{pmatrix}. \qquad (1)$$

The components E_x and H_y correspond to the *TE* or *E*-polarization mode and A is the respective impedance. Accordingly, E_y and H_x defines the *TM* or *H*-polarization mode with its impedance B. It has been established that the distortions of the electric field can be modeled using a real tensor $\boldsymbol{C}$ as

$$\begin{pmatrix} Ex \\ Ey \end{pmatrix}_d = \begin{pmatrix} c_1 & c_2 \\ c_3 & c_4 \end{pmatrix} \begin{pmatrix} Ex \\ Ey \end{pmatrix}. \qquad (2)$$

Behind the simplicity of this equation there are extensive studies that led to its development (e.g. Berdichevsky and Dimitriv, 1976; Bahr, 1988). Substituting (1) in (2) we obtain

$$\begin{pmatrix} Ex \\ Ey \end{pmatrix}_d = \begin{pmatrix} -c_2 B & -c_1 A \\ -c_4 B & c_3 A \end{pmatrix} \begin{pmatrix} Hx \\ Hy \end{pmatrix}. \quad (3)$$

If we now rotate the system of coordinates by an angle θ the components of the distorted electric field in the rotated system are

$$\begin{pmatrix} E'x \\ E'y \end{pmatrix}_m = \begin{pmatrix} \cos\theta & -\sin\theta \\ \sin\theta & \cos\theta \end{pmatrix} \begin{pmatrix} Ex \\ Ey \end{pmatrix}_d. \quad (4)$$

The components of the magnetic field need to be rotated too. Solving for the unprimed coordinates and substituting the result along with equation (4) back into equation (3), the resulting equation relates the electric and magnetic fields in the primed coordinates. The corresponding impedance is

$$Zm = \begin{pmatrix} \cos\theta & -\sin\theta \\ \sin\theta & \cos\theta \end{pmatrix} \begin{pmatrix} -c_2 B & -c_1 A \\ -c_4 B & c_3 A \end{pmatrix} \begin{pmatrix} \cos\theta & \sin\theta \\ -\sin\theta & \cos\theta \end{pmatrix}. \quad (5)$$

Notice that in equation (5) the columns of the distorted impedance before rotation have the same phase because the distorting factors are real. After rotation the elements of Z_m are all different combinations of *A* and *B* and their phases are mixtures of the phases of the two modes. This is illustrated in Figure 1 using the impedances of sounding # 11 of the synthetic data set COPROD2S1 made available in MTnet by Varentsov (1998). The calculations were made using $c_1 = 1.97, c_2 = -0.77, c_3 = 0.35$ and $c_4 = 0.64$.

A useful factorization

Groom and Bailey (1989) proposed to factorize or decompose the tensor ***C*** such that

$$Zm = RTSAZ_2R^T, \quad (6)$$

where

$$A = g\begin{pmatrix} 1-s & 0 \\ 0 & 1+s \end{pmatrix} = \begin{pmatrix} a & 0 \\ 0 & b \end{pmatrix}, \quad (6a)$$

$$T = \frac{1}{\sqrt{1+t^2}}\begin{pmatrix} 1 & -t \\ t & 1 \end{pmatrix}, \quad (6b)$$

$$S = \frac{1}{\sqrt{1+e^2}}\begin{pmatrix} 1 & e \\ e & 1 \end{pmatrix}, \quad (6c)$$

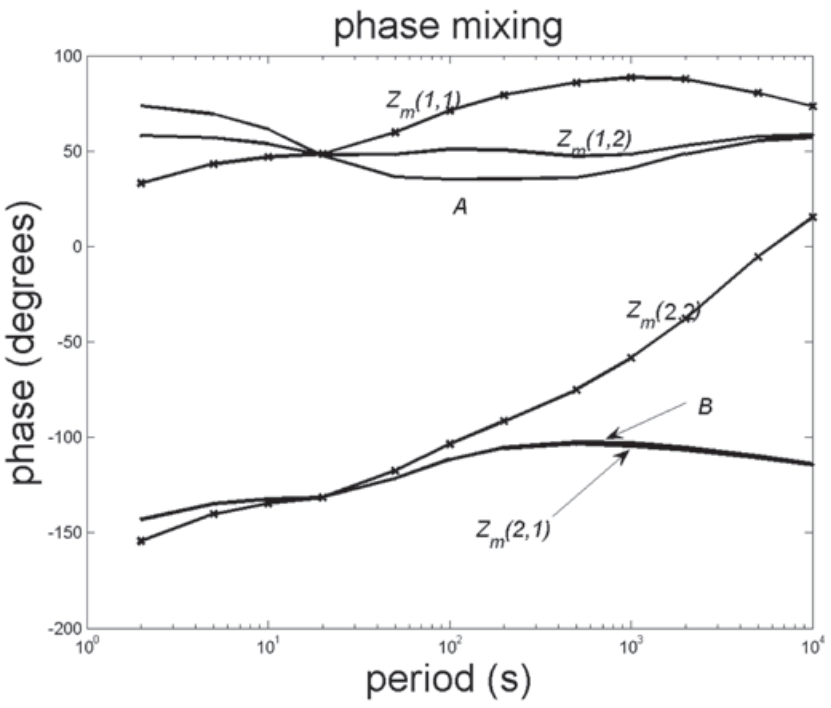

Figure 1. *A* and *B* correspond to the TE and TM modes of sounding # 11 of the synthetic data set COPROD2S1 made available in MTNet.dias.ie by Varentsov (1998). When $\theta \neq 0$ in equation (5) the elements of the resulting impedance all are mixtures of the phases of *A* and *B*. Calculations were made using $c_1 = 1.97, c_2 = -0.77$, $c_3 = -0.35$ and c_4 = 0.64. The graphs correspond to the phase of the impedance.

and

$$R = \begin{pmatrix} \cos\theta & -\sin\theta \\ \sin\theta & \cos\theta \end{pmatrix}, \qquad (6d)$$

Notation is changed a little as indicated in equation (6a). The tensor ***A*** accounts for anisotropy and the scalar *g* for the site gain. All together they simulate static shifts on impedances *A* and *B*. We simply use *a* and *b* as the corresponding factors, instead of the more elegant arrangement with *g* and *s*. Tensor ***T*** twists the electric field so the parameter *t* is called twist. Tensor ***S*** produces a shear-like effect so the parameter *e* is called shear. ***R*** is simply a rotation matrix to account for the coordinate system to be off an angle θ from strike. Twist and shear are expressed in degrees such that *t* and *e* are the tangent of the corresponding angles.

Figure 2 illustrates what each of the operators does to an undistorted unitary electric field. The undistorted field varies from (0,1) to (0,-1) to cover different initial directions to allow a pattern to emerge. Each operator can be thought to be the distortion tensor in equation (2) as applied to an undistorted electric field. Twist is a simple rotation of the electric field similar to the rotation of coordinates, and it could be thought to be an overlap of the latter. However, this is not so because the rotation of coordinates involves both electric and magnetic fields or, equivalently, the whole impedance tensor and not only the electric field. Another important comment about this factorization or decomposition is that it does not reduce or increase the number of distorting parameters; it just spreads them in a useful way for their recovery from the elements of Z_m.

The absorption of static factors

The impedance tensor, distorted or undistorted, can be mathematically transformed into an exactly equivalent set of 8 real numbers. We consider in the next sections some of these transformations. Groom and Bailey (1989) factorization, although

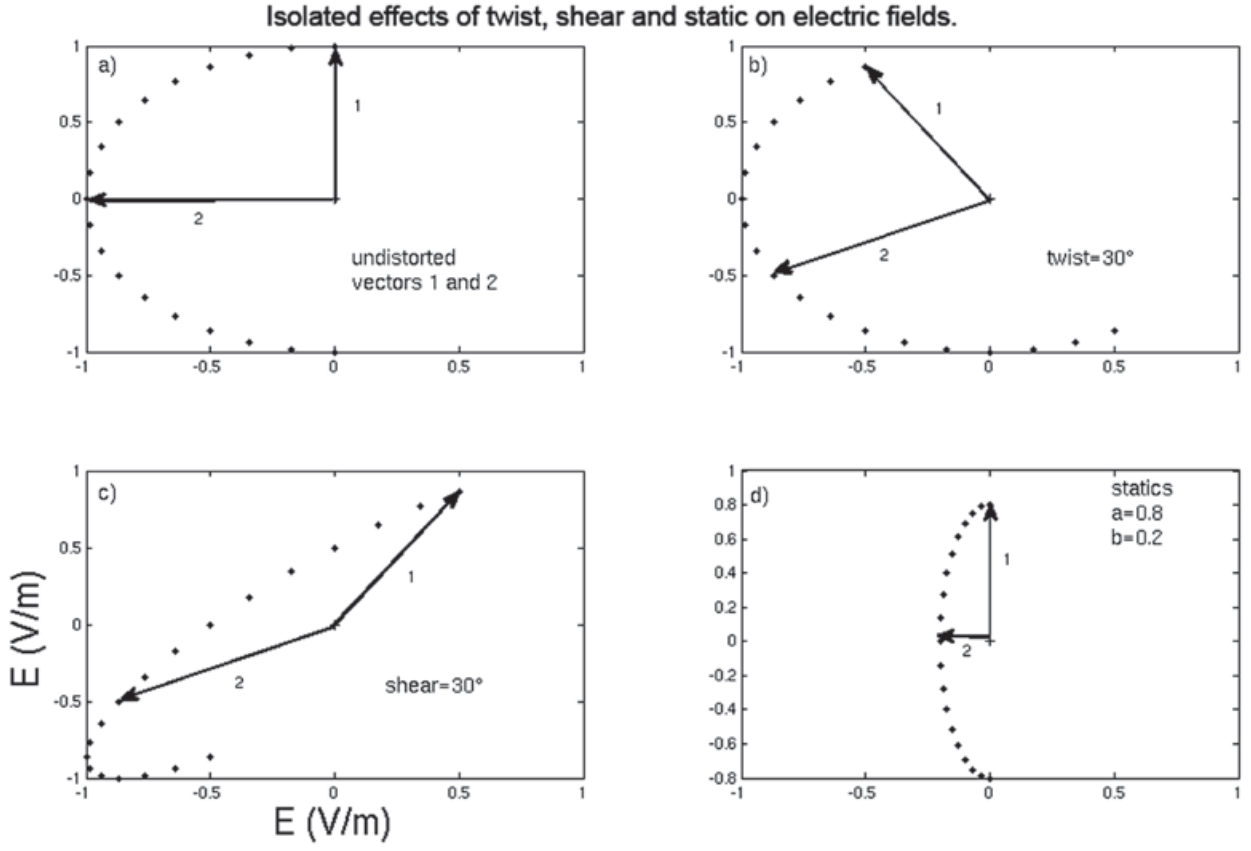

Figure 2. The effect of the individual distortion tensor ***T, S*** and ***A*** are illustrated in a), b) and c), respectively. The figures illustrate what each of the operators does to an undistorted unitary electric field shown in a). The undistorted field varies from (0,1) to (0,-1) to cover different initial directions to allow a pattern to emerge. Each operator can be thought to be the distortion tensor in equation (2) as applied to a unitary and undistorted electric field. The figure is inspired in a similar one in Groom and Bailey (1989).

mathematically expressed, is not a mathematical decomposition in the same sense that these others are. It is more a convenient proposal to allow for the distortions to be estimated from the elements of Z_m through an inverse procedure. They do it by neutralizing the two distortion factors *a* and *b* due to static, simply by placing ***A*** next to Z_2 The unknowns now become *aA* and *bB*.

This reduction in the number of unknowns accomplishes two things. Z_m on the left side of equation (6) provides with 8 real numbers as data, and on the right side we have 9 unknowns: θ, *t, e, a, b* and four real numbers to make Z_2. This means that without this absorption the inversion cannot even be attempted. However, this is not the most important reason because the relative number of data can be increased by using many frequencies and by forcing θ, *t* and *e* to be the same for all frequencies. The second reason is more fundamental because it cannot be dealt with except by doing what they did. It is universally acknowledged that static distortions factors cannot be determined from the impedance tensor alone, and that independent information is needed to resolve them (e.g. Pellerin and Hohmann, 1990; Ledo *et al*., 2002). By absorbing the static factors into *A* and *B* the problem is solvable. We can mimic the recovery of static shifted curves by explicitly solving for them in equation (6). The recovery equation is

$$AZ_2 = S^{-1}T^{-1}R^T Z_m R \ . \qquad (7)$$

First we compute a distorted Z_m using equation (6). The undistorted Z_2 is the same sounding used in Figure1. The distortions are as follow: two different static factors *a=2* and *b=3* in one case and *a=3* and *b=2* in the other, and the same θ, *t* and *e* for both cases. The distorted, undistorted and recovered curves are shown in Figure 3. Notice that the recovered curves are scaled versions of each other, but the disturbed ones are not. Note also that the recovered curves are scaled versions of the original *TE* or *A* curve.

In general, Z_m depends on θ, *t, e, a* and *b,* as indicated by equation (6). In other words, all of them are needed to fit experimental impedances. The Groom and Bailey (1989) approach does not use the static factors to fit Z_m, but this does not

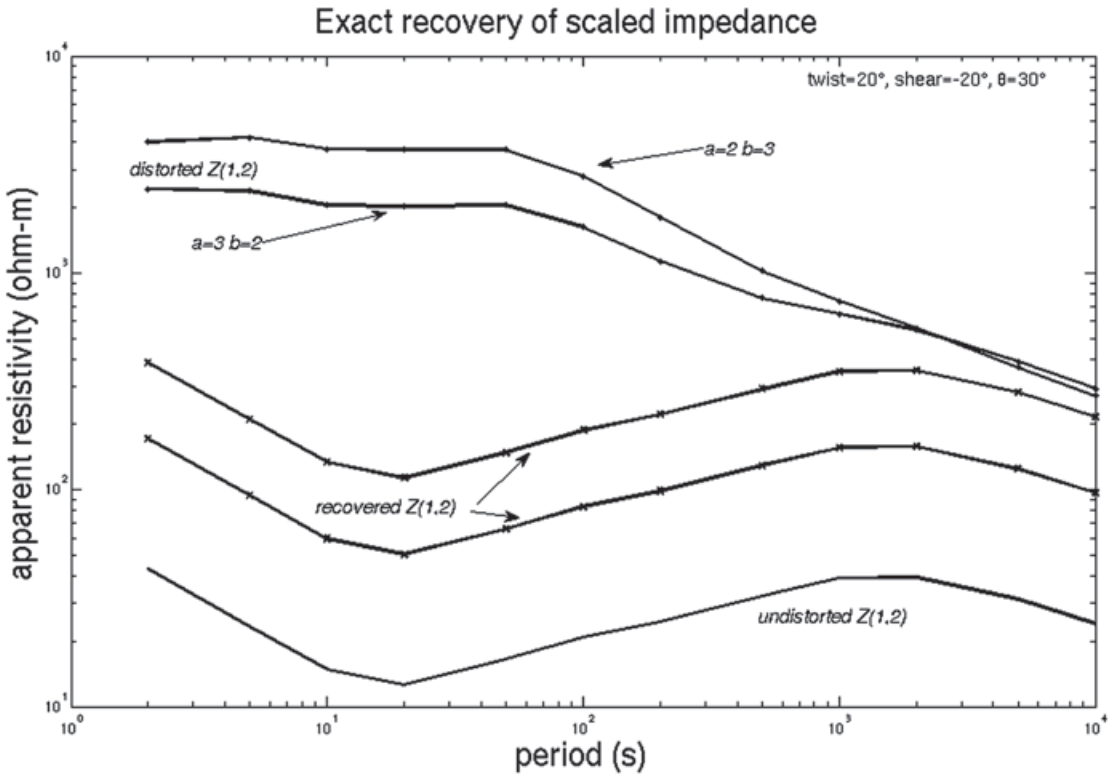

Figure 3. The recovery of undistorted TE impedances using equation (7) is correct save for the static factors. The distorted Z_m is computed using equation (6) and the indicated distorting parameters of twist, shear and strike. The undistorted Z_2 is the same sounding used in Figure1. Notice that the recovered curves are scaled versions of each other, but the disturbed ones are not. Note also that the recovered curves are scaled versions of the original *TE* or *A* curve. In this instance it is pretended that we know the distorting parameters of twist, shear and strike in equation (7).

mean that Z_m is immune to them. In other words, the unprocessed Z_m is immune to none of the distorting parameters: twist, shear, static and strike. This is a natural starting point to analyze other responses derived from Z_m that are immune to one or more types of distortions.

When dealing with invariants, we can dispense of the rotation matrix and its transpose and use the simplified expression

$$Z_m = \frac{1}{\sqrt{1+t^2}}\frac{1}{\sqrt{1+e^2}}\begin{pmatrix} -(e-t)B & (1-te)A \\ -(1+te)B & (e+t)A \end{pmatrix}. \quad (8)$$

This equation follows from (6) by carrying out the multiplications. Again, we assume that *a* is absorbed in *A* and *b* in *B*.

Results

Immunity to twist

The first invariant to examine is the classical determinant of the impedance tensor (Berdichevsky and Dimitriv, 1976). In the absence of distortions, the determinant is simply given as

$$\det(Z_m) = AB \ . \quad (9)$$

In general, when the four elements are present in the tensor, the determinant is given as

$$\det(Z_m) = Z_m(1,1) * Z_m(2,2) - Z_m(2,1) * Z_m(1,2) \ . \quad (10)$$

To determine the effect of distortions we must substitute equation (8) into equation (10).

The result is

$$\det(Z_m) = \left(\frac{1-e^2}{1+e^2}\right)AB \ . \quad (11)$$

The twist parameter *t* cancels in the algebra but not the shear parameter *e*. The effect on the determinant is equivalent to modify the static factors on either *A* or *B,* or both. With no static effects the amplitude of the determinant would still be smaller than the actual one if shear distortions are present. On average, we might expect the static factors of the determinant to be biased towards values less than unity.

An invariant closely related to the determinant is the parallel impedance (Romo *et al.* 2005) which is given as

$$Z_{mp}^2 = \frac{2\det^2(Z_m)}{(Z_m^2(1,1) + Z_m^2(1,2) + Z_m^2(2,1) + Z_m^2(2,2))} = \frac{2\det(Z_m)}{tr(Z_m^T Z_m)} \ . \quad (12)$$

Making *t=e=0* in equation (8) and using equation (12), the undistorted parallel impedance is

$$Z_{mp}^2 = 2\left(\frac{(AB)^2}{A^2+B^2}\right) \ . \quad (13)$$

On the other hand, the general case reduces to

$$Z_{mp}^2 = 2\left(\frac{1-e^2}{1+e^2}\right)^2\left(\frac{(AB)^2}{A^2+B^2}\right) \ . \quad (14)$$

Again, the distorted impedance is immune to twist, but not to shear and, of course neither to static, which is hidden in *A* and *B*. The effect of shear is most effective on the parallel impedance than on the determinant because of the square. This is illustrated in Figure 4 for both invariants. The quantity plotted is the traditional apparent resistivity $|Z|^2/(\omega\mu_0)$, where ω stands for angular frequency and μ_0 is the permeability of free space.

Immunity to twist and shear

It is interesting how in the previous section twist separates quite neatly from shear, to leave only the latter as an active distorter. In this section we report an invariant that leaves no trace of both twist and shear. This invariant we call the series equivalent (Romo *et al*., 2005) corresponds to half the sum of squares of the elements of the impedance tensor (Szarka and Menvielle, 1997). This is

$$Z_{ms}^2 = \frac{1}{2}[Z_m^2(1,1) + Z_m^2(1,2) + Z_m^2(2,1) + Z_m^2(2,2)] = \frac{1}{2}tr(Z_m^T Z_m) \ . \quad (15)$$

When *t=e=0*, this reduces to

$$Z_{ms}^2 = \frac{1}{2}(A^2+B^2) \ . \quad (16)$$

In general, substituting equation (8) in (15) leads to

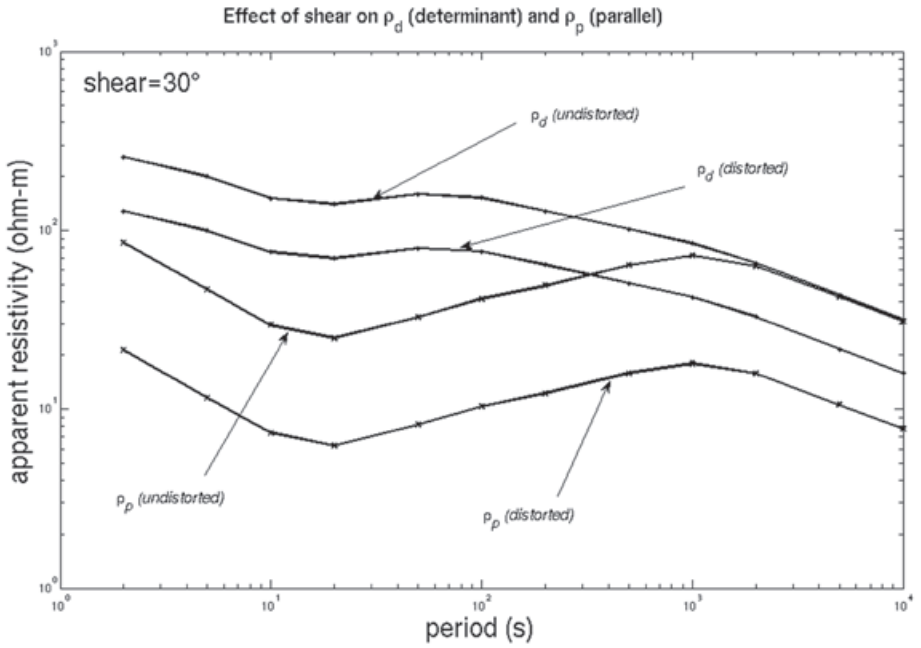

Figure 4. Aside from statics, the amplitudes of the determinant and of the parallel impedance are distorted only by shear. This is illustrated in this figure where it can be observed that according to theory the effect is more effective on the parallel impedance.

$$Z_{ms}^2 = \frac{1}{2}\left(\frac{1}{\sqrt{1+t^2}}\frac{1}{\sqrt{1+e^2}}\right)^2 (1+e^2+t^2+e^2t^2)(A^2+B^2) \quad . \quad (17)$$

It turns out that this reduces to the undistorted series impedance, which means that this type of invariant response is immune not only to strike, but also to both twist and shear. Of course, it is still affected by static because *A* and *B* have absorbed *a* and *b*, the two static factors.

The distorted parallel impedance given by equation (14) differs from the undistorted impedance by a real factor that depends on shear. This implies that the corresponding phase is immune to shear, and because the complex impedance was already immune to strike and twist, this implies that the phase of the parallel impedance is immune to all three distorting parameters. The phase is given as

$$\psi_{mp} = \tan^{-1}\left\{\frac{\mathrm{Im}(AB/\sqrt{A^2+B^2})}{\mathrm{Re}(AB/\sqrt{A^2+B^2})}\right\} \quad . \quad (18)$$

Immunity to strike, twist and shear isolates static effects. It can be appreciated in both equation (16) and (18) that static factors will produce phase mixing. This is illustrated in Figure 5 for the phase of the series impedance. Static effects, absent in the phase of the TE and TM modes, can severely distort the phase of the series impedance. Care must be taken before or while inverting the data. The same applies to the phase of the parallel impedance, for while the factors cancel in the product *AB*, they do not within the square root sign.

Immunity to twist, shear and statics

Equation (11) indicates explicitly that the determinant is affected by shear through a multiplicative factor. On the other hand, implicitly it is affected by static though another factor (*ab*), which comes from the absorption of *a* and *b* into *A* and *B*. All together they compose a single factor that vanishes when determining the phase of the determinant. That is

$$\psi_{md} = \tan^{-1}\left\{\mathrm{Imag}(\sqrt{AB})/\mathrm{Real}(\sqrt{AB})\right\} \quad . \quad (19)$$

The phase of the determinant is then immune to shear and static, along with twist and strike that shares with the complex determinant. We have arrived at a standstill, for there is nothing that we can vary that alters the phase of the determinant.

Invariance is not sufficient

The twist tensor as defined in equation 6(b) is a rotation matrix that changes the direction of the electric field. This may seem to indicate that all invariants are immune to twist, as are the three invariants analyzed so far. However, this is not the case. Consider the two invariant eigenvalues of Eggers (1983), which are given by the quadratic formula

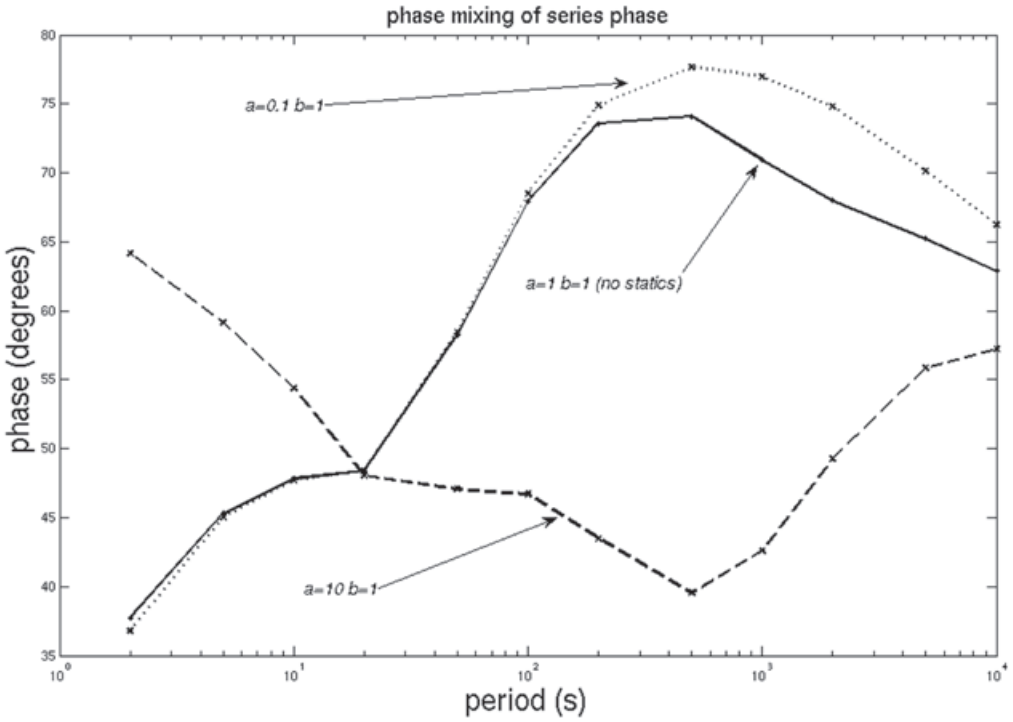

Figure 5. Immunity to strike, twist and shear isolates static effects as in the case of equation (16) for the series impedance. Unfortunately, if *A* and *B* are affected by statics (*a* and *b* different from unity) this produces a static-dependent phase mixing that is not present in the original impedances *A* and *B*. This is illustrated in this figure. Static effects, absent in the phase of the TE and TM modes, can severely distort the phase of the series impedance. The same applies to the phase of the parallel impedance, for while the factors cancel in the product *AB*, they do not within the square root sign in equation (18).

$$\lambda^{\pm} = \frac{-\alpha_2 \pm \sqrt{\alpha_2^2 - 4\det(Z_m)}}{2} \quad . \qquad (20)$$

where

$$\alpha_2 = Z_m(2,1) - Z_m(1,2) \ . \qquad (21)$$

To see how the distortions affect these invariants we need to use the general expression for Z_m given in equation (10). Let us first substitute Z_m in (20) when t=e=0. The result is

$$\lambda^{\pm} = \frac{B + A \pm \sqrt{[B-A]^2}}{2} \quad . \qquad (22)$$

In this case the eigenvalues reduce to either *A* or *B* and in the distorted case to

$$\lambda^{\pm} = \frac{(1+te)B + (1-te)A \pm \sqrt{[(1+te)B - (1+te)A]^2 - 4(t^2 - e^2)AB}}{2\sqrt{1+t^2}\sqrt{1+e^2}} \quad . \qquad (23)$$

This is about the minimum expression one can obtain for the distorted eigenvalues. It can be observed that *t* and *e* are present in the expression and that there is no possible way that those in the numerator cancel out with those in the denominator. It is also clear that the effect of twist and shear cannot be absorbed as equivalent static factors on *A* and *B,* although they can in several places in the expression. The factor *(1+te)* multiplies *B* and *(1-te)* multiplies *A*, both outside and within the square root. However, the absorption cannot be completed for the product *AB* within the square root. Summarizing, the two eigenvalues are not immune to any of the distortions. Figure 6 illustrates this with the phase of the two eigenvalues using different factors for twist, shear and static. Notice that the curves show phase mixing of the original phases of *A* and *B*.

Invariance is not necessary

We now come to a very interesting response that can be derived from the impedance tensor. It is called the phase tensor and was proposed by Cadwell *et al*. (2004). This response is immune to twist, shear and static and it is not invariant. The measured impedance is separated into its real and imaginary parts as

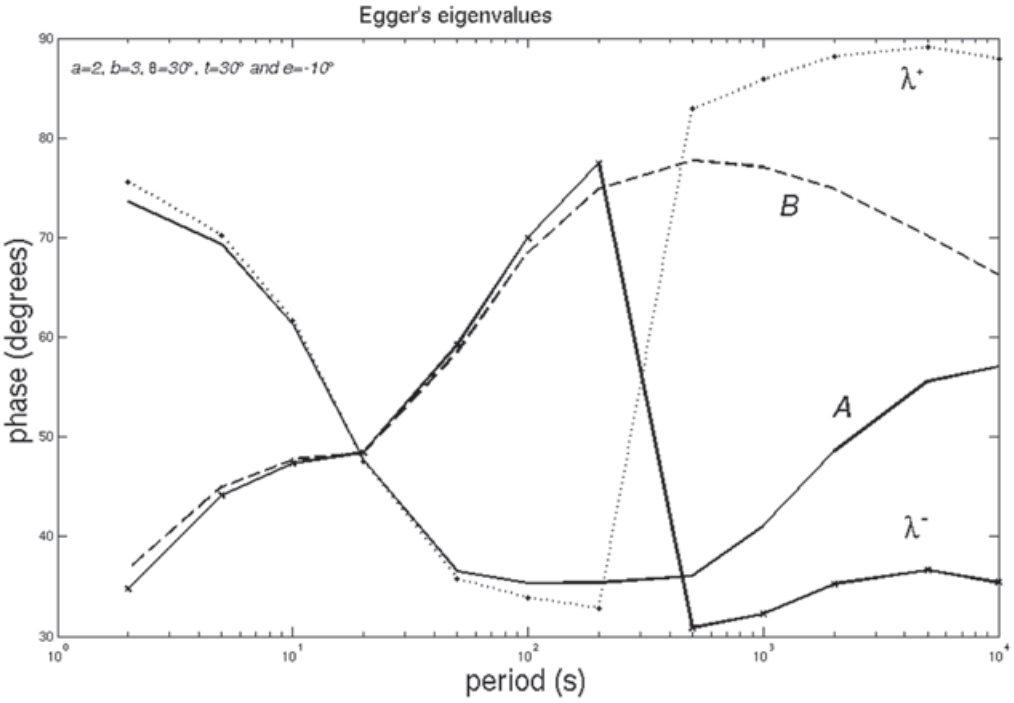

Figure 6. Eggers' eigenvalues, the invariants defined by equation (23) are not immune to any of the distortion parameters of twist, shear and statics. This is illustrated here with the phase of the two eigenvalues. This case demonstrates that invariance under rotation is not a sufficient condition for immunity to any of the other distortions.

$$Z_m = X_m + iY_m \ . \qquad (24)$$

If Z_m were a simple complex number, the tangent of its phase would be its imaginary part divided by its real part. In other words, the tangent of its phase would be the inverse of its real part multiplied by its imaginary part. But Z_m is not a simple complex number, it is a tensor. However, nothing prevents to multiply the inverse of the real tensor by the imaginary tensor. That is

$$\Phi = X_m^{-1} Y_m = \begin{pmatrix} \Phi_{11} & \Phi_{12} \\ \Phi_{21} & \Phi_{22} \end{pmatrix} . \qquad (25)$$

The product is a dimensionless tensor whose elements can be interpreted as the tangent of an angle. So far there is nothing impressive about this. However, let us now enquire about the effect of the different distortions on this dimensionless tensor. The undistorted tensor can be written as

$$Z_2 = X_2 + iY_2 \ . \qquad (26)$$

Substituting this into (6) and doing the operation as in (25) we have that

$$\Phi = (RTSAX_2R^T)^{-1}(RTSAY_2R^T) \ . \qquad (27)$$

Performing the operations there results that ***T***, ***S*** and ***A*** cancel with their corresponding inverses. The expression reduces to

$$\Phi = RX_2^{-1}Y_2R^T \ . \qquad (28)$$

The phase tensor depends only on strike. This is a very important property because it allows obtaining the strike direction independently of the distorting parameters. Figure 7 illustrates the dependence of diagonal elements of the phase tensor as strike is varied.

Series, parallel and determinant impedances

The properties of the determinant in relation to distortions are well known (e.g. Arango *et al*., 2009) and derive from the fact that if $Z_m = CZ_2$, then $det(Z_m) = det(C)\ det(Z_2)$. Given that C is real the phase of $det(Z_m)$ is the same as the phase of $det(Z_2)$. Stated in this way this result is more general than that of equation (11), which assumes that the undistorted impedance is 2-D. The results for the series and parallel impedances derived above also assume a 2-D undistorted impedance. This means that for real data, seldom fully 2-D, we should expect the results to hold exactly for the determinant and only approximately for series and parallel. This issue is explored in the next three figures. First, we present a reference case

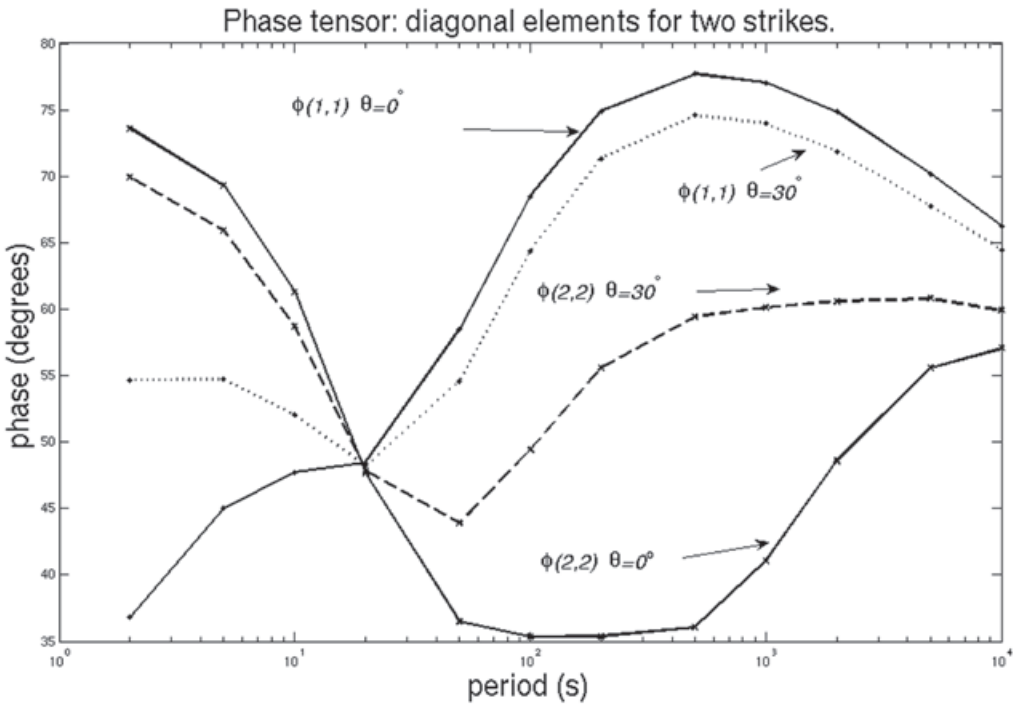

Figure 7. Contrary to the invariants, the phase tensor depends on strike and at the same time it is immune to all other distortions. This is a very important property because it allows obtaining the strike direction independently of the distorting parameters. This figure illustrates the dependence of the diagonal elements of the phase tensor as strike is varied. The phase tensor is an example of a response that is not invariant but is immune to distortions. This result, together with that of Figure 6, imply that invariance is neither sufficient not necessary for immunity to distortions, and that each response must be evaluated on its own.

using synthetic 2-D data. What we have done is to distort the original TE and TM data using equation (6) and then compute the three invariants of Z_m. It can be observed in Figure 8c and 8d that both apparent resistivity and phase curves of the series impedance are immune to the distortions. The comparison is made for three shears, 0, 30 and 40 degrees. Strike direction and twist are not recorded because these and the other results presented below are exactly the same regardless of the value of these parameters. According to theory the only distortion left is due to shear and this is what Figure 8 shows. The determinant and the parallel apparent resistivities, as shown in Figure 8a and 8c, suffer a downward shift as predicted by equations (11) and (14), respectively. The shift being more pronounced the larger the shear, and the shift of the parallel resistivity being larger than that of the determinant, as it should be according to theory. It can also be observed in Figures 8b and 8c that the corresponding phases are not affected by shear.

The results using field data are presented in Figures 9 and 10. We chose soundings from the COPROD2 and BC87 data sets (Jones, 1993a, 1993b). It can be observed that in both cases the corresponding curves behave very much like those using synthetic data. We used equation (6) to further distort both soundings with different strike directions, twists and shears and then computed the three invariants. It can be observed that the phases of the three invariants are immune to the changes of the distorting parameters, implying that they are free of distortions except for the implicit static factors. Notice that the phases of the determinant are exactly the same for the three shears (Figures 9b and 10c) and that those of the series and parallel depart a little from each other (Figures 9d and 10d). As mentioned before, this is because the determinant makes no assumption about dimensionality while the other two assume a 2-D undistorted impedance. Overall, the phases for the three shears are reasonably close considering that a shear of 40 degrees is close to the maximum of 45 degrees.

The example drawn from the BC87 data set illustrates an important point about what is removed and what remains to be done to completely clean the data. Notice that at short periods the series and parallel apparent resistivities (Figure 10c) are both horizontal for the null shear, and that the latter is depressed in relation to the former. This suggests that the parallel apparent resistivity curve has an intrinsic shear distortion that is depressing it from the undistorted series resistivity. This would lead us to shift the curve

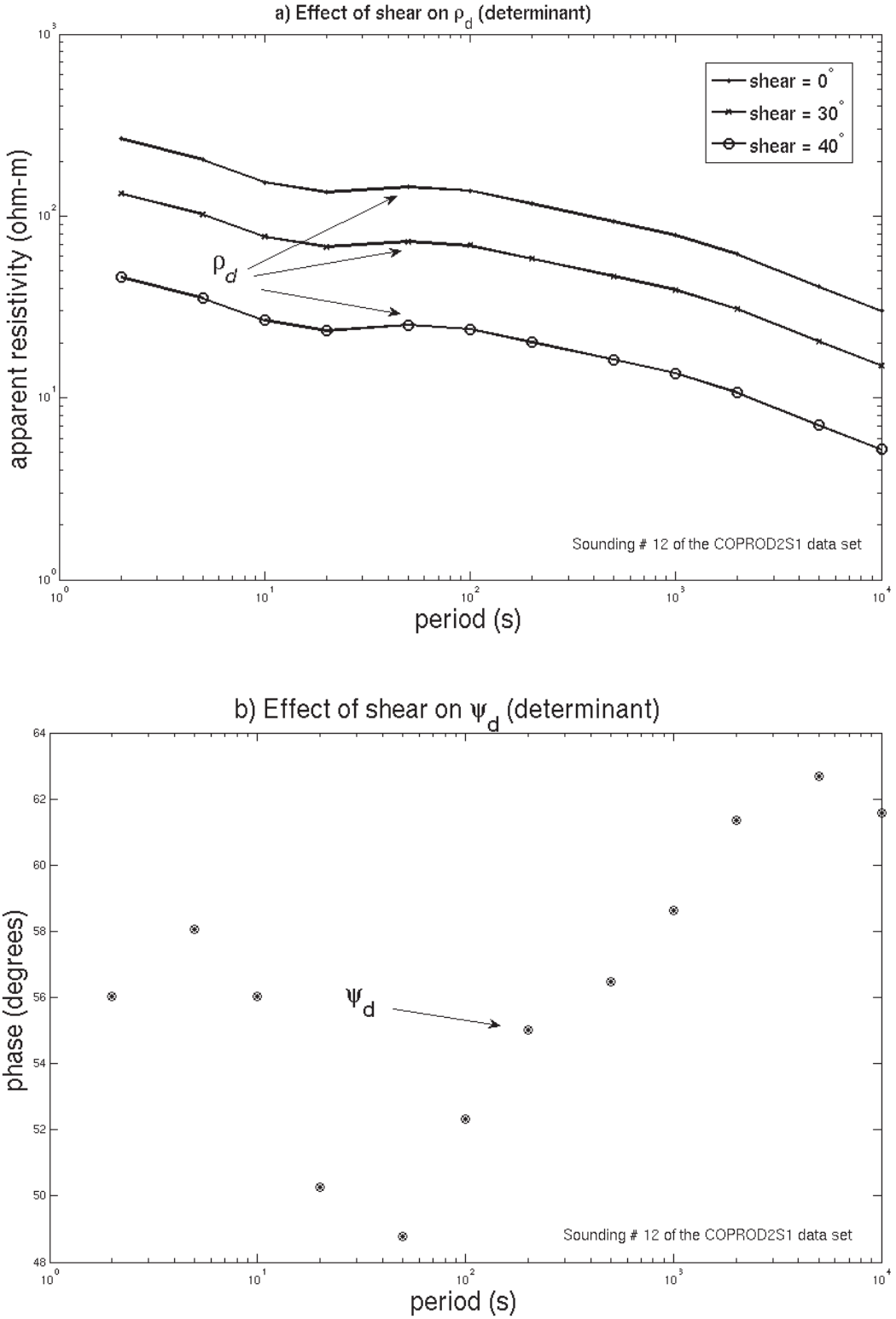

Figure 8. Synthetic TE and TM data are distorted using equation (6) and then invariants of Z_m are computed. It can be observed in b) and d) that the phases of the determinant (ψ_d), series (ψ_s), and parallel (ψ_p) impedances are immune to distortions, in agreement to theory. The corresponding amplitudes shown in a) and c), also in agreement to theory, are scaled versions of the originals (shear = 0 degrees). This includes the series impedance which is immune to this scaling due to shear. Strike direction and twist are not recorded because the results are exactly the same regardless of the values of these parameters.

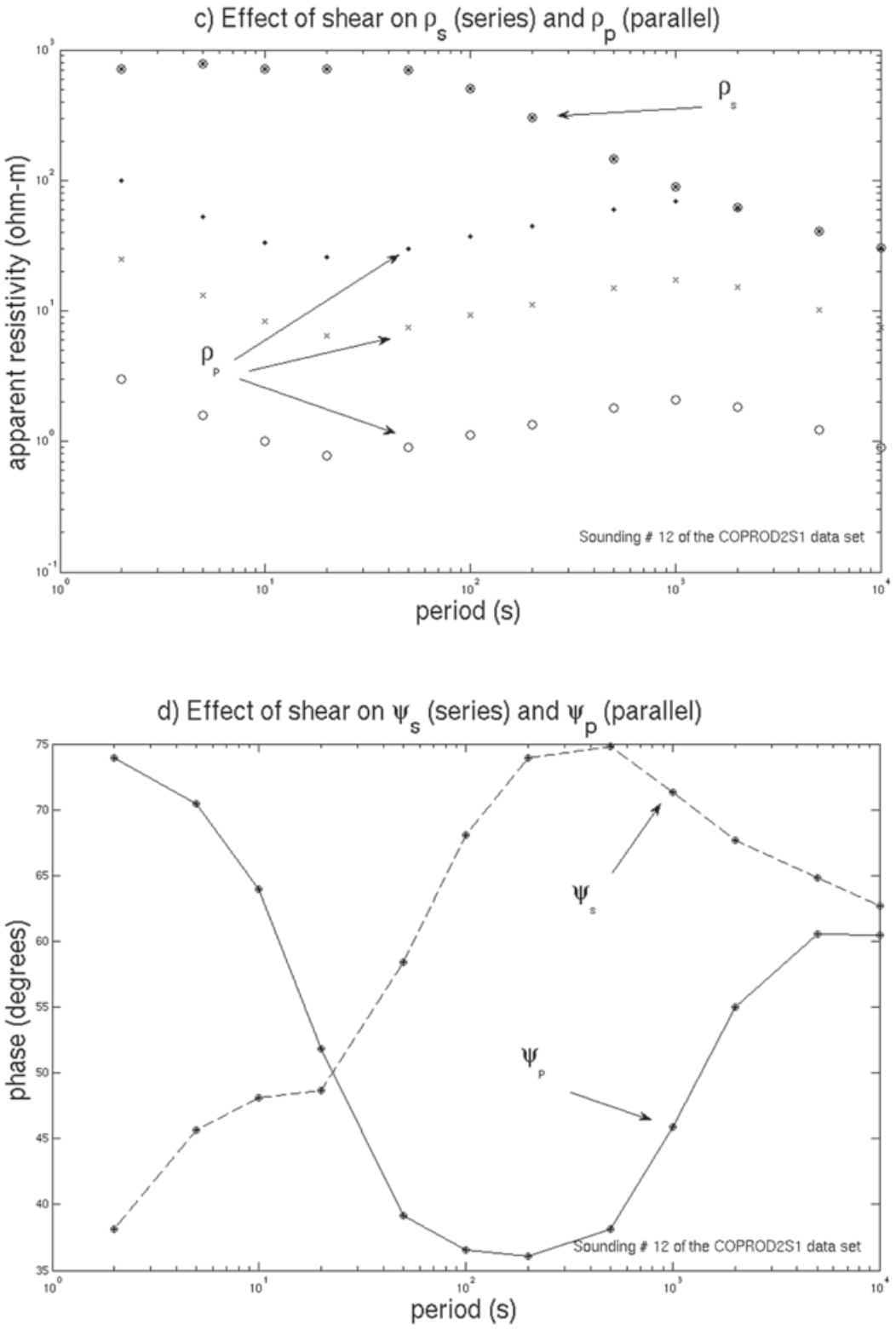
c) Effect of shear on ρs (series) and ρp (parallel)
apparent resistivity (ohm-m)
period (s)
ρs
ρp
Sounding # 12 of the COPROD2S1 data set
d) Effect of shear on ψs (series) and ψp (parallel)
phase (degrees)
period (s)
ψs
ψp
Sounding # 12 of the COPROD2S1 data set

Figure 8.

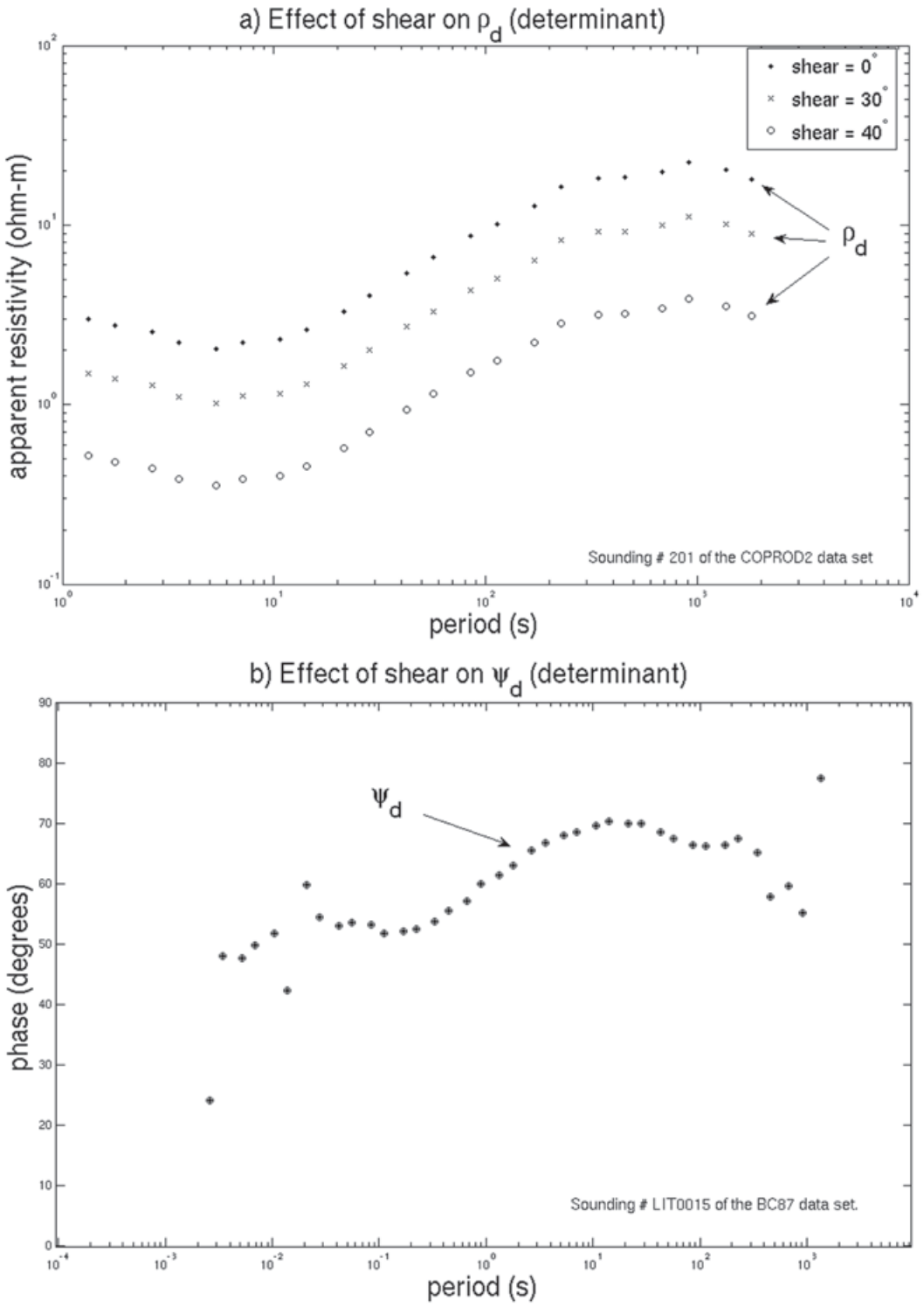

Figure 9. Results for the determinant, series and parallel impedances using field data from the COPROD2 data set, show that the corresponding curves behave very much like those of Figure 8 using synthetic data. We used equation (6) to further distort both soundings with different strike directions, twists and shears and then computed the three invariants. It can be observed that the phases of the three invariants shown in b) and d) are immune to the changes of the distorting parameters, implying that they are free of distortions except for the implicit static factors. Notice that the phases of the determinant are exactly the same for the three shears and that those of the series and parallel depart a little from each other. As mentioned in the main text, this is because the determinant makes no assumption about dimensionality while series and parallel assume a 2-D undistorted impedance. The amplitudes shown in a) and c) are scaled versions of the originals (shear = 0 degrees) in agreement to theory. This includes the series invariant which is immune to this scaling due to shear. Overall, the phases for the three shears are reasonably close considering that a shear of 40 degrees is close to the maximum of 45 degrees.

Figure 9. (Cont.)

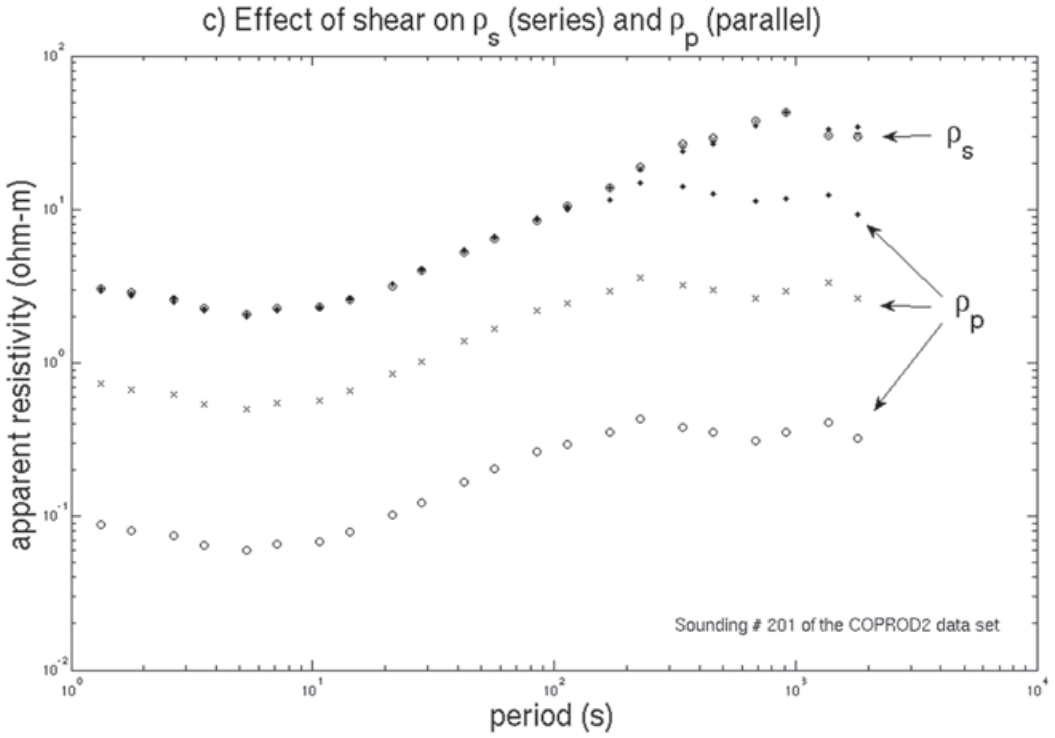

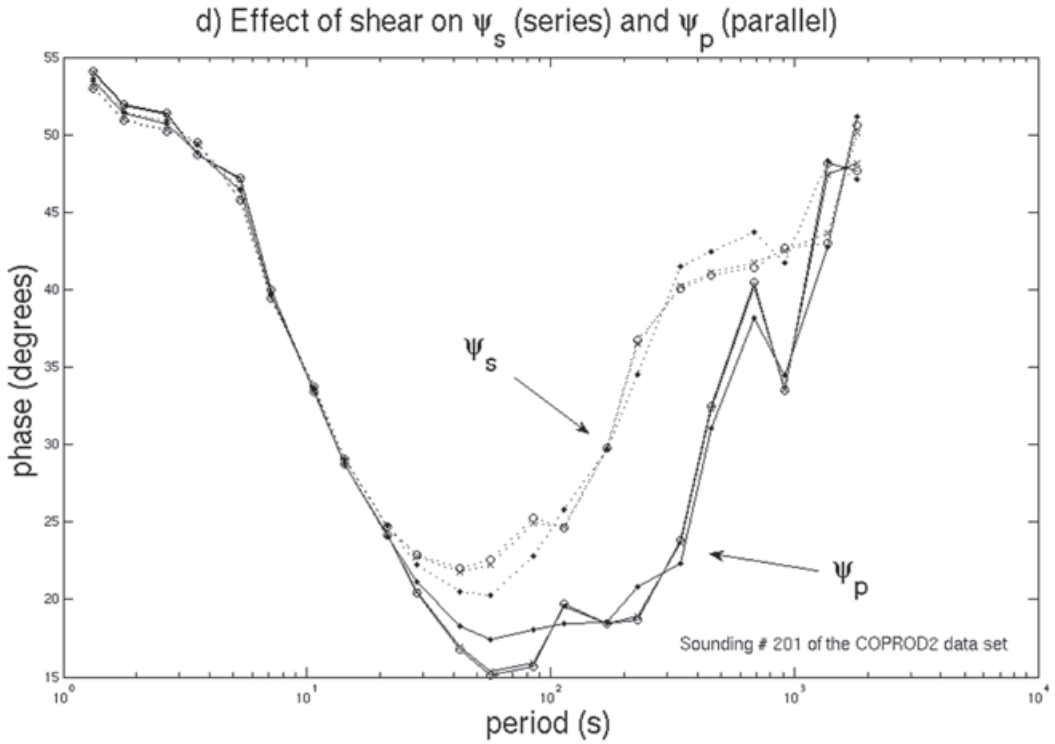

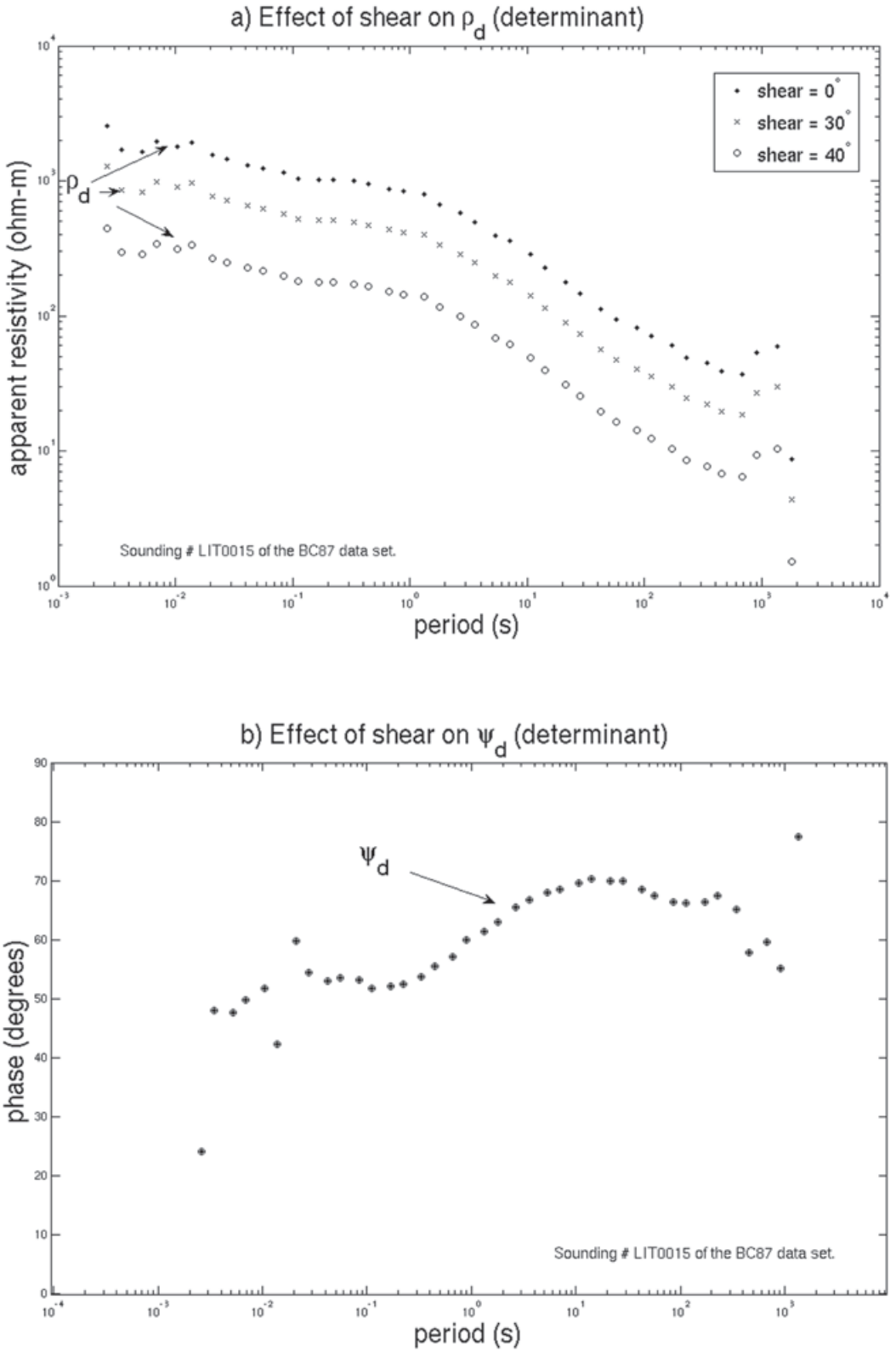

Figure 10. Results for the determinant, series and parallel impedances using field data from the BC87 data set, show that the corresponding curves behave very much like those of Figures 8 and 9. It can be observed in c) that there is already a significant downwards shift of the parallel amplitude with respect to series that is not related to the added shear scaling. As discussed in the main text, this could be due to a preexisting shear distortion or to static effects. The rest of the curves in a), b) and d) follow the same patterns as in Figures 8 and 9. Notice that, as in the other tests, the series amplitude is immune to the scaling introduced by the shear distortion as predicted by equation (17).

Figure 10. (Cont.)

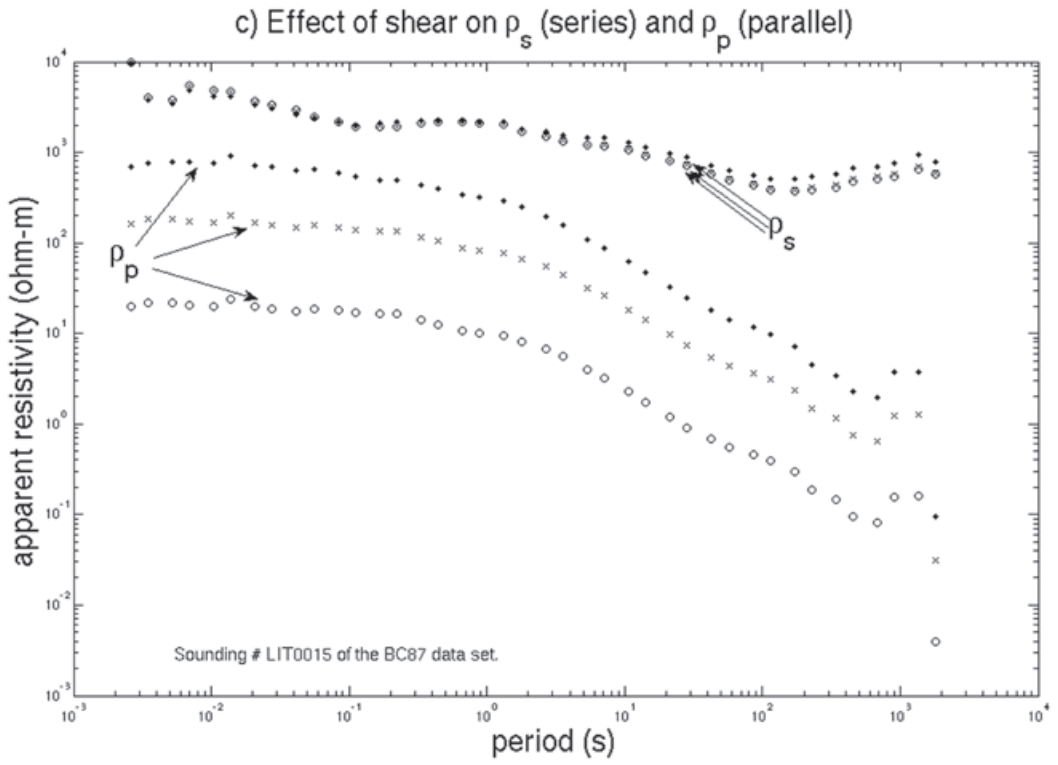

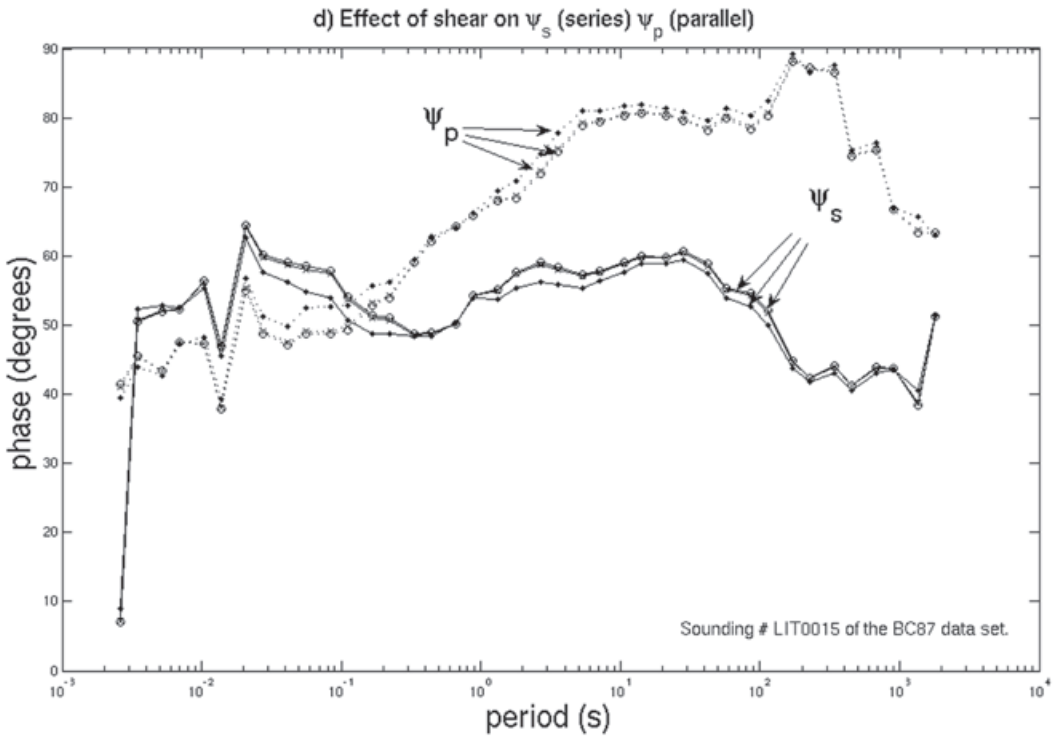

upwards and leave the phase unchanged to undo the effect of shear. However, the fact is that we do not know whether this shift is due to shear or static. The parallel resistivity curve could also be lifted by playing with the implicit static factors, in which case the phase curve would have to be modified according to equation (18). Deciding which of the two is the proper way to proceed is outside the scope of this first communication. The present results are encouraging to continue the process of advancing our knowledge of the series and parallel invariants, whose properties are just beginning to be understood.

Conclusion

Galvanic distortions of magnetotelluric data can be neutralized by some invariants of the impedance tensor. Except for strike direction, invariants are devised without any thought about distortions. However, as it turns out for the case of 2-D data, the 3-D distorting effects can gradually be neutralized by an also gradual averaging process. Series and parallel impedances are averages of the tensor elements and, in turn, the determinant is an average of the series and parallel impedances. This gradual immunity is summarized in Table 1. The new results include: a) The amplitude of the series impedance is affected only by statics, being immune to twist, shear and strike, and so are the phases of series and parallel; b) the amplitude of the parallel impedance is immune to twist and strike but not to shear and statics. These results place the series and parallel impedances midway between invariants that are not immune to any of the distortions, like Egger's eigenvalues, and the phase of the determinant which is immune to all of them.

Table 1. The table summarizes the immunity of the different responses to the four distorting parameters, strike, twist, shear and statics.

	Strike	Twist	Shear	Statics
Eggers's eigenvalues	yes	no	no	no
Parallel amplitude	yes	yes	no	no
Determinant amplitude	yes	yes	no	no
Series amplitude	yes	yes	yes	no
Series phase	yes	yes	yes	no
Parallel phase	yes	yes	yes	no
Phase tensor	no	yes	yes	yes
Determinant phase	yes	yes	yes	yes

Acknoledgments

We would like to thank CONACYT for Grant # 47922. We would also like to thank Alan Jones for providing the COPROD2 and BC87 data sets, and to the anonymous reviewers for useful comments and suggestions.

Bibliography

Antonio-Carpio R., Romo J.M., Frez J., Gómez-Treviño E., Suárez-Vidal F., 2011, Electrical resistivity imaging of a seismic region in northern Baja California, México, *Geofísica Internacional*, 50, 23-39.

Arango C., Marcuello A., Ledo J., Queralt P., 2009, 3D magnetotelluric characterization of the geothermal anomaly in the Llucmajor aquifer system (Majorca, Spain), *J. Appl..Geophys.*, 68, 479-488.

Bahr K., 1988, Interpretation of the magneto-telluric impedance tensor, regional induction and local telluric distortion, *Journal of Geophys.,* 62**,** 119-127.

Berdichevsky M.N., Dmitriev V.I., 1976, Basic principles of interpretation of magnetotelluric curves, in *Geoelectric and geothermal studies*, pp. 165-221, Ed. Adam, A., Akademini Kiado.

Caldwell T.G., Bibby H.M., Brown C., 2004, The magnetotelluric phase tensor, *Geophys. J. Int.*, 158, 457–469.

Eggers D.E., 1982, An Eigenstate formulation of the magnetotelluric impedance tensor, *Geophys.*, 47, 1204-1214.

Groom R.W., Bailey R.C., 1989, Decomposition of magnetotelluric impedance tensors in the presence of local three-dimensional galvanic distortion, *J. Geophys. Res*., 94, 1913-1925.

Jones A.G., 1993a, The BC87 dataset: data and tectonic setting. *J. Geomag. Geoelectr*., 45, 1089-1105.

Jones A.G., 1993b, The COPROD2 dataset: Tectonic setting, recorded MT data, and comparison of models. *J. Geomag. Geoelectr*., 45, 933-955.

Ledo J., Jones A.G., 2001, Regional electrical resistivity structure of the southern Canadian Cordillera and its physical interpretation. *J. Geophys. Res*., 106, 30755-30769.

Ledo J., Gabás A., Marcuello A., 2002, A static shift levelling using geomagnetic transfer functions. *Earth Planets and Space*, 54, 493-498.

Pellerin L., Hohmann G.W., 1990, Transient electromagnetic inversion: A remedy for magnetotelluric static shifts. *Geophys.*, 55, 1242-1250.

Romo J.M., Gómez-Treviño E., Esparza F., 2005, Series and parallel transformations of the magnetotelluric impedance tensor: theory

and applications. *Phys. Earth Planet Int.*, 150, 63-83.

Simpson F., Bahr K., 2005, Practical magnetotellurics, *Cambridge University Press*. Cambridge. 254 pp.

Szarka L., Menvielle M., 1997, Analysis of rotational invariants of the magnetotelluric impedance tensor. *Geophys. J. Int*., 129, 133-142.

Varentsov I.M., 1998, 2D synthetic data sets COPROD-2S to study MT inversion techniques: Presented at the 14th Workshop on Electromagnetic Induction in the Earth. Available in MTNet.

Geofísica Internacional (2013) 52-2: 153-157

Original paper

Dark Matter: A Result of nonadditive gravitational forces

Jesús Arturo Robles-Gutiérrez*, Ernesto Lacomba Zamora†, Jesús Martiniano Arturo Robles-Domínguez, Cinna Lomnitz and María Eugenia Robles-Gutiérrez

Received: April 22, 2012; accepted: October 02, 2012; published on line: March 22, 2013

Resumen

Basándonos en los datos experimentales en fluidos encontramos, en referencias Robles-Domínguez *et al.* (2007) y Robles-Gutiérrez *et al.* (2010), que en el Campo Electromagnético existen realmente nuevas fuerzas no-aditivas entre 3 o más moléculas; postulamos que también existen nuevas fuerzas no-aditivas en el Campo Gravitacional y al agregarlas a la Ley de Gravitación Universal de Newton éstas dan lugar a la Masa Obscura.

Palabras clave: materia oscura, fuerzas no aditivas.

Abstract

Experimental data in fluids suggest that nonadditive electromagnetic forces between 3 or more molecules account for the existence of critical points, triple states and phase transitions (Robles-Domínguez *et al.*, 2007; Robles-Gutiérrez *et al.*, 2010). Similar nonadditive forces between 3 or more molecules in the gravitational field incorporated into Newton's universal gravitational law may also explain the existence of dark matter.

Key words: Dark Matter, nonadditive forces.

J.A. Robles-Gutiérrez*
C. Lacomba†
J.M.A. Robles-Domínguez
Universidad Autónoma Metropolitana
México DF, México
**Corresponding author: rodj@xanum.uam.mx*

C. Lomnitz
Instituto de Geofísica,
Universidad Nacional Autónoma de México
Ciudad Universitaria
Delegación Coyoacán, 04510
México DF, México

M.A. Robles-Gutiérrez
Universidad Panamericana
México DF, México

Introduction

Zwicky (1933) interpreted some observations of the Coma Cumulus and concluded that its gravitational mass is several times the luminous mass. He called the difference the *dark mass.* This work is regarded as the starting point of the Dark Matter problem. Sciama (1993) discussed several theories intended to explain this interesting phenomenon, including the existence of new particles which do not emit electromagnetic radiation but contribute to the gravitational mass, but without experimental confirmation. Other solutions involve a mathematical modification of Newton's laws but insufficient physical reasons in support of such modification have been presented.

Robles-Domínguez (2007) and Robles-Gutiérrez (2010) proposed new intermolecular forces in field theory that arise from interactions between three and more molecules. We showed that such interactions have not been previously considered, and that such nonadditive electromagnetic forces are needed in order to account for the experimental data on critical points in fluids, triple states, and liquid-solid phase transitions. We call these forces *nonadditive* because their mathematical form differs from that of binary, or additive, forces. Nonadditive forces are important within relatively short distances. In gases the mean intermolecular distances are large and nonadditive forces are not significant as compared with additive forces. In liquids and solids, however, the density is large and the mean intermolecular distance is very short. In this case the nonadditive forces may overcome the additive forces. We show that the existence of liquid and solid phases is experimental proof for the existence of nonadditive forces.

In Section 2 of this paper we provide a short derivation of the equation of state in fluids from statistical mechanics as provided in greater detail elsewhere (Robles-Domínguez, 2007; Robles-Gutiérrez, 2010). This derivation includes nonadditive forces. In Section 3 we apply the equivalent equation from section 2 to the gravitational field using data from Begeman (1987) on galaxy NGC 3198, and we show how dark mass will arise.

2. Nonadditive forces in fluids

Molecules in a fluid interact mainly through the electromagnetic field: the gravitational, weak and strong nuclear fields are irrelevant. We consider a monocomponent fluid that contains N molecules at an absolute temperature T, inside a volume V, which is described in Statistical Mechanics by the canonical partition function Z:

$$Z(T,V,N)=\int_{\Gamma}\exp(-\beta E)\,d\Gamma\,, \qquad (1)$$

where $\beta=\frac{1}{k_BT}$, k_B is Boltzmann's cons-tant, E is the Energy of the system, $\Gamma=\Gamma\left(\underline{r}_i,\underline{p}_i\,,i=1...N\right)$ is the phase space of the system, $\underline{r}_i$ and $\underline{p}_i$ are the vector position and momentum of the ith particle, N is the total number of molecules, V is the volume of the system, and T is the absolute temperature. We may write

$$E=K+\Phi \qquad (2)$$

where K is the total kinetic energy of the system and Φ is the total potential energy; and

$$d\Gamma=\prod_{i=1}^{N}d\underline{r}_i\,d\underline{p}_i \qquad (3)$$

as we are considering a single-component fluid.

Integration of (1) over the momenta is well known (Reichl, 1998) and the result is

$$Z(T,\,V,\,N)=(N!\lambda^{3N})^{-1}\int\!\!\ldots\!\int d\underline{r}_1\ \ldots\ d\underline{r}_N\,\exp(-\beta\Phi) \qquad (4)$$

where $\lambda=h(2\pi mk_BT)^{-\frac{1}{2}}$ and h is Planck's Constant.

2.1 van der Waals equation of state

Equation (4) considers only the positions of all N molecules in the system. Ornstein and van Kampen (in Reichl, 1998), consider than the molecules interact with the next binary additive potential energy

$$\Phi\left(\left|\underline{r}_i-\underline{r}_j\right|\right)=\begin{cases}+\infty=\Phi_{hc}, & \left|\underline{r}_i-\underline{r}_j\right|<a\\ \Phi_2\left(\left|\underline{r}_i-\underline{r}_j\right|\right)<0, & \left|\underline{r}_i-\underline{r}_j\right|>a\end{cases} \qquad (5)$$

where hc stands for "hard core". The subscript *2* denotes binary additive interaction; $\underline{r}_i$ and $\underline{r}_j$ are position of molecules i and j respectively, and it is assumed that the molecules have a hard core of radius a and a smooth attractive binary-additive interaction Φ_2 with a very long range. Ornstein and van Kampen assume that the density is high enough and the range of the attractive interaction is wide enough so that many molecules will interact simultaneously. Volume V may be divided in cells of volume Δ large enough to contain many molecules but small enough so that the attraction

between molecules within a given cell is constant regardless of separation in the cell. If the number of molecules in cell α is N_α we may write, from (4) and (5):

$$Z(T,V,N) = (N!\lambda^{3N})^{-1} \sum_{\{N_\alpha\}}{}' \frac{N!}{\Pi_\alpha N_\alpha!} \left[\Pi_\alpha \gamma(N_\alpha)\right] \exp\left\{\frac{1}{2}\beta \sum_{\alpha,\alpha'} \Phi_{\alpha,\alpha'} N_\alpha N_{\alpha'}\right\}$$
$$\approx \left(\frac{1}{\lambda_T^{3N}}\right) \sum_{\{N_\alpha\}}{}' \exp\left(\sum_\alpha \left\{N_\alpha \ln\left(\frac{\Delta - N_\alpha\delta}{N_\alpha}\right) + N_\alpha + \frac{1}{2}\beta \sum_{\alpha'} \Phi_{\alpha,\alpha'} N_\alpha N_{\alpha'}\right\}\right) \quad (6)$$

where

$$\gamma(N_\alpha) = (\Delta - N_\alpha\delta)^{N_\alpha} \quad (7)$$

and δ is the volume of the hard core of one molecule.

The most probable distribution of molecules in V at thermodynamic equilibrium is the uniform distribution

$$N_\alpha = \frac{N}{V}\Delta \quad (8)$$

for all α, and defining

$$\frac{W_0}{\Delta} = \sum_{\alpha'} \Phi_{\alpha,\alpha'} \quad (9)$$

for all α.

We use mean field theory and the definition of Helmholtz energy A:

$$A(T,V,N) = -\frac{1}{\beta} \ln Z(T,V,N) \ . \quad (10)$$

The thermodynamics of the systems is deduced from Helmholtz energy *A*, ie,: fluids. Pressure p is defined as

$$p = -\left(\frac{\partial A}{\partial V}\right)_{T,N} \ . \quad (11)$$

Using equations (5) through (11) we obtain van der Waals equation of state

$$p = \frac{\frac{N}{V}}{\beta\left(1 - \frac{N}{V}\delta\right)} - \frac{1}{2}\left(\frac{N}{V}\right)^2 W_0 \ . \quad (12)$$

Let us express this equation in terms of fluid density:

$$\rho = \frac{mN}{V} \quad (13)$$

where m is the mass of one molecule; and we find

$$p = \frac{\rho}{\beta(m - \rho\delta)} + a\rho^2 \quad (14)$$

where

$$a = -\frac{W_0}{2m^2} \ . \quad (15)$$

In equation (14) the first term of the right-hand side contains the hard core contribution and the second contains all binary-additive interactions. This equation can approximately represent the pressure of the gaseous phase but cannot describe the pressures of the liquid and solid phases in the fluid (Reichl, 1998).

In the van der Waals equation of state (14), we note three important properties:

1. The second term on the right-hand side contains *all* binary-additive intermolecular interactions;

2. The two terms on the right-hand side are linearly independent in a functional-analysis sense; and

3. This equation cannot reproduce the experimental data in fluids.

Fourier theory (Kolmogorov and Fomin, 1961) may be used to describe a function as a Fourier series. Properties 2 and 3 above mean that the van der Waals equation contains only two terms of the infinite series which we need to reproduce the experimental data of fluids. Property 1 means that the last right-hand terms must be expressed in terms of new forces. Thus in terms of linearly independent nonadditive forces, the third term will contain all third-order nonadditive interactions, the fourth term all fourth-order nonadditive interactions and so on. The total pressure may be written as follows:

$$p = p_{hc} + p_2 + p_3 + p_4 + \dots \ , \quad (16)$$

where p_{hc} contains the hard core interactions, p_2 the total scalar additive binary potential energy, p_3 the total scalar third-order or triadic nonadditive potential energy, p_4 the total scalar fourth-order

(or tetradic) nonadditive potential energy, and so on. Thus

$$p_{hc} = \frac{\rho}{\beta(m - \rho\delta)} \tag{17}$$

$$p_2 = a\rho^2 = a_2\rho^2 \tag{18}$$

$$p_3 = a_3\rho^3 \tag{19}$$

$$p_4 = a_4\rho^4 \tag{20}$$

Equations (17), (18), etc. constitute an infinite Fourier series of independent linear functions.

The hard core cannot allow the fluid volume to vanish and the density cannot be infinite: thus the Fourier series can converge.

Nonadditive forces in the gravitational field

In Robles-Gutiérrez *et al*. (2010), we postulated the existence of nonadditive gravitational forces in the gravitational field. Before we extend the theory to galaxies let us describe the astronomical observations of galaxy NGC 3198 (Begeman, 1987). Figure 1 shows Begeman's graph of rotational velocity vs. radius in minutes of arc between the vector from Earth to the object and the vector from Earth to the center of NGC 3198. The distance from Earth to NGC 3198 is *9.2 Mpc.* The maximum distances of masses from the center of the galaxy should provide information on the total mass of the galaxy.

The galaxy may be likened to a gas inside a jar. The jar exerts a pressure on the gas. In a state of equilibrium the pressure should be constant everywhere in the gas. In the case of a galaxy

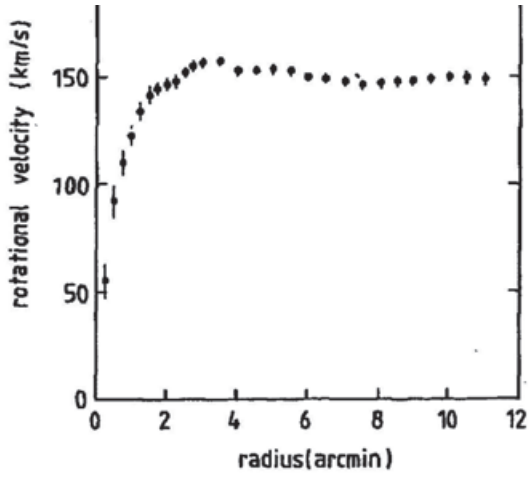

Figure 1. Observations of NGC 3198 (From Begeman, 1987).

the peripherical stars plus gas are confined to a galactic volume by a pressure called galactic pressure, which equals gravity per unit area. It is equal to the centripetal force per unit area, and it is not identical at all points of the galaxy.

The centripetal force on an object l is equal to the gravitational force on this object, which is the sum of all gravitational interactions, additive and nonadditive:

$$F_{i\,centrip} = F_{l\,grav} = \sum_{j=2}^{\infty} F_{lj} \quad , \tag{21}$$

where subscript l refers to the peripheral stars or gas clouds observed by Begeman in NGC 3198 galaxy and subscript j refers to the forces. Let j = 2 refer to binary additive forces, j = 3 to ternary nonadditive forces and so on. We omit the hard-core term because m_l is far away from the galaxy.

If we divide (21) by the unit of area we obtain the equation of the pressures, as in a fluid:

$$p_{l\,centrip} = p_{l\,grav} = \sum_{j=2}^{\infty} p_{lj} \quad . \tag{22}$$

But a similar expression should obtain for the centripetal and gravitational accelerations, after dividing equation (21) by m_l which is necessary because the mass m_l is unknown. Thus the centripetal acceleration equals the gravitational acceleration g_l generated by the total galaxy mass including the dark mass, over m_l, which is the sum of all binary-additive contributions g_{l2} plus all third-order nonadditive accelerations g_{l3}, and so on, over m_l:

$$a_{l\,centrip} = g_{l\,grav} = \sum_{j=2}^{\infty} g_{lj} \quad . \tag{23}$$

Here the first term of the summand is Newton's acceleration of gravity:

$$a_{l\,centrip} = g_{l\,grav} = G\frac{M_{l\,\mathrm{lum}}}{r_l^2} + g_{l3} + g_{l4} + \cdots, \tag{24}$$

Written out as

$$a_{l\,centrip} = g_{l\,grav} = \frac{GV_l}{r_l^2}\frac{M_{l\,\mathrm{lum}}}{V_l} + g_{l3} + g_{l4} + \cdots = \frac{GV_l}{r_l^2}\rho_l + g_{l3} + g_{l4} + \cdots \tag{25}$$

By analogy with the case of a fluid we may write g_l in terms of an infinite density series:

$$a_{l\,centrip} = \frac{GV_l}{r_l^2}\rho_l + g_{l3} + g_{l4} + \cdots = B_{l2}\rho_l + B_{l3}\rho_l^2 + \cdots \tag{26}$$

where the density ρ_l equals the luminous mass M_{llum} within a sphere of radius r_l from the center of the galaxy to m_l over the volume of the sphere. Equation (26) may be written

$$a_{l\,centrip} = \frac{GV_l}{r_l^2}\rho_l + g_{l3} + g_{l4} + \cdots = \frac{G}{r_l^2}M_{l\,lum} + B_{l3}\rho_l^2 + \cdots = \frac{G}{r_l^2}M_{l\,lum} + \frac{B_{l3}}{V_l^2}M_{l\,lum}^2 + \cdots \tag{27}$$

or

$$a_{l\,centrip} = \frac{G}{r_l^2}M_{l\,lum} + \frac{B_{l3}}{V_l^2}M_{l\,lum}^2 + \cdots = \frac{G}{r_l^2}M_{l\,lum}\left(1 + \frac{\frac{B_{l3}}{V_l^2}M_{l\,lum}^2}{\frac{G}{r_l^2}M_{l\,lum}} + \cdots\right) = \frac{G}{r_l^2}\left[M_{l\,lum}\left(1 + \frac{B_{l3}r_l^2 M_{l\,lum}}{GV_l^2} + \cdots\right)\right] \tag{28}$$

If

$$\frac{B_{l3}r_l^2 M_{l\,lum}}{GV_l^2} + \cdots > 0 \tag{29}$$

this term will contribute to dark matter.

The series of equation (28) converges because the density is finite. We may consider only the first and second terms of the series and neglect the small higher terms. Thus

$$a_{l\,centrip} = \frac{V_l^2}{r_l} = \frac{G}{r_l^2}\left[M_{l\,lum}\left(1 + \frac{B_{l3}r_l^2 M_{l\,lum}}{GV_l^2}\right)\right]. \tag{30}$$

from which

$$\frac{M_{dark}}{M_{l\,lum}} = \frac{B_{l3}r_l^2 M_{l\,lum}}{GV_l^2} \tag{31}$$

and the terms inside the square brackets are the real mass.

Begeman (1987) obtained the following values of r_l=30 *kcp*, V_c=150 km/s for this galaxy:

$$\frac{M_{dark}}{M_{l\,lum}} = 2.99 \tag{32}$$

From Equations (30), (31) and (32) we find

$$M_{l\,lum} = 78.236 * 10^{39}\ kg\,, \tag{33}$$

and by introducing this value in (31) we obtain, for l=30 *kcp*,

$$B_{l3} = 9.89036 * 10^{-30}\ m^7\left(s^2 kg^2\right)^{-1} > 0 \tag{34}$$

As this value is positive, we find that

$$M_{real} > M_{l\,lum}\ . \tag{35}$$

This result proves that the dark mass must be due to the presence of nonadditive forces.

Conclusions

Whenever nonadditive interactions, that are multi-body terms, are taken into account, Newton's law of universal gravitation is sufficient to explain the astronomical observations of a "dark mass". The example of Galaxy NGC 3198 (where substantial amounts of dark matter had been detected) shows that nonadditive terms in Equation (25), a generalization of Newton's law of gravitation, can provide a satisfying explanation of the difference between luminous and gravitational matter.

Acknowledgments

The valuable contribution of L.A. Sylvia Robles Gutiérrez is gratefully acknowledged.

Bibliography

Begeman K.H., 1987, Rotation Curves of Spiral Galaxies, Ph. D. Thesis, University of Groningen.

Kolmogorov A.N., Fomin S.V., 1961, *Elements of the Theory of Functions and Functional Analysis,* 2, Graylock Press, New York.

Reichl L.E., 1998, *A Modern Course in Statistical Physics*, University of Texas Press, Austin.

Robles-Domínguez J.M.A., Robles-Gutiérrez J.A., Lomnitz C., 2007, An Equation of State for more than two phases, with an application to the Earth's mantle, *Geofísica Internacional,* 40, 3 155-161.

Robles-Gutiérrez J.A., Robles-Domínguez J.M.A., Lomnitz C., 2010, A generalized equation of state with an application to the Earth's mantle. *Geofísica Internacional,* 49, 2, 77-82.

Sciama D.W., 1993, *Modern Cosmology and the Dark Matter Problem*. Cambridge University Press, Cambridge.

Geofísica Internacional (2013) 52-2: 159-172

Original paper

On the estimation of the maximum depth of investigation of transient electromagnetic soundings: the case of the Vizcaino transect, Mexico

Carlos Flores*, José M. Romo and Mario Vega

Received: May 03, 2012; accepted: January 30, 2013; published on line: March 22, 2013

Resumen

Probamos un método propuesto en la literatura para estimar la profundidad máxima de investigación (PMI) de sondeos electromagnéticos transitorios (TEM) de bobina central con datos del transecto Vizcaíno; un perfil de 38 sondeos TEM que cruza la península de Baja California. Se confirma la validez de esta técnica al comparar la PMI con la interfase más profunda de 16 modelos estratificados. En estos sondeos, todos ellos localizados en la cuenca Vizcaíno, los datos medidos no están afectados por polarización inducida. Los modelos indican la presencia de un conductor buzante interpretado como una zona de intrusión salina con una gran extensión lateral de más de 70 km. Los otros 22 sondeos, localizados sobre rocas ígneas y metamórficas, muestran cambios en la polaridad de los voltajes que indican la presencia de efectos de polarización inducida. Los modelos estratificados Cole-Cole de estos sondeos sugieren una disminución importante en la PMI. Esto es confirmado al analizar el comportamiento en profundidad de las densidades de corriente. También se analiza el nivel de ruido de un conjunto de datos que comprende cerca de 2000 voltajes de tiempo tardío de aproximadamente 400 sitios TEM adquiridos en el noroeste de México. No se encontró una diferencia entre los niveles de ruido estacionario de invierno y verano, posiblemente debido a que prácticamente no hay tormentas eléctricas en esta parte de México.

Palabras clave: sondeos electromagnéticos transitorios, profundidad máxima de investigación, polarización inducida.

Abstract

We test an approach proposed in the literature for estimating the maximum depth of investigation (MDI) of in-loop transient electromagnetic soundings (TEM) with data from the Vizcaino transect, a profile of 38 TEM soundings crossing the Baja California peninsula. The validity of this approach is confirmed by comparing the MDI with the deepest interface of 16 stratified models. In these soundings, all located over the Vizcaino basin, the measured data are not affected by induced polarization. The models indicate the presence of a dipping conductor interpreted as a zone of seawater intrusion with a large lateral extension of over 70 km. The remaining 22 soundings, located over igneous and metamorphic rocks, show reversals in the voltage polarity, indicating the presence of induced polarization effects. The layered Cole-Cole models for these soundings suggest a significant decrease in the MDI. This is confirmed by analyzing the depth behavior of the subsurface current densities. We further analyze the noise level of a data set comprising close to 2000 late-time voltages of about 400 TEM sites acquired in northwestern Mexico. No difference was found between the stationary noise levels of winter and summer, presumably because near thunderstorms are practically absent in this part of Mexico.

Key words: transient electromagnetic soundings, maximum depth of investigation, induced polarization.

C. Flores*
J.M. Romo
M. Vega
Departamento de Geofísica Aplicada
Centro de Investigación Científica
y Educación Superior de Ensenada
Carretera Ensenada-Tijuana Núm. 3918
Zona Playitas, Ensenada
Baja California, México 22860
*Corresponding author: cflores@cicese.mx

Introduction

The transient electromagnetic (TEM) method is based on the induction of electric current in the ground by a transmitter loop. When a DC current injected into the loop is abruptly turned off, an electric field is induced in the ground, which generates the flow of subsurface currents. These currents rapidly vary in time and space, producing a transient magnetic field in the vicinity of the transmitter. The time variation of this field is sensed with the voltage induced in a coil laid on the ground surface. Placing this coil at the center of the loop is known as the in-loop array. The shape and intensity of the measured voltage is a function of the resistivity subsurface distribution. The method has been used extensively in a variety of applications, such as groundwater exploration, mineral and oil prospecting, buried-metal detection, and geologic mapping.

A frequently asked question during the planning of in-loop transient electromagnetic soundings is, "What is the maximum depth of investigation (MDI) if a square loop of dimensions L by L is used as the transmitting source?" There is no simple answer to this question. Although the MDI does depend on the loop dimensions, it also depends on other parameters. Several estimates of the MDI have been reported in the literature (McNeill, 1980; Fitterman, 1989; Spies, 1989). In this work we adopt and test that proposed by Spies (1989), which is the most clear and complete.

In this paper we start with a brief description of Spies method followed by a presentation of the Vizcaino data and inverted models. Then, we discuss some modifications to Spies expression to be applied to the inverted models. Finally, soundings affected by induced polarization are analyzed.

The maximum depth of investigation

Based on the asymptotic behavior of the late-time voltages at the center of a circular loop over a two-layered earth, Spies (1989) proposed the following expression for the MDI,

$$D_{\max} \approx 0.55\left(\frac{I A_T \rho_1}{\beta}\right)^{0.2} \qquad (1)$$

where I is the current injected into the loop, A_T is the area of the loop, ρ_1 is the resistivity of the first layer, and β is V_N/A_R, the voltage noise level (V_N) over the effective area of the receiving coil (A_R). Clearly, this depth not only depends on the size of the transmitting loop, but also on four other parameters; two of them of instrumental character (injected current and area of the receiving coil), a subsurface geophysical parameter (layer resistivity), and an environmental parameter (voltage noise level).

Figure 1 shows the behavior of the normalized voltages induced in a horizontal coil located at the center of an L by L square loop over a two-layer earth for three L/d ratios and five ρ_2/ρ_1 ratios, where d is the first layer thickness and ρ_1 and ρ_2 are the layer resistivities. These curves for a square loop are similar to the circular loop responses presented by Spies (1989). Both axes are dimensionless. In the abscissas the variable τ is a normalized time, being the square root of the diffusion depth $\left(\delta = \sqrt{2t\rho/\mu_0}\right)$ in the first layer over its thickness. Spies noticed that the time at which the different curves separate at least 20% (denoted as departure time) does not have a strong dependency on the L/d or ρ_2/ρ_1 ratios, so he approximated it as unity. That is,

$$\tau_d = \frac{2t\rho_1}{\mu_0 d^2} \approx 1 \qquad (2)$$

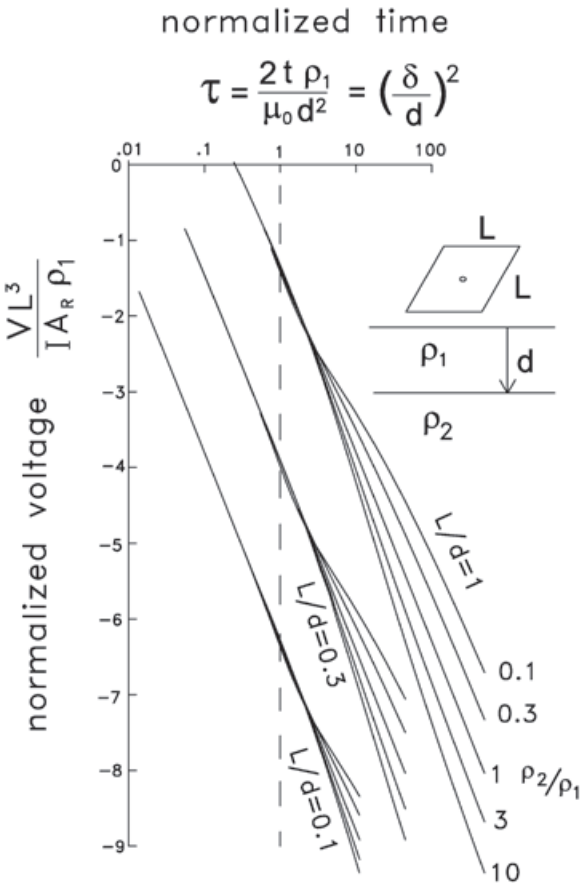

Figure 1. Log-log plots of the in-loop normalized voltage against normalized time for a square loop over a two-layered earth. Three L/d ratios and five ρ_2/ρ_1 ratios are considered. The unity departure time is indicated

By solving for t in (2), substituting it into the late-time asymptotic voltage approximation,

$$V^{\text{late}} \approx \frac{I L^2 A_R}{20}\left(\frac{\square_0^5}{\pi^3 \rho_1^3 t^5}\right)^{1/2}, \qquad (3)$$

and replacing d by $D_{\max}$ and V_{late}/A_R by β, Spies obtained expression (1).

The voltage noise level may have significant variations both in time and space. The main source of natural EM noise affecting TEM soundings are the spherics, which are electromagnetic transients generated by lightning discharges (Ward, 1967). A spheric usually propagates directly to the sounding site if the lightning is nearby or by multiple reflections in the earth-ionosphere waveguide if it occurs at large distances. Several values have been proposed for the natural noise level after the voltages are averaged: 10^{-9} (Fitterman, 1989), $2\text{x}10^{-10}$ (McNeill, 1980), and different ranges for winter (from $1\text{x}10^{-10}$ to $5\text{x}10^{-10}$) and summer (from $2\text{x}10^{-9}$ to $1\text{x}10^{-8}$) (Spies, 1989), all of them in units of V/m^2 (Figure 2a). If we consider a nominal value of $5\text{x}10^{-10}$ V/m^2, the maximum depth of investigation becomes

$$D_{\max} \approx 40\left(I A_T \rho_1\right)^{0.2} \qquad (4)$$

When logarithmic axes for both depth and resistivity of the first layer are used, expression (4) plots as a straight line. This is illustrated in Figure 2b, where the range of depths covered by a sounding with a 40 by 40 m loop and 11.3 A of injected current is shown as the shaded area. The $D_{\min}$ line indicates the minimum depth of investigation, which depends on the first layer resistivity and the shortest time ($t_{\min}$) of the particular data acquisition system $\left(D_{\min} = \sqrt{2 t_{\min} \rho_1 / \square_0}\right)$. The maximum depths of investigation would be 280 or 710 m if the first layer had resistivities of 1 or 100 Ωm, respectively. For a loop of 400 by 400 m and a current of 6.5 A the maximum depth of investigation clearly increases. However, notice that although the size of the loop increased tenfold, the $D_{\max}$ values (640 and 1600 m) increased only by a factor of about 2.3 .

The Vizcaino transect

Figure 3 shows the location of the Vizcaino Transect, a profile of 38 TEM soundings running through the Vizcaino desert with a direction approximately perpendicular to the main trend of the Baja California peninsula. These data were originally acquired to apply the static shift correction to the same number of magnetotelluric soundings (Romo *et al*., 2001). The sounding sites are approximately 6 km apart**.** The transect crosses three geologic environments. In the SW part of the profile Mesozoic rocks typical of oceanic crust outcrop. These units belong to the Cochimi terrane (Sedlock *et al*., 1993). The central part is underlain by the late-Mesozoic-Cenozoic sedimentary rocks of the Vizcaino basin. The geologic column found at the Suaro-1 hole (see location in Figure 3), an exploratory well drilled by Petróleos Mexicanos (García-Domínguez, 1976), gives useful information of the basin lithology. The stratigraphic sequence is, from top to bottom: 60 m of unconsolidated Holocene-Pleistocene sands and soil; 1190 m of fine-grained clastics belonging to the early Paleocene-Eocene Bateque formation; 970 m of interbedded shales, sandstones and some conglomerates of the Late-Cretaceous Valle formation; 355 m of limestones and tuffaceous siltstones of the Early-Cretaceous Alisitos formation. The total depth reached by the Suaro-1 hole was 2640 m. According to the interpretation of the gravity data of the area

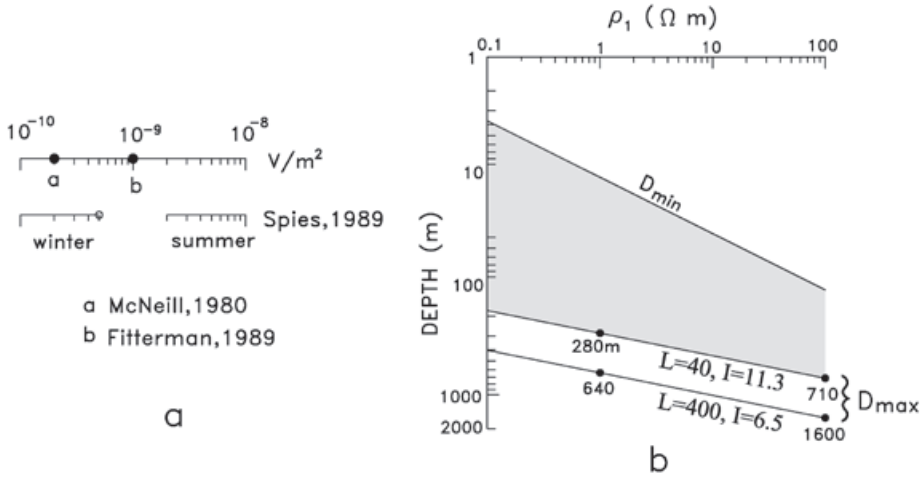

Figure 2. a) Suggested noise levels in the averaged voltage. b) Depth ranges investigated by two soundings over a two-layered subsurface when a $5\text{x}10^{-10}$ V/m^2 noise level is assumed.

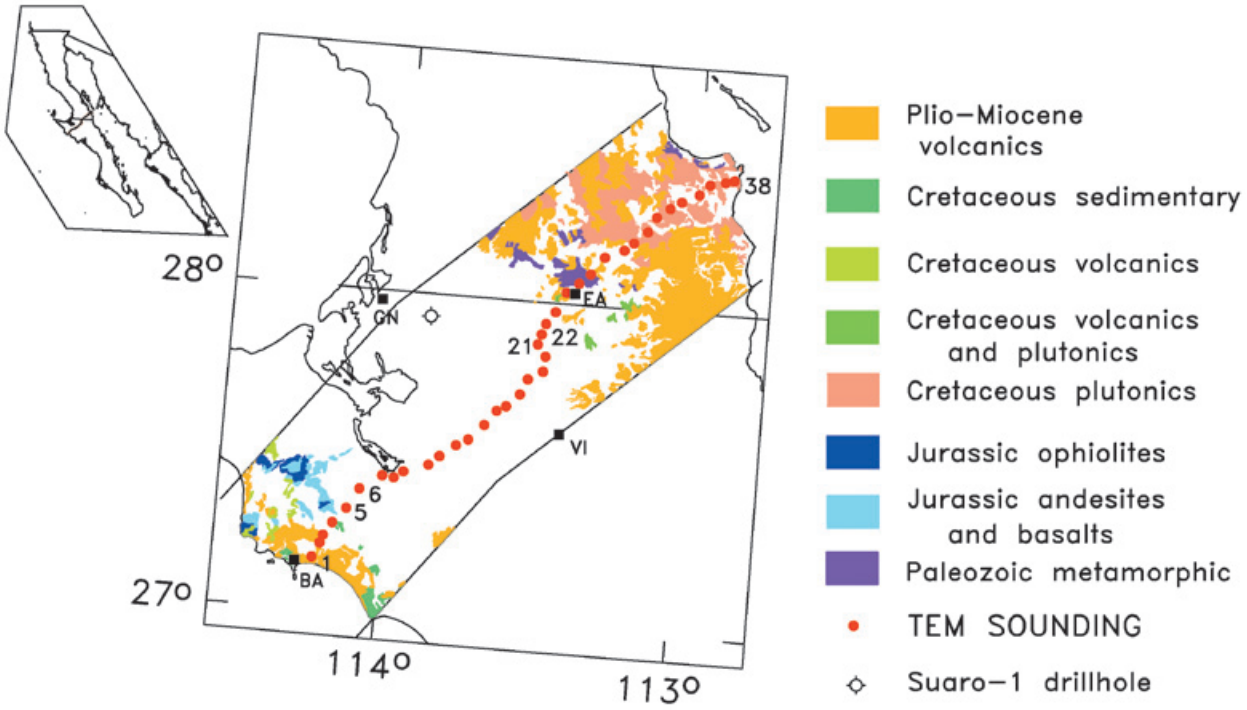

Figure 3. Location and generalized geology (after Delgado Argote, 2000) in the vicinity of the Vizcaino transect. Solid dots denote the 38 TEM soundings. Abbreviations: BA Bahía Asunción, GN Guerrero Negro, VI Vizcaino, EA El Arco. The location of the Suaro-1 drillhole is indicated.

(García-Abdeslen *et al*., 2005), the maximum basin thickness is close to 4 km. As a relative gravity high lies close to our TEM traverse, a shallower depth to the basement is expected in its vicinity. In the NE part of the transect subduction-related volcano-plutonic rocks outcrop. This region, defined by Sedlock *et al*. (1993) as the Yuma terrane, comprise Paleozoic-Mesozoic metamorphic rocks and Cretaceous rocks typical of a volcanic arc. Some areas of the SW and NE portions are covered by Tertiary volcanic rocks of andesitic and basaltic compositions, which form mesas at the topography highs.

All soundings were acquired with a Geonics TEM57 system in the in-loop array, employing 150 by 150 m loops and a 100 m^2 effective area circular coil. The currents injected to the loops were close to 8.5 A. The three available repetition frequencies were used (30, 7.5, and 3 Hz). The stacking times for these frequencies were 128, 256, and 256 s, respectively, resulting in stacked voltages representing the average of about 7700, 3800, and 1500 individual voltage decays. At least three realizations for each repetition frequency were carried out, from which the final average voltage and standard error were estimated.

Figure 4 displays the observed data (symbols) and estimated standard deviations (error bars) for a number of selected soundings. The data quality is generally good. All soundings from 1 to 5 and from 22 to 38 have a change of sign in the measured voltages. These sites are located in the southwestern and northeastern portions of the profile, where volcanic, crystalline or metamorphic rocks outcrop. For in-loop soundings the presence of a voltage sign reversal is diagnostic of the presence of a frequency-dependent or dispersive subsurface resistivity (Weidelt, 1982), that is, the presence of Induced Polarization (IP) in the ground. In contrast, the soundings located in the Vizcaino basin, from sites 6 to 21, have positive voltages at all times indicating the presence of a non-polarizable resistivity. Both voltage and apparent resistivity data as a function of time are shown for the non-polarizable soundings (sites 8, 14, 19, 20, and 21 in Figure 4). For those affected by IP the corresponding apparent resistivity data are not displayed because they are undefined when the voltages are negative (sites 3, 26, and 38 of Figure 4). We will discuss first the results for the non-polarizable soundings (6 to 21).

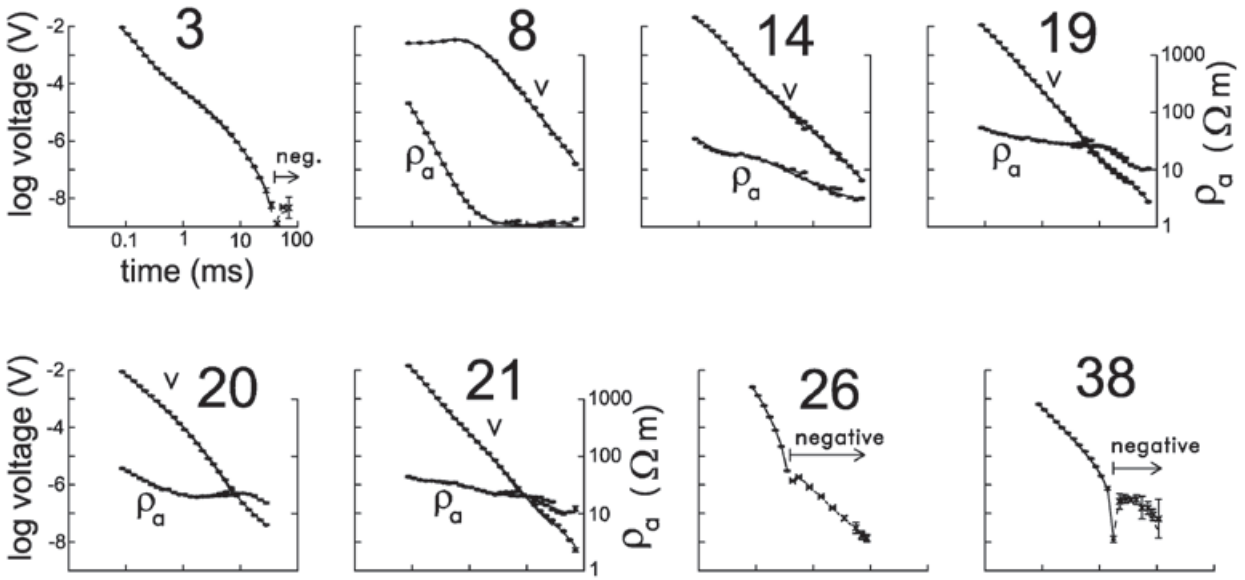

Figure 4. Observed data (symbols) and calculated responses (solid and dashed curves) for selected soundings. Both voltage and apparent resistivities are displayed for the non-dispersive soundings (8, 14, 19, 20, and 21). Only the voltages are shown for soundings affected by Induced Polarization (3, 26, and 38). Negative voltages are indicated.

Non-polarizable soundings

All these soundings were inverted to layered models using a linearized least squares algorithm (Jupp and Vozoff, 1975). The solid lines of Figure 4 correspond to the calculated responses of the inverted models. The fit between observed and calculated responses is good (the average misfit error is 1.4). The layer resistivities and depths are shown in the section of Figure 5, where the maximum depths of investigation (to be discussed below) are also included as stars. Because of the large separation between soundings (about 6 km), it is difficult to carry out lateral correlations between neighboring models. However, an outstanding feature can be noticed; under the thick line shown in Figure 5 all resistivities are less than 3.2 Ωm. This conductive zone outcrops in sites 7, 8, and 9, where a remnant of the highly saline Ojo de Liebre lagoon occurs, and gradually deepens away to the southwest and northeast. These features suggest that this anomalous zone is due to a saline intrusion of large lateral extent (the horizontal distance between sites 8 and 21 is 73 km). This desert area is characterized by a very low rainfall (about 50 mm/year). This seawater intrusion could have been produced by natural physical processes, without anthropogenic influence, because there is not groundwater extraction in this Biosphere Reserve Area except in the vicinity of the Vizcaino town (see location in Figure 3). The profile approaches this locality at sounding 17, which is 15 km to the north of this town. We do not see a perturbation in the depth to the conductor in the vicinity of this sounding, which would be an expected feature if groundwater pumping is the driving force of the intrusion.

Before applying the MDI expression to the Vizcaino models, we address three points: a) a more detailed estimation of the departure time, b) the noise level is estimated from the actual field data, and c) the adaptation of expression (1) to multi-layered models.

Instead of approximating the departure time as unity, we estimated it from graphs such as those shown in Figure 1 for different resistivity contrasts and L/d ratios. These responses were calculated with the following procedure. The transient voltage due to an ideal current step turn-off is,

$$v^{off} = -\square_0 A_R \frac{\partial h_z}{\partial t} \tag{5}$$

The time derivative of the vertical magnetic field is obtained from the Fourier sine transform (Newman *et al*., 1986)

$$\frac{\partial h_z}{\partial t} = \frac{2}{\pi}\int_0^\infty \mathrm{Im}\left[H_z(\omega)\right]\sin(\omega t)\,d\omega \tag{6}$$

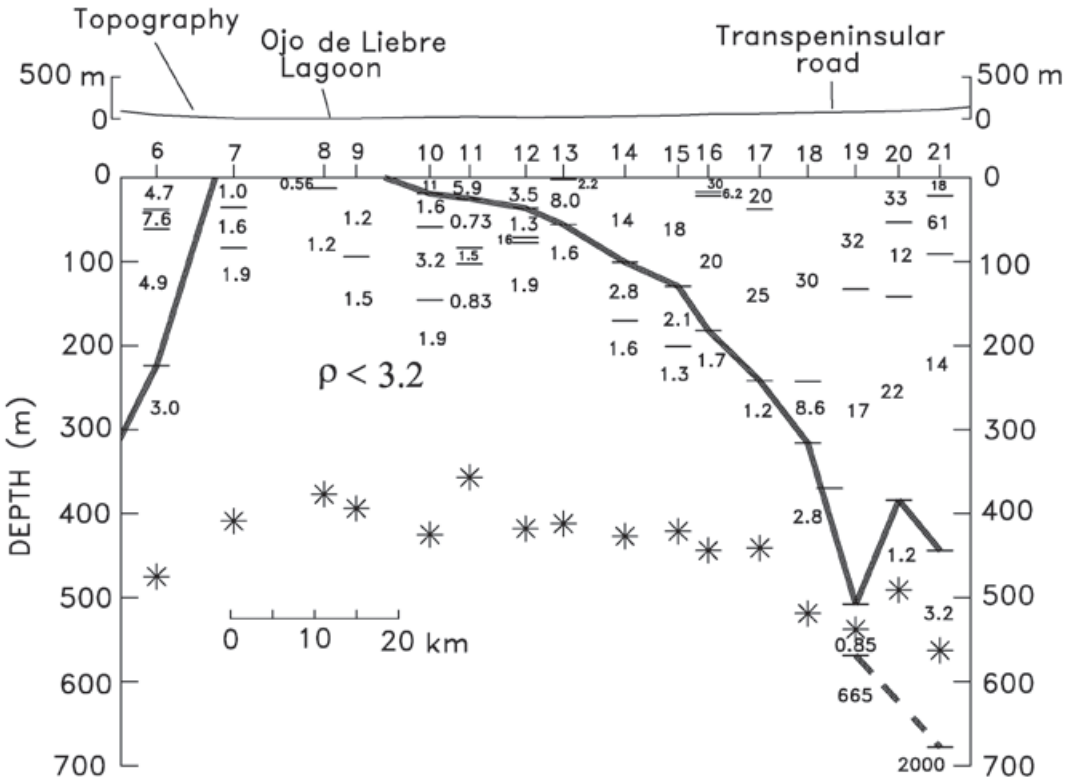

Figure 5. Section with the inverted resistivities and layer depths from the non-polarizable TEM soundings. The section and the topography have vertical exaggerations of 100 and 10, respectively. The estimated maximum depths of investigation are displayed with asterisks.

The filter weights proposed by Anderson (1979) are used to calculate this transformation from the frequency domain to the time domain. The vertical component of the magnetic field in the frequency domain ($H_z(\omega)$) produced by a rectangular loop requires integrating the field of a horizontal electric dipole along the wire forming the loop. The field at the receiver coil located at $P(0, 0, 0)$ produced by one side of a rectangular loop of dimensions $2a$ by $2b$ over a layered earth has the form,

$$H_z(\omega) = \frac{b\,I}{4\pi}\int_{-a}^{a}\frac{1}{R}\left[\int_0^{\infty} K\left(\lambda,\omega,\rho_j,d_j\right)J_1(\lambda R)\,d\lambda\right]dx' \qquad (7)$$

with $R = \left[x'^2 + b^2\right]^{1/2}$. In this expression ω is the angular frequency, I is the current in the loop, K is the kernel of the Hankel transform and J_1 (.) is the Bessel function of order 1. The kernel corresponds to the vertical component of the magnetic field produced by a horizontal electric dipole on a layered earth (Ward and Hohmann, 1987). It depends on the layer thicknesses d_j and the resistivities of each layer ρ_j. Similar expressions hold for the remaining sides of the loop. This Hankel transform is evaluated with a convolution with the filter proposed by Anderson (1975). The integration along the loop was carried out with a Gauss-Legendre method.

The two graphs shown in Figure 6 are the percentage differences between the two-layered voltages and the homogeneous half-space voltages as a function of normalized time. The solid dots are the departure times, i.e. where the difference is greater than +/- 20%. These departure times have a small dependence on the L/d ratio, but show a larger dependence on the resistivity ratios.

Instead of using any of the noise levels proposed above and depicted in Figure 2a, we estimated it directly from the data. Figure 7a shows a bilogarithmic plot of 1955 late-time measured voltages and their associated percentage standard errors. This data set, denoted here as "NW-Mexico", was constructed from the voltages of 386 sounding sites acquired during several years in 18 different zones in northwestern Mexico. Although the data set includes a variety of loop sizes, ranging from 10 by 10 m to 400 by 400

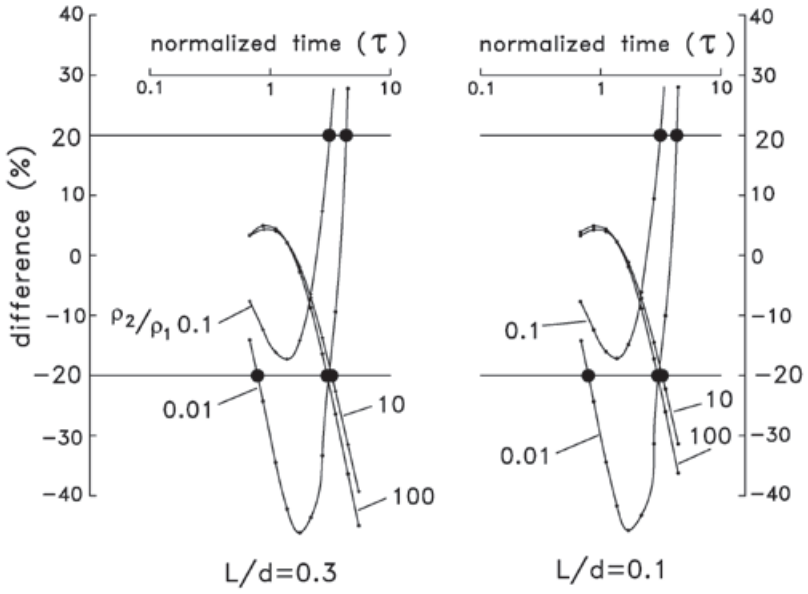

Figure 6. Percent differences between the two-layered voltages and the homogeneous earth voltages as a function of normalized time for two L/d ratios and four ρ_2/ρ_1 ratios. The departure times (+/- 20% differences) are indicated with solid circles.

m, 84% of the voltages were acquired with loops greater or equal to 150 by 150 m. These voltages are the result of three averaging steps designed to increase the signal to noise ratio: averaging in variable-size time-windows (also known as binning), stacking using the repetitive nature of the source current, and averaging with different realizations, that is, measuring the sounding several times. The standard errors presented in Figure 7 are calculated from the last averaging step, the errors from the first steps are not available in the commercial acquisition systems. This figure shows a clear and expected feature; as the voltage magnitude decreases its standard error increases due to the influence of the ambient electromagnetic noise. We assume the voltage dispersion is the result of the sum of a stationary plus a random process. The stationary component was estimated by a weighted least squares linear fit. A similar assumption was considered by Zhou and Dahlin (2003) for the analysis of dc voltage noise in the resistivity method. To accommodate the variable amount of averaging in these data we assigned error bars to the ordinates (not shown for clarity). The size of the error bars is proportional to $1/\sqrt{N}$, where N is the total amount of points involved in the average, that is, voltages that consider more averaging values have smaller

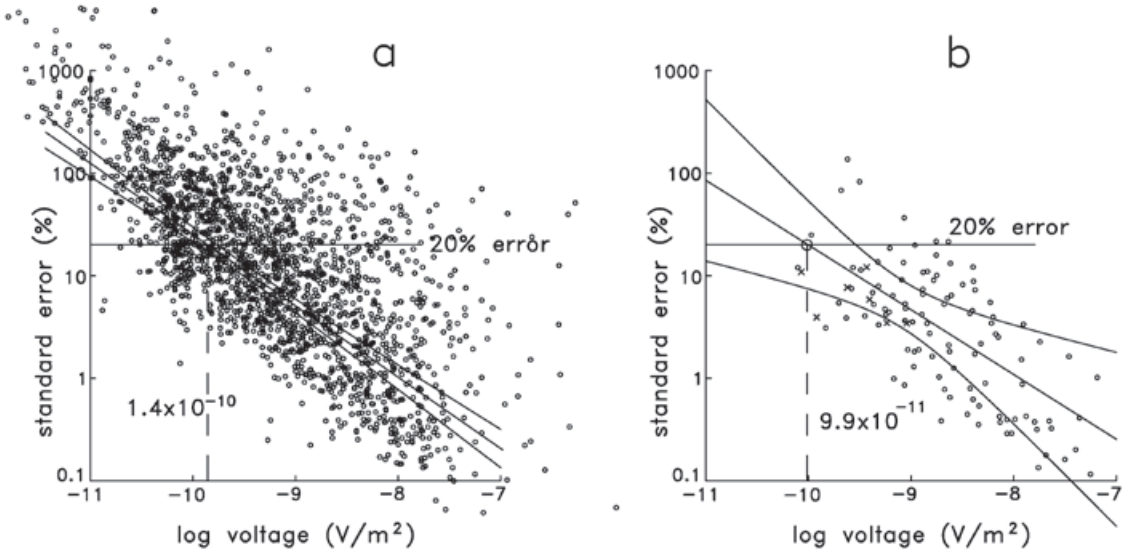

Figure 7. Log-log plots of standard error *vs.* voltage for the NW-Mexico (a) and Vizcaino (b) late-time data sets. The best fitting lines, 95% confidence level envelopes, and 20% error voltages are also shown.

error bars. The best fitting line for this data set and the predicted voltage with a 20% error (14 x 10^{-11} V/m^2) are shown in Figure 7a. This value is close to 20 x 10^{-11} V/m^2, the value suggested by McNeill (1980) as a typical noise level, shown in Figure 2a. The envelopes around the best fitting line indicate the boundaries of the 95% confidence level (Montgomery and Runger, 1994), that is, we can assert with this confidence level that the true straight line falls within the envelopes. Figure 7b shows the same analysis applied to 114 late-time voltages of the Vizcaino transect, where the estimated 20% error voltage is 9.9 x 10^{-11} V/m^2. This will be the noise value used in expression (1) to estimate the MDI.

Expression (1) is based on a two-layered earth. The cumulative conductance is used to adapt it to a multilayered subsurface (Spies, 1989). Figure 8 illustrates this for sounding 21. The cumulative conductance at any depth (d) is defined by

$$S_c(z) = \int_0^z \frac{z'}{\rho(z')} dz'$$

where $\rho(z')$ are the inverted layer resistivities (Figure 8a). Having determined $S_c(z)$, the average resistivity $\rho_{av}(z)$ at any depth can be found with $\rho_{av}(z) = d/S_c(z)$. The model resistivities, cumulative conductance, and average resistivity as a function of depth are displayed in Figure 8b. Then, the first layer resistivity of expression (1) can be replaced by the average resistivity to obtain an expression of the maximum depth of investigation as a function of depth. For example, by using the average loop moment (1.935x10^5 Am^2), noise level (9.92x10^{-11} V/m^2), and the departure time for a resistivity contrast ρ_2/ρ_1=100, this expression is $D_{max}(z) \approx 366[\rho_{av}(z)]^{0.2}$. This function is shown in Figure 8c. When D_{max} is equal to depth gives the required solution. Graphically, this occurs when the D_{max} curve intersects the unit slope line passing through the origin, as shown in Figure 8c. For this stratified model the maximum depth of investigation is 560 m.

Figure 9a displays with solid dots the depth to the deepest interface interpreted in the inverted models of the non-dispersive soundings. The minimum (D_{min}) and maximum (D_{max}) depths of investigation are also shown. The four D_{max} lines correspond to the four resistivity contrasts ρ_1/ρ_{av} of 100, 10, 0.1, and 0.01 . These were calculated using the typical current (8.6 Amp), loop size (150 m), estimated noise level (9.92x10^{-11} V/m^2), and the calculated departure times. The shaded area indicates the range of depths explored with these soundings assuming a substratum 100 times more resistive than the average resistivity. The corresponding D_{max} values are also shown with stars in the section of Figure 5. In all models the MDI is greater than the deepest interface, except for soundings 19 and 21. Sounding 20 could probably fall in this case, but equipment malfunction prevented recording the latest time voltages. The discrepancy between the MDI and

MODEL

layer	ρ (Ωm)	thick (m)	depth (m)
1	18	22	22
2	61	69	91
3	14	353	444
4	3.2	234	678
5	2000		

a

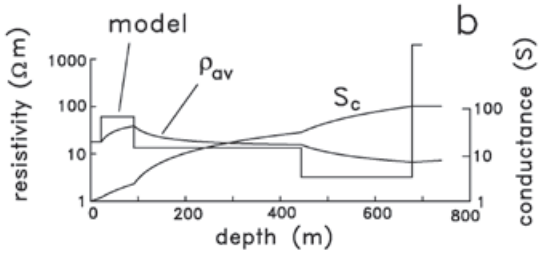

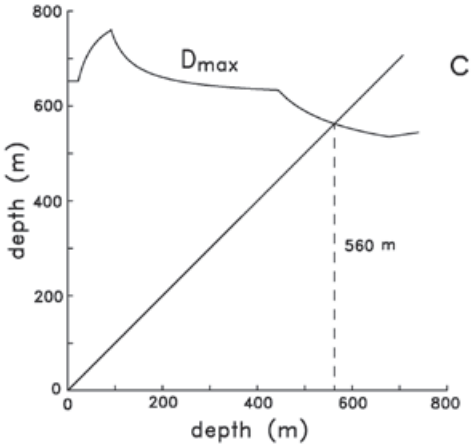

Figure 8. a) Inverted model of sounding 21. b) Model and average resistivity as a function of depth. The cumulative conductance is also shown. c) Variation of D_{max} with depth.

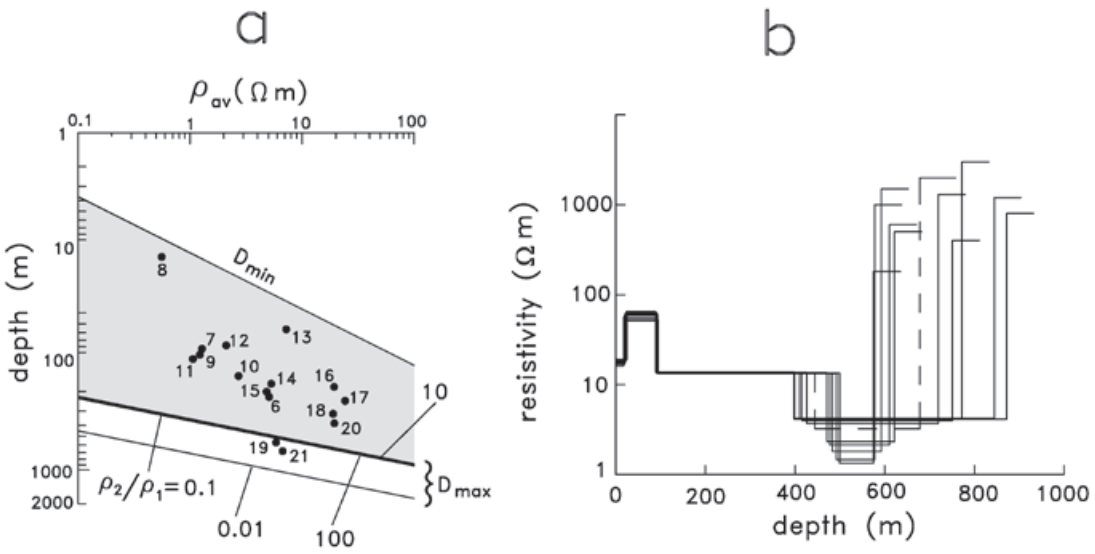

Figure 9. a) Depth versus average resistivity plot for the 16 non-polarizable models. Solid dots are the depths to the deepest layer interface. b) Eleven layered models that reproduce the data of sounding 21 with approximately the same misfit error. The dashed line corresponds to the model of minimum misfit error.

the deepest interface is 120 m for model 21 and 50 m for model 19. This would suggest that either the MDI estimation is not valid or that the deepest interface in these two models is not supported by the data. The latter option seems untrue because a better fit is obtained when the resistive basement is considered. This apparent contradiction is solved when a careful examination of the models for these two soundings indicates that they suffer from an intense equivalence problem in the conductive layer overlying the resistive substratum. This is illustrated in Figure 9b for the model of sounding 21, which shows 11 different models that reproduce the observed voltages with nearly the same misfit error. All these models have practically the same fourth-layer conductance, that is, there are a large number of possible combinations of thickness over resistivity. Then, if we choose a model with the fourth layer about 120 m thinner, keeping its conductance unaltered, the discrepancy between the MDI and the deepest interface no longer exists. Furthermore, the late-time voltage errors for this sounding (shown with crosses in Figure 7b) are systematically lower than the nominal 20% level, which would result in a slightly greater MDI value. A similar situation occurs for sounding 19.

Most of the spheric energy arises in the thunderstorm centers of Central Africa, Central-South America, and Southeastern Asia (Ward, 1967), producing noise that varies diurnally, seasonally, and with latitude. Attenuation of spheric noise is determined by the height of the lower ionosphere and the conductivity of the earth and ionosphere, in such a way that the wave generally propagates more efficiently at night. McCracken *et al*. (1984) report an increase in spheric noise by a factor of ten from winter to summer and by a further factor of ten from high latitudes (39º S) in southern Australia to low latitudes (12º S) in northern Australia. It is interesting then, to test if our NW-Mexico data set of late-time voltages show a similar difference between the noise level of soundings acquired in winter with those measured in summer. Figure 10 shows the dispersion plots for these seasons with the corresponding weighted linear fits and their 95% confidence level envelopes. In this analysis we considered six-month periods, winter from October to March and summer from April to September. The estimated stationary noise levels are $4.4 \leq 13 \leq 26 \times 10^{-11}$ V/m^2 in winter and $12 \leq 15 \leq 18 \times 10^{-11}$ V/m^2 in summer (the uncertainties are estimated from the 95% confidence envelopes). Although the summer noise level is slightly higher than the winter level, they are not statistically different as their uncertainties overlap. This conclusion is still valid if, instead of considering six-month seasons, we consider three-months (winter from January to March and summer from July to September). Then, our data do not support the difference of one order of magnitude in the seasonal noise level suggested by McCracken *et al.* (1984). We think the explanation for this unexpected result might reside in the characteristics of the rainy season in northwestern Mexico. The rainy season in this region occurs in winter, not in summer, and the rain episodes are rarely accompanied by lightning.

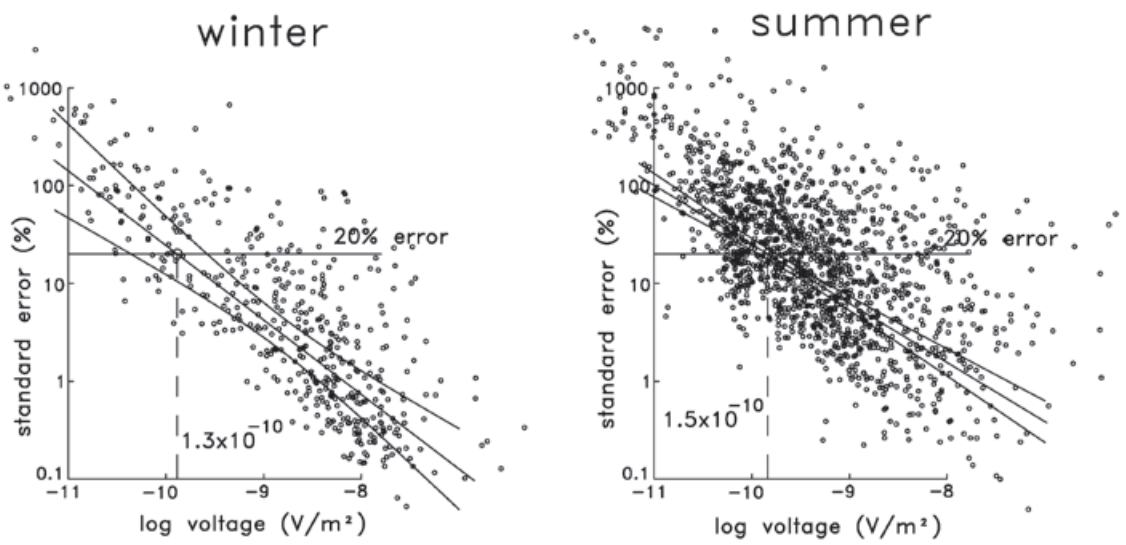

Figure 10. Dispersion graphs of the NW-Mexico data set for winter and summer.

Polarizable soundings

As mentioned above, soundings from 1 to 5 and from 22 to 38 were affected by IP. Figure 4 show the negative late-time voltages for three selected soundings, characteristic of the presence of IP. The most common way to represent the IP phenomena is with the Cole-Cole model (Cole and Cole, 1941; Pelton *et al*., 1978), which describes the frequency dependent resistivity with

$$\rho(\omega) = \rho_0 \left[1 - m\left(1 - \frac{1}{1 + (i\omega\tau)^c} \right) \right] \quad (8)$$

where ρ_0 is the zero-frequency or direct current resistivity (Ωm), m is the chargeability (dimensionless), τ is the time constant (seconds), and c is the frequency exponent (dimensionless). The four parameters have different ranges of variation. The chargeability and the frequency exponent can vary from 0 to 1. The dc resistivity and the time constant have wide ranges, from 10^{-2} to 10^5 Ωm and from 10^{-5} to 10^4 s, respectively.

The voltages of these soundings were inverted to layered dispersive models using the linearized least squares algorithm of Jupp and Vozoff (1975). The solution of the forward problem required by the inversion was calculated with the same numerical procedure outlined above in expressions (5) to (7) but with the following four modifications:

a) The resistivity in each layer in the kernel of expression (7) is no longer constant, but now depends on the frequency as the Cole-Cole dispersion model (8).

b) To circumvent the time-consuming integration along the loop, each loop side is divided into N wire segments of equal length, approximating each segment by an equivalent electric dipole (Stoyer, 1990), considering at least three equivalent dipoles for each loop side.

c) Before applying the Fourier transform, the effect of the receiver coil finite bandwidth is incorporated by multiplying the transfer function of the coil by $H_z(\omega)$.

d) Finally, the effect of the actual current waveform (linear turn-off periodic ramps) is accounted for by using the procedure described by Fitterman and Anderson (1987). This approach requires extrapolating the voltage response beyond the last late-time gate. We fitted an exponential function to the last five voltages to perform this extrapolation, calculating additional voltages points if necessary.

In the inversion process of the sounding voltages we tried to obtain the simplest possible models. We started from a simple polarizable homogeneous subsurface, increasing the model structure by considering a two-layered medium with only one polarizable layer, and so on. This searching process was stopped when a reasonably low misfit error was obtained. Only at one site (sounding 37) we could not obtain any model that reproduced the data. The remaining 21 models resulted of two layers, but in 10 of them

one of the layers is not dispersive. The average misfit error for this set of models is higher (2.5) than the corresponding average (1.4) of the non-polarizable models. The four Cole-Cole parameters for each layer and the thickness of the first layer are shown in Figure 11. The following features can be deduced from the behavior of these parameters:

a) The lateral correlation between parameters of contiguous models is quite poor, indicating that the Cole-Cole models are not regional but local. Given the large separation between soundings, this is not surprising.

b) The mean depth to the second layer (60 m) is significantly less than the mean depth to the deepest layer in the non-polarizable models (155 m). This suggests that the maximum depth of exploration is significantly reduced when the subsurface is polarizable. For these cases we cannot use expression (1) to estimate the maximum depth, simply because frequency-independent resistivities were employed in its derivation. No similar expression has been proposed in the literature, apparently because the number of possible parameter combinations is too large; for a two layer model, instead of three parameters for the non-polarizable case, there are nine parameters for the polarizable case. To support the argument of a decreased depth of exploration we calculated the subsurface current density at selected times after the current shut-off for a non-polarizable model (sounding 21, Figure 12a) and a polarizable model (sounding 26, Figure 12b). The source in both models is a 150 by 150 m loop located at the origin where a dc current of 1 A is injected. The current density contours are plotted only in the quadrant $x \geq 0$, $z \geq 0$; in the quadrant $x \leq 0$, $z \geq 0$ the contours have the same shape but with opposite polarity. As a reference, the measured responses of these models are shown in Figure 4. For the model of sounding 21 (Figure 12a), the two times correspond to the earliest (90 μs) and latest (70 ms) recorded times. At 90 μs the maximum current density is located in the close vicinity of the loop and has a magnitude of close to 30 x 10^{-6} A/m^2. At 70 ms the maximum has migrated down and sideways, while its intensity has decreased substantially to about 10 x 10^{-10} A/m^2. This attenuation and migration of the maximum current density with time was nicknamed as "smoke rings" by Nabighian (1979). Notice that the maximum has been trapped by the conductive layer of resistivity 3.2 Ωm and that little current is flowing in the resistive substratum. This explains why the resistivity of the fifth layer is poorly resolved (Figure 9b).

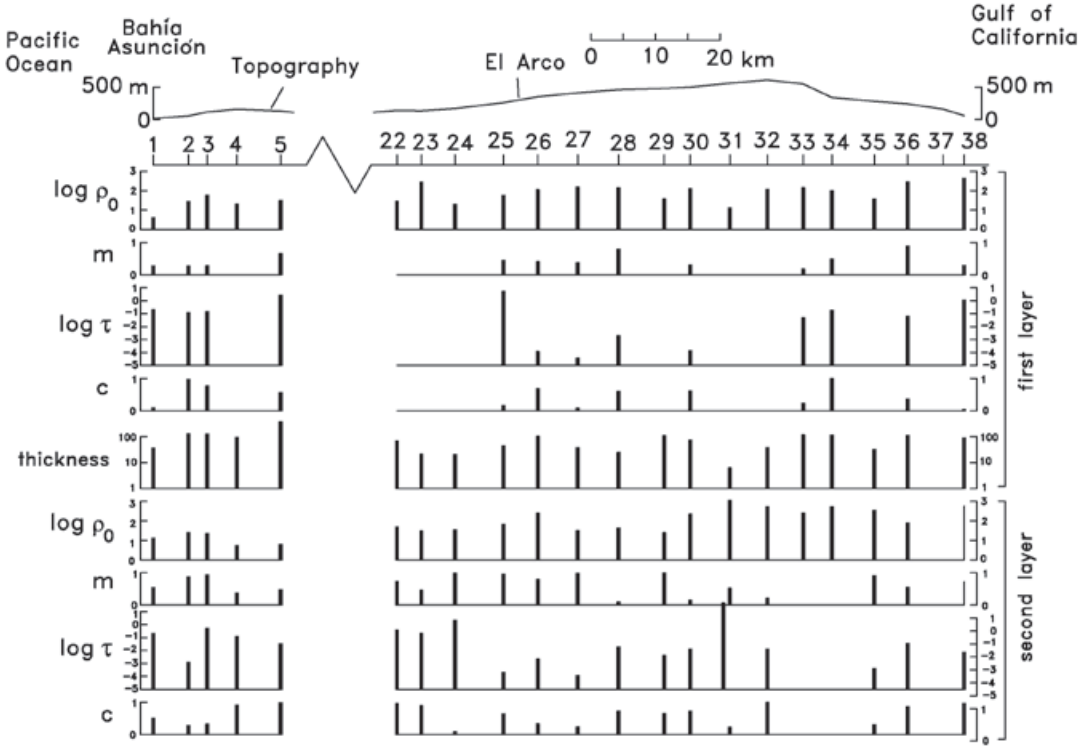

Figure 11. Parameters of the inverted Cole-Cole models of the polarizable soundings. The topography has a vertical exaggeration of 10.

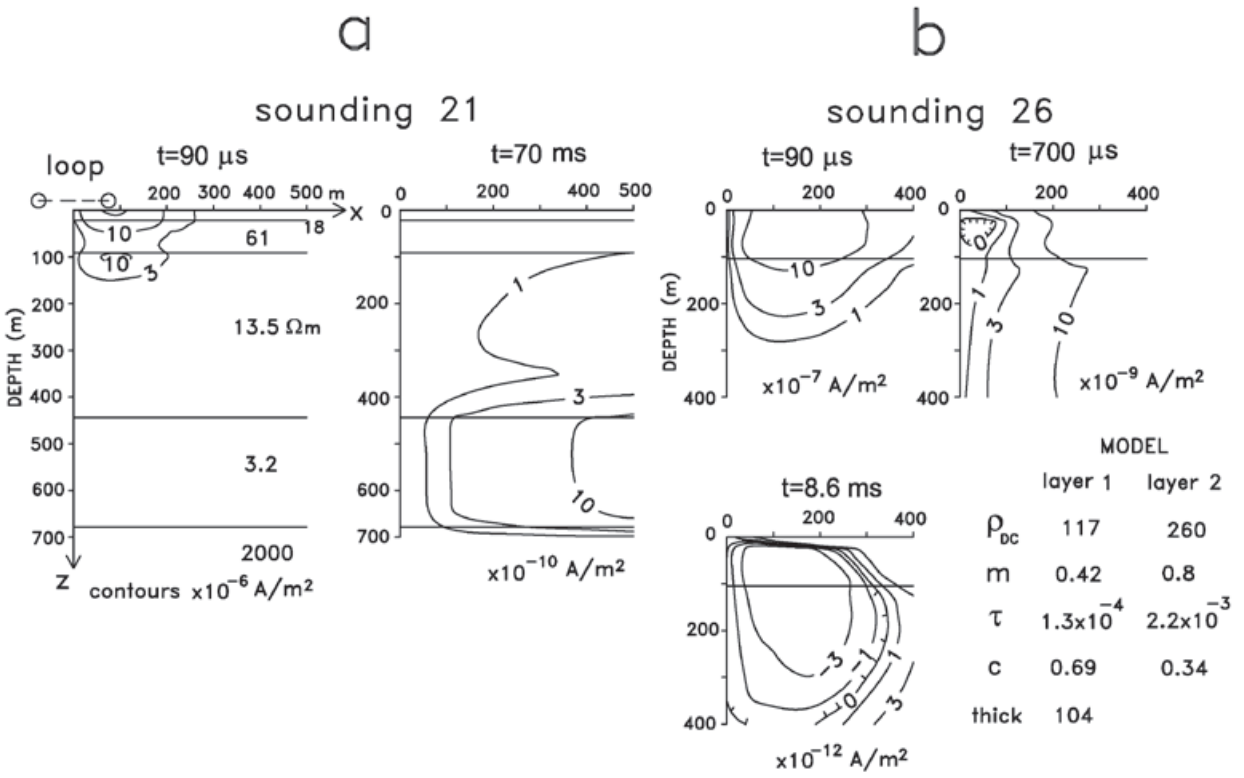

Figure 12. Contours of current density at different times for the non-polarizable model of sounding 21 (a) and the polarizable model of sounding 26 (b). The source is a 150 by 150 m loop with 1 A current. The multiplicative factor for the current densities is indicated in each panel.

The eight Cole-Cole parameters and thickness of the first layer for the polarizable model are indicated in Figure 12b. The current densities are shown at three times: earliest (90 μs), intermediate (700 μs) and latest (8.6 ms). Instead of 70 ms as the latest time, we chose 8.6 ms because for later times the voltages flatten, suggesting the noise level has been reached. At 90 μs the maximum is in the first layer and has a magnitude of 10 x 10^{-7} A/m^2. At 700 μs the maximum has attenuated, deepened and moved away from the loop. Notice that close to the loop a zone of negative values, bounded by the zero contour, has developed. Within this contour the current has reversed its direction. This instant corresponds with the time where the voltage changes polarity (see Figure 4). At 8.6 ms the subsurface region with reversed direction has increased in area but its magnitude has also been attenuated. Smith and West (1988) proposed a physical model for the induced current in a polarizable subsurface circuit. The total induced current is the sum of a Fundamental Induced Current (FIC) and a Polarization Current (PC). These two current modes are not separable. The PC always opposes the sense of the FIC. As the FIC usually decays faster than the PC, at late times the PC is greater, producing the negative late-time voltages at the surface. This behavior is similar to the current densities of Figure 12b. At the shortest time the FIC dominates, producing the positive voltages in the receiver. At 700 μs the total current close to the loop has changed its direction because the PC is greater than the FIC, resulting then negative voltages at the receiver. At the latest time the PC clearly dominates the FIC. The end product of these two current modes opposing each other at all times is a diminished depth of investigation.

It is worth mentioning that inverting only the positive voltages of a sounding affected by IP with an algorithm that does not include a polarizable resistivity will give an incorrect result. The opposing Polarization Current is present at all times, not only in late times when the surface voltages have changed sign.

c) The zero-frequency resistivities in the southwestern (SW) group of soundings (6.6 < 16 < 38 Ωm) are lower than those of the northeastern (NE) group (36 < 110 < 340 Ωm). The +/- one standard deviations in these estimates are not symmetric with respect to the

mean because they are defined in a logarithmic scale. The relatively low values in the SW group might be due to membrane polarization associated with the presence of clay in sands (Ward, 1990). In the NE group the likely source of IP is metallic polarization due to mineral grains with electronic conduction, such as sulphides and/or magnetite. In this zone the large El Arco porphyry copper deposit (Coolbaugh *et al*., 1995) is located, where significant IP anomalies have been measured (Farías, 1978; Flores and Peralta-Ortega, 2009). Other four IP anomalous zones in the vicinity of our traverse were surveyed and associated with the presence of pyrite, magnetite or copper sulphides by Farías (1978).

Conclusions

We showed the method proposed by Spies (1989) is a reliable technique for estimating the MDI. In 14 out of the 16 non-polarizable soundings the MDI was deeper than the deepest interface estimated from the inversion of the data. In the remaining two models we found the reverse situation, leading to an apparent discrepancy. However, this discrepancy was explained by an equivalence problem associated with a conductive layer and by a lower noise level. Two minor modifications were applied to the Spies expression before using it; a refinement in the departure time by considering different resistivity contrasts, and the estimation of the noise level directly from the field data. The MDI turns out to be a very useful tool for estimating how far beyond the last interface is being explored. An interesting result was obtained in the spatial character of the Vizcaino data; all soundings located on the Vizcaino basin were not affected by induced polarization, but those placed on plutonic, volcanic or metamorphic rocks were affected.

The dipping conductor of resistivities less than 3.2 Ωm was interpreted as the intrusion of saline water in the granular sediments of the Vizcaino basin. Its large lateral extent of more than 70 km is not common. For polarizable soundings the Spies method is not valid. We do not propose an analogous method for this situation but show that the MDI is significantly reduced compared to that of non-polarizable models. The estimated stationary noise level for the NW-Mexico data set was 1.4×10^{-10} V/m^2, close to the 2×10^{-10} V/m^2 value reported by McNeill (1980). No difference was found in the noise level between summer and winter in this data set.

Acknowledgements

This work was funded by CICESE and CONACYT projects. We thank S. Espinoza, H. Benitez, F. Uribe, and J. Parra for their invaluable help during the field work.

Bibliography

Anderson W.L., 1975, Improved digital filters for evaluating Fourier and Hankel transform integrals, United States Geological Survey Report GD-75-012.

Anderson W.L., 1979, Numerical integration of related Hankel transforms of order 0 and 1 by adaptive digital filtering, *Geophys.,* 44, 1287-1305.

Cole K.S., Cole R.H., 1941, Dispersion and absorption in dielectrics, *J. Chem. Phys.,* 9, 341.

Coolbaugh D.F., Osoria-Hernández A., Echávarri-Pérez A., Martínez-Müller R., 1995, El Arco porphyry copper deposit, Baja California, Mexico. In: Pierce, F.W. and Bolm, J.G. (Eds.), Porphyry copper deposits of the American Cordillera, *Arizona Geological Society Digest,* 20, 524-538.

Delgado Argote L.A., 2000, Evolución tectónica y magmatismo Neógeno de la margen oriental de Baja California Central, Ph.D. Thesis, Univ. Nacional Autónoma de México, Instituto de Geología, 175 pp.

Farías R., 1978, Geophysical exploration of the El Arco-Calmalli mining district, Baja California, Mexico, M.Sc. Thesis, Dept. of Geosciences, The University of Arizona, 59 pp.

Fitterman D.V, Anderson W.L., 1987, Effect of transmitter turn-off time on transient soundings, *Geoexploration*, 24, 131-146.

Fitterman D.V., 1989, Detectability levels for central induction transient soundings, *Geophys.,* 54, 127-129.

Flores C., Peralta-Ortega S.A., 2009, Induced polarization with in-loop transient electromagnetic soundings: A case study of mineral discrimination at El Arco porphyry copper, Mexico, *J. Appl. Geophys.,* 68, 423-436.

García-Abdeslem J., Romo J.M., Gómez-Treviño E., Ramírez-Hernández J., Esparza-Hernández F.J., Flores-Luna C.F., 2005, A constrained 2D gravity model of the Sebastián Vizcaíno Basin, Baja California Sur, Mexico, *Geophys. Prospec.,* 53, 755-765.

García-Domínguez G., 1976, Prospección geológica en Baja California, Tercer Simposium de Geología del Subsuelo, PEMEX, Superintendencia General de Exploración, Distrito Frontera Norte, Reynosa, México, 31-49.

Jupp D.L.B., Vozoff K., 1975, Stable iterative methods for the inversion of geophysical data, *Geophys. J. R. Astr. Soc.,* 42, 957-976.

McCracken K.G., Pik J.P., Harris R.W., 1984, Noise in EM exploration systems, *Expl. Geophys.,* 15, 169-174.

McNeill J.D., 1980, EM37 Ground transient electromagnetic system: Calculated depth of exploration, Technical Note TN-10, Geonics Limited, 13 pp.

Montgomery D.C., Runger G.C. 1994, Applied statistics and probability for engineers, John Wiley and Sons, 784 pp.

Nabighian M.N., 1979, Quasi-static transient response of a conducting half-space: An approximate representation, *Geophys.,* 44, 1,700-1,705.

Newman G.A., Hohmann G.W., Anderson, W.L., 1986, Transient electromagnetic response of a three-dimensional body in a layered earth, *Geophys.,* 51, 1608-1627.

Pelton W.H., Ward S.H., Hallof P.G., Sill W.R., Nelson P.H., 1978, Mineral discrimination and removal of inductive coupling with multifrequency IP, *Geophys.,* 43, 588-609.

Romo J.M., García Abdeslem J., Gómez Treviño E., Esparza F., Flores Luna C., 2001, Resultados preliminares de un perfil geofísico a traves del desierto de Vizcaíno en Baja California Sur, México, *GEOS Boletín Unión Geofísica Mexicana,* 21, 2, 96-107.

Sedlock R.I., Ortega-Ramirez F., Speed R.C., 1993, Tectonostratigraphic terranes and tectonic evolution of Mexico, *Special Paper 278, Geol. Soc. Amer.*

Spies B.R., 1989, Depth of investigation in electromagnetic sounding methods, *Geophys.,* 54, 872-888.

Smith R.S., West G.F., 1988, Inductive interaction between polarizable conductors: An explanation of a negative coincident-loop transient electromagnetic response, *Geophys.,* 53, 677-690.

Stoyer C.H., 1990, Efficient computation of transient sounding curves for wire segments of finite length using an equivalent dipole approximation, *Geophys. Prospec.,* 38, 87-100.

Ward S.H., 1967, The electromagnetic method, in Hansen et al (eds.), Mining Geophysics. Volume II. Theory, Soc. of Exploration Geophysicists, 224-372.

Ward S.H., Hohmann G.W., 1987, Electromagnetic theory for geophysical applications. In: Nabighian, M.N. (Ed.), Electromagnetic methods in Applied Geophysics – Theory, vol. 1, 130-311, Society of Exploration Geophysicists.

Ward S.H., 1990, Resistivity and induced polarization methods, in Ward, S.H. (ed.), Geotechnical and Environmental Geophysics, Vol. I: Review and Tutorial, 147-189, Soc. of Exploration Geophysicists, Tulsa, Oklahoma.

Weidelt P., 1982, Responses characteristics of coincident loop transient electromagnetic systems, *Geophys.,* 42, 1325-1330.

Zhou B., Dahlin T., 2003, Properties and effects of measurement errors on 2D resistivity imaging surveying, *Near Surf. Geophys.,* 1, 105-117.

Geofísica Internacional (2013) 52-2: 173-196

Original paper

Ometepec-Pinotepa Nacional, Mexico Earthquake of 20 March 2012 (M_w7.5): A preliminary report

Universidad Nacional Autónoma de México Seismology Group*
(with contribution from Universidad Autónoma Metropolitana, Azcapozalco, México, D.F.)

Received: February 02, 2013; accepted: February 15, 2013; published on line: March 22, 2013

Resumen

A partir de un análisis de los datos locales y regionales del sismo somero e inverso de Ometepec-Pinotepa Nacional (M_w 7.5), del 20 de marzo de 2012, se determinó la localización de su hipocentro en 16.254°N 98.531°W, aproximadamente 5 km fuera de la costa a una profundidad de 20 km. Durante los primeros 4 segundos de la ruptura, el deslizamiento fue relativamente pequeño. Esta fase inicial fue seguida por dos parches de gran deslizamiento, uno de ellos echado arriba del hipocentro, hacia el SE, y el otro echado abajo, hacia el norte. El área de ruptura total, estimada a partir de la inversión de registros de movimientos fuertes cercanos a la fuente, es de ~25 km × 60 km. El sismo fue seguido por un número excepcionalmente grande de réplicas. El área de réplicas coincide espacialmente con la observada en el doblete de 1982 (M_w7.0, 6.9). Sin embargo, el momento sísmico del sismo de 2012 es ~3 veces mayor al de la suma de los momentos del doblete, indicando que las características generales de la ruptura de los dos episodios sísmicos difieren. El área de escaso deslizamiento cerca del hipocentro y las áreas de gran deslizamiento de los dos parches se distinguen por una actividad relativamente pequeña de réplicas. Sin embargo, se observa una clara y sorprendente alineación de las réplicas en dirección NE al este del epicentro. Los cocientes de la energía radiada y el momento sísmico (E_s/M_0) de cinco sismos en la región de estudio revelan que dichos cocientes son, en el caso de sismos cercanos a la trinchera, un orden de magnitud más pequeños que los observados en eventos que ocurren echado abajo (e.g., los sismos de 2012 y de Copala de 1995). Los sismos cercanos a la trinchera son conocidos por producir una aceleración máxima (*PGA*) baja. La información disponible sugiere que la interfase de la placa en la región puede ser dividida en tres dominios en dirección del echado: (1) De la trinchera a una distancia de 35 km echado abajo. En este dominio ocurren sismos de M~6 a 7 con valores bajos de (E_s/M_0). Estos eventos generan un gran número de réplicas. No se sabe si el área donde no han ocurrido rupturas en este dominio de la interfase se desliza asísmicamente (deslizamiento estable) o si se encuentra parcialmente acoplada. (2) De 35 a 100 km a partir de la trinchera. Este dominio está sísmicamente acoplado y es en donde ocurre el deslizamiento *stick-slip*, generando grandes sismos. Probablemente, parte del dominio se encuentra condicionalmente estable. (3) De 100 a 200 km a partir de la trinchera. En este dominio se han reportado eventos de deslizamiento lento (SSE) y tremores no volcánicos (NVT).
El sismo causó daños severos en y cerca de los poblados de Ometepec y Pinotepa Nacional. La *PGA* excedió 1 g en un sitio blando de la región epicentral. Los valores de *PGA* observados en sitios duros en función de la distancia epicentral concuerdan razonablemente bien con las leyes de atenuación derivadas a partir de datos de sismos mexicanos interplaca. El sismo se sintió fuertemente en la Ciudad de México. La *PGA* en Ciudad Universitaria, un sitio duro en la capital del país, fue de 12 gales. Registros de movimientos fuertes en la ciudad desde 1985 muestran que los valores de *PGA* durante el sismo de 2012 no fueron excepcionales, y que movimientos similares en la ciudad ocurren ~ una vez cada tres años.

Palabras clave: sismo de Ometepec-Pinotepa Nacional de 2012, sismo interplaca, deslizamiento y energía radiada, movimiento del terreno.

* UNAM Seismology Group includes all researchers and technicians of Institute of Geophysics and Institute of Engineering, UNAM, who work in the field of seismology and engineering seismology.

Abstract

An analysis of local and regional data produced by the shallow, thrust Ometepec-Pinotepa Nacional earthquake (M_w 7.5) of 20 March 2012 shows that it nucleated at 16.254°N 98.531°W, about 5 km offshore at a depth of about 20 km. During the first 4 seconds the slip was relatively small. It was followed by rupture of two patches with large slip, one updip of the hypocenter to the SE and the other downdip to the north. Total rupture area, estimated from inversion of near-source strong-motion recordings, is ~25 km × 60 km. The earthquake was followed by an exceptionally large number of aftershocks. The aftershock area overlaps with that of the 1982 doublet (M_w7.0, 6.9). However, the seismic moment of the 2012 earthquake is ~3 times the sum of the moments of the doublet, indicating that the gross rupture characteristics of the two earthquake episodes differ. The small-slip area near the hypocenter and large-slip areas of the two patches are characterized by relatively small aftershock activity. A striking, intense, linear NE alignment of the aftershocks is clearly seen. The radiated energy to seismic moment ratios, (E_s/M_0), of five earthquakes in the region reveal that they are an order of magnitude smaller for near-trench earthquakes than those that occur further downdip (e.g., 2012 and the 1995 Copala earthquakes). The near-trench earthquakes are known to produce low A_{max}. The available information suggests that the plate interface in the region can be divided in three domains. (1) From the trench to a distance of about 35 km downdip. In this domain M~6 to 7 earthquakes with low values of (E_s/M_0) occur. These events generate large number of aftershocks. It is not known whether the remaining area on this part of the interface slips aseismically (stable sliding) or is partially locked. (2) From 35 to 100 km from the trench. This domain is seismically coupled where stick-slip sliding occurs, generating large earthquakes. Part of the area is probably conditionally stable. (3) From 100 to 200 km from the trench. In this domain slow slip events (SSE) and nonvolcanic tremors (NVT) have been reported.
The earthquake caused severe damage in and near the towns of Ometepec and Pinotepa Nacional. The *PGA* exceeded 1 g at a soft site in the epicentral region. Observed *PGA*s on hard sites as a function of distance are in reasonable agreement with the expected ones from ground motion prediction equations derived using data from Mexican interplate earthquakes. The earthquake was strongly felt in Mexico City. *PGA* at CU, a hard site in the city, was 12 gal. Strong-motion recordings in the city since 1985 demonstrate that *PGA*s during the 2012 earthquake were not exceptional, and that similar motion occurs about once in three years.

Key words: 2012 Ometepec-Pinotepa Nacional earthquake, interplate earthquake, slip and radiated energy, ground motion.

Introduction

The Ometepec-Pinotepa Nacional earthquake of 20 March 2012 (M_w7.5) initiated near the mexican coast at the border between the states of Oaxaca and Guerrero. It was a shallow thrust earthquake which ruptured the interface of the subducting oceanic Cocos and overriding continental North America plates. An Earthquake Engineering Research Institute (EERI) special report on the earthquake (Juárez García *et al.*, 2012) states that in the epicentral zone "almost 2,000 houses collapsed or were judged to be total losses, over 3,000 houses sustained heavy damage, and over 3,000 were reported with minor damage." The earthquake was strongly felt in Mexico City.

The earthquake was recorded in the epicentral zone at Pinotepa Nacional station (PNIG) which is equipped with a broadband seismograph, an accelerograph, and a GPS receiver with a sampling interval of 1 s (Figure 1). This station is operated by the National Seismological Service (SSN, Servicio Sismológico Nacional) of Instituto de Geofísica, Universidad Nacional Autónoma de México (UNAM). Data from PNIG are transmitted in real-time to Instituto de Geofísica, UNAM. There were several accelerographs in and near the epicentral zone (elements of seismic alert systems for Mexico City and the City of Oaxaca) which produced strong-motion recordings. There were also a few GPS stations in the area, operating in an autonomous mode, from which coseismic static displacement field could be retrieved. Following the earthquake, a portable network of seven seismic stations was installed in the epicentral area to record aftershocks. At regional distances, the earthquake was recorded by broadband seismographs and accelerographs. The event produced numerous accelerograms in the Valley of Mexico and the City of Oaxaca.

Based on the analysis of a subset of this large data set, we present preliminary results on the location of the mainshock and aftershocks, slip distribution on the fault, relationship of the aftershock area with the slip distribution, radiated seismic energy, attenuation of *PGA* as a function of distance, and ground-motion characteristics in the Valley of Mexico. When possible, we compare the 2012 earthquake with other large Mexican subduction thrust earthquakes, including the

1982 Ometepec doublet (M_w6.9, 7.0) which may have broken roughly the same segment of the plate boundary and the 1995 Copala earthquake (M_w7.3) which ruptured the adjacent one. These comparisons help put this earthquake in proper perspective with respect to the other shallow thrust earthquakes along the Mexican subduction zone.

Tectonic Setting and Previous Earthquakes in the Region

In the area of interest, the oceanic Cocos plate subducts below Mexico at a relative convergence rate of 6 cm/yr in the direction N34°E (DeMets *et al.*, 1990). Shallow, thrust earthquakes along the Pacific coast of Oaxaca, which occur as a consequence of the subduction, exhibit some special characteristics. (1) Large earthquakes seem to occur periodically with a recurrence period of 30-50 years (Singh *et al.*, 1981). (2) The statistics of earthquakes in the region suggests occurrence of characteristic earthquakes of magnitude around 7.6 (Singh *et al.*, 1983). (3) The rupture process of the earthquakes, as seen on teleseismic Galitzin and long-period WWSSN seismograms, is remarkably simple to the east of 98.2°W but becomes more complex to the west (Chael and Stewart, 1982; Singh and Mortera, 1991).

Several parallel ridges of seamounts have been mapped on the sea floor of the Cocos plate in the area (Kanjorski, 2003). These seamounts are oriented 15–20° from orthogonal to the trench axis (Figure 1). Kanjorski (2003) suggests that characteristics of seismicity in the region are affected by subduction of the seamounts. The oceanic crust is segmented along the seamount-parallel faults at the subduction zone ("slivered" ocean crust model). During large earthquakes each slivered piece of the subducted plate, generally, ruptures independently, the dimension being controlled by the spacing of the parallel seamount chains (50-100 km). We note that the rupture area of the 1982 doublet mostly falls between two parallel faults. As we show later, the rupture area of the 2012 earthquake also lies between these faults and overlaps with that of the 1982 doublet. Based on analysis of local seismicity, Yamamoto *et al.* (2002, 2013) suggest that the upper plate in the region is also segmented.

Table 1 lists large shallow, thrust earthquakes in the region which have occurred since 1900 near the coast between the latitudes of 95.0°W and 99.0°W. The region covered in this table includes south east Guerrero. Figure 1 shows the epicenters of these earthquakes. When the aftershock area of an earthquake is reasonably

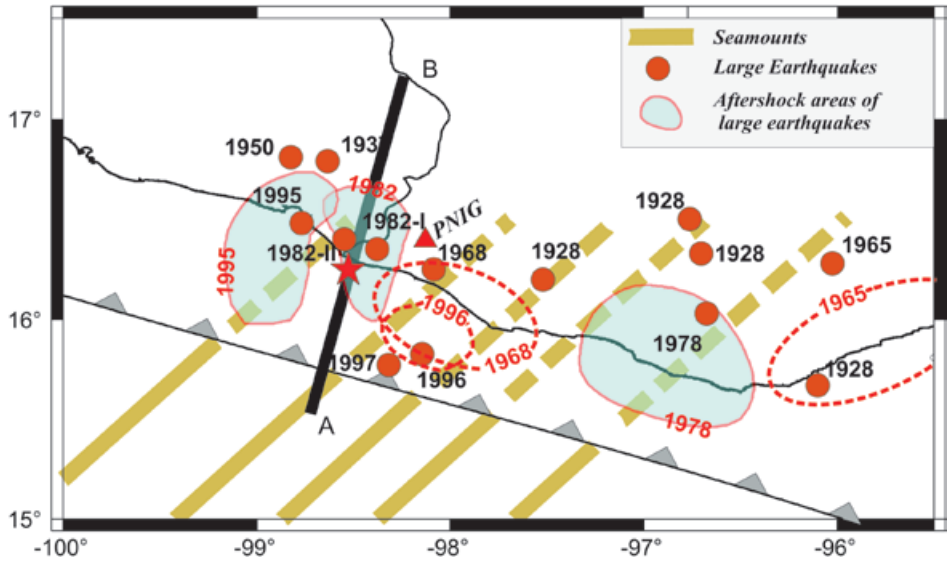

Figure 1. Tectonic map of the region showing epicenters of large, shallow, thrust earthquakes in Oaxaca and SE Guerrero (1928-present; Table 1) and their aftershock areas if known (closed contour if reliable, dashed otherwise; see text). Epicenter of the Ometepec-Pinotepa Nacional 2012 event is indicated by a star. Epicenter of the 1997 (M_w6.7) event, of relevance to the study (see text), is given. Parallel thick green lines: faults along seamount lineaments offshore (continuous) and their prolongation inland (dashed), taken from Kanjorski (2003). PNIG is a station equipped with broadband seismometer, accelerometer, and GPS receiver. A schematic section along A-A' is shown in Figure 16.

well known from local and regional seismograms, it is illustrated by a contour of unbroken line in the figure. These include aftershock areas of the central Oaxaca earthquake of 1978 (Singh *et al.*, 1980) and the Ometepec doublet (Nava, 1984). For these earthquakes portable seismographs were deployed in the field. For the 1995 Copala earthquake, both aftershock and slip areas (Courboulex *et al.*, 1997) are shown. We roughly estimated the aftershock area of the 1996 earthquake, using local, single-station, three-component seismograms at PNIG. This area is illustrated in Figure 1 by a contour of broken line. There is more uncertainty in the aftershock areas of 1965 and 1968 earthquakes which were estimated from seismograms at regional distances. Hence, these areas are also shown by broken contours. For pre-1965 events the figure only shows the epicenters; even these are poorly known. Due to uncertainty in the location of the large pre-1965 earthquakes, the recurrence periods of the events, especially in south east Guerrero, are also uncertain.

Seismic Recordings in and near the Epicentral Zone

The station PNIG, which, as mentioned earlier, was located near the epicentral region (Figures 1 and 2) and equipped with a broadband seismograph, an accelerograph, and a GPS receiver, played an important role in the analysis of the earthquake. There were seven other accelerographs in the region which recorded the event (Figure 2).

After a few seconds of recording, the data stream at PNIG was lost for ~ 4 hours. Much of the seismic data, including the mainshock accelerogram, were retrieved soon after communication was re-established. The broadband seismograms were clipped during the mainshock. Figure 3a shows acceleration, velocity, and displacement at PNIG (velocity and displacement were obtained from direct integration of the acceleration). The traces begin at the arrival of P wave. The displacements on NS, EW, and Z components, 25 s after P-wave arrival, are – 9.0, - 8.0, and - 8.0 cm, respectively.

Since 2011, the GPS network operated by the SSN has been reconfigured to transmit high-rate data in real time. At the time of the Ometepec-Pinotepa Nacional earthquake, the PNIG GPS permanent station had been recently set up, and the real-time processing scheme had not been yet implemented. We performed a high-rate post-processing of PNIG GPS data using Gipsy-Oasis software (Gregorius, 1996) to obtain displacement records. Figure 3b compares the displacement field obtained from double numerical integration of PNIG accelerographic records (continuous line) and from GPS 1 Hz data (red crosses). As can be seen, the GPS continuous stream failed for almost 1 minute, probably due to electrical supply failure. Displacement recovered by double numerical integration agrees well with that obtained from the GPS data in the first 10 s. The displacement field from double integration becomes unreliable after about 25 s which is manifested by the drift in the traces. After about 60 s, the displacements on

Table 1. Large, shallow earthquakes near the coast of Oaxaca and south east Guerrero (95-99°W) since 1900.

Date	Lat., °N	Lon., °W	Magnitude[1]	Segment
22/03/1928	15.67	96.10[2]	7.5[10]	East Oaxaca
17/06/1928	16.33	96.70[2]	7.8 (M^s?)	Central Oaxaca
04/08/1928	16.20	97.52[2]	7.4 (M^s)	West Oaxaca
09/10/1928	16.50	96.76[2]	7.6[10]	Cenyral Oaxaca
23/12/1937	16.79	98.63[3]	7.5[10]	Copala?
14/12/1950	16.81	98.82[3]	7.3[10]	Copala?
23/08/1965	16.28	96.02[4]	7.5[5]	East Oaxaca
02/08/1968	16.25	98.08[4]	7.3[5]	West Oaxaca
29/11/1978	16.03	96.67[5]	7.7[5]	Central Oaxaca
07/06/1982	16.35	98.37[6]	7.0[11]	Ometepec
07/06/1982	16.40	98.54[6]	6.9[11]	Ometepec
14/09/1995	16.48	98.76[7]	7.3[12]	Copala
25/02/1996	15.60	98.30[8]	7.1[12]	Offshore Pinotepa Nacional
20/03/2012	16.25	98.53[9]	7.5[12]	Ometepec-Pinotepa Nacional

[1] M_w unless otherwise specified; [2] Núñez-Cornú and Ponce (1989); [3] Nishenko and Singh (1987); [4] Quintanar (1985); [5] Chael and Stewart (1982); [6] Nava (1984); [7] Courboulex *et al*. (1997); [8] From local/regional data; [9] This study (see Table 2); [10] Anderson *et al*. (1989); [11] Astiz and Kanamori (1984); [12] Global CMT catalog (http://www.globalcmt.org).

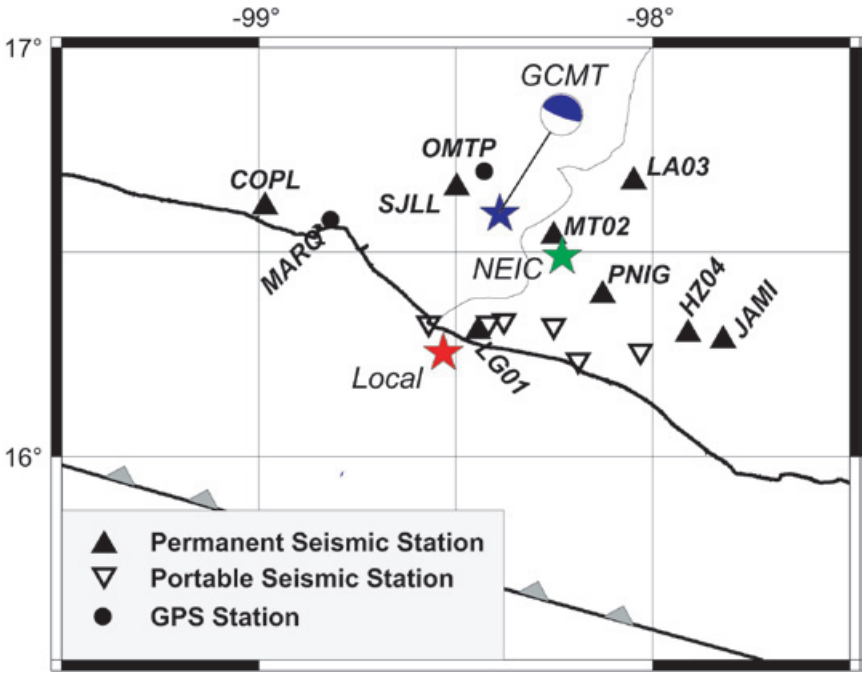

Figure 2. Black triangles: permanent seismic stations (equipped with accelerometers, except PNIG which is also instrumented with a broadband sensor and a GPS receiver). Inverted white triangles: portable seismic stations. Dots: autonomous GPS site. Stars: mainshock locations from local data (red) and from NEIC (green). The centroid location (blue star) and the associated focal mechanism are from GCMT.

NS, EW, and Z components from GPS data at PNIG are - 6.0, - 10.0, and - 5.0 cm (Figure 3b). For comparison, DeMets (personal communication, 2012) reports NS and EW coseismic static displacements at PNIG as - 8.8 and - 11.0 cm. We note that, for the SSN network, this is the first time that displacements retrieved from acceleration and from GPS data can be compared at the same site.

Acceleration and velocity time-histories at six other epicentral strong motion stations are illustrated in Figures 4 and 5, respectively. We note that *PGA* of ½ g was exceeded at two stations. At SJLL, the *PGA* on NS, EW, and Z components were 1070, 1070, and 1040 gal, respectively. This is the highest *PGA* ever recorded above Mexican subduction zone. High *PGA* at this station is clearly related to a site effect. An examination of the spectra shows a strong peak at 3.6 Hz. *PGA* at station LA03 reached 726 gal. Here again, the spectra are peaked at 6.5 Hz, suggesting a strong site effect. *PGA*, however, did not exceed ½ g at any firm strong-motion site, in agreement with previous observations along the Mexican subduction zone (Singh *et al.*, 1989). A relatively low *PGA* was recorded at PNIG which is also a firm site. The highest PGV (91 cm/s) was observed at LG01.

Mainshock Location

Locating the mainshock presented the usual difficulties associated with large events recorded at local distances. The SSN broadband network is relatively sparse. There were only 4 stations within a radius of 200 km of the epicenter. The broadband seismograms at PNIG and most other regional stations within a radius of ~300 km from the source were clipped on *S* wave. However, all SSN stations are equipped with accelerometers. We used accelerations (or velocities derived by simple integration) to read the *S* phase. We also used recordings from autonomous local and regional accelerographs [(*S*-*P*) time if absolute time was found to be incorrect]. It was difficult to read *S*-wave reliably on local stations. *P*-wave at PNIG clearly showed that the rupture initiated SW of the station. In the location of the earthquake, the azimuth of the hypocenter from PNIG (250°) was taken into account. The depth was fixed to 20 km as it is the typical depth of plate interface below the Mexican coast. A crustal model, modified from Iglesias *et al.* (2001), was used in the location of the mainshock and the aftershocks. The model consisted of three layers over a half space: layer 1, thickness = 5.2 km, V_s = 3.45 km/s, density = 2.68 gm/cm^3; layer 2, thickness = 10.5 km, V_s = 3.50 km/s, density = 2.70 gm/cm^3; layer 3, thickness = 5.2 km, V_s = 3.45 km/s, density = 2.84 gm/cm^3; half space, V_s = 4.45 km/s, density = 3.23 gm/cm^3. A Poisson solid was assumed to estimated V_p. Seismograms were converted to SeisAn format (Havskov and Ottemöller, 1999) and earthquakes were located using an algorithm by Lienert and Havskov (1995).

The locations of the mainshock obtained in this study and the one reported by NEIC, U.S. Geological Survey are listed in Table 2 and shown

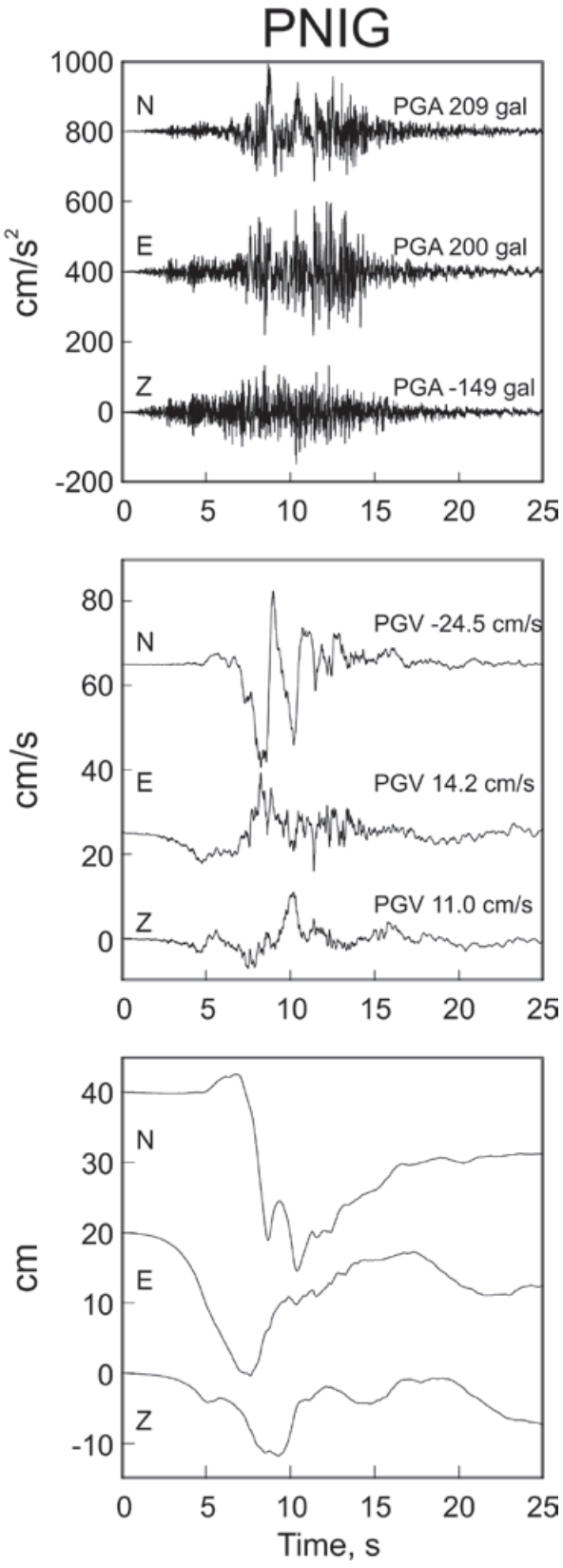

Figure 3. (a) Accelerations, velocities, and displacements at PNIG. (b) Comparison of displacement obtained from double integration (continuous line) and GPS data (crosses) at station PNIG. Note that GPS data was lost from 10 s to 60 s after the arrival of the *P* wave.

in Figure 2. The table also lists CMT solutions, including centroid depth, reported by several sources. We note that the NEIC location is 58 km to N40°E of the location from local/regional data.

Location of Aftershocks

We obtained preliminary epicenter locations of 458 aftershocks which occurred in the first 30 hours by reading azimuth and *P* and *S* times at PNIG. The depth was fixed at 20 km and the crustal model mentioned above was used in the location. The epicenters of the events are shown in Figure 6. As mentioned earlier, a network of seven portable digital seismographs was deployed in field (Figure 2). The network became operational about 30 hours after the mainshock. We located 1235 aftershocks which occurred during the next four days using data from 4 to 7 stations. These are shown in Figure 6. To check the accuracy of the epicenters of the early aftershocks based on PNIG only, we selected the largest 50 events which were recorded by the portable network and compared the locations with those determined from PNIG alone. The difference in the epicentral locations is about 10 km on average. The four-day aftershocks (beginning 30 hours after the origin time) roughly define a 50 km × 60 km area. This area is larger than the first 30-hour area which is about 40 km × 60 km, indicating expansion with time. Several clusters of aftershocks are visible in Figure 6. A lineament of aftershocks, oriented ~N45°E, occurs near PNIG. These clusters and the lineament may be related to bathymetric features on the subducted Cocos plate. We note, however, that they do not coincide with the subducted seamount chains.

Figure 6 shows the GCMT centroid epicenter and focal mechanism of the mainshock from the GCMT catalog. This location is near the north end of the aftershock area, perhaps related to the shift of the NEIC epicenter to north east of the epicenter estimated from the local and regional data. The figure also displays epicenters and focal mechanisms of all large aftershocks. The epicenters are from local and regional data while the focal mechanisms are from GCMT catalog. Most of these larger aftershocks are located at the edge of the aftershock area. The largest aftershock occurred on 2 April 2012 (H = 12 km; M_w6.1). It has a normal-faulting focal mechanism and is located in the overriding plate. It may have been causally related to the mainshock through stress interaction. An earthquake of similar mechanism occurred about 20 km NW of Acapulco, along the coast, near the town of Coyuca, on 8 October 2001 (M_w5.8). These events suggest that in situ stress in the upper plate near the coast in these regions is extensional, probably a consequence of tectonic erosion or trench roll back (Pacheco and Singh, 2010).

Figure 3b.

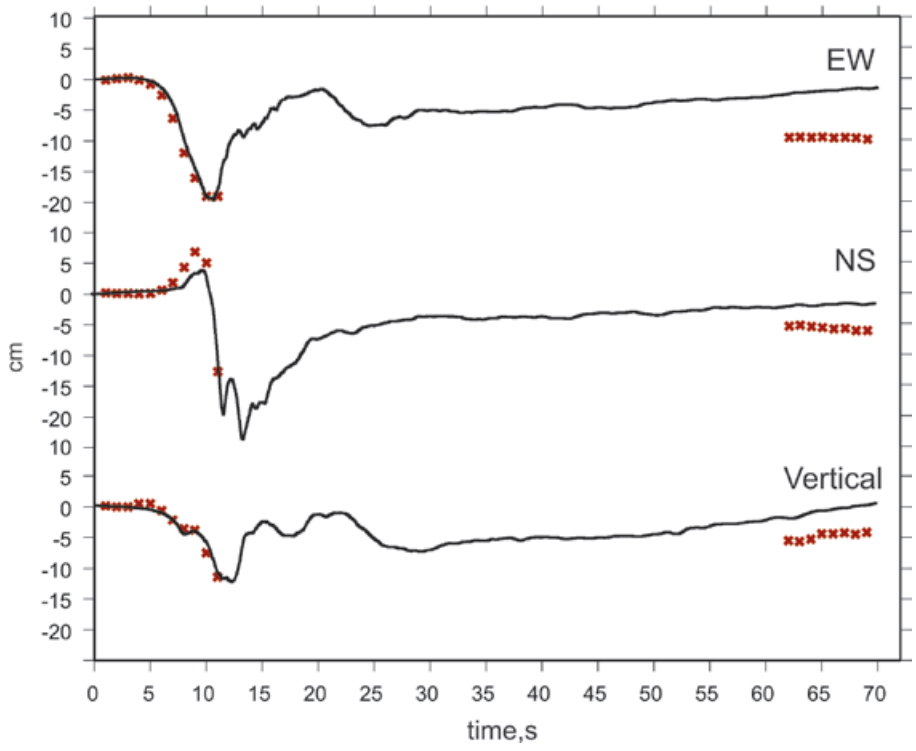

Figure 7 compares the aftershock areas of the 2012 earthquake estimated from 30-hour and seven-day activity, with that of seven-day aftershock area of the 1982 doublet (Nava, 1984). The areas roughly overlap. However, the sum of moments of the doublet (5.6×10^{19} Nm, Astiz and Kanamori, 1984) is only about 1/2 to 1/3 of the moment of the 2012 earthquake (1.3×10^{20} to 1.98×10^{20} Nm). It is possible that the 2012 event broke an area which was larger than the doublet area but included it, suggesting a variable rupture mode (Kanamori and McNally, 1982).

Table 2. Some source parameters of the 20 March 2012, Ometepec-Pinotepa Nacional earthquake.

Source Origin Time	Lat., °N	Lon., °W	*H*, km	Strike, °	Dip, °	Rake, °	M_0, Nm
This study 18:02:45.2	16.254	98.531	20*	-	-	-	-
Regional W-phase+	16.252	98.342	19	287	15	83	1.3×10^{20}
NEIC 18:02:48	16.662	98.188	20	-	-	-	-
USGS, CMT 18:03:14.00	16.822	97.990	21	289	12	78	1.8×10^{20}
USGS, W-phase CMT, 18:02:48.00	16.462	97.874	15	283	13	71	1.4×10^{20}
Global CMT 18:02:54.9	16.60	98.39	15.4	296	10	95	1.98×10^{20}

* Depth fixed.
+ Based on an algorithm implemented at Instituto de Geofísica, UNAM, which uses regional waveforms recorded on SSN broadband stations. The depth was fixed in the inversion and a grid search was performed for the centroid location.

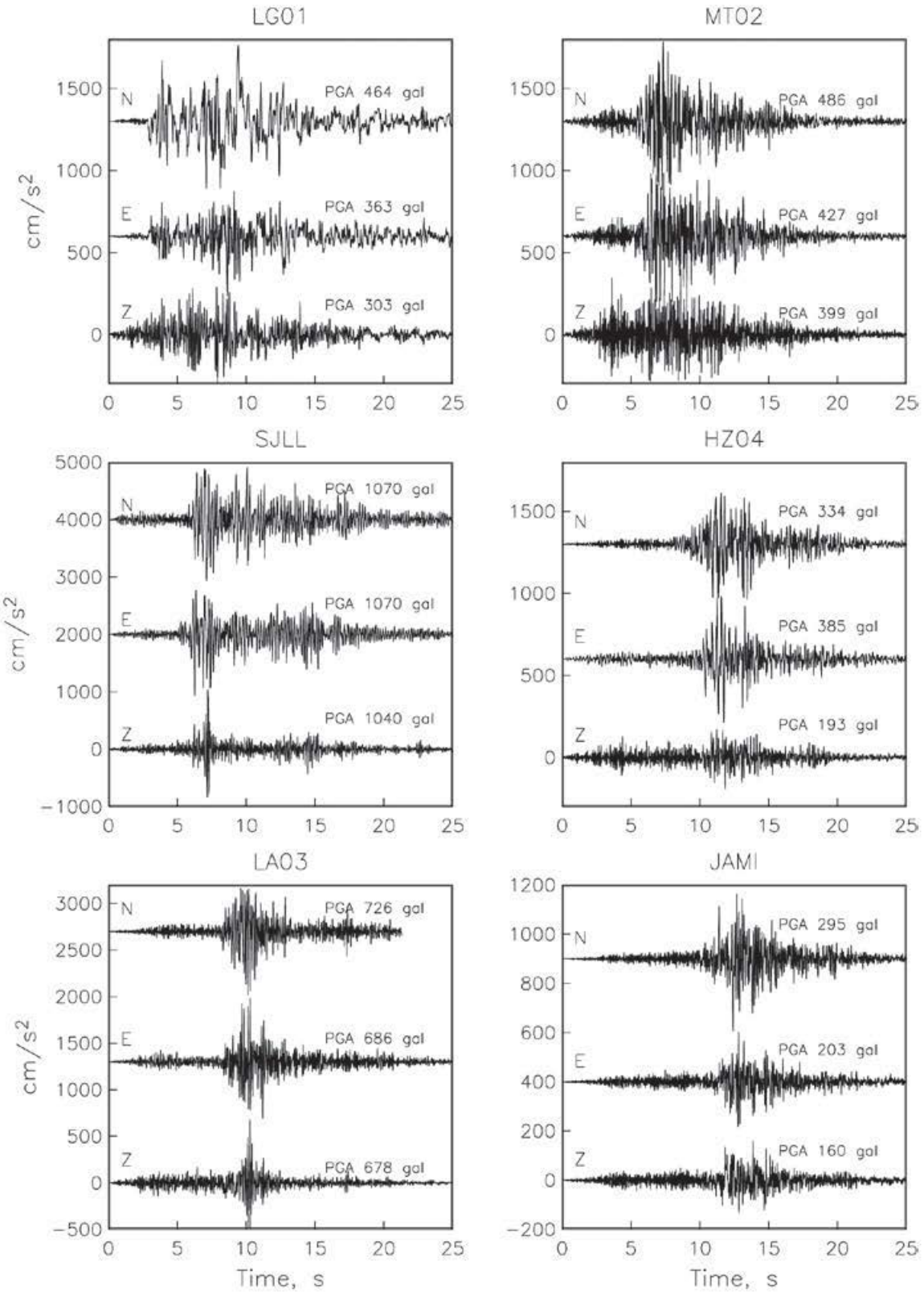

Figure 4. Accelerations at six other stations in/near the epicentral region.

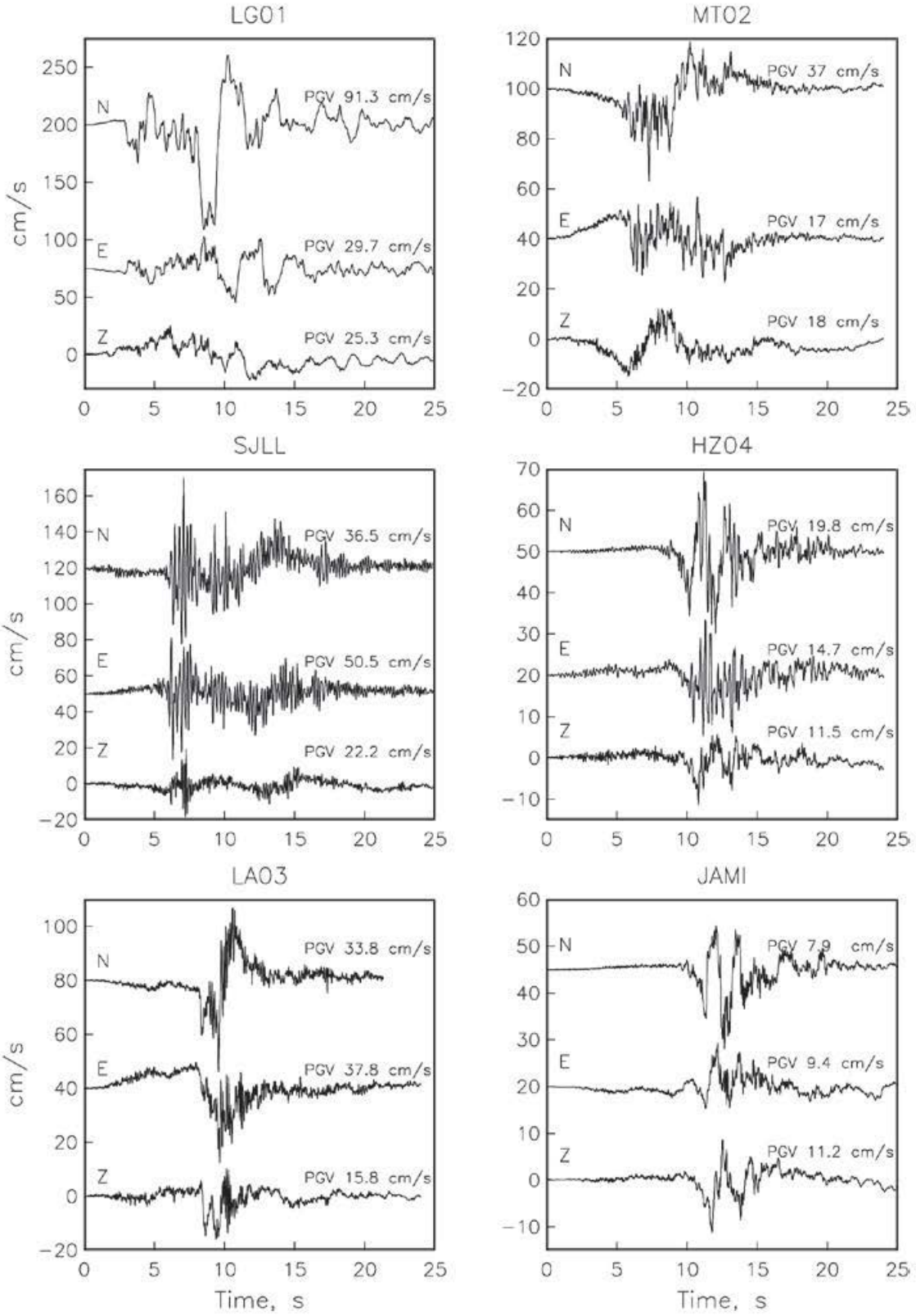

Figure 5. Velocities at the six stations in/near the epicentral region.

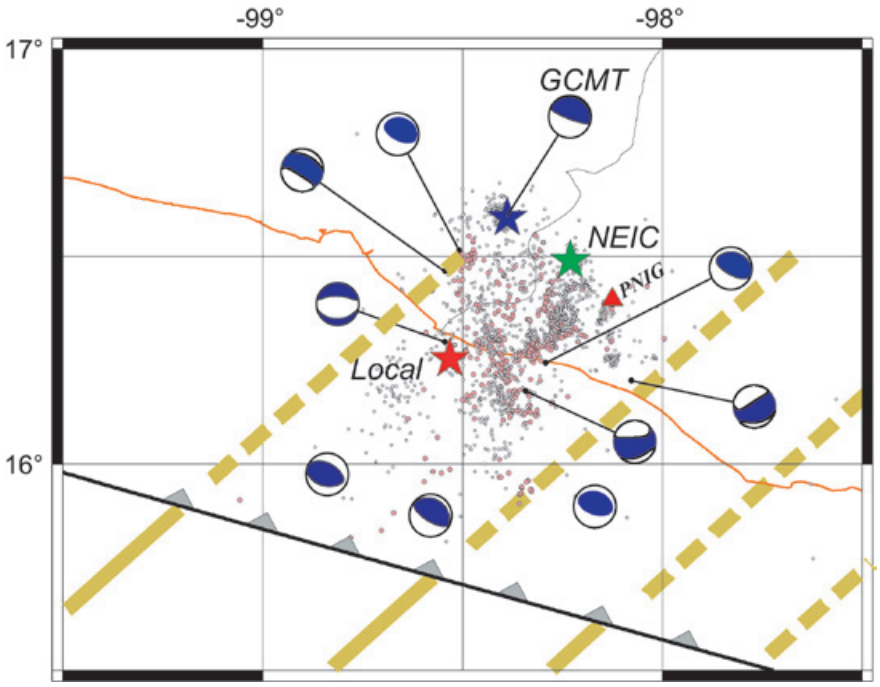

Figure 6. Aftershocks locations. Pink circles: first 30 hours; white circles: 4 days beginning 30 hours from origin time. Several concentrated patches and alignments of aftershocks are visible. Triangle: Permanent station PNIG. Stars: mainshock locations from local data (red), NEIC (green), and GCMT. The centroid location (blue star) and the associated focal mechanism are from GCMT. Focal mechanisms of all aftershocks listed in the GCMT catalog are plotted at their epicenters from local data. Parallel thick green lines: faults along seamount lineaments offshore (continuous) and their prolongation inland (dashed), taken from Kanjorski (2003).

Number of aftershocks

There was a general perception that the aftershocks activity following the 2012 earthquake was unusually intense. The number of aftershocks may be a reflection of the degree of heterogeneity on and near the fault plane. If there is a regional variation in the number of aftershocks then its knowledge is also useful to civil protection authorities. Thus, it is important to know whether the number of aftershocks of the 2012 event was truly large or only a subjective perception. The SSN network has been undergoing expansion and improvement. For this reason, it is not possible to compare the statistics of aftershocks of this earthquake with those of previous large events based on the SSN catalog. Therefore, we used U. S. Geological Survey Earthquake Data

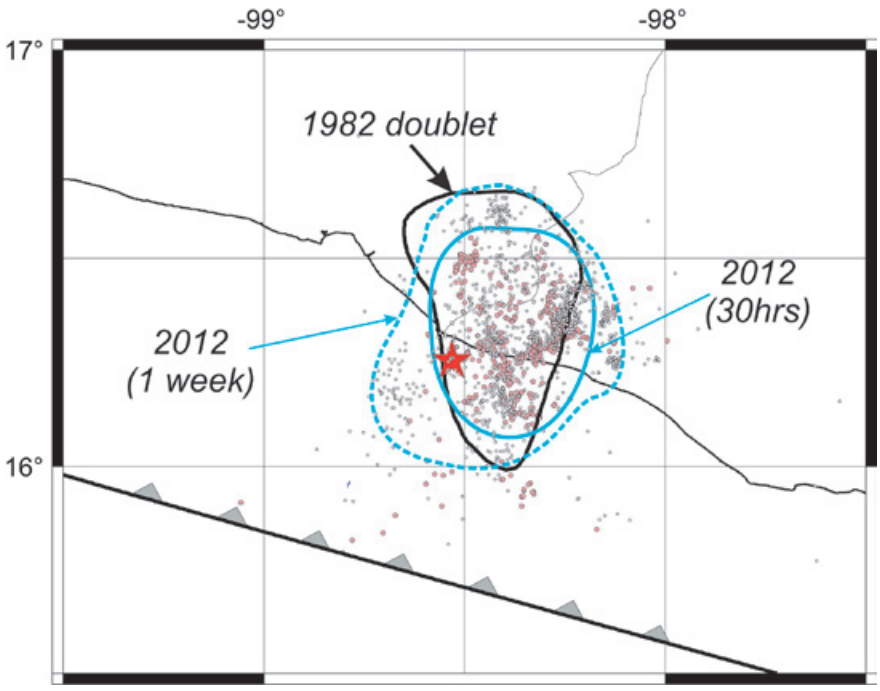

Figure 7. Location of thirty-hour (pink circles) and seven-day aftershocks (circles) of the 2012 earthquake. Continuous and dotted blue contours outline the 30-hour and seven-day estimated aftershock area. For comparison, one-week aftershock area of the 1982 doublet (Nava, 1984) is also shown (black contour). Red star denotes the epicenter location.

Base (http://earthquake.usgs.gov/earthquakes/eqarchives/epic/epic_rect.php). For our analysis, we isolated aftershocks of all shallow, thrust events with $M_w \geq 6.9$ which occurred along the Mexican subduction zone, from Jalisco-Colima to Oaxaca, beginning 1963 when the World-Wide Standard Seismograph Network became operational. The database lists body-wave magnitude, m_b, of small and moderate earthquakes and M_s or M_w for large earthquakes. For many, recent moderate earthquakes M_w rather than m_b is listed. For each earthquake we extracted seismicity during the next 30 days in an area which was chosen to be somewhat larger than the expected rupture area. Table 3 gives $N(m_b)$, where N is the number of events with magnitude $\geq m_b$. N is listed for m_b = 4.5 and 5.0. The number includes the mainshock. M_w of moderate earthquakes is taken as m_b. The catalog is probably complete for $m_b \geq 5.0$. Events 5 and 10 in Table 3 are doublets. For these events the 30-day period was counted from the second shock. The seismic moments of the two shocks were added before computing M_w which is listed in the table.

Figure 8a shows the location of the mainshocks. The plot of $N(m_b \geq 5)$ versus M_w of the mainshock is illustrated in Figure 8b. To quantify the lack or access of aftershocks, we assume that $N \alpha A$, where A is the rupture area (Singh and Suárez, 1988). Since $M_w \alpha (2/3)\log M_0 \alpha \log A$, it follows that if $N \alpha A$ then $\log N \alpha M_w$. N versus M_w data is fitted with $\log N = M_w + C$. The line defined by this relation, shown in Figure 8b, serves to measure lack or excess of aftershocks for the earthquakes listed in Table 3. The figure shows that events 1 and 5 (Colima-Jalisco 1995 and Michoacán 1985) were the two most deficient ones in the production of aftershocks, while events 11 and 12 (Offshore Pinotepa 1996 and Ometepec-Pinotepa Nacional

Table 3. Number of aftershocks of large, shallow, thrust earthquakes along the Mexican subduction zone (modified from Singh and Suárez, 1988).

Event No.	Segment	Date (d/m/y)	Lat., °N Lon., °W	Depth, km	M_0, 1020 Nm	M_w	Observed N 30-day period) $m_b \geq 4.5$	$m_b \geq 5.0$
1	Colima-Jalisco	06/10/1995	18.8 104.5[a]	15[b]	11.50[b]	8.0	15	5
2	Tecomán, Colima	22/01/2003	18.63 104.13[c]	26[b]	2.05[b]	7.5	5	3
3	Colima	30/01/1973	18.39 103.21[d]	31[d]	3.00[d]	7.6	4	3
4	Colima-Michoacán	30/04/1986	18.25 102.92[b]	21[b]	0.31[b]	6.9	5	1
5	Michoacán	19/09/1985	18.14 102.71[e]	17[f]	10.05[f]	8.1	15	5
		21/09/1985	17.62 101.82[e]	22[f]	2.90[f]			
6	Playa Azul	25/10/1981	17.75	27[f]	0.70[b]	7.2	5	3
7	Petatlán	14/03/1979	17.46 101.46[h]	20[i]	2.70[i]	7.6	12	6
8	San Marcos	25/04/1989	16.6 99.5[j]	15[b]	0.24[b]	6.9	3	2
9	Copala	14/09/1995	17.0 99.0[k]	22[b]	1.31[b]	7.3	9	2
10	Ometepec	07/06/1982	16.25 98.34[l]	20[m]	0.29[m]	7.1	10	3
		07/06/1982	16.32 98.45[l]	10-15[m]	0.27[m]			
11	Off-shore Pinotepa	25/02/1996	15.60 98.30[n]	15[b]	0.55b	7.1	23	7
12	Ometepec-Pinotepa	20/03/2012	16.254 98.531[n]	20[n]	1.98[b]	7.5	44	14
13	W. Oaxaca	02/08/1968	16.25 98.08[o]	21[i]	1.00[i]	7.3	5	3
14	C. Oaxaca	29/11/1978	16.03 96.67[p]	18[i]	3.2[i]	7.6	19	6
15	E. Oaxaca	23/08/1965	16.28 96.02[o]	25[i]	1.7[i]	7.4	4	3

[a] Pacheco *et al*. (1997); [b] Global CMT catalog (http://www.globalcmt.org); [c] Singh *et al*. (2003); [d] Reyes *et al*. (1979); [e] UNAM Seismology Group (1986); [f] Astiz *et al*. (1987); [g] Havskov *et al*. (1983); [h] Valdés-González and Novelo (1998); [i] Chael and Stewart (1982); [k] Courboulex *et al*. (1997); [l] Nava (1984); [m] Astiz and Kanamori (1984); [n] This study; [o] Quintanar (1985); [p] Singh *et al*. (1980).

2012) were the two most prolific ones. The relative abundance of aftershocks and simplicity of large earthquakes as seen in the region of the study may reflect both a relative abundance of heterogeneities at small scale but smooth fault plane at larger scale.

Slip on the Fault from Inversion of Teleseismic Data

Immediately after the earthquake, teleseismic body and surface waves were inverted to map slip on the fault by groups at NEIC and Caltech (http://earthquake.usgs.gov/earthquakes/eqinthenews/2012/usc0008m6h/finite_fault.php; http://www.tectonics.caltech.edu/slip_history/2012_Mexico/index.html). These inversions use the NEIC hypocenter (16.662°N, 98.188°W, H = 20 km; Table 2). The results show a compact, nearly circular source whose dimension can be approximated by a square area of 35 km × 35 km. As a consequence of using the NEIC hypocenter, in these inversions the slip patch is located well inland, far north from our epicenter. Here we use the same simulated annealing, wavelet domain algorithm used by NEIC (Ji *et al.*, 2002a,b) to invert teleseismic body and surface waves for the slip on the fault plane. We use an expanded data set compared to the one used for the rapid solution by USGS: a total of 29 *P*-waves, 15 *S*-waves, 30 Rayleigh waves and 20 Love waves. We use the hypocenter determined in this study (Table 2). We invert for the magnitude, direction and duration of slip at each subpatch of the fault. The slip-rate function of each fault is parameterized by an asymmetric cosine function (Ji *et al.*, 2002a). The timing of the initial slip is constrained to follow a rupture velocity of 3 km/s. First the body-wave arrivals were aligned on theoretical travel times based on a 1D Earth model. However, we found large apparent time shifts between observed and calculated seismograms, caused by the 3D structure of the Earth. The systematic variation of these shifts with azimuth is probably also responsible for the large mislocation of the hypocenter by global agencies, mentioned above. To minimize the effect of unmodeled 3D

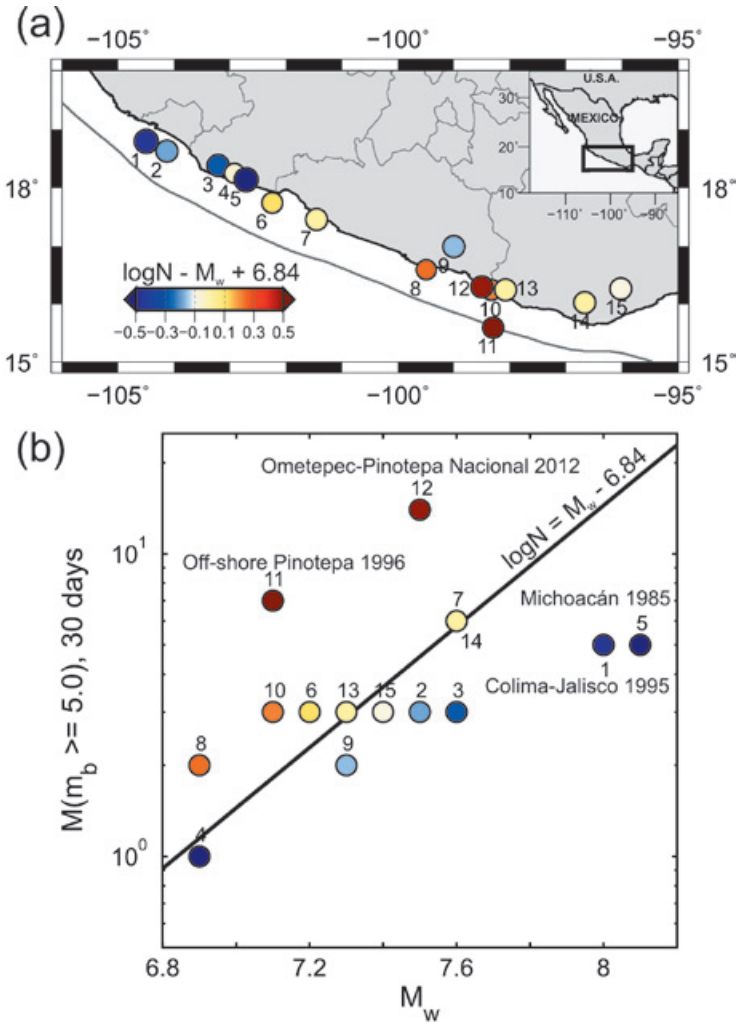

Figure 8. (a) Location of large shallow thrust earthquakes along the Mexican subduction zone whose one-month aftershocks (m_b ≥ 4.5 and ≥ 5) are studied in the paper. The numbers are keyed to event number in Table 3. (Right) $N(m_b > 5)$ versus M_w. The excess and deficiency of aftershocks can be estimated with respect to the straight line log$N$ = M_w - 6.84 (see text). Note that events 12 (2012, M_w7.5) and 11 (1996, M_w7.1) produced the two most and events 1 (1995, M_w8.0) and 5 (1985, M_w7.6) generated the least amount of aftershocks.

structure on the result, we manually aligned the body-wave phases on the first observable arrival in the seismogram. At stations where we could not identify the first arrival, we aligned them to be consistent with neighboring stations. The alignment of the traces is a difficult task as the first arrivals are small relative to the noise level at many stations. Furthermore, comparing the teleseismic waveforms to the ones observed locally we found that the initial weak rupture (see more detail in the following section) was not seen in any of the teleseismic records. To account for this small initial slip near the hypocenter, we shifted all the traces by two seconds. The distribution of slip on the fault plane determined by the inversion is shown in Figure 9a. There are two separate regions of slip, both to the East of the hypocenter, one updip and the other one downdip. Each area of slip is about 30 km in diameter and a maximum slip of almost 2 m. It should be emphasized that this is a preliminary solution and that the pattern depends critically on the alignment of the body waves. The solutions we obtained using unaligned seismograms, as well as aligned but not shifted by a constant, have one patch of slip to the north of the hypocenter, similar to the solutions of the groups at NEIC and Caltech. The shift of two seconds is what allows the rupture to get further from the hypocenter before the large slip occurs, in effect allowing two different slip patches. Allowing a much smaller rupture velocity at the beginning could alter this result. However, we note that the two-patch slip model predicts static displacements that are in better agreement with those observed at nearby GPS stations than the one patch model and it is also in better agreement with the slip model obtained from regional data (following section).

Slip on the Fault from Inversion of Near-Source Data

We inverted the near-source band-pass filtered displacement traces to map the slip on the fault. Because the times at some accelerographs were incorrect, we corrected them using the computed expected *P* arrival times. The accelerograms were baseline corrected, integrated to obtain velocities, and they were then bandpass filtered (0.025 - 1.0 Hz). These traces were integrated to obtain the displacements. The data at station HZ04 were ignored since the traces at nearby JAMI station (Figure 2) were of much better quality. From a visual inspection of the integrated traces and preliminary results of the inversion, we rejected the vertical displacement seismograms for LG01, SJLL, and LA03 stations (dashed lines in Figure 10).

We assumed that the faulting was confined to a 90 km × 90 km area (Figure 7) which has an azimuth = 295°, dip = 13°, and rake = 91°, in rough accordance with the GCMT solution. This area was divided in 18 × 18 subfaults. The

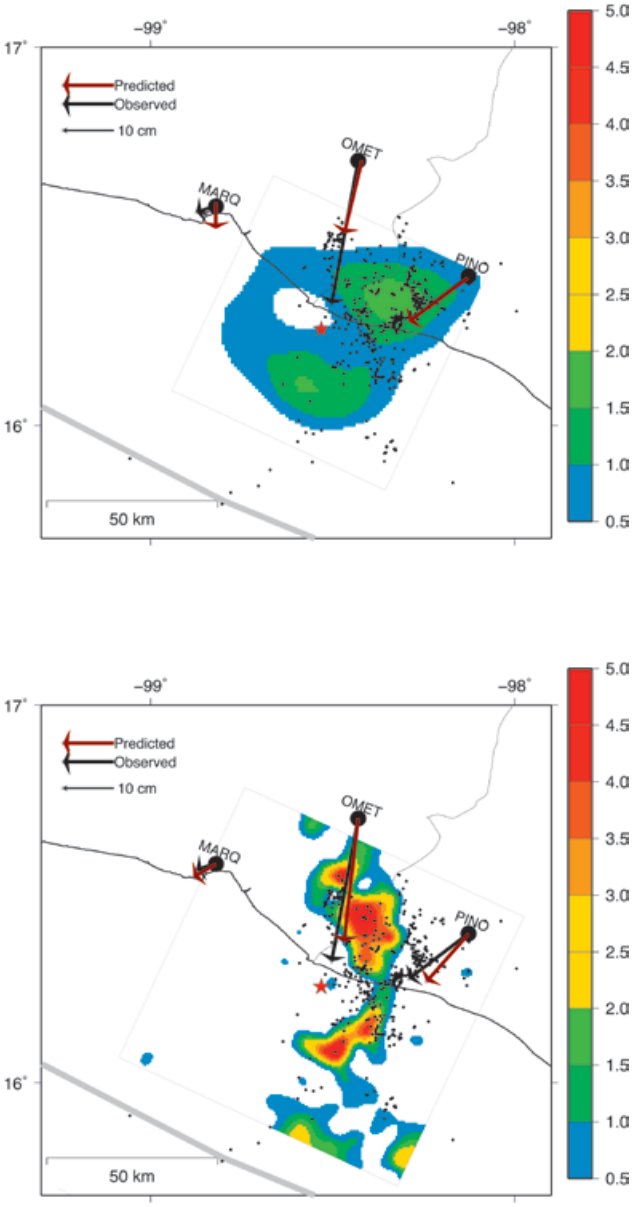

Figure 9. Inversion of slip on the fault using (top) teleseismic body- and surface-wave displacements, (bottom) local band-pass filtered (0.025-1.0 Hz) displacements (see text). Star: mainshock epicenter from local data. Black dots: 30-hour aftershocks. Note that both models indicate that little slip occurred near the hypocenter and the aftershock activity was relatively low near areas of large slip. Arrows show observed and predicted coseismic horizontal displacement vectors

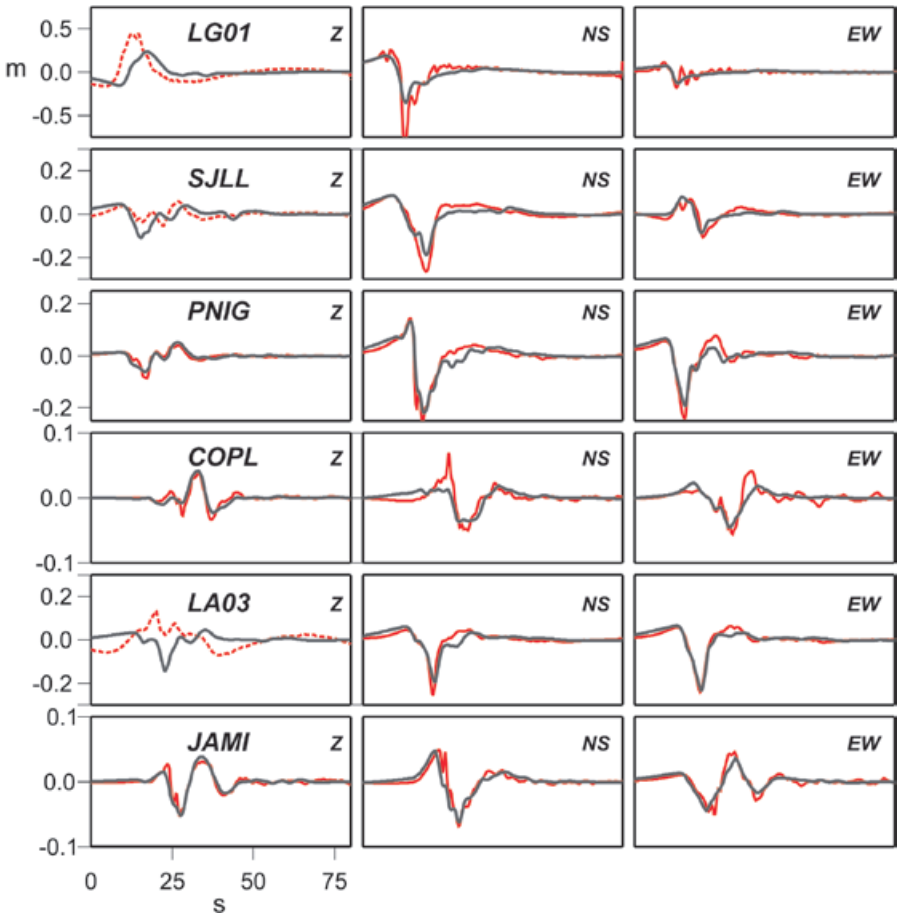

Figure 10. Observed displacement seismograms used in the near-source inversion (red lines) and the corresponding synthetics (gray lines). Some components were neglected in the inversion because of their poor quality (dashed red lines).

depth of the fault at the hypocenter (16.254°N, 98.531°W) was 20 km. The inversion was performed in the frequency domain (Cotton and Campillo, 1995) using a simulated annealing inversion scheme (Iglesias *et al.*, 2002). The displacement spectrum, $u_i(\omega)$, at the i^{th} station can be written as

$$u_i(\omega) = \sum_{k=1}^{n} s_k e^{-i\omega t_k} g_{ki}(\omega)\ F_k[R_k, \omega], \quad (1)$$

where n is the number of subfaults; t_k, the rupture time (time elapsed from origin time to the initial rupture for each subfault); S_k, the average displacement for k^{th} subfault; $g_{ki}(\omega)$, the displacement transfer function for unitary slip in the k^{th} subfault recorded at the i^{th} station; and $F_k[R_k, \omega]$, the source time function depending on rise time R_k. Following Hernandez *et al.* (2001), we chose

$$F_k[R_k, \omega] = \frac{\pi R_k}{4 \sinh\left(\frac{\pi \omega R_k}{4}\right)}. \quad (2)$$

We attempted to invert for R_k. However, after several tests we found that R_k could not be resolved. Thus, in further inversions we fixed R_k = 1.7 s.

Synthetic seismograms for each subfatult to each station were computed using discrete wave number algorithm (Bouchon, 1982). The crustal model used in the inversion is given above. We took Q_s = 350 and Q_p = 600.

The differences between observed and synthetic spectra (real and imaginary parts) were minimized at all the discrete frequencies between 0.025 and 1.0 Hz. Each subfault was composed of 49 source points whose rupture was delayed in time by assuming a constant rupture velocity (V_r = 3.0 km/s). The details of the method are given in Hernandez *et al.* (2001) and Iglesias *et al.* (2002).

The result of the inversion is shown in Figure 9b and the observed and synthetic waveforms are illustrated in Figure 10. The fit is reasonable. The inversion yields a seismic moment of 1.1×10^{20} Nm (M_w7.3). The observed coseismic static

displacements at PINO (the same station as PNIG), OXTP, and MRQL (Figure 2) were not used in the inversion. Thus, it is reassuring that the predicted static horizontal displacements at these stations, corresponding to the inverted slip, agree well with the observations (Figure 9b).

The inversion shows small slip near the hypocenter. Large slip occurs on two patches: one patch is located updip from the hypocenter towards the south-east while the other one is located downdip towards north. Significant slip is confined within an area of ~25 km × 60 km (1500 km^2). The static stress drop, $\Delta\sigma$, during the earthquake can be estimated from the relation $\Delta\sigma = (1/2)\ (7\pi^{3/2}/16)\ (M_0/A^{3/2})$ where A is the fault area (Eshelby, 1957). With $M_0 = 1.98\times10^{20}$ Nm and A = 1500 km^2, we obtain $\Delta\sigma$ = 4.3 MPa.

Back-projection source imaging using teleseismic *P* waves recorded at USArray in northeast USA shows a dominant westward rupture propagation (L. Meng and J. P. Ampuero, personal communication, 2012). This network, however, has no resolution to detect along dip rupture propagation, which we find to be the dominant direction of rupture (Figure 9).

From Figure 9b we note that the aftershock activity is relatively low in areas of large slip. Do the two patches correspond to the individual events of the 1982 doublet? Comparison of the doublet epicenters (Figure 1) with the two patches (Figure 9b) does not support this. However, the errors in the locations of the 1982 doublet are probably too large to reach a definitive conclusion.

Radiated Seismic Energy

Seismic moment, M_0, and radiated seismic energy, E_s, are the two basic source parameters of an earthquake. We computed E_s of five recent, large, earthquakes in the region using teleseismic *P*-wave recordings following the method of Boatwright and Choy (1986). The estimate of the energy flux was obtained from the integral of the squared velocity spectrum of the *P*-wave group (*P*, *pP*, and *sP* waves), corrected for attenuation and site effect (Pérez-Campos, 2002; Pérez-Campos *et al.*, 2003). The total *P*-wave energy was then estimated using covariance-weighting least squares (Pérez-Campos and Beroza, 2001), and correcting for geometrical spreading and radiation pattern. We used q = 15.58 (Boatwright and Choy, 1986), the partitioning between *S*- and *P*-wave energy, to estimate the total radiated seismic energy. Table 4 lists E_s and E_s/M_0 values of the 2012 and other earthquakes in the region. We note that E_s/M_0 of the 1996 and 1997 earthquakes, both located off-shore, near the trench (Figure 1), are an order of magnitude smaller than for the other three events which broke the plate interface further downdip (Figure 11). These earthquakes, like some other events near the trench of the Mexican subduction zone, also gave rise to unusually low *PGA* (Iglesias *et al.*, 2003). Low E_s/M_0 is typical of near-trench earthquakes (e.g., Lay *et al.*, 2012).

Rupture areas of most large Mexican subduction zone earthquakes straddle the coast, seldom reaching the trench. Those that do (e.g., 1995 Colima-Jalisco, M_w8.0 earthquake) may cause large tsunami. Thus, for tsunami mitigation, it is critically important to know the state of seismic coupling on the updip part of the plate interface. Certainly, there is evidence of near-trench coupling off-shore Pinotepa and Colima-Jalisco. The great 1787 Oaxaca earthquake (M~8.4 - 8.6), which produced the largest historically documented tsunami in Mexico (Núñez-Cornú *et al.*, 2008; Suárez and Albini, 2009), suggests that a significant length of near-trench interface in the region may be capable of strain accumulation. The interface may rupture in moderate M6.5-7.0 earthquakes (as in the case of 1997 and 1996 events) and, occasionally, during great earthquakes when several asperities break in one single episode (1787 event).

Table 4. Radiated seismic energy, E_s, and E_s / M_0 of the 2012 and other large earthquakes in the region.

Earthquake	M_0, Nm	E_s	E_s / M_0	M_w / M_S
24/10/1993	1.01×10^{19}	3.29×10^{14}	3.26×10^{-5}	6.6 / 6.6
14/09/1995	1.31×10^{20}	1.54×10^{15}	1.18×10^{-5}	7.3 / 7.2
25/02/1996	5.55×10^{19}	1.84×10^{14}	3.34×10^{-6}	7.1 / 6.9
19/07/1997	1.19×10^{19}	3.86×10^{13}	3.24×10^{-6}	6.7 / 6.3
20/03/2012	1.98×10^{20}	6.16×10^{15}	3.11×10^{-5}	7.5 / 7.6

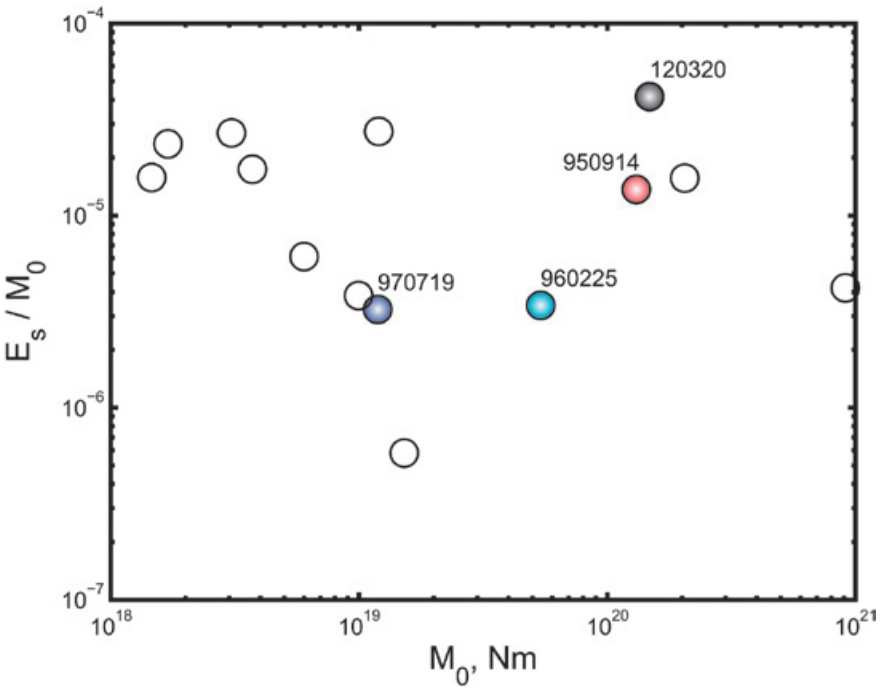

Figure 11. E_s/M_0 versus M_0 plot of shallow, thrust earthquakes along the Mexican subduction zone. Earthquakes of the region of interest are identified by their dates. E_s has been estimated from teleseismic *P* waves.

Observed and Predicted Ground Motions in Mexico

Prediction of ground motions from future earthquakes is critically important in seismic hazard analysis. Although first accelerographs in Mexico date back to 1962, it was not until 1985 that a modern accelerographic network, called the Guerrero Accelerograph Array, became operational (Anderson *et al.*, 1994). This network covered the coastal region of Guerrero and part of Michoacán. It also included a few stations inland and an attenuation line from the Guerrero coast to Mexico City. The 1985 Michoacán earthquake was well-recorded by this newly-installed network. Since 1985, strong-motion stations in Mexico have steadily increased in number. The data have been used to develop ground motion prediction equations (GMPE).

The recordings from the 2012 earthquake permit a check on the GMPE for interface earthquakes (Arroyo *et al.*, 2010). Figure 12 shows plots of observed and predicted *PGA* at hard sites as a function of R_{rup}, *the closest distance from the site to the rupture area*. Here $PGA = [(A_n^2 + A_e^2)/2]^{1/2}$ (A_n and A_e are the peak accelerations on NS and EW components, respectively). The predictions are reasonable for $R_{rup} < 400$ km, beyond which they underestimate the observations. This is expected since only data at distances of $R_{rup} < 400$ km were used by Arroyo *et al.* (2010) in the regression analysis. In any case, ground motions at such large distances are of little importance in earthquake engineering.

Figure 13 shows *PGA* contours in Mexico for the 2012 earthquake. These contours were obtained from recorded data (shown by triangles) using a Bayesian interpolation technique. We note that the maximum contour roughly coincides with the maximum slip on the fault (Figure 9). Figure 13 also shows municipalities where significant structural damage was observed. These municipalities received federal funds for recovery and reconstruction of the affected population (http://dof.gob.mx/nota_detalle.php?codigo=5241891&fecha=03/04/2012; http://dof.gob.mx/nota_detalle.php?codigo=5241892&fecha=03/04/2012).

Ground Motion in Mexico City

The 2012 earthquake was strongly felt in Mexico City. Initially it was thought that the city had survived well the onslaught of the largest earthquake since 1985. Figure 14 compares accelerograms and Fourier spectra of the 2012 (M_w7.5) and the 1995 Copala (M_w7.3) earthquakes at CU, a hill-zone site in city. Figure 15 illustrates the corresponding plots at SCT, a site in the lake-bed zone. The distance from the two sources to Mexico City is roughly equal. The *PGA*s during the two earthquakes at each of these sites are nearly the same (Tables 5 and 6). The same is true for Fourier amplitude spectra at frequencies greater than about 1 Hz. At lower frequencies, the Fourier amplitudes of the 2012 earthquake are somewhat greater than of the 1995 event, in agreement with their relative moment magnitudes.

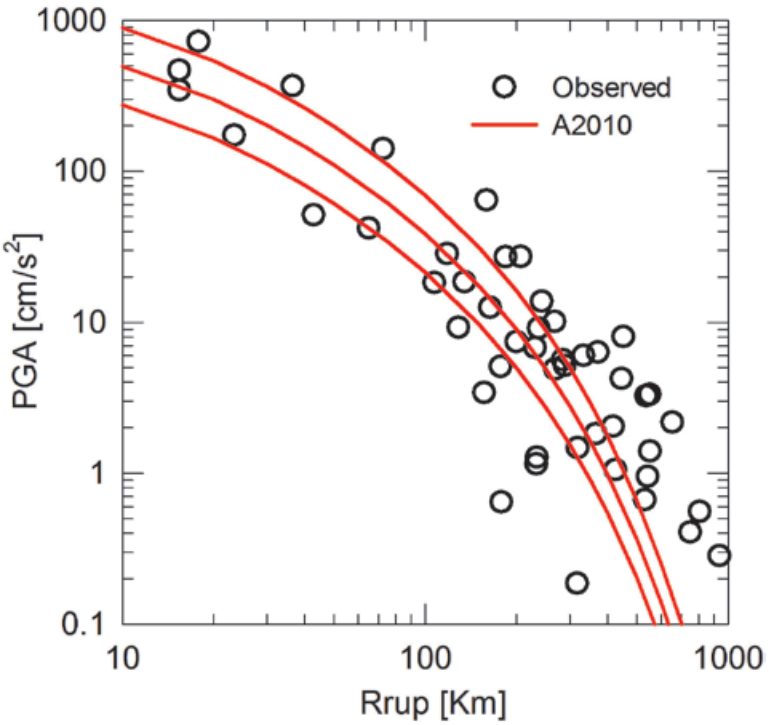

Figure 12. Observed (circles) and predicted (red lines) *PGA* values for 14, 50 and 84 percentiles versus R_{rup}, the closest point on the rupture surface. Predictions are from Arroyo *et al.* (2010).

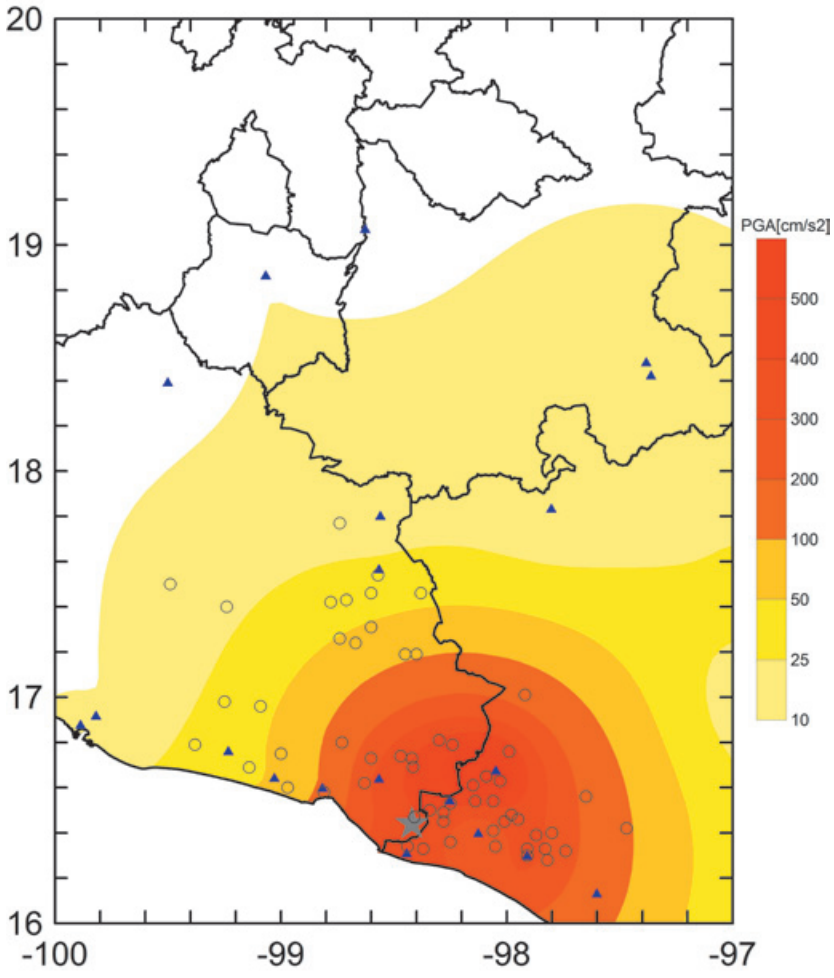

Figure 13. *PGA* contours. Star: center of maximum slip (Figure 9). Triangles: location of accelerographic stations on hard sites. Open circles: municipalities where significant structural damage was observed.

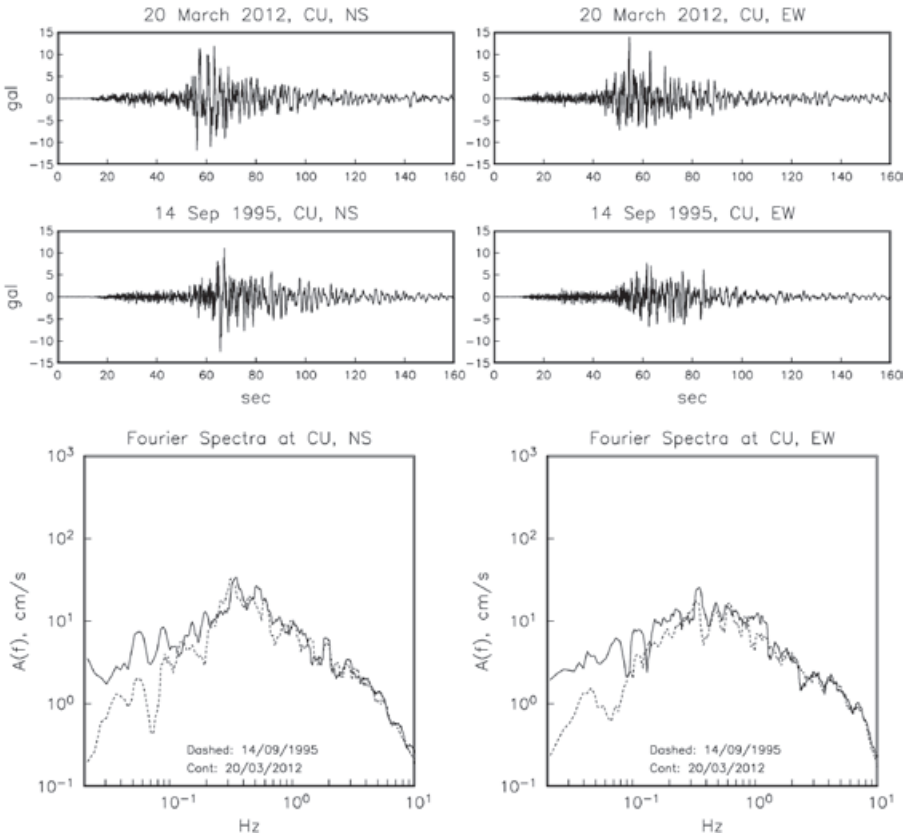

Figure 14. Comparison of accelerograms and Fourier spectra of the 2012 Ometepec-Pinotepa Nacional (M_w7.5) and the 1995 Copala (M_w7.3) earthquakes at CU, a typical hill-zone site.

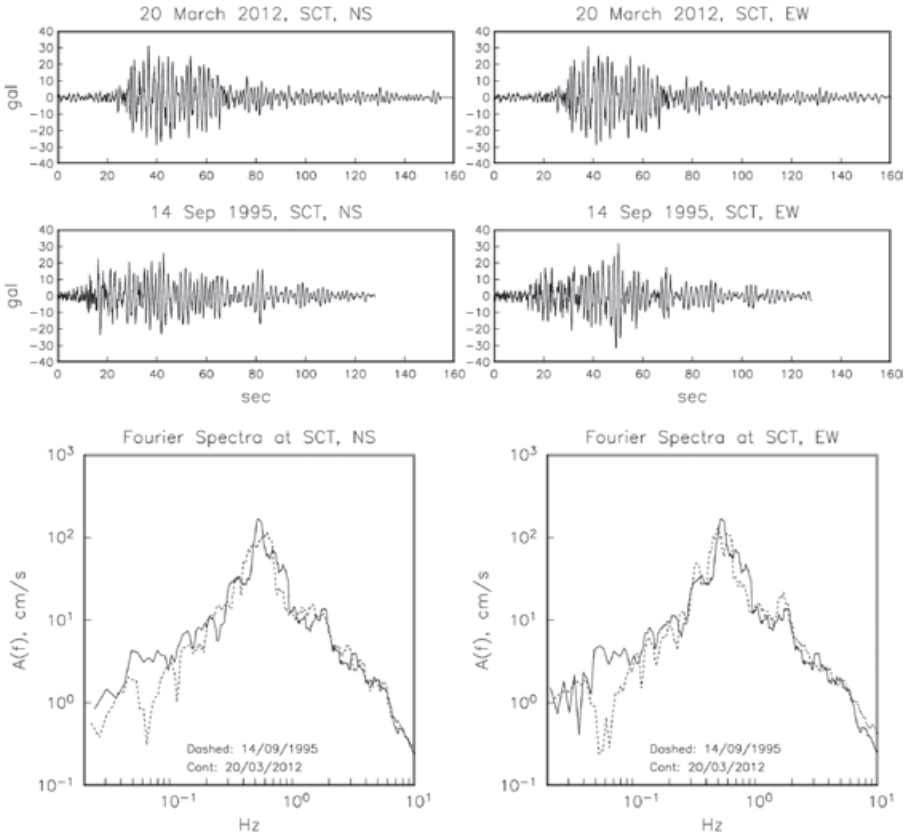

Figure 15. Same as Figure 13 but at SCT, a site in the lake-bed zone.

Table 5. Ten earthquakes with largest recorded *PGA* at CU, a site in the hill zone of Mexico City, during the period 1985-2012 listed in descending order. Local earthquakes are excluded.

Date	Lat., °N	Lon., °W	*H*, km	M_w	R to CU, km	*PGA*, gal	Type#
19/09/1985	18.14	102.71	22	8.0	395	29.8	T
11/12/2011	17.82	99.94	57	6.4	194	19.2	IS
21/09/1985	17.62	101.82	22	7.5	338	13.9	T
21/07/2000	18.11	98.97	50	5.8	146	12.8	IS
20/03/2012	16.25	98.53	20	7.5	317	12.0	T
25/04/1989	16.58	99.48	17	6.9	307	11.9	T
15/06/1999	18.13	97.54	60	6.9	226	11.6	IS
14/09/1995	16.73	98.54	22	7.3	297	10.3	T
22/05/2009	18.10	98.43	46	5.8	160	8.6	IS
30/09/1999	16.03	96.96	40	7.4	437	7.8	IS

T: Shallow subduction thrust earthquake
IS: Intraslab earthquake

Table 6. Ten earthquakes with largest recorded *PGA* at SCT, a site in the lake-bed zone of Mexico City, during the period 1985-2012 listed in descending order. Local earthquakes are excluded.

Date	Lat., °N	Lon., °W	*H*, km	M_w	*R* to CU, km	*PGA*, gal	Type#
19/09/1985	18.14	102.71	22	8.0	395	132.1	T
25/04/1989	16.58	99.48	17	6.9	307	38.8	T
20/03/2012	16.25	98.53	20	7.5	317	34.2	T
15/06/1999	18.13	97.54	60	6.9	226	30.0	IS
14/09/1995	16.73	98.54	22	7.3	297	29.5	T
30/09/1999	16.03	96.96	40	7.4	437	28.9	IS
11/12/2011	17.82	99.94	57	6.4	194	20.8	IS
22/01/2003	18.63	104.13	10	7.4	537	19.8	T
21/07/2000	18.11	98.97	50	5.9	136	18.8	IS
10/12/1994	17.98	101.52	49	6.4	288	13.4	IS

T: Shallow subduction thrust earthquake
IS: Intraslab earthquake

Ten earthquakes which have produced largest *PGA* at CU since 1985 are listed in Table 5. *PGA* during the 2012 earthquake is 12.0 gal, the fifth largest in the table. Annual exceedance rate of 10 gal is about 0.3. We note that eight out of the 10 events gave rise to roughly similar *PGA*, between 8 and 14 gal. Thus, the 2012 earthquake was not exceptional in terms of *PGA*. Note that the *PGA* at CU during the 1985 earthquake was 30 gal, two and half times greater than during the 2012 event.

Table 6 is similar to Table 5 but for SCT. *PGA* at SCT during the 2012 earthquake was 34 gal, which is the third largest in the table. Annual exceedance rate of 20 gal at this site is about 0.3. During five out of the 10 events the *PGA* at SCT was between 29 and 39 gal. Again, the *PGA* at SCT during the 2012 earthquake was not exceptionally large (roughly four times less than during 1985 earthquake).

A Possible Interpretation

The 2012 Ometepec-Pinotepa Nacional earthquake may be understood as a single event in a stochastic process:

Stress accumulation→ Quiescence→ EARTHQUAKE→ Stress drop→ Regional deformation→ Aftershock sequence→ Stress accumulation→ Quiescence→ EARTHQUAKE→ Stress drop→ Regional deformation→ Aftershock sequence→…

where time runs from left to right, and the embedded process of stress accumulation shifts its localization at random (Castaños *et al*., 2013). Causality appears to require a different process which, however, never happens:

Stress accumulation→ Foreshock sequence→EARTHQUAKE→Stress drop→Regional deformation→ Quiescence→ Stress accumulation→ Foreshock sequence→ EARTHQUAKE→ Stress drop→ Regional deformation →Quiescence→…

In other words, if all earthquakes are caused by precursory stress accumulation the current logic requires that the seismicity in the region should increase *before* the main shock, not afterwards. The reason is the Coulomb failure criterion

$$\tau = \sigma \tan\Phi + c,$$

where the stress σ on the fault builds up gradually with time while the shear strength τ remains constant. Here $\tan\Phi$ is the coefficient of internal friction and c is the cohesion. The hypothesis of stress buildup before earthquakes remains a fundamental feature of earthquake theory.

But the Coulomb failure criterion admits two symmetrically opposite interpretations: (1) the regional stress σ increases in time until it matches or exceeds the constant strength τ of the fault, or (2) the shear strength τ of the fault decays in time until it is overcome by the stationary regional stress σ. Symmetry with respect to time translation yields conservation of energy, as predicted by a famous theorem of Noether (1918): "Every differentiable symmetry in a physical system must be associated with a conserved quantity".

The Cocos plate subducts the North America plate at a relative convergence rate of 6 cm/yr in the N34°E direction (DeMets *et al.*, 1990). The stochastic process described above is merely a random discretization of the steady-state subduction process. The physics of this process requires that fluctuations in the state of stress will be consistent with the Second Law of Thermodynamics: "Earth system processes perform work by degrading sources of free energy, thereby producing entropy" (Kleidon and Lorenz, 2005). This fits the Coulomb failure criterion in its second interpretation, i.e., the shear strength τ of the fault decays in time until it is overcome by the stationary regional stress σ.

What could be the cause of fluctuations in strength on the subduction zone? The answer has to do with the ubiquitous process of stress corrosion in the presence of water. In the active Guerrero subduction zone segmentation is closely related to water content (Husker and Davis, 2009). After a major earthquake the rupture heals at a roughly constant rate with a half-life of 20 years (Castaños *et al*., 2013). Aftershocks are related to the healing process, so that the aftershock region is about the same as the rupture region which has not yet healed.

Summary and Conclusions

The 2012 Ometepec-Pinotepa Nacional nucleated about 5 km offshore, near the border between the states of Guerrero and Oaxaca, at a depth of about 20 km. The epicenter reported by NEIC is 58 km toward N40°E. This large difference in the location is partly due to weak beginning of the earthquake so that *P* phase read at local and regional distances may not correspond to that read at teleseismic distances. In addition, there are such factors as teleseismic station distribution and the velocity structure of the subduction zone which cause a systematic bias of the NEIC epicenters of Mexican earthquakes to be shifted towards the NE (see, e.g., Singh and Lermo, 1985).

As a consequence of the mislocation mentioned above, the area of slip distribution mapped from inversion of teleseismic waves by different groups is also shifted to the NE with respect with the one mapped from our inversion of local displacement seismograms. Our preliminary inversion of teleseismic data, using the hypocenter reported here and time shifting discussed above, agrees well with the inversion of the local data. The inversion of local data reveals two patches of large slip, one updip towards SW of the hypocenter and the other downdip to the N. The slip is small near the hypocenter during the first 4 s of rupture. This seems to suggest that the earthquake nucleated in an area of low strength and little strain accumulation. The rupture then broke two stronger asperities. Significant slip extends 25 km updip and 35 km downdip from the coast, and for a length of about 25 km along the strike. This defines a rupture area of about 25 km × 60 km.

Our slip area roughly coincides with the 30-hour aftershock area. We note that there is relative lack of aftershocks near the hypocenter where the slip is small, as well as in the areas of large slip. This is a pattern reported for many earthquakes (see Das and Henry, 2003 for a review). The aftershocks of the 2012 earthquakes cluster in several patches; in addition a large number of them are aligned in the northeast direction towards the station PNIG. This may be related to heterogeneities on the plate interface related to the subducting bathymetric features. The earthquake produced unusually large number of aftershocks, suggesting more heterogeneous interface on this segment than others along the Mexican subduction zone west of 95°W. We note, however, that neither the NE alignment of the aftershocks nor the two patches of large slip coincide with the prolongation of the sea mounts inland.

Although the aftershock areas of 2012 and 1982 doublet roughly overlap, the sum of the seismic moments of the doublet is only about 1/3 that of the 2012 earthquake. Thus, the two events are not a repeat of each other. The 2012 event may have ruptured the doublet fault area plus an additional area, suggesting a variable rupture mode.

The region is an excellent laboratory to study different seismic phenomena related to the subduction process. As sketched in Figure 16, the plate interface can be divided in three domains based on their seismic characteristics. This division is similar to the conceptual model proposed by Lay *et al.* (2012). Moderate to large thrust earthquakes (M ~ 6-7), accompanied by large number of aftershocks, occur on the uppermost "slow earthquake" domain. This domain extends from the trench up to a downdip distance of about 35 km (depth ≤ 15 km). The earthquakes are characterized by low radiated energy to seismic moment ratio, E_s/M_0. They also give rise to very low accelerations. A part of the area in this domain may either be creeping (stable sliding) or may be partially locked. The next domain covers a distance range of 35 to 100 km from the trench and depth range of 15-25 km. It is seismically coupled and ruptures in large earthquakes (M ~7-7.5). A fraction of the area is conditionally stable and slips during large events. The domain further downdip, in the distance range of 100 to 200 km from the trench, is very likely the site of slow seismic events (SSEs) and nonvolcanic tremors (NVTs). SSEs and NVTs have been reported in the instrumented adjacent areas of Guerrero to the northwest (*e.g.*, Kostoglodov *et al.,* 2003, 2010; Payero *et al.,* 2008) and central Oaxaca to the southeast (Brudzinski *et al.*, 2007, 2010). These phenomena have not yet been documented in Ometepec-Pinotepa Nacional region which presently lacks adequate instrumentation.

It is possible that the 2012 earthquake was triggered by the SSE which occurred in the adjacent southeast region during late 2011 and mid-2012 (Graham *et al.*, 2012). At present the details of temporal and spatial evolution of the SSE is not available. We note, however, that the earthquake nucleated offshore, probably more than 75 km updip from the region of SSE. Furthermore, one of the patches of large slip was updip from the hypocenter. To establish a causal relation between the two events, these observations would have to be satisfactorily explained.

The earthquake produced the first recording in which the *PGA* exceeded 1 g above the Mexican subduction zone. It was, however, at a soft site. From a seismic engineering point of view, it is reassuring that the observed *PGA* as function of distance is well-explained by ground motion prediction equation derived from Mexican data. The earthquake was strongly felt in Mexico City. The *PGA* at CU, a typical hill-zone site, and at SCT, a representative lake-bed zone site, was 12 and 20 gal, respectively. These *PGA*s were not unusually large; they occur once in about 3 years.

Acknowledgments

UNAM Seismology Group includes all researchers and technicians, as well as students, of Institute of Geophysics and Institute of Engineering, UNAM, who work in the field of seismology and engineering seismology. In case of a significant earthquake in Mexico, the Group informally coordinates its efforts in data collection from autonomous stations, field deployment of seismographs and accelerographs, analysis of the

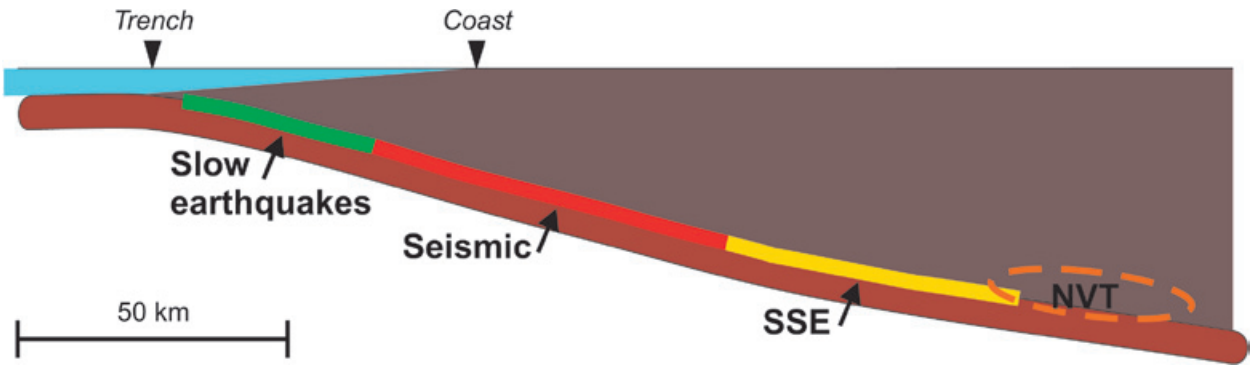

Figure 16. A schematic section along line AB in Figure 1. The plate interface is divided in three domains. Green line: upper most domain which extends up to 35 km from the trench (depth range 5-15 km). Earthquakes (M ~6-7) in this domain have low (E_s/M_0), give rise to low *PGA*, and generate many aftershocks. This domain is marked "slow earthquakes" in the figure. Red line: domain of seismic coupling where large earthquakes (M ~7-7.5) occur (marked "seismic" in the figure). It extends from 35 to 100 km from the trench (depth range 15 to 25 km). Yellow line: domain of slow slip events (SSE) and nonvolcanic tremor (NVT). Extends from 100 to 200 km from the trench (depth >25 km).

data, and elaboration of a preliminary report. The credit of the work is shared by all.

We thank Civil Protection authorities of the State of Oaxaca, Centro de Instrumentación y Registros Sísmicos (CIRES) and Centro Nacional de Prevención de Desastres (CENAPRED) for making available to us the recordings of the mainshock. We are indebted to H. Kanamori for sharing his unpublished results with us and for many fruitful discussions on the 2012 earthquake during his visit to UNAM in August 2012**.** We appreciate comments and suggestions by H. Kanamori, L. Astiz, R. Castro and C. Mendoza who were reviewers of the manuscript. The research was supported by Conacyt project 82599, and PAPIIT-UNAM projects IN112411 and IN111411-2.

Bibliography

Anderson J.G., Brune J.N., Prince J., Quaas R., Singh S.K., Almora D., Bodin P., Oñate M., Vásquez R., Velasco J.M., 1994, The Guerrero accelerograph network. *Geofísica Internacional*, 33, 341-372.

Anderson J.G., Singh S.K., Espíndola J.M., Yamamoto J., 1989, Seismic strain release in the Mexican subduction thrust. *Phys. Earth Planet. Inter.*, 58, 307-322.

Arroyo D., García D., Ordaz M., Mora M.A., Singh S.K., 2010, Strong ground-motion relations for Mexican interplate earthquakes. *J. Seismol.*, Doi 10.1007/s10950-010-9200-0.

Astiz L., Kanamori H., 1984, An earthquake doublet in Ometepec, Guerrero, Mexico. *Phys. Earth Planet. Inter.*, 34, 24-45.

Astiz L., Kanamori H., Eissler H., 1987, Source characteristics of earthquakes in the Michoacan seismic gap in Mexico. *Bull. Seismol. Soc. Am.*, 77, 1326-1346.

Boatwright J., Choy G.L., 1986, Teleseismic estimates of the energy radiated by shallow earthquakes. *J. Geophys. Res.*, 91, 2095-2112.

Bouchon M., 1982, The complete synthetics of crustal seismic phases at regional distances. *J. Geophys. Res.*, 87, 1735-1741.

Brudzinski M.R., Cabral-Cano E., Correa-Mora F., DeMets C., Márquez-Azúa B., 2007, Slow slip transients along the Oaxaca subduction segment from 1993 to 2007. *Geophys. J. Int.*, 171, 523-538, DOI:10.1111/j.1365-246X.2007.03542.x.

Brudzinski M.R., Hinojosa-Prieto H.R., Schlanser K.M., Cabral-Cano E., Arciniega-Ceballos A., Diaz-Molina O., DeMets C., 2010, Nonvolcanic tremor along the Oaxaca segment of the Middle America subduction zone. *J. Geophys. Res.*, 115, B00A23, doi:10.1029/2008JB006061.

Castaños H., Joshi A., Lomnitz C., Zhang C.-J., 2013, Famous failures: A natural history of disaster, in *Extreme Events*, AGU Monographs, in press.

Chael E.P., Stewart G.S., 1982, Recent large earthquakes along the middle American trench and their implications for the subduction process. *J. Geophys. Res.*, 87, 329-338.

Cotton F., Campillo M., 1995, Inversion of strong ground motion in the frequency domain: application to the 1992 Landers, California earthquake. *J. Geophys. Res.*, 100, 3961-3975.

Courboulex F., Singh S.K., Pacheco J.F., Ammon C., 1997, The 1995 Colima-Jalisco, Mexico, earthquake (Mw 8): A study of the rupture process. *Geophys. Res. Lett.,* 34, 1019-1022.

Das S., Henry C., 2003, Spatial relation between main earthquake slip and its aftershock distribution. *Rev. Geophys.*, 3-1 - 3-23, doi: 10.1029/2003RG000119.

DeMets C., Gordon R.G., Argus D.F., Stein S., 1990, Current plate motions, *Geophys. J. Int.*, 101, 427-478.

Eshelby J.D., 1957, The determination of the elastic field of an ellipsoidal inclusion, and related problems. *Proceedings of the Royal Society of London, Series A*, 241, 376-396.

Graham S., Cabral Cano E., Kostoglodov V., Cotte N., Radiguet M., Walpersdorf A., Santiago J.A., Brudzinski M., McCaffrey R., DeMets C., 2012, Animations and modeling of the 2012 slow slip event beneath southern Mexico and the accompanying 20 March 2012 Mw=7.4 Ometepec earthquake. UGM Reunión anual 2012; *GEOS*, *Unión Geofísica Mexicana*, 32, 263.

Gregorius T., 1996, Gipsy–OASIS II How it works, manual for class of GIPSY. Jet Propulsion Laboratory, California Institute of Technology, Pasadena, EUA.

Havskov J., Ottemöller L., 1999, Electronic Seismologist: SeisAn earthquake analysis software. *Seism. Res. Lett.*, 70, 532-534.

Havskov J., Singh S.K., Nava E., Dominguez T., Rodriguez M., 1983, Playa Azul, Michoacan, Mexico, earthquake of 25 October 1981 (Ms = 7.3). *Bull. Seismol. Soc. Am.*, 73, 449-457.

Hernandez B., Shapiro N., Singh S.K., Pacheco J., Cotton F., Campillo M., Iglesias A., Cruz V., Gómez J.M., Alcántara L., 2001, Rupture history of September 30, 1999 intraplate earthquake of Oaxaca, Mexico (Mw=7.5) from inversion of strong motion. *Geophys. Res. Lett.*, 28, 363-366.

Husker A., Davis P.M., 2009, Tomography and thermal state of the Cocos plate subduction beneath Mexico City. *J. Geophys. Res.*, 114, B04306 doi:10.1029/2008JB006039.

Iglesias A., Cruz-Atienza V.M., Shapiro N.M., Singh S.K., Pacheco J.F., 2001, Crustal structure of south-central Mexico estimated from the inversion of surface-wave dispersion curves using genetic and simulated annealing algorithms. *Geofísica Internacional*, 40, 181-190.

Iglesias A., Singh S.K., Pacheco J.F., Alcántara L., Ortiz M., Ordaz M., 2003, Near trench Mexican earthquakes have anomalously low peak accelerations. *Bull. Seismol. Soc. Am.*, 93, 953-959.

Iglesias A., Singh S.K., Pacheco J.F., Ordaz M., 2002, A source and wave propagation study of the Copalillo, Mexico, earthquake of 21 July 2000 (Mw 5.9): Implications for seismic hazard in Mexico City from inslab earthquakes. *Bull. Seismol. Soc. Am.*, 92, 1060-1071.

Ji C., Wald D.J., Helmberger D.V., 2002a, Source description of the 1999 Hector Mine, California, earthquake, Part I: Wavelet domain inversion theory and resolution analysis. *Bull. Seismol. Soc. Am*., 92, 1192-1207.

Ji C., Wald D.J., Helmberger D.V., 2002b, Source description of the 1999 Hector Mine, California, earthquake, Part II: Complexity of slip history. *Bull. Seismol. Soc. Am*., 92, 1208-1226.

Juárez García H., Gómez Bernal A., Rangel Núñez J.L., Tena-Colunga A., Roldán Islas J., Pelcastre Pérez E., 2012, Learning from earthquakes: The March 20, 2012, Ometepec, Mexico earthquake. EERI Special Earthquake Report.

Kanamori H., McNally K.C., 1982, Variable rupture mode of the subduction zone along the Ecuador-Colombia coast. *Bull. Seismol. Soc. Am.*, 72, 1241-1253.

Kanjorski N.M., 2003, Cocos plate structure along the middle America subduction zone off Oaxaca and Guerrero, Mexico: Influence of subducting plate morphology on tectonics and seismicity. Ph. D. thesis University of California, San Diego.

Kleidon A., Lorenz R.D., 2005, Entropy production in Earth system processes, in *Non-equilibrium Thermodynamics and the Production of Entropy,* A. Kleidon and R.D. Lorenz, eds., Springer, New York.

Kostoglodov V., Husker A., Shapiro N.M., Payero J.S., Campillo M., Cotte N., Clayton R., 2010, The 2006 slow slip event and nonvolcanic tremor in the Mexican subduction zone. *Geophys. Res. Lett*., 37, doi: 10.1029/2010GL045424.

Kostoglodov V., Singh S.K., Santiago J.A., Larson K.M., Lowry A.R., Bilham R., 2003, A large silent earthquake in the Guerrero seismic gap, Mexico. *Geophys. Res. Lett*., 15, doi:10.1029/2003GL017219.

Lay T., Kanamori H., Ammon C.J., Koper K.D., Hutko A.R., Ye L., Yue H., Rushing T.M., 2012, Depth-varying rupture properties of subduction zone megathrust faults. *J. Geophys. Res.*, 117, B4, doi:10.1029/2011JB009133.

Lienert B.R., Havskov J., 1995, A computer program for locating earthquakes both locally and globally. *Seism. Res. Lett.*, 66, 26-36.

Nava E., 1984, Estudio de los temblores de Ometepec del 7 de junio de 1982, y sus replicas. Tesis Licenciatura (Ingeniero Geofísico), Facultad de Ingeniería, UNAM.

Nishenko S.P., Singh S.K., 1987, The Acapulco-Ometepec, Mexico, earthquakes of 1907-1982: Evidence for a variable recurrence history. *Bull. Seismol. Soc. Am.*, 77, 1359-1367.

Noether E., 1918, Invariante Variationsprobleme, *Nachr. König. Gesellsch.Wiss., Göttingen, Math-phys. Klasse***,** 235–257.

Núñez-Cornú F.J., Ortiz M., Sánchez Aguilar J.J., 2008, The great 1787 Mexican tsunami, *Nat. Hazards*, doi:10.1007/s11069-008-9239-1.

Núñez-Cornú F., Ponce L., 1989, Zonas sísmicas de Oaxaca, México: Sismos máximos y tiempos de recurrencia para el período 1542-1988. *Geofísica Internacional*, 28, 587-641.

Pacheco J.F., Singh S.K., 2010, Seismicity and state of stress in Guerrero segment of the Mexican subduction zone. *J. Geophys. Res.*, 115, B01303, doi:10.1029/2009JB006453.

Pacheco J.F., Singh S.K., Domínguez J., Hurtado A., Quintanar L., Jiménez Z., Yamamoto J., Gutiérrez C., Santoyo M., Bandy W., Guzmán M., Kostoglodov V., Reyes G., Ramírez C., 1997, The October 9, 1995 Colima-Jaslico,

Mexico earthquake (Mw 8): An aftershock study and a comparison of this earthquake with those of 1932. *Geophys. Res. Lett.*, 24, 2223-2226.

Payero J.S., Kostoglodov V., Shapiro N., Mikumo T., Iglesias A., Pérez-Campos X., Clayton R.W., 2008, Nonvolcanic tremor observed in the Mexican subduction zone. *Geophys. Res. Lett*., 35, L07305, doi: 10.1029/2007GL032877.

Pérez-Campos X., 2002, A comprehensive study of the seismic energy. Ph. D. Thesis, Stanford University.

Pérez-Campos X., Beroza G.C., 2001, Mechanism dependent scaling of radiated seismic energy. *J. Geophys. Res.*, 106, 11,127-11,136.

Pérez-Campos X., Singh S.K., Beroza G.C., 2003, Reconciling teleseismic and regional estimates of seismic energy, *Bull. Seism. Soc. Am.*, 93, 2123-2130.

Quintanar L., 1985, Variaciones espacio–temporales de la sismicidad en la región costera de Oaxaca de 1950 a 1982 (mb 4.3). *Master's thesis*, Facultad de Ciencias; Universidad Nacional Autónoma de México, México D.F., México.

Reyes A., Brune J.N., Lomnitz C., 1979, Source mechanism and aftershock study of the Colima, Mexico earthquake of January 30, 1973. *Bull. Seismol. Soc. Am.*, 69, 1819-1840.

Singh S.K., Havskov J., Astiz L., 1981, Seismic gaps and recurrence periods of large: A reexamination earthquakes along the Mexican subduction zone. *Bull. Seismol. Soc. Am.*, 71, 827-843.

Singh S.K., Havskov J., McNally K., Ponce L., Hearn T., Vassiliou M., 1980, The Oaxaca, Mexico earthquake of 19 November, 1978: A preliminary report on aftershocks. *Science*, 207, 1211-1213.

Singh S.K., Lermo J., 1985, Mislocation of Mexican earthquakes as reported in international bulletins. *Geofísica Internacional*, 24, 333-351.

Singh S.K., Mortera F., 1991, Source-time functions of large Mexican subduction earthquakes, morphology of the Benioff age of the plate and their tectonic implication. *J. Geophys. Res.*, 96, 21487-21502.

Singh S.K., Ordaz M., Rodríguez M., Quaas R., Mena E., Ottaviani M., Anderson J.G., Almora D., 1989, Analysis of near-source strong motion recordings along the Mexican subduction zone. *Bull. Seismol. Soc. Am.,* 79, 1697-1717.

Singh S.K., Pacheco J.F., Alcántara L., Reyes G., Ordaz M., Iglesias A., Alcocer S.M., Gutierrez C., Valdés C., Kostoglodov V., Reyes C., Mikumo T., Quass R., Anderson J.G., 2003, A preliminary report on the Tecomán, Mexico earthquake of 22 January 2003 (Mw 7.4) and its effects. *Seismol. Res. Lett.*, 74, 279-289.

Singh S.K., Rodríguez M., Esteva L., 1983, Statistics of small earthquakes and frequency of occurrence of large earthquakes along the Mexican subduction zone. *Bull. Seismol. Soc. Am.*, 73, 1779-1796.

Singh S.K., Suárez G., 1988, Regional variation in the number of aftershocks (mb ≥ 5) of large, subduction-zone earthquakes (Mw ≥ 7.0). *Bull. Seismol. Soc. Am.*, 78, 230-242.

Suárez G., Albini P., 2009, Evidence for great tsunamigenic earthquakes (M 8.6) along the Mexican subduction zone. *Bull. Seismol. Soc. Am.*, 99, 892–896.

UNAM Seismology Group, 1986, The September 19, 1985, Michoacan earthquake: Aftershock distribution and history of rupture. *Geophys. Res. Lett.*, 13, 573-576.

Valdés-González C., Novelo-Casanova D.A., 1998, The Western Guerrero, Mexico, seismogenic zone from the microseismicity associated to the 1979 Petatlan and 1985 Zihuatanejo earthquakes. *Tectonophysics*, 287, 271-277.

Yamamoto J., Quintanar L., Jimenez Z., 2002, Why earthquake doublets in the Ometepec, Guerrero, Mexico subduction area? *Phys. Earth Planet. Inter.*, 132, 131-139.

Yamamoto J., González-Moran T., Quintanar L., Zavaleta A.B., Zamora A., Espindola V.H., 2013, Seismic pattern of the Guerrero-Oaxaca, Mexico región, and its relationship to the continental margin structure. *Geophys. J. Int.*, 192, 375-389, DOI:10.1093/gji/ggs025.